Surface functionalized iron oxide nanoparticles for applications in biomedical sciences

Joel Kuhn

Submitted for the degree Doctor of Philosophy

Heriot-Watt University

School of Engineering and Physical Sciences

May 2021

Abstract

This thesis focuses on the functionalization of iron oxide nanoparticles (Fe_3O_4) and their applications in biomedical sciences. Each chapter represents an independent research project that has been conducted within a different collaboration. For each project, magnetic Fe_3O_4 iron oxide nanoparticles have been functionalized or modified to suit its requirements. This thesis aims to show how versatile and most promising Fe_3O_4 iron oxide nanoparticles are, and how their unique properties in size, shape, and magnetism can be utilized for a broad range of applications in biomedicines.

Chapter 2 focuses on magnetic resonance (MR), computed tomography (CT), and intravascular ultrasound (IVUS) as essential diagnostic imaging techniques and how iron oxide nanoparticles can potentially be used as contrast agents across all three imaging modalities. Contrast agents are commonly used to enhance the imaging quality and thus provide more detail for assessment. However, previous studies using nanoparticles for MR and CT were prepared with surface coating stabilizers, which in turn can compromise the use in clinical studies. In this chapter, gold-iron oxide nanoparticles (Au*MNP) are presented as a multi-modal contrast agent. Using a chemically grafting method without stabilizers, presenting nanoparticles with pristine surfaces that allow for further functionalization in molecularly targeted theragnostic applications.

In Chapter 3, the response of HepaRG liver cells to nanoparticles is examined in two methods, 2D and 3D cell culturing. By analyzing the cell response in 2D and 3D cultures an accurate estimation of the toxicity of nanoparticles can be made. The toxicity of iron oxide was assessed using commercially available cell assays (CellTiter-Glo and PrestoBlue), however, the experiments suggested some restrictions that could alter the data and therefore resemble inaccurate results. For this purpose, non-invasive imaging techniques based on impedance (xCELLigence system) and Coherent Anti-Stokes Raman Scattering (CARS) were used to analyze the cell toxicity. The results showed that those methods provided a much deeper insight into the cell viability and proliferation of HepaRG cells. Furthermore, valuable data on the immediate effects in real-time and long-term exposures can be captured of the same culture.

Chapter 4 presents the cell internalization process of iron oxide nanoparticles, captured using the unique holographic cell imaging technique of a HoloMonitor M4 microscope. In most cases where the cell internalization process is monitored, only one or two cells can be visualized and tracked at the same time. This is not the case with this technique, where hundreds of cells can be simultaneously visualized, analyzed, and monitored over time. Unlike single-cell observation, the system takes pictures of the cell culture at a high capture rate, allowing to observe and interpret the cell dynamics, cell morphologies, and cell reactions to nanoparticles (e.g., toxicity and apoptosis). Measuring the kurtosis and skewness of MCF-7 cancer cells for 72 hours after nanoparticle exposure, showed that cell splitting and proliferation took place, and no extraordinary

damages or cell death was caused by the internalization of the particles. Furthermore, every step of the internalization process was monitored and captured in visible data for the first time.

Chapter 5 demonstrates magnetic molecularly imprinted polymer networks and spheres (MMIPs) for the selective binding of antibiotics. MIPs are polymers that can be synthesized with highly selective and reusable binding sites. Their combination with magnetic iron oxide can be used as a useful tool to monitor and remove antibiotic pollutants from freshwater sources and food products. MMIPs are prepared using a microemulsion technique containing vinyl-functionalized iron oxide to selectively bind the model antibiotics erythromycin (ERY) and ciprofloxacin (CPX). The results show that MMIPs prepared using this technique are highly selective towards their respective template molecule in methanol/water and milk matrix, are recyclable, and most importantly open to modification.

In Chapter 6, zebrafish larvae are exposed to polyethylene glycol coated iron oxide supported gold nanoparticles for further toxicity assessment. In general, toxicological data is gathered *in vivo*, however, the translational values from *in vitro* to *in vivo* are sometimes questionable due to the complexity of the organism. Zebrafish larvae are used as an intermediate method for *in vivo* experiments, as they can be used 96 hours after hatching, unlike larger animals such as mice, rats, or rabbits which take a much longer time to reach adulthood, sometimes up to 3 months. Also, a single female zebrafish can spawn about 200-300 eggs per week, which can generate an extensive data set from a small-scale experimental setup. The results presented in this chapter showed a 100% survival rate of all exposed zebrafish larvae between a range of concentrations from 0 - 2mM (0 - 463.1 mg/L).

Chapter 7 summarizes the key findings and developments presented in this thesis, suggestions for future work within each research project, and proposes future applications.

Chapter 8 includes a list of journal publications produced from this thesis.

Dedication

I dedicate this thesis to my parents, Eberhard Joachim Kuhn and Lorefil Kuhn, who have given me strength and support throughout my whole life and never held back to share god's love with me.

Acknowledgments

Table of contents

CHAPTER 3

Impedance-based measurements and CARS imaging as advanced techniques to assess the cytotoxicity of nanomaterials on liver cells *in vitro*.

CHAPTER 4

Monitoring the cell internalization of iron oxide nanoparticles using a holographic imaging system

CHAPTER 5

Magnetic molecularly imprinted polymer networks and spheres (MMIPs) for the selective binding of antibiotics

CHAPTER 6

Zebrafish larvae as *in vivo* model system for the characterization of iron oxide supported gold nanoparticles with polyethylene glycol coating

CHAPTER 7

Key findings and developments, future work, and possible applications

CHAPTER 8

Journal publications produced from this thesis

Research Thesis Submission

Please note this form should be bound into the submitted thesis.

Name:	Joel Kuhn		
School:	Engineering and Physical Sciences		
Version: *(i.e. First, Resubmission, Final)*	Final	Degree Sought:	Doctor of Philosophy

Declaration

In accordance with the appropriate regulations I hereby submit my thesis and I declare that:

1. The thesis embodies the results of my own work and has been composed by myself
2. Where appropriate, I have made acknowledgement of the work of others
3. The thesis is the correct version for submission and is the same version as any electronic versions submitted*.
4. My thesis for the award referred to, deposited in the Heriot-Watt University Library, should be made available for loan or photocopying and be available via the Institutional Repository, subject to such conditions as the Librarian may require
5. I understand that as a student of the University I am required to abide by the Regulations of the University and to conform to its discipline.
6. I confirm that the thesis has been verified against plagiarism via an approved plagiarism detection application e.g. Turnitin.

ONLY for submissions including published works
Please note you are only required to complete the Inclusion of Published Works Form (page 2) if your thesis contains published works)
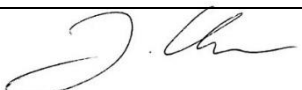
7. Where the thesis contains published outputs under Regulation 6 (9.1.2) or Regulation 43 (9) these are accompanied by a critical review which accurately describes my contribution to the research and, for multi-author outputs, a signed declaration indicating the contribution of each author (complete)
8. Inclusion of published outputs under Regulation 6 (9.1.2) or Regulation 43 (9) shall not constitute plagiarism.

* *Please note that it is the responsibility of the candidate to ensure that the correct version of the thesis is submitted.*

Signature of Candidate:		Date:	11.05.2021

Submission

Submitted By *(name in capitals):*	JOEL KUHN
Signature of Individual Submitting:	
Date Submitted:	17.05.2021

For Completion in the Student Service Centre (SSC)

Limited Access	Requested	Yes		No		Approved	Yes		No	
*E-thesis Submitted (**mandatory for final theses**)*										
Received in the SSC by *(name in capitals):*					Date:					

Inclusion of Published Works

Declaration

This thesis contains one or more multi-author published works. In accordance with Regulation 6 (9.1.2) I hereby declare that the contributions of each author to these publications is as follows:

Citation details	J. Kuhn, G. Aylaz, E. Sari, M. Marco, H. H. P. Yiu, and M. Duman, Selective binding of antibiotics using magnetic molecular imprint polymer(MMIP) networks prepared from vinyl-functionalized magnetic nanoparticles, J. Hazard. Mater., **2020**, 387, 121709.
Author 1	J. Kuhn (research and writing)
Author 2	G. Aylaz (research and writing)
Signature:	
Date:	31.07.2020

Citation details	J. Kuhn, G. Papanastasiou, C-W. Tai, CM Moran, MA, Jansen, AAS Tavares, RJ Lennen, CA Corral, CJ Wang, AJW Thomson, CC Berry, HHP Yiu, Tri-modal imaging of gold-dotted magnetic nanoparticles for magnetic resonance imaging, computed tomography, and intravascular ultrasound: an *in vitro* study, Nanomedicine, **2020**, 15, 2433-2445.
Author 1	J. Kuhn (research and writing)
Author 2	G. Papanastasiou (research and writing)
Signature:	
Date:	26.08.2020

Citation details	G. Aylaz, J. Kuhn, ECHT Lau, C-C Yeung, VAL Roy, M. Duman, HHP Yiu, Recent developments on magnetic molecular imprinted polymers (MMIPs) for sensing, capturing, and monitoring pharmaceutical and agricultural pollutants, J. Chem. Technol. Biotechnol., **2021**, 96, 1151-1160.
Author 1	G. Aylaz (research and writing)
Author 2	J. Kuhn (research and writing)
Signature:	
Date:	11.02.2020

CHAPTER 1

1.1. Introduction

Research on magnetic nanoparticles (MNPs) is becoming increasingly important for many industrial and scientific communities, such as chemistry, material science, and particularly biochemistry and biomedicine [1.1]. Due to their sizes ranging from 1 to 100 nm, nanoparticles have shown unique, specific, and controllable properties when compared to macroscopic-sized particles. A significant change of the particles properties takes place when the particle sizes are reduced from macro- to nanoscale, where the particles now present unique optical, electronic, magnetic, and physicochemical properties [1.1-1.14].

For various research fields and industries, iron oxide nanoparticles have established themselves as one of the most promising nanoparticles. Iron oxide is a mineral compound that can be found throughout nature [1.16], has a crystalline structure, and occurs with different structural and magnetic properties [1.17]. Hematite and magnetite are the main forms of iron oxide and their crystal structure can be "defined in terms of close-packed planes of oxygen anions with iron cations in octahedral or tetrahedral interstitial sites" (Figure 1.1) [1.18-1.21].
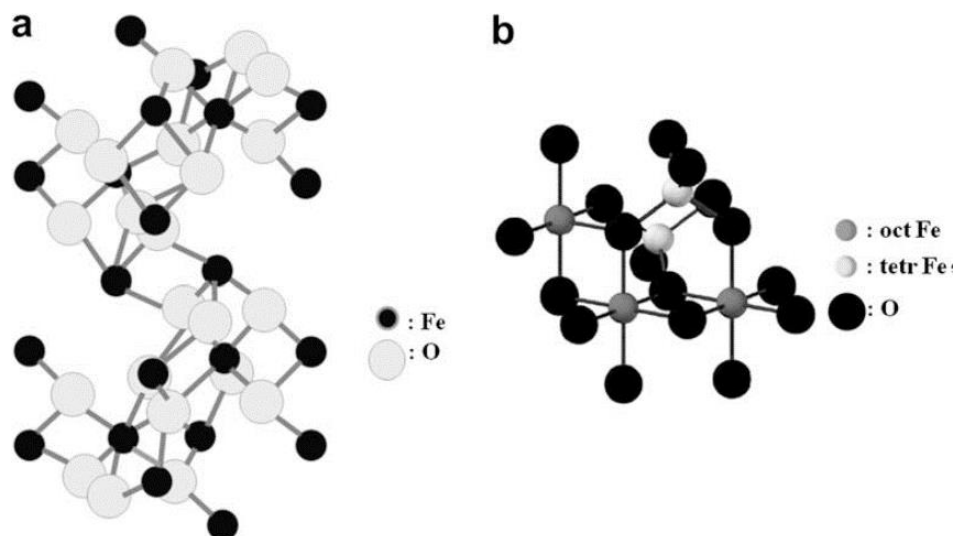
Figure 1. 1: Crystal structure of (a) hematite, which has a rhombohedral centred hexagonal structure and a close-packed oxygen lattice, in which two-thirds of the octahedral sites are occupied by Fe^{3} ions and (b) magnetite with a cubic shape, where four main oxygen atoms are arranged in a regular tetrahedron about the divalent atom. [1.20., 1.22.].

Much research has been done to exploit the unique properties of iron oxide nanoparticles [1.15-1.21]. Ultimately leading to an increase of nanoparticles entering the commercial market each year [1.23]. The nanoparticles have been functionalized, optimized, and modified in their properties to suit various industrial needs and are frequently added to new products in catalysis, pigments, food additives, sunscreens, cosmetics, and many more [1.24].

As magnetic nanoparticles have a nontoxic metal constituent, high biocompatibility, and a large surface area, which allows for manipulation and functionalization, especially biochemistry and biomedicines are embracing a novel and very promising research area. Biosciences have already successfully utilized iron oxide nanoparticles for magnetic cell labeling, cell separation, tracking or immobilization, and therapeutic purposes in hyperthermia or drug delivery [1.6-1.8]. Diagnostic purposes, such as magnetic iron oxide nanoparticles as contrast agents for magnetic resonance imaging (MRI) are currently under intense investigation [1.9, 1.10.] Furthermore, iron oxide nanoparticles showed great potential for targeted drug or gene delivery for cancer treatment and therapy [1.11-1.14.]. However, the vast amount of iron oxide nanoparticle-based applications has not reached its maximum yet and more research areas could benefit from its unique qualities. Based on the requirements, iron oxide can be synthesized and functionalized in various ways like no other nanomaterial.

1.2. Synthesis

Most used magnetic iron oxide nanoparticles for biomedical applications and nanomedicines have a core size between 5 nm and 100 nm. Some of them have been clinically tested and were commercialized for use *in vivo*. Controlling the growth of the crystal structure is a key factor for well-prepared iron oxide-based MNPs. For instance, Do et al. reported that the amount of PEI showed considerable effects on the size of metal oxide nanoparticles and their clusters [1.25]. With this size and cluster controlling property polyethyleneimine can be regarded as an active stabilizer for the synthesis of magnetic iron oxide nanoparticles. Nowadays, there are plenty of guides and reported methods for their synthesis. Whether they are prepared through hydrothermal synthesis, micro emulsion, or co-precipitation, they all have their advantages and disadvantages [1.26-1.28]. It is obligatory to choose the correct method for the right purpose and intended use of the magnetic iron oxide nanoparticles. When choosing the synthetic pathway, it is important to consider appropriate reaction conditions, firstly to avoid losing the desired functionalization but also to achieve the best results in terms of the required quantity of MNPs, their particle size, and size distribution.

Thermal decomposition in the presence of surfactants leads to a synthesis of magnetic nanoparticles with a small size lower than 10 nm [1.29]. Fe_3O_4 can be prepared by heating iron (III) acetylacetonate ($Fe(acac)_3$) to over 250 °C in the presence of a chelating surfactant, which controls the growth of Fe_3O_4 during decomposition. Oleic acid is very suitable as a surface-active chelating agent as it possesses a hydrophilic head, which can form coordination bonds with metal ions [1.29].

Co-precipitation is the easiest synthesis pathway for good results in the quantity and quality of Fe_3O_4 magnetic nanoparticles. It is a simple one-step method with a reaction time within 24 hours and the product is easy to isolate. The following pictures (Picture 1, a and 1, b) demonstrate the simplicity of separating Fe_3O_4 magnetic nanoparticles from toluene by using a NdFeB magnet.
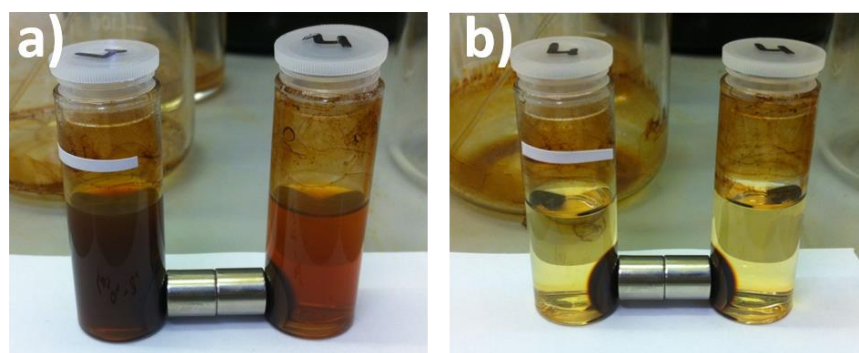
Picture 1: Separation of iron oxide nanoparticles in toluene by the external application of a NdFeB magnet; captured at $t_1=1$ second and $t_2=3$ seconds.

However, the co-precipitation must react under an inert environment (N_2, He_2, etc.) to prevent Fe_3O_4 NP's from oxidizing to Fe_2O_3 by atmospheric air. [1.27] Co-precipitation with fast mixing means adding a base into an aqueous solution of iron (II) and iron (III) salt to form nano-scaled crystals of Fe_3O_4. The mixing rate, reaction temperature, and the presence of a polymer, which hinders the growth of Fe_3O_4 crystals, allow to control and influence their size.

Synthesizing iron oxide nanoparticles by **micro emulsion** can be carried out following the same principle as co-precipitation. In this method, the growth of nanocrystals is controlled using micelles in a water-in-oil emulsion. Those micelles are the result of a self-assembling surfactant to some specific nanostructures on the interface of a two-phased mixture. Using a water-in-oil emulsion is a possibility to prepare magnetic iron oxide nanoparticles with a narrow size lower than 10 nm [1.27].

After comparing the three methods above by their effectiveness in MNP production, co-precipitation is the only one that can be extended up to a kilogram level. However, magnetic nanoparticles prepared on large scale tend to have wider size distributions of around 50 ± 10 nm.

1.3. Iron oxide nanoparticles for biomedical applications

As previously mentioned, nano-scaled iron oxide has unique properties which can be utilized in many ways. By coating or grafting certain chemicals onto the surface of the nanoparticles (functionalization), the properties and characteristics of the nanoparticle are changed and can be used for the intended purpose. Table 1 shows a list of Fe_3O_4 nanoparticles that have been functionalized with specific functional molecules, so they can be utilized for their various biomedical applications.

Table 1: Examples of functionalized magnetic nanoparticles with bioactive species for their individual biomedical applications [1.30].

Coating material	MNP type	Specific functional molecule	Application
Dextran	Fe_3O_4	Transferrin	Targeted MRI [1.31]
	γ-Fe_2O_3 (10 nm)	Folic acid	Magnetic hyperthermia [1.32.]
Chitosan	Fe_3O_4 (20 nm)		MRI [1.33.]
	Fe_3O_4 (8-11 nm)	Papain	Biocatalysis [1.34.]
	Fe_3O_4 (10-16 nm)	FITC	Fluorescence imaging [1.35.]
Starch	Fe_3O_4 (8 nm)	AGKGTPSLETTP peptide (A54) and doxorubicin	Drug delivery (doxorubicin) [1.36.]
Polylysine	Fe_3O_4 (35 nm)		Cell labelling [1.37.]
	Fe_3O_4		Gene delivery [1.38.]
Polyethylene glycol	Fe_3O_4 (10 nm)	Methotrexate	MRI and drug delivery [1.39.]
Polyvinyl alcohol	Fe_3O_4	Cy3.5, Texas Red	Cell labeling [1.40.]
Polyethyleneimine	Fe_3O_4 (11-25 nm)		Gene delivery [1.41.]
	Fe_3O_4 (5-10 nm)		Gene delivery [1.42.]
Aminopropyl silica	Fe_3O_4 (15 nm)	^{188}Re	Radiotherapy [1.43.]

1.3.1. Cell response and toxicity

Since iron oxide nanoparticles are used and investigated for various biomedical applications it is of the highest interest to determine their effects on cell and tissue cultures *in vivo* and *in vitro*. Therefore, gathering toxicological data and developing reliable assessments for the nanoparticles' health and hazard potential is essential. Conventional approaches to determine the cytotoxicity of nanomaterials include (a) testing the cell response after nanoparticle exposure and include the measurement of intra- and extra cellular chemicals that are expressed when the cells endure stress or apoptosis (cell death) [1.44], (b) measuring the cell proliferation with and without nanoparticles and (c) monitoring the cell viability after nanoparticle exposure. However, the specific properties of iron oxide nanoparticles, such as the smaller size but larger surface, high catalytic reactivity, and distinctive optical properties compared to macroscopic materials, can interfere with conventional experimental approaches [1.45]. Therefore, alternative methods such as impedance-based measurements and coherent anti-stokes Raman scattering (CARS) are introduced and have gained much attention from the scientific community. This will be further discussed in Chapter 3 of this thesis.

1.3.2. Gene and drug delivery

Iron oxide-based magnetic nanoparticles have been developed and optimized for biomedical purposes for years now [1.3-1.8]. Constant output in literature confirms that there are always new pathways established for their functionalization and preparation, improving their efficiency and stability. Research on the topic has been growing faster than ever before. Fe_3O_4 for DNA binding and delivery has already been developed and clinically tested [1.3-1.8]. Binding organic functional groups onto their surface enables them not only to bind DNA but also other negatively charged biomolecules such as small interfering RNA (siRNA) [1.46] and proteins like bovine serum albumin (BSA)[1.47, 1.48]. Hartono et al. synthesized nanocarriers based on covalently bonded PEI iron oxide, which act as an excellent supplier of siRNA into osteosarcoma cancer cells, resulting in an appreciable decrease of its cellular viability [1.49]. Cancer treatments became one major biomedical sector, using iron oxide nanoparticles. Functionalized nanoparticles for targeted drug delivery reduced the necessary therapeutic use of pharmaceuticals (e.g. cytotoxic drugs) and therefore reduced their side effect. The possibility of targeting specific cells or tissues in the human body offers a new dimension to treat cancers and other diseases. Treating different kinds of human disorders, especially cancers, using

multifunctional MNP's is being pushed forward every year. Veiseha et al. modified iron oxide nanoparticles with polyethylene glycol (PEG), siRNA, and a cationic polymer layer to evaluate the safety and ability to promote gene silencing in three types of cells mimicking human cancer of the brain, breast, and prostate (C6/GFP$^+$, MCF-7/GFP$^+$, and TC2/GFP$^+$). Three types of cationic polymer layers have been tested for their safety ability to promote gene silencing, poly-arginine (pArg), polylysine (pLys), and polyethyleneimine (PEI). The assay revealed that iron oxide MNP's coated with pArg showed to be the most effective in promoting gene knockdown and least toxic than the other polymers. [1.46]

However, as pArg can be used for the promotion of gene knockdown, in particular, PEI has also the ability to bind and deliver biomolecules through the body. For example, Peipei et al. used a combination of both and reported that the cancer drug daunorubicin (DNR) became more biocompatible when it is conjugated with Fe_3O_4 NPs. [1.50] Daunorubicin inhibits the enzymatic effect of Topoisomerase type II, which regulates the opening and closure of double-stranded DNA (dsDNA) to two single-stranded (ssDNA) by cutting the phosphate backbone. An increasing amount of this enzyme induces DNA breaks, which block the transcription of DNA to RNA during cell division. This leads to cell apoptosis (cell death). Killing cancer cells is one effective way to treat cancer, but it needs to ensure that the healthy adjacent cells are not affected.

Zhang et al. modified magnetic Fe_3O_4 nanoparticles with polyethylene glycol (PEG) to improve their intracellular uptake. After the injection of modified MNP's into mouse macrophage (RAW 264.7) and human breast cancer (BT20) cells for 48 hours, the MNP's were internalized into the cells. A study using inductively coupled plasma atomic emission spectroscopy (ICP-AES) indicated that the uptake amount into the macrophage cells was lower than the uptake of unfunctionalized nanoparticles. Resisting protein absorption and thus avoiding the particle recognition by macrophage cells [1.51.] means delivering a special drug or medicine to a targeted cell without being incorporated. Therefore, MNP's can be labeled as precious retrievable nanotools.

1.3.3. MRI and CT

Magnetic Fe_3O_4 nanoparticles have found great applications in magnetic resonance imaging (MRI), where they are used and investigated as contrast agents and drug delivery agents in cancer treatment [1.9., 1.10., 1.31, 1.39.]. MRI is a non-invasive medical diagnostic technique using a strong magnetic field and radio frequency to produce detailed pictures of organs, soft tissue, bones, and almost any other part of the human body. Unlike X-ray examinations or computed tomography (CT), which is based on ionizing radiation, MRI uses the principle of realigning protons in the body [1.9, 1.10.]. After the external magnet has lined up the protons, short shocks of radio waves are sent to the desired part of the body, distracting the up-lined protons from their natural alignment. When the radio waves are switched off, the protons return to their usual alignment, emitting radio signals which are then collected by the receivers. These signals create a 3D image of the inside of the body. Because protons e.g. of the bone realign at a different speed (relaxation time) as the protons from soft tissue, distinct signals are emitted. Those signals are finally displayed as different types of tissues. Malformations such as tumors or cancer tissues are then identifiable by a radiologist.

There are two main types of relaxation processes, longitudinal (T_1) and transverse (T_2) relaxation (Figure 1. 2). The longitudinal relaxation is also known as T_1 relaxation and describes the process of transferring magnetic energy into the system and the surrounding tissue and measuring how fast the magnetization recovers. This recovery process happens along the z-direction (longitudinal). T_1 refers to the time it takes for the tissue to recover 63% of its original longitudinal magnetization. T_2, also known as transverse relaxation, is the loss of transverse magnetization after excitation. When the protons in the tissue are excited by the magnetic pulse, they start to randomize their orientation within the transverse plane. Once the excitation is stopped, the transverse magnetization is measured until 63% of the original signal remains [1.52]. The combination of both relaxation times (T_1 and T_2) generates tissue-specific signature relaxation times.
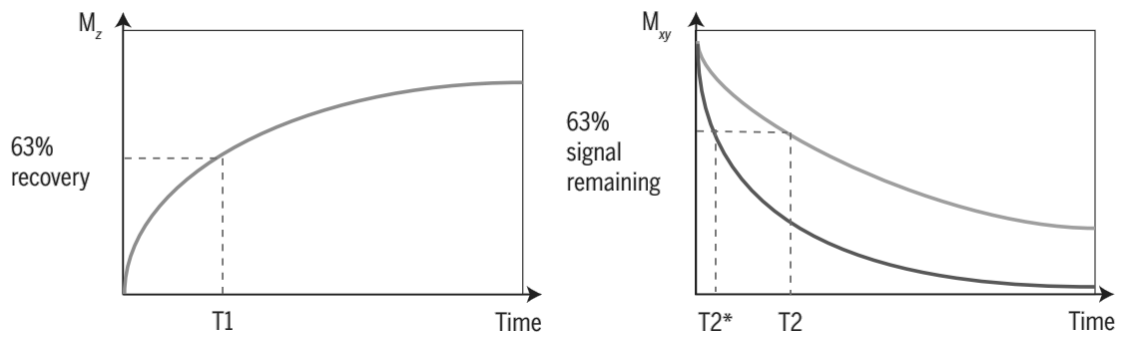
Figure 1. 2: Relaxation curves of T_1, T_2 and T_2^* relaxation curves [1.52.].

During the past years, iron oxide has been examined as a signal enhancing contrast agent for magnetic resonance imaging by changing the relaxation time of the targeted tissue. Changing the relaxation time that the protons need to realign will lead to an improved image and thus to a better differentiation between the targeted and the surrounding tissues.

1.3.4. *In vivo* testing

In vitro testing has two major limitations, (a) only particular and individual cells can be tested in their response to nanoparticles exposure and (b) the cells have different physiologies than they would behave *in vivo* (e.g. they are flat and spread across the culture dish, rather than being compact and tightly packed). Therefore *in vivo* models are required to evaluate the metabolism and effects of nanoparticles in a fully functioning organism. Understanding and analyzing their behavior in a complete metabolic system gives great insight into their toxicology, metabolic pathway, and most importantly their endpoints (i.e. liver, spleen, and lungs) [1.53]. Depending on their size and surface characteristics iron oxide nanoparticles are usually quickly recognized by the immune system, transported to the liver and spleen, and lungs, which then clear the nanoparticles from the system [1.54]. Currently, the most promising surface modification of iron oxide nanoparticles is a coating with polyethylene glycol, which is known to be biocompatible and minimizes the clearance by the RES system [1.55]. This ultimately leads to longer circulation times and improved pharmacokinetic properties.

Two common *in vitro* models that are currently used to evaluate toxicological effects of iron oxide nanoparticles on the body focus on mice [1.56 -1.58.] and zebrafish [1.59.-1.61.]. This is mainly due to their relatively small size, easy handling, maintenance, and affordability.

1.4. Summary and perspectives

Iron oxide nanoparticles have shown great potential in various research areas and have proven themselves as unique, multifunctional, and most importantly, modifiable tools for modern research. Their small particle size, large surface area, and magnetism have made them valuable tools in biomedical research areas, such as digital imaging (MRI, CT, Ultrasound) and toxicity screening (colorimetric assays, impedance measurements). 2D cell and 3D *in vitro* models and *in vivo* applications have been used to analyze their toxicologic effects on various cell lines and how they behave in a fully functioning organism. Furthermore, surface functionalization by coating the particles with functional groups and combining the core material (iron oxide) with other nanomaterials (i.e. gold) has made the nanoparticles highly customizable for any intended purpose. Much research has been done in the past decades and much more can be expected in the future.

This thesis demonstrates how versatile and most promising Fe_3O_4 iron oxide nanoparticles are, and how their unique properties in size, shape, and magnetism can be utilized for a broad range of applications in biomedicine. Various research projects within this Ph.D. have led to great insight into their versatility, toxicity, and modification, and are presented in the individual chapters. The individual chapters aim to show, where Fe_3O_4 can improve state-of-the-art biomedical analytics and applications, how these nanoparticles can be modified for those specific purposes. The application of iron oxide nanoparticles has found many purposes in the scientific community, however, this Ph.D. focused on applications in multimodal imaging, real-time holographic imaging, molecularly imprinted polymers, and *in vitro* and *in vivo* toxicology.

1.5. References

[1.1]   C. Chen, X. Jiang, Y. Valentino K., A. Yu; Design and construction of polymerized glucose coated Fe_3O_4 magnetic nanoparticles for delivery of aspirin, Powder Technology 236, **2013**, 157-163.

[1.2.] R. J. Aitken, M. Q. Chaudhry, A. B. A. Boxall, M. Hull; Manufacture and use of nanomaterials: current status in the UK and global trends; Occupational Medicine, **2006**, 56, 300-306.

[1.3.] M. Lewin, N. Carlesso, C.-H. Tung, X.-W Tang, D. Cory, D.T. Scadden, R. Weissleder; Tat peptide-derivatized magnetic nanoparticles allow *in vivo* tracking and recovery of progenitor cells; Nature Biotechnology, **2000**, 18, 410-414.

[1.4.] D. Wang , J.B. He , N. Rosenzweig , Z. Rosenzweig; Superparamagnetic Fe_2O_3 Beads−CdSe/ZnS Quantum Dots Core−Shell Nanocomposite Particles for Cell Separation; Nano Letters, **2004**, 4, 409–413.

[1.5.] J-H Lee, J-W Kim, J.Cheon; Magnetic Nanoparticles for Multi-Imaging and Drug Delivery; Mol. Cells, **2013**; 35; 274-284.

[1.6.] Q A Pankhurst, N T K Thanh, S K Jones, J Dobson; Progress in applications of magnetic nanoparticles in biomedicine; Journal of Physics D., Applied Physics, **2009**, 42, 4001.

[1.7.] S A. Meenach, J. Z. Hilt, K. W. Anderson, Poly(ethylene glycol)-based magnetic hydrogel nanocomposites for hyperthermia cancer therapy, Acta Biomaterialia, **2010**, 6, 1039-1046.

[1.8.] M. Namdeo, S. Saxena, R. Tankhiwale, M. Bajpai, Y. M. Mohan, S. K. Bajpai, Magnetic Nanoparticles for Drug Delivery Applications; Journal of Nanoscience and Nanotechnology, **2008**, 8, 3247-3271.

[1.9.] J. R. McCarthy, R. Weissleder, Multifunctional magnetic nanoparticles for targeted imaging and therapy, Advanced Drug Delivery Reviews, **2008**, 60, 1241–1251.

[1.10.] M-K Yoo, I-K Park, H-T Lim, S-J Lee, H-L Jiang, Y-K Kim, Y-J Choi, M-H Cho, C-S Cho, Folate–PEG–superparamagnetic iron oxide nanoparticles for lung cancer imaging; Acta Biomaterialia, **2012**, 8, 3005-3013.

[1.11.] B Ankamwar, T C Lai, J H Huang, R S Liu, M Hsiao, C H Chen and Y K Hwu; Biocompatibility of Fe_3O_4 nanoparticles evaluated by *in vitro* cytotoxicity assays using normal, glia and breast cancer cells; Nanotechnology, **2010**, 21, 075102.

[1.12.] Y. Chang, X. Meng, Y. Zhao, K. Li, B. Zhao, M. Zhu, YP Li, XS Chen, JY Wang; Novel water-soluble and pH-responsive anticancer drug nanocarriers: Doxorubicin–PAMAM dendrimer conjugates attached to superparamagnetic iron oxide nanoparticles (IONPs); Journal of Colloid and Interface Science, **2011**, 363, 403-409.

[1.13.] A V Bychkova; Multifunctional biocompatible coatings on magnetic nanoparticles; Russian Chemical Reviews, **2012**, 81, 1026.

[1.14.] A-H Lu, E. L. Salabas, F. Schüth; Magnetic Nanoparticles: Synthesis, Protection, Functionalization, and Application; Angewandte Chemie International Edition, **2007**, 46, 1222-1244.

[1.15.] R.M. Cornell and U. Schwertmann, The iron oxides: structure, properties, reactions, occurrences. Wiley VCH, ISBN 978-3-527-30274-1.

[1.16.] U. Schwertmann, Occurrence and Formation of Iron Oxides in Various Pedoenvironments. In: J.W.Stucki, B.A.Goodman, U.Schwertmann (eds) Iron in Soils and Clay Minerals, NATO ASI Series (Series C: Mathematical and Physical Sciences), **1988**, 217.

[1.17.] M. Krispin, A. Ullrich, A. and S. Horn, Crystal structure of iron-oxide nanoparticles synthesized from ferritin. J Nanopart Res., **2012**, 14, 669.

[1.18.] E. A. Campos, D. V. B. S. Pinto, J. I. S. de Oliveira, E. da Costa Mattos and R. de Cassia Lazzarini Dutra, J. Aerosp. Technol. Manag., São José dos Campos, **2015**, 7, 267-276.

[1.19.] RM Cornell, U. Schwertmann, The iron oxides: structure, properties, reactions, occurrences and uses, Weinheim: Wiley-VCH, 2000.

[1.20.] R. Zboril R, M. D. Petridis D, Iron (III) oxides from thermal processes-synthesis, structural and magnetic properties, Mossbauer spectroscopy characterization, and applications, Chem Mater., **2002**, 14, 969-982, DOI: 10.1021/cm0111074

[1.21.] S. Babay, T. Mhiri, M. Toumi, Synthesis, structural and spectroscopic characterizations of maghemite g-Fe2O3 prepared by one-step coprecipitation route. J Mol Struct., **2015**, 286-293, doi: 10.1016/j.molstruc.2014.12.067.

[1.22.] A.S. Teja, P.-Y. Koh, Progress in Crystal Growth and Characterization of Materials, **2009**, 55, 22-45.

[1.23.] Magnetite Nanoparticles Market Size, Share & Trends Analysis Report By Application (Bio-medical, Electronics, Energy, Wastewater Treatment), By Region, And Segment Forecasts, 2019 – 2025, **2019**, Report ID: GVR-3-68038-765-0.

[1.24.] R. J. Aitken, M. Q. Chaudhry, A. B. A. Boxall, M. Hull; Manufacture and use of nanomaterials: current status in the UK and global trends; Occupational Medicine, **2006**, 56, 300-306.

[1.25.] MA Do, GJ Yoon, JH Yeum, M Han, YM Chang, JH Choi; Polyethylenimine-mediated synthesis of superparamagnetic iron oxide nanoparticles with enhanced sensitivity in T_2 magnetic resonance imaging; Colloids, and Surfaces B: Biointerfaces, **2014**, 122 752–759.

[1.26.] C. Han, W. Cai, W. Tang, G. Wang, C. Liang; Protein-assisted hydrothermal synthesis of ultrafine magnetite nanoparticle built-porous oriented fibres and their structurally enhanced adsorption to toxic chemicals in solution; Journal of Materials Chemistry, **2011**, 21, 11188-11196.

[1.27.] Z. L. Liu, X. Wang, K. L. Yao, G. H. Du, Q. H. Lu, Z. H. Ding, J. Tao, Q. Ning, X. P. Luo, D. Y. Tian, D. Xi; Synthesis of magnetite nanoparticles in W/O microemulsion; Journal of Materials Science, **2004**, 39, 2633-2636.

[1.28.] Q. Zhang, M. S. Thompson, A. Y. Carmichael-Baranauskas, B. L. Caba, M. A. Zalich, Y-N Lin, O. Thompson Mefford, R. M. Davis, J. S. Riffle; Aqueous Dispersions of Magnetite Nanoparticles Complexed with Copolyether Dispersants: Experiments and Theory; Langmuir, **2007**, 23, 6927–6936.

[1.29.] H H P Yiu; Engineering the multifunctional surface on magnetic nanoparticles for targeted biomedical applications: a chemical approach, Nanomedicine, **2011**, 6, 1429 – 1446.

[1.30.] J. Kuhn, Biomedical applications of functionalized magnetic nanoparticles (MNP's): Functionalised MNP's for Gene binding and Delivery, Bachelor's Thesis, **2015**.

[1.31.] D. Hogemann, L. Josephson, R. Weissleder, JP Basilion; Improvement of MRI probes to allow efficient detection of gene expression; Bioconjugate Chem., **2000,** 11, 941 – 946.

[1.32.] F. Sonvico, S. Mornet, S. Vasseur; Folate-conjugated iron oxide nanoparticles for solid tumor targeting as potential specific magnetic hyperthermia mediators: synthesis, physicochemical characterization, and *in vitro* experiments. Bioconjugate Chem., **2015**, 16, 1181 – 1188.

[1.33.] EH Kim, HS Lee, BK Kwak, BK Kim; Synthesis of ferrofluid with magnetic nanoparticles by sonochemical method for MRI contrast agent; J. Magnet. Magnet. Mater., **2005**, 289, 328 – 330.

[1.34.] YY Liang, LM Zhang; Bioconjugation of Papain on superparamagnetic nanoparticles decorated with carboxymethylated chitosan biomacromolecules, **2007,** 8, 1480 – 1486.

[1.35.] YQ Ge, Y Zhang, SY He, F Nie, GJ Teng, N Gu; Fluorescence modified chitosan-coated magnetic nanoparticles for high efficient cellular imaging; Nanoscale Res. Lett., **2009**, 4, 287 – 295.

[1.36.] Y. Yang Y, JS Jiang JS, B. Du, ZH Gan, M Qian, P Zhang; Preparation and properties of a novel drug delivery system with both magnetic and biomolecular targeting; J. Mater. Sci. Mater. Med., **2011**, 22, 301 – 307.

[1.37.] EV Gromann, MH Yang, CP Reinhardt, JS Weinberg, DE Vaccaro; Polycationic nanoparticles: (1) synthesis of a polylysine-MION conjugate and its application in labelling fibroblasts; J. Cardiovasc. Trans. Res., **2011**, 4, 30 – 40.

[1.38.] Z. Li, J Xiang, W Zhang, Nanoparticle delivery of anti-metastatic NM23-H1 gene improves chemotherapy in a mouse tumor model; Cancer Gene. Ther., **2009**, 16, 423 – 429.

[1.39.] Kohler N, Sun C, Fichteholtz A, Gunn J, Fang C, Zhang MQ; Methotrexate-immobilized poly(ethylene glycol) magnetic nanoparticles for MR imaging and drug delivery; Small, **2006,**2, 785 – 792.

[1.40.] Schultze K, Koch A, Petri-Fink A; Uptake and biocompatibility of functionalized poly(vinylalcohol) coated superparamagnetic maghemite nanoparticles by synoviocytes *in vitro*; J. Nanosci. Nanotechnol., **2006**, 6, 2829 – 2840.

[1.41.] Arsianti M, Lim M, Marquis CP, Amal R. Polyethylenimine based magnetic iron-oxide vector: the effect of vector component assembly on cellular entry mechanism, intracellular localization, and cellular viability. Biomacromolecules, **2010**, 11, 2521 – 2531.

[1.42.] Arsianti M, Lim M, Marquis CP, Amal R; Assembly of polyethylenimine-based magnetic iron oxide vectors: insights into gene delivery; Langmuir, **2010**, 26, 7314 – 7326.

[1.43.] Cao JQ, Wang YX, Yu JF et al.; Preparation and radiolabelling of surface-modified magnetic nanoparticles with rhenium-188 for magnetic targeted radiotherapy; J. Magnet. Magnet. Mater., **2004**, 277, 165 – 174.

[1.44.] R. Krętowski, M. Kusaczuk, M. Naumowicz, J. Kotyńska, B. Szynaka and M. Cechowska-Pasko, The Effects of Silica Nanoparticles on Apoptosis and Autophagy of Glioblastoma Cell Lines, Nanomaterials (Basel), **2017**, 8, 230.

[1.45.] B. Drasler, P. Syre, K. G. Steinhauser, A. Petri-Fink and B. Rothen-Rutishauser, *In vitro* approaches to assess the hazard of nanomaterials, Nano Impact, **2017**, 99-116.

[1.46.] O. Veiseh, F. M. Kievit, HJ Mok, J. Ayesh, C. Clark, C. Fang, M. Leung, H. Arami, J. O. Park, M Zhang; Cell transcytosing poly-arginine coated magnetic nanovector for safe and effective siRNA delivery; Elsevier, Biomaterials, **2011**, 32, 5717–5725.

[1.47.] M. Mikhaylova, D. K. Kim, C. C. Berry, A. Zagorodni, M. Toprak, A. S. G. Curtis, M. Muhammed; BSA Immobilization on Amine-Functionalized Superparamagnetic Iron Oxide Nanoparticles.; Chem. Mater., **2004**, 16, 2344−2354.

[1.48.] Pan B. F., Gao F., Gu H. C.; Dendrimer Modified Magnetite Nanoparticles for Protein Immobilization. J. Colloid Interface Sci., **2005**, 284, 1−6.

[1.49.] S. B Hartono, M. Yu, W. Gu, J. Yang, E. Strounina, XL Wang, S. Qiao, CZ Yu; Synthesis of multifunctional large pore mesoporous silica nanoparticles as gene carriers; Nanotechnology, **2014**, 25, 055701.

[1.50.] PP Xu, JY Li, BO Chen, XM Wang, XH Cai, H Jiang, CL Wang, HJ Zhang; The Real-Time Neurotoxicity Analysis of Fe_3O_4 Nanoparticles Combined with Daunorubicin for Rat Brain *In vivo*; Journal of Biomedical Nanotechnology, **2012**, 8, 417-423.

[1.51.] Y. Zhang, N. Kohler, M. Zhang; Surface modification of superparamagnetic magnetite nanoparticles and their intracellular uptake; Elsevier, Biomaterials, **2002**, 23, 1553–1561.

[1.52.] J. L. Bloem, M. Reijnierse, T. W. J. Huizinga, and A. H. M. van der Helm-van Mil, Magnetic Resonance Imaging: The Underlying Principles, Journal of Orthopaedic & Sports Physical Therapy, **2011**, 41, 806-819.

[1.53.] M. Ajdary, M. A. Moosavi, M. Rahmati, M. Falahati, M. Mahboubi, A. Mandegary, S. Jangjoo, R. Mohammadinejad, and R. S. Varma; Health Concerns of Various Nanoparticles: A Review of Their *in vitro* and *in vivo* Toxicity, Nanomaterials, **2018**, 8, 634.

[1.54.] B. Fadeel, Hide and Seek: Nanomaterial Interactions with the Immune System, Front. Immunol., **2019**, 133.

[1.55.] S. Nie, Understanding and overcoming major barriers in cancer nanomedicine, Nanomedicine, **2010**, 5, 523-528.

[1.56.] S. Zanganeh, G. Hutter, R. Spitler, O. Lenkov, M. Mahmoudi, A. Shaw, J. S. Pajarinen, H. Nejadnik, S. Goodman, M. Moseley, L. M. Coussens and H. E. Daldrup-Link, Iron oxide nanoparticles inhibit tumour growth by inducing pro-inflamatory macrophage polarization in tomour tissues, Nat. Nanotechnol., **2016**, 11, 986-995.

[1.57.] M. S. Bohley, E. Birch, F. J. Baumann, A. E. Dillinger, E. R. Tamm, and A. M. Goepferich, Design of dye and superparamagnetic iron oxide nanoparticle loaded lipid nanocapsules with dual detectability *in vitro* and *in vivo*, Int. J. Pharm., **2020**, 585, 119433.

[1.58.] B. R. Smith and S. S. Gambhir, Nanomaterials for *In vivo* imaging, Chem. Rev., **2017**, 117, 901-986.

[1.59.] L. Evensen, P. L. Johansen, G. Koster, K.Z. Zhu, L. Herfindal, M. Speth, F. Fenaroli, J. Hildahl, S. Bagherifam, C. Tulotta, L. Prasmickaite, G. M. Mælandsmo, E. Snaar-Jagalskad, and G. Griffiths, Zebrafish as a model system for characterization of nanoparticles against cancer, Nanoscale, **2016**,8, 862-877.

[1.60.] M. Magro, D. Baratella, E Bonaiuto, J. de Almeida Roger, G. Chemello, S. Pasquaroli, L. Mancini, I. Olivotto, G. Zoppellaro, J. Ugolotti, C. Aparicio, A. P. Fifi, G. Cozza, G. Miotto, G. Radaelli, D. Bertotto, R. Zboril and F. Vianello, Stealth Iron Oxide Nanoparticles for Organotropic Drug Targeting, Biomacromolecules, **2019**, 20, 1375-1384.

[1.61.] F. Ahmad, X. Y. Liu, Y. Zhou, H. Z. Yao, F, F. Zhao, Z. X. Ling, and C. Xu, Assessment of Thyroid Endocrine System Impairment and Oxidative Stress Mediated by Cobalt Ferrite ($CoFe_2O_4$) Nanoparticles in Zebrafish Larvae, Environ. Toxicol., **2015**, 31, 2068-2080.

CHAPTER 2

Iron oxide-gold nanoparticles for multimodal contrast enhancement in magnetic resonance, computed tomography, and intravascular ultrasound imaging

2.1. Introduction Medical imaging techniques are extensively used for the non-invasive diagnosis of various diseases [2.1., 2.2.]. Among medical imaging techniques, magnetic resonance imaging (MRI), computed tomography (CT), and ultrasound (US) are widely available and commonly used in the clinical setting [2.3., 2.4.]. Due to intrinsic technical disparities, these imaging techniques have different advantages and limitations, which determine their diagnostic performance across clinical specialties. MRI benefits from no radiation exposure, high soft-tissue contrast, and high spatial and temporal resolution and is capable of molecular and functional multi-parametric imaging [2.1.-2.5.]. However, it is limited by long imaging times between 15 to 90 minutes and is not suitable for patients with claustrophobia or MR contraindications [2.4, 2.5.]. CT provides a physical representation of the tissue attenuation properties, high spatial and temporal resolution, and fast imaging, but is associated with radiation exposure and lower soft-tissue contrast compared to MRI [2.1.-2.4., 2.6]. Ultrasound is often used for early disease assessment and compared to other imaging modalities is an inexpensive, real-time imaging technique with no radiation exposure [2.1., 2.3., 2.4., 2.7.]. Among important ultrasound applications, intravascular ultrasound (IVUS) is commonly used in cardiology to determine the hemodynamic significance of atherosclerotic plaques [2.1., 2.3.]. The main limitations of ultrasound are that it is operator-dependent and sub-optimal for obese patients and air-filled organs, as the ultrasound beams are attenuated and therefore increase the background noise and artifacts in the images [2.7.]. To capitalize on the advantages of each of the individual techniques, the development of multi-modal imaging methodologies is a fast-growing research area in deriving clinically relevant complementary diagnostic information and identifying the optimum imaging modalities across various diseases [2.1-2.4, 2.8, 2.9].

Contrast agents are commonly employed in MRI, CT and ultrasound scans to enhance the qualitative diagnostic information acquired and to obtain quantitative diagnostic information through the extraction of dynamic measurements and image-derived biomarkers [2. 3, 2.5, 2.7, 2.9]. Since the imaging techniques are based on different physical principles, the development of specific contrast agents which build upon utilizing these principles are required for multi-modal imaging. However, the kinetic properties of different contrast agents vary considerably, leading to significant disparities in

biodistribution and tissue uptake thus, compromising the design, optimization, and cross-validation of multi-modal imaging protocols [2.10]. Hence, one single agent carrying multi-modal contrast capabilities is required.

Various nanoparticles (NPs) (inorganic, organic, and hybrid) have been developed as contrast agents for diagnostic imaging techniques [2.11]. Among these, magnetic iron oxide (Fe_3O_4) NPs have been commercialized for clinical MRI contrast [2.12], as they benefit from low toxicity and are detectable by MR even at low concentrations [2.13-2.15]. Gold (Au) NPs are among the most promising for CT contrast since they have a high atomic number (abundant electrons for CT contrasting), good biocompatibility, controllable synthesis, and easy modification [2.16, 2.17]. In the context of multi-modal imaging, previous studies have developed several methodologies for synthesizing Au/Fe_3O_4 hybrids with different morphologies [2.17-2.22]. These morphologies include Au clusters on Fe_3O_4 to form "strawberry-like" NPs [2.17, 2.18], Au shell structures with a Fe_3O_4 core [2.19, 2.20], Au encapsulated Fe_3O_4 star-shaped NPs, and Janus dumbbell-like particles (Figure 2. 1) [2.21, 2.22]. However, previous synthetic routes have used stabilizers before or after the reaction of the MNP component with Au and thus, have not focused on keeping either component surface pristine. If possible, pristine NP surfaces could support further functionalization of Au/Fe_3O_4 hybrids, such as for simultaneous molecularly targeted diagnosis and therapy applications [2.11].
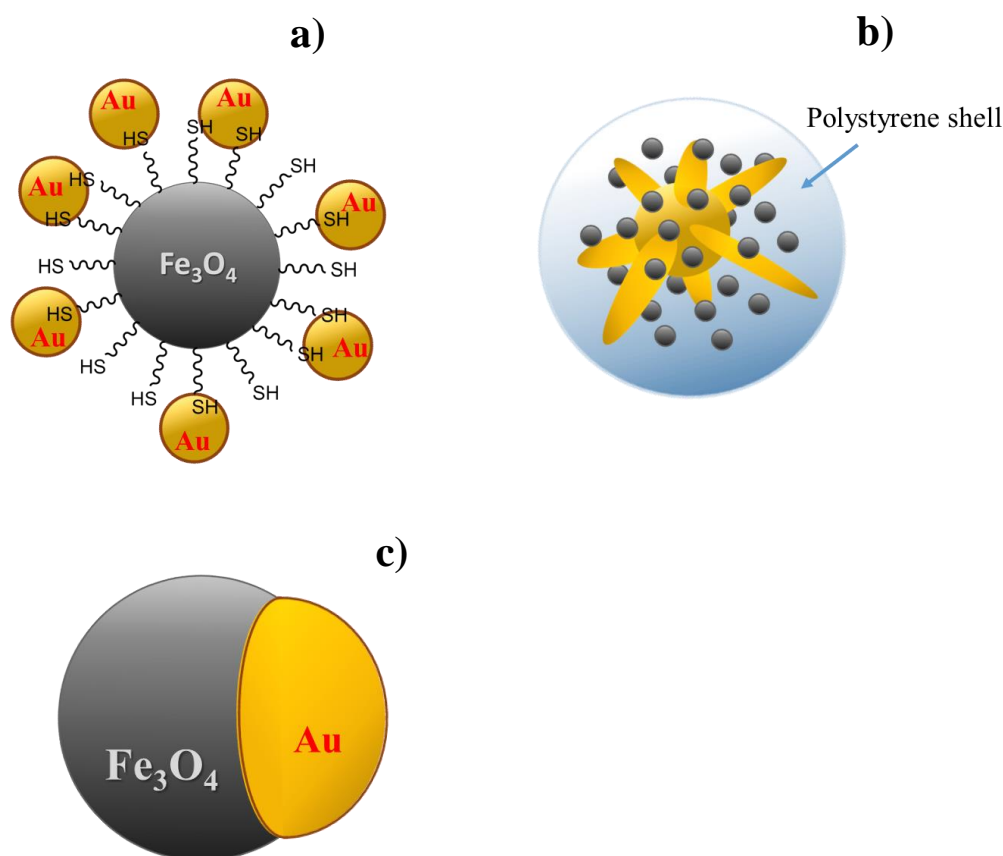
Figure 2. 1: Simplified structures of Au/Fe$_3$O$_4$ particles with "strawberry-like" structure (a), "star-shaped" nanoparticle (b), and "dumbbell" nanoparticle (c).

Synthesis of multimodal contrasting agents with combined NP properties is not straightforward, due to different chemical criteria that need to be satisfied for each component (such as in formation chemistry, pH control, and/or when specific functional groups are needed for coupling). Possible interference between the NP precursors and/or between chemical functional groups on the NP surface will result in undesirable assemblies, such as in agglomeration and/or even in the deactivation of functional groups and NP surfaces [2.23]. Hence, developing a direct deposition route whilst aiming to keep either component pristine for further functionalization, could contribute towards optimizing the next generation of multi-modal/multi-functional contrast agents.

In terms of imaging assessments, previous studies have mainly examined MR and CT contrasting ability of Au/Fe$_3$O$_4$ hybrids [2.18-2.20], whilst some have demonstrated signal changes in photoacoustic imaging due to the presence of the Au component [2.21, 2.22]. Furthermore, the MR contrast enhancement ability of Au/Fe$_3$O$_4$ hybrids has been assessed using mainly T$_2$-weighted imaging sequences, where the differences in the T$_2$ relaxation time of various tissues are depicted [2.18-2.22].

Investigating the contrasting ability of Au/Fe_3O_4 hybrids across T_1- and T_2-weighted sequences used for high spatial resolution anatomical MR imaging, CT, and ultrasound, which are among the most widely used imaging techniques in the clinical setting [2.1-2.4], is therefore highly required.

In this chapter, the synthesis of Au-dotted Fe_3O_4 NPs (Au*MNPs) via a direct deposition route, with variable Au content is presented. Compared with previous Au*MNPs synthesis pathways, in which individual particle surfaces were covered with stabilizers before or after the reaction with Au [2.17-22], the method presented in this chapter keeps the surfaces of both components pristine for further functionalization. This can efficiently support future molecularly targeted diagnosis and therapy applications. This method is simple and scalable. We have also extensively assessed for the first-time tri-modal signal changes due to concentration increases of these Au*MNPs across both a T_1- and a T_2-weighted sequence on MRI scans, on CT scans, and IVUS B-mode scans. We finally evaluated the toxicity of these Au*MNPs in breast cancer cells and assessed whether they have the potential to be optimized as a tri-modal contrast agent for clinical research and diagnosis.

2.2. Experimental

2.2.1. Materials

Magnetite nanoparticles (Fe_3O_4 NPs, 98%, 20-30 nm) and chloroauric acid tetrahydrate ($HAuCl_4 \cdot 4H_2O$, 99.9%) were purchased from Alfa Aesar. Urea (AR grade) was supplied by Fisher Scientific. Polyethylene glycol (PEG, Mw = 400) was purchased from Sigma Aldrich. All water used was deionized water. Dulbecco's Modified Eagle Medium (DMEM) growth medium with 10% FBS and 1% penicillin-streptomycin was supplied by Sigma (D5671). Ethidium homodimer (EthD-1) and Calcein AM (0.1% in DMEM) were purchased as a kit (LIVE/DEAD™ Viability/Cytotoxicity Kit) supplied by Invitrogen™. Glutaraldehyde (25% EM grade 1 (G5882), Sigma Aldrich UK) and sodium cacodylate buffer (0.1M) were supplied by AGAR Scientific Ltd (AGR1104). Tannic acid was purchased from TAAB Laboratory and Microscopy Ltd. Methanol and ethanol were purchased from VWR BDH Chemicals. Uranyl acetate and osmium tetra oxide were purchased from OXKEM Ltd. Hexamethyldisilazane (HMDS, 99%) was supplied by Sigma Aldrich UK. All chemicals were used as supplied without further purification.

2.2.2. *Preparation of Au*MNP particles and characterization*

Au was deposited onto Fe_3O_4 NPs using a method adapted from the preparation of Au/Fe_3O_4 catalyst. Depending on the designated Au:Fe wt. ratio, 36 mg (5%), 72 mg (10%), or 144 mg (20%) chloroauric acid tetrahydrate ($HAuCl_4 \cdot 4H_2O$) was dissolved in deionized water and added to a suspension of 300 mg Fe_3O_4 NP in 50 mL deionized water Urea (100 mg) was then added dropwise to the reaction suspension and this suspension was sonicated for a further 6 h. The solid samples were then separated using a NdFeB magnet and washed using deionized water for a minimum of 10 times. Samples of three Au:Fe wt. ratios 5%w/w, 10%w/w and 20%w/w were prepared. PEG-coated Au*MNP was carried out by coating PEG (Mw = 400) onto particle surface following a published procedure for all Au:Fe wt. ratios (Figure 2. 2) [2.24]. For imaging experiments, samples with Au*MNP concentrations ranging from 0.01 to 0.4 mM were appropriately prepared to derive quantitative metrics from MR, CT, and IVUS experiments.
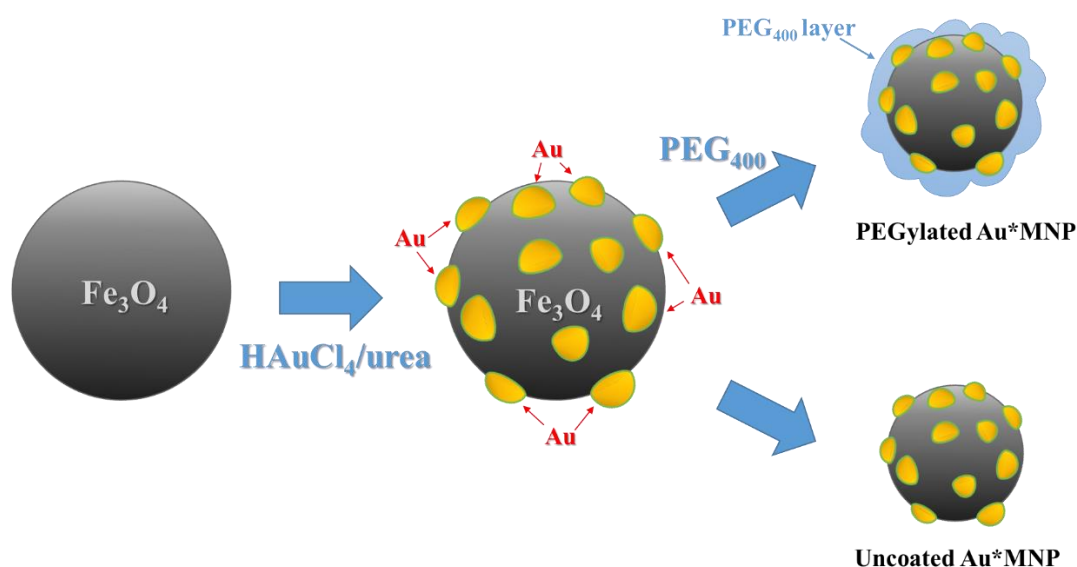
Figure 2. 2: Schematic illustrations for the synthesis pathway for Au*MNPs. First, the deposit of Au-particles on the iron oxide surface, followed by the optional coating with polyethylene glycol (PEG).

PEG-coated and unfunctionalized Au*MNP samples were characterized using Transmission electron microscopy (TEM), X-ray diffraction (XRD), and Fourier Transform Infrared Spectroscopy (FTIR). TEM and Scanning TEM (STEM) were carried out in a JEOL JEM 2100 microscope operated at 200 kV. The microscope is equipped with a Schottky field-emission gun and ultrahigh-resolution pole-piece (Cs = 0.5 mm). The TEM images were recorded by a Gatan Ultrascan 1000 camera. High-angle annular dark-field (HAADF-STEM), known as Z-contrast imaging, and bright-field STEM (BF-

STEM) were acquired simultaneously by a JEOL ADF and Gatan BF detector, respectively. For sample preparation, 20 μl of a sample was drop-casted on a copper grid with carbon supporting films and then air-dried. Powder X-ray diffraction (PXRD) patterns were recorded using a Bruker D8 ADVANCE diffractometer with Cu $K\alpha_1$ radiation and a step size of 0.01°. FTIR spectra were recorded using a Nicolet is5 FTIR spectrometer (Thermo Scientific), fitted with an iD7 ATR-Diamond (KBr).

2.2.3. Cell culture, cytotoxicity, and imaging

The human breast cancer cell line MCF-7 was employed in this study. Cells were expanded in Dulbecco's Modified Eagle Medium (DMEM) growth medium with 10% Fetal Bovine Serum (FBS) and 1% penicillin-streptomycin and maintained at 37°C in 5% CO_2 until ~90% confluent. Cells were seeded at a density of $1x10^4$ cells per ml for experiments, unless stated otherwise, and were cultured for 24 hours before the addition of the Au*MNP treatments (10 μg/mL). The same cell line not exposed to Au*MNP treatments was used as controls.

To assess cell viability, live/dead staining was conducted using Ethidium homodimer (EthD-1) (0.1% in DMEM) and Calcein AM (0.1% in DMEM) (Invitrogen™ LIVE/DEAD™ Viability/Cytotoxicity Kit, for mammalian cells). After both 24 hours and 7-day culture with either 10 or 100 µg/mL Au*MNPs, the media from the MCF-7 cells was removed and replaced with fresh media containing both EthD-1 and Calcein; the cells were incubated for 30 minutes at 37°C. After this, the cells were washed with fresh 37°C media and were visualized under a fluorescence microscope (Zeiss Axiovert 200M).

To observe MCF-7 interaction with the Au*MNPs, the cells were fixed and processed for SEM following 1 and 3 days of culture. The cells were fixed in 1.5% glutaraldehyde in 0.1M sodium cacodylate buffer for 1 hour, washed in cacodylate buffer for 10 minutes, then incubated in 1% osmium buffer for one hour at room temperature. Cell samples were washed twice in cacodylate buffer (5 minutes) and incubated in 1% tannic acid (in buffer) for 1 hour at room temperature. After washing, cells were dehydrated twice in methanol gradients (30, 50, 70%; 5 minutes), incubated in 2% uranyl acetate for 30 minutes, then further dehydrated in 90% methanol for 5 minutes and 100% ethanol for 10 minutes. Finally, cells underwent HMDS dehydration (5 minutes), stored in a desiccator, sputter coated in gold-palladium (using a Quorum Q150t ES), and mounted onto stands to be viewed under a JEOL JSM 6400 SEM (running at 10kV). The .tiff images were captured using Olympus Scandium software.

Cellular uptake of Au*MNP was also analyzed via TEM. Cells were seeded at a density of 4×10^4 cells per mL onto Thermanox coverslips (13 mm diameter) and cultured to develop a confluent monolayer of cells. At this point, the NPs were added by changing the medium to media containing NPs. The cells were then further cultured for 24 hours. Cells were subsequently fixed with 1.5% glutaraldehyde in PBS for 2 hours and washed for 10 minutes with PBS. Cells were then post-stained for 60 minutes with 1% osmium tetroxide in phosphate buffer, and post-fixed in 1% buffer followed by 0.5% uranyl acetate for 1 hour, before being taken through alcohol dehydration increments and left in resin (propylene oxide Epon 812 resin mix (1:1)) overnight. Cell layers were captured in pure resin and cured overnight in an oven. Blocks were then cut into ultrathin sections, stained with 2% methanolic uranyl acetate and Reynolds lead citrate, and viewed under a Tecnai T20 (200 kV for cells).

2.2.4. MR imaging and analysis

To assess the MR contrast enhancement ability of the MNP component in our samples, Au*MNP samples were imaged in a 7.0 Tesla preclinical MRI scanner (Agilent Technologies, Santa Clara, CA, USA) at Edinburgh Preclinical Imaging Laboratory, using a 72 mm internal diameter volume coil. For T_1-weighted imaging, a fast spin echo pulse sequence was used with an echo train length of 8, repetition time (TR) 1000 ms, echo time (TE) 5.99 ms, flip angle 90°, and slice thickness of 2 mm, across 5 different slice positions to obtain full spatial coverage of samples. Images were reconstructed on a 256 x 256 pixel grid with a pixel size of 0.31 mm x 0.31 mm. For T_2-weighted imaging, a multi-echo multi-slice gradient echo sequence was used to acquire a series of 25 images across the same 5 slice positions as above with TR 2000 ms, TE 6.70 ms, flip angle 90°, and a slice thickness of 2 mm. Images were reconstructed on a 256 x 256 pixel grid with 0.62 mm x 0.62 mm pixel size.

MR images were analyzed in Matlab (MathWorks Inc., Natick, USA), using a customized in-house MR analysis software [5]. T_1 signal changes were assessed by extracting signal intensities from T_1-weighted images of all individual samples. Signal intensities were extracted by using standardized circular regions of interest at the center of each sample tube (excluding the boundary areas) in Matlab. T_2 signal changes were estimated by fitting the transverse relaxation time equation (1) in the T_2-weighted signal curves extracted across all successive TEs for each sample tube:

$$M_{xy} = M_0 e^{-\frac{t}{T_2}} \quad (1)$$

where M_{xy} is the MR signal detected in the x-y plane by the scanner detector, M_0 is the initial net magnetization and t is the TE.

2.2.5. CT imaging and analysis

To assess the CT contrast enhancement of the Au component in our samples, Au*MNP samples were imaged on a second-generation Mediso micro PET/CT scanner (nanoPET/CT, Mediso, Hungary) at the Edinburgh Preclinical Imaging Laboratory. The quality assurance was performed daily on the Mediso nanoPET/CT, as previously described [25]. The CT imaging parameters were tube voltage 50 kVp, exposure time 300 ms, slice thickness 0.38 mm, matrix 324 x 324, and pixel size 0.38 mm x 0.38 mm. Attenuation coefficients were numerically normalized to the attenuation coefficient of water in our calibrated scanner environment and all CT image pixels were automatically converted into Hounsfield Units (HU):

$$HU = 1000 \frac{\mu - \mu_{water}}{\mu_{water} - \mu_{air}}$$

where μ is the linear attenuation coefficient in a pixel measured by the CT scanner, and μ_{water} and μ_{air} are the linear attenuation coefficients of water and air, respectively. CT images were analyzed using PMOD (PMOD Technologies, Zurich, Switzerland). A cylindrical volume of interest (VOI) was drawn at the center of each sample tube (excluding the boundary areas) and was used to quantify the mean HU values and standard deviation.

2.2.6. Ultrasound imaging and analysis

To assess the ultrasound echogenicity, the samples were scanned using a Boston Scientific Clearview intravascular ultrasound (IVUS) scanner with an Atlantis SR Pro catheter and with a nominal center frequency of 40MHz. The catheter was inserted into each of the samples and an image was acquired on the scanner and downloaded onto a computer using an 8 bit, 20MHz, image capture card (PicPort CameraTec AG, Weisslingen, Switzerland). The setup of the scanner was identical for all acquisitions. Images were read and analyzed using Matlab, where the average signal intensity and standard deviation were measured from each sample (excluding the boundary areas).

2.3. Results and Discussion

2.3.1. Characterizations of Au*MNP nanoparticles

The TEM micrograph in Figure 2. 3, a and b reveal that these Au*MNP possess a "strawberry-like" structure, with the Au nanoparticles (seeds) having a narrow size distribution dotted on the Fe_3O_4 MNP surface. At 20% Au, it can be seen from the TEM micrograph (Figure 2. 3, c) that unattached Au nanoparticles were also formed. The Fe_3O_4 surface reached full saturation with Au NP "seeds" at 10% Au. Indeed, this protocol was adapted from Au on Fe_3O_4 catalyst preparation, and 10% Au tends to be the upper limit [2.26].
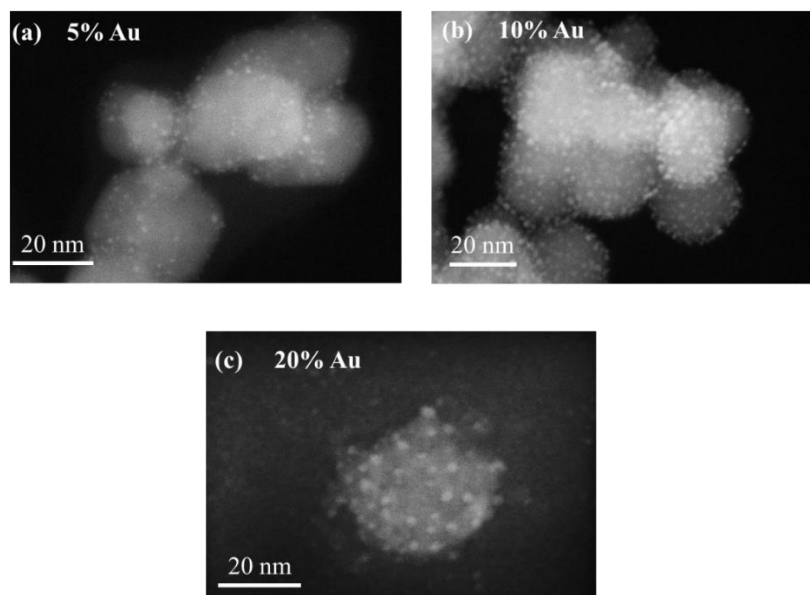
*Figure 2. 3: TEM images for (a) 5% Au*MNP, (b) 10% Au*MNP, and (c) 20% Au*MNP samples. Showing the individual gold particles (light spots) on the iron oxide surface (large circles).*

Au seeds dotted on Fe_3O_4 nanoparticles with a similar structure have been reported [2.18], but those were prepared with a thiol-layer on the Fe_3O_4 surface (see Figure 2. 1). The synthesis protocol, adapted from catalysts preparation has avoided the use of organosilane [26], keeping the Fe_3O_4 surface pristine for binding with other molecules and available for further functionalization. Due to the small size of these Au NP seeds, these cannot be observed from the XRD pattern (Figure 2. 4). FTIR spectra in Figure 2. 5**Error! Reference source not found.** depicted the PEG coating on the 10% Au*MNP samples, compared with the unfunctionalized MNPs. The spectrum showed five bands at 1155, 1420, 1470, 2870, and 2985 cm^{-1}, which are characteristic of PEG. The band at 1155 cm^{-1} can be attributed to the stretching mode of the ether linkage (-C-O-C-). The other four peaks are assigned to the CH_2 bending vibrations (1419 and 1470 cm^{-1}) and the symmetric (2869 cm^{-1}) and asymmetric (2985 cm^{-1}) stretching modes of the $-CH_2$ repeating unit in PEG.
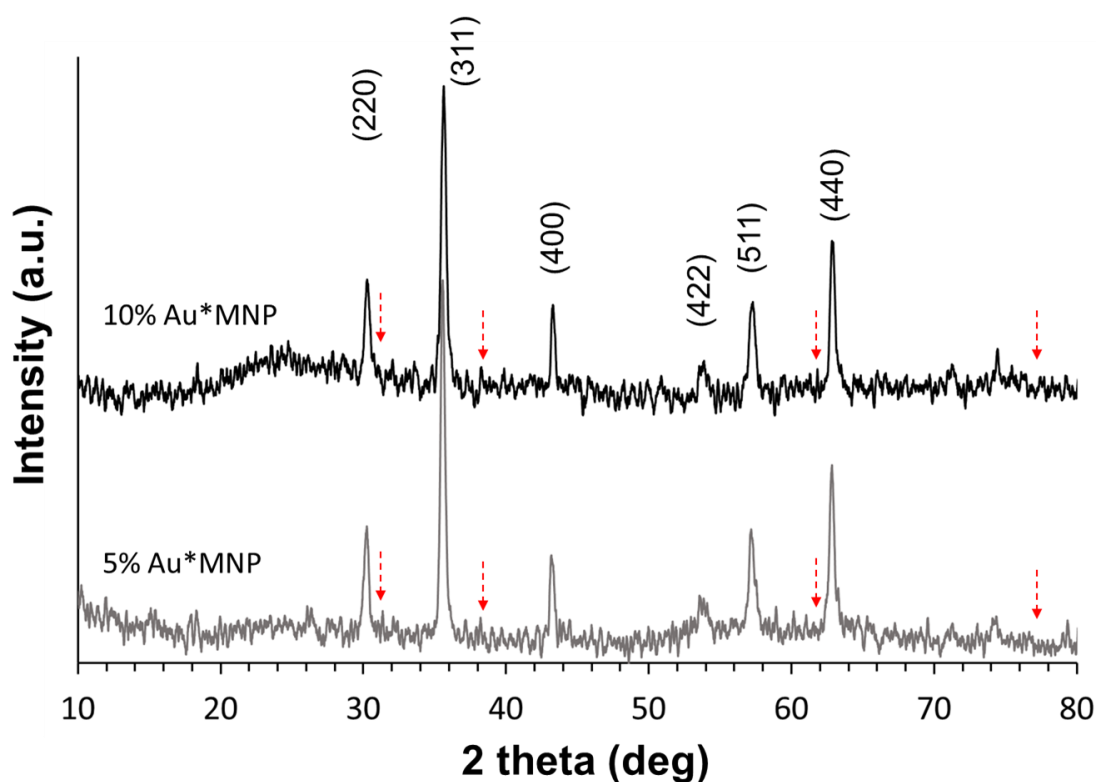
*Figure 2. 4: XRD patterns for 5% and 10% Au*MNP samples with indexes for Fe_3O_4 magnetite. The red arrows are indicating theoretical diffraction peaks for Au which were not seen in the XRD patterns due to their small particle size.*
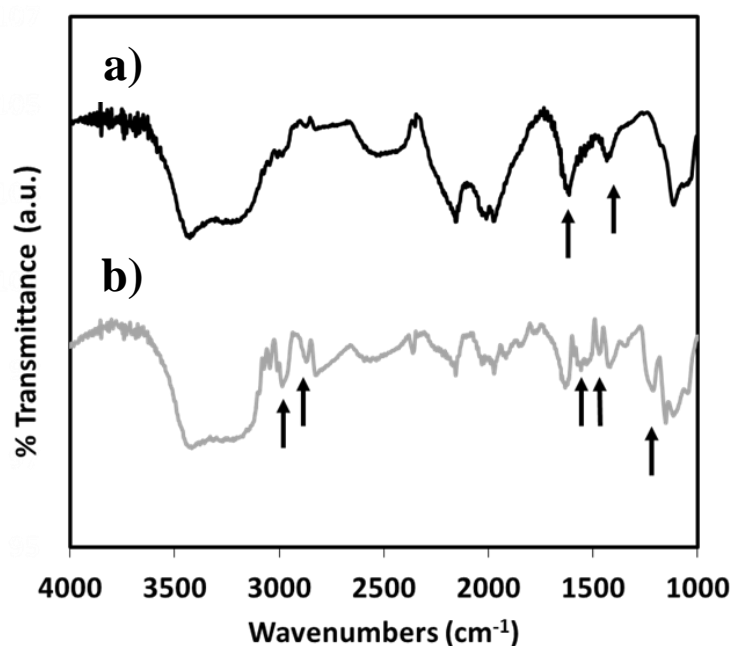
*Figure 2. 5: FTIR spectra for 10% Au*MNPs (a) without PEG and (b) with PEG coating. The arrows highlight the characteristic bands of UREA and PEG that have been used in their synthesis.*

The synthesis method we presented here is adapted from large-scale preparation for "metal-on-metal oxide" catalysts. However, there are several advantages from this method that can be useful for other research areas. First, it is scalable up to 1 g per batch scale, which is a significant advantage over other methods for a similar type of materials. As in catalysis, there are a wide range of metal-metal oxide combinations that can be adapted using this method, and the combinations are not limited to Au and Fe_3O_4. Moreover, the reagents used were considered biocompatible, e.g., urea as the reductant. This is aimed at high biocompatibility of the final contrast agent. Unlike other published methods, there is also no organic functionalization, e.g., thiol groups, performed on the MNP surface (between the Au and Fe_3O_4 nanoparticles) [2.17-22]. As such, the surfaces of each component were kept pristine for further functionalization. This is essential when further functionalities are required, e.g. targeting molecules, for localization of the contrast agent on specific sites of interest [2.11]

2.3.2. Effects on cells and cytotoxicity

Calcein AM and ethidium homodimer staining demonstrated no adverse effects on cell culture at both 10µg/mL and 100µg/mL concentrations and for both unfunctionalized and PEG-coated Au*MNPs (10%), at both time points (1 day and 7 days) (Figure 2. 6). Cells multiplied in number over the time course followed, suggesting a limited influence on cell proliferation. Studying the cell membrane interactions and subsequent uptake of the Au*MNPs, MCF-7 cells were exposed to 10 µg/mL of 10% Au*MNPs (unfunctionalized and PEG-coated) and studied by SEM and TEM. The SEM images of MCF-7 cells 24 h post Au*MNP exposure can be seen in Figure 2. 7. The cells were like control cells in terms of their adherence (cell spreading), morphology, and size (Figure 2. 7, upper panel). Au*MNPs were visible on the cell surface, with increased levels of membrane activity, typically via F-actin protrusions (white arrowheads, Figure 2. 7) which were evident in cells treated with the PEG-coated Au*MNPs. This may suggest active cell internalization.

Calcein AM 1 day
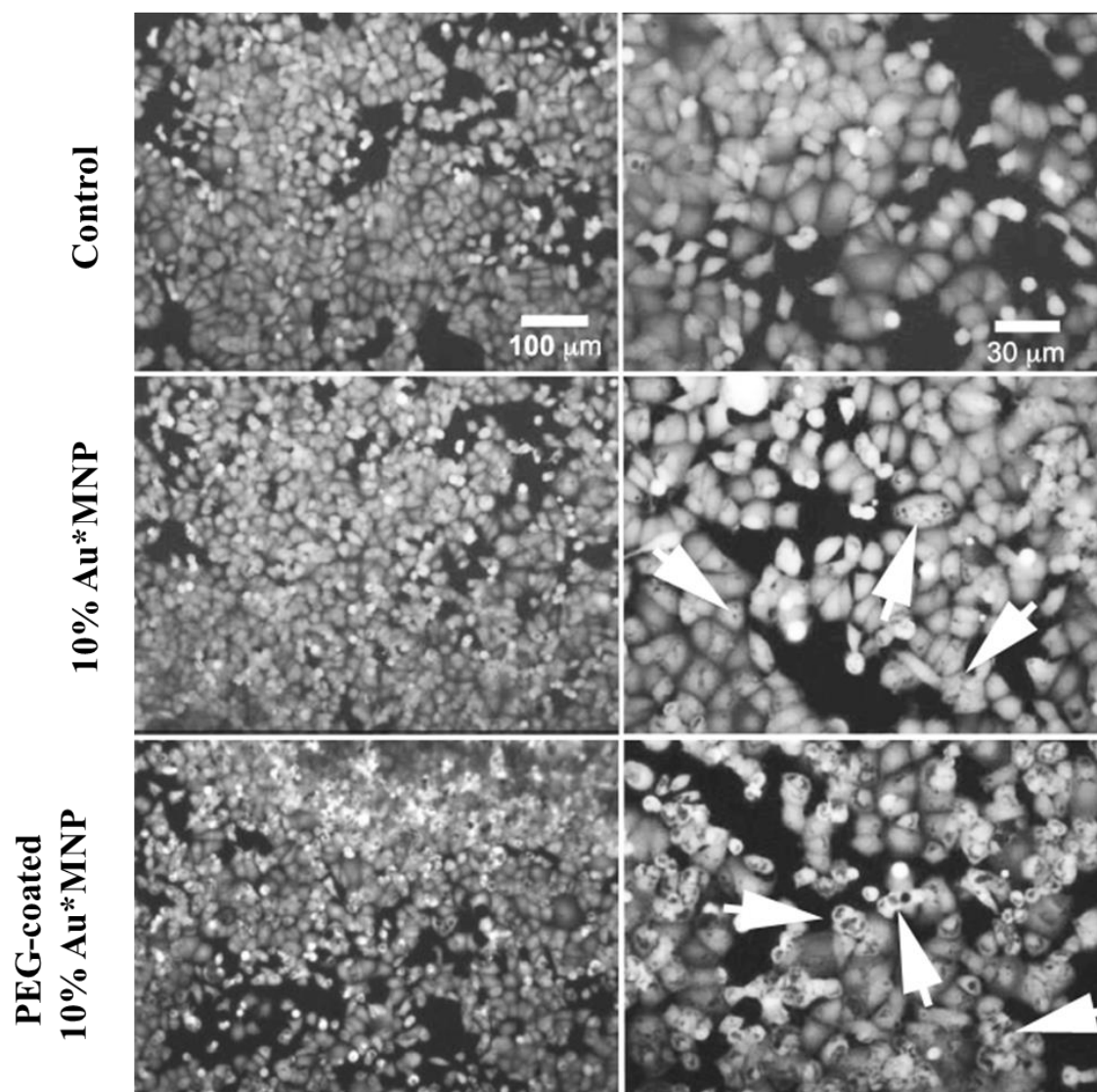
Figure 2. 6: Cell images for Calcein AM assay. White arrowheads indicate the internalized Au*MNP samples within the MCF-7 cell culture after 1-day exposure to 10% Au*MNPs
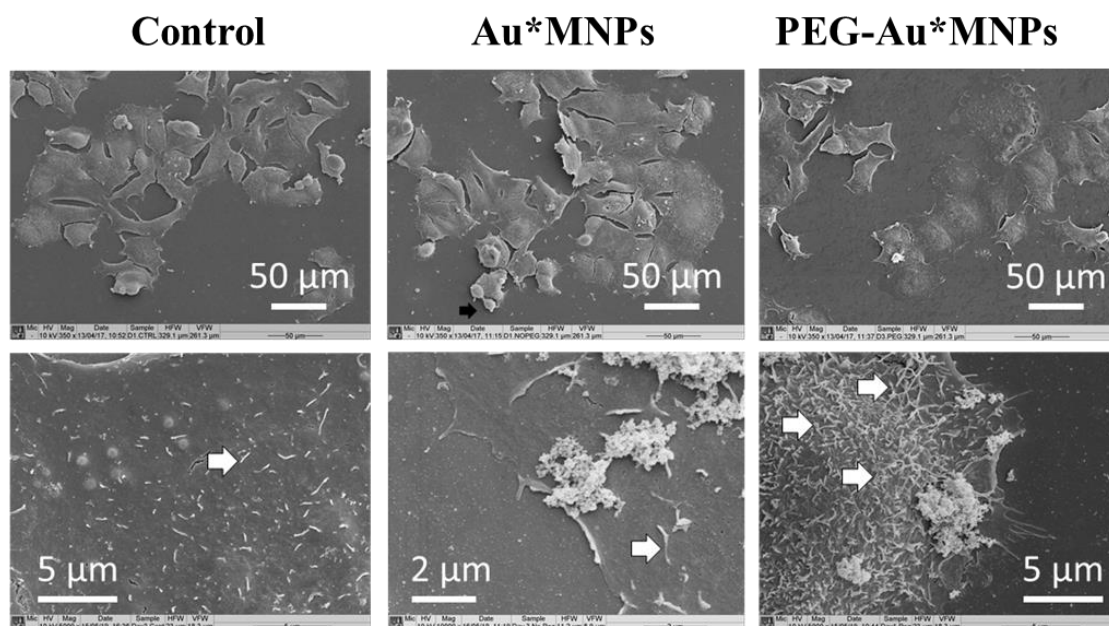
Figure 2. 7: SEM images of MCF-7 cells exposed with 10% Au*MNPs after 24 h. White arrowheads on SEM indicate the F-actin protrusions on cell surfaces.

The TEM images of cells were taken after 24 h exposure to Au*MNPs (see Figure 2. 8). Both unfunctionalized and PEG-coated Au*MNPs were observed in vesicles/ endosomes within the cell cytoplasm. From the images, PEG-coated Au*MNPs showed a higher internalization, compared to the unfunctionalized NPs. Moreover, the PEG-coated Au*MNPs aggregates were less dense than the unfunctionalized NPs. This is consistent with similar observations from reports using PEG-coated NPs [2.27-2.30]. Overall, compared with the controls, Au*MNPs did not damage cells upon internalization.

Control	Au*MNPs	PEG-Au*MNPs
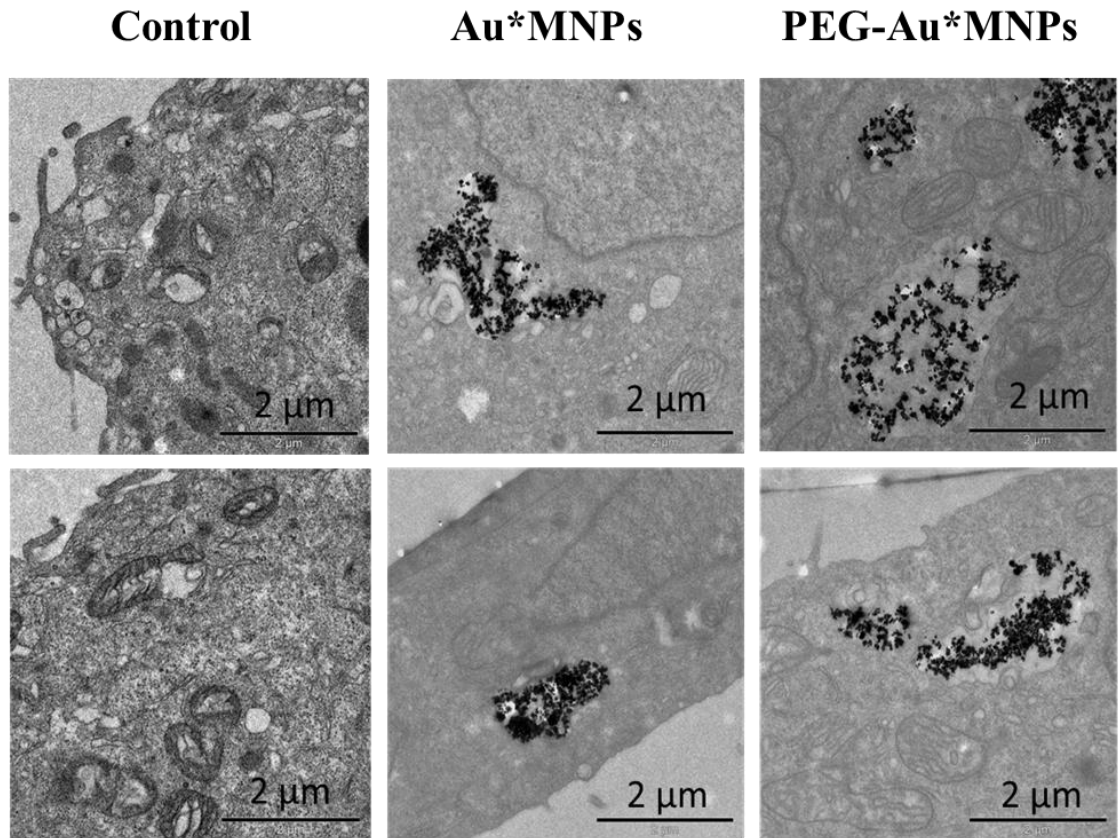
Figure 2. 8: TEM images of MCF-7 cells exposed with 10% Au*MNPs after 24 h. Showing agglomerations of iron oxide nanoparticles (black dots) in the cell culture (gray matter).

2.3.3. Contrast enhancement ability in MRI

In this study, MR imaging was used to assess for the first time a) the "negative" contrast enhancement ability of our Au*MNPs samples using both T_1 and T_2-weighted sequences used for anatomical imaging and b) to investigate whether different Au concentrations may affect the MR contrast enhancement of the MNPs. Clear signal reductions were observed in both the T_1- and T_2-weighted MR images, as MNPs concentrations increased [from 0.01 to 0.2 mM Fe] (Figure 2. 9). The fast spin echo and multi-slice gradient echo sequence used for T_1- and T_2-weighted MR images (see Experimental Section) respectively can both achieve high-quality anatomical imaging *in vivo* [2.31]. In the clinical setting, T_1- and T_2-weighted MR protocols used for anatomical imaging can provide important complementary information of organ-tissue morphology and are routinely combined across various applications [2.25, 2.26]. Previous biomaterial synthesis studies have mainly focused on assessing T_2-weighted signal reductions in the presence of Au*MNPs [2.18-2.22]. Different from previous studies which aimed to synthesize smaller diameter MNPs (<5 nm) to increase their r_1 relaxivity and reinforce them as "positive" contrast agents for functional T_1-weighted imaging [2.17, 2.33], our larger diameter (20-30 nm)

Au*MNPs effectively reduced the MR signal in a T_1-weighted sequence. This sequence is routinely used for high spatial resolution anatomical imaging. Our Au*MNPs were therefore shown to have "negative" contrast ability for high spatial resolution MR anatomical imaging, using both T_1- and T_2-weighted protocols.
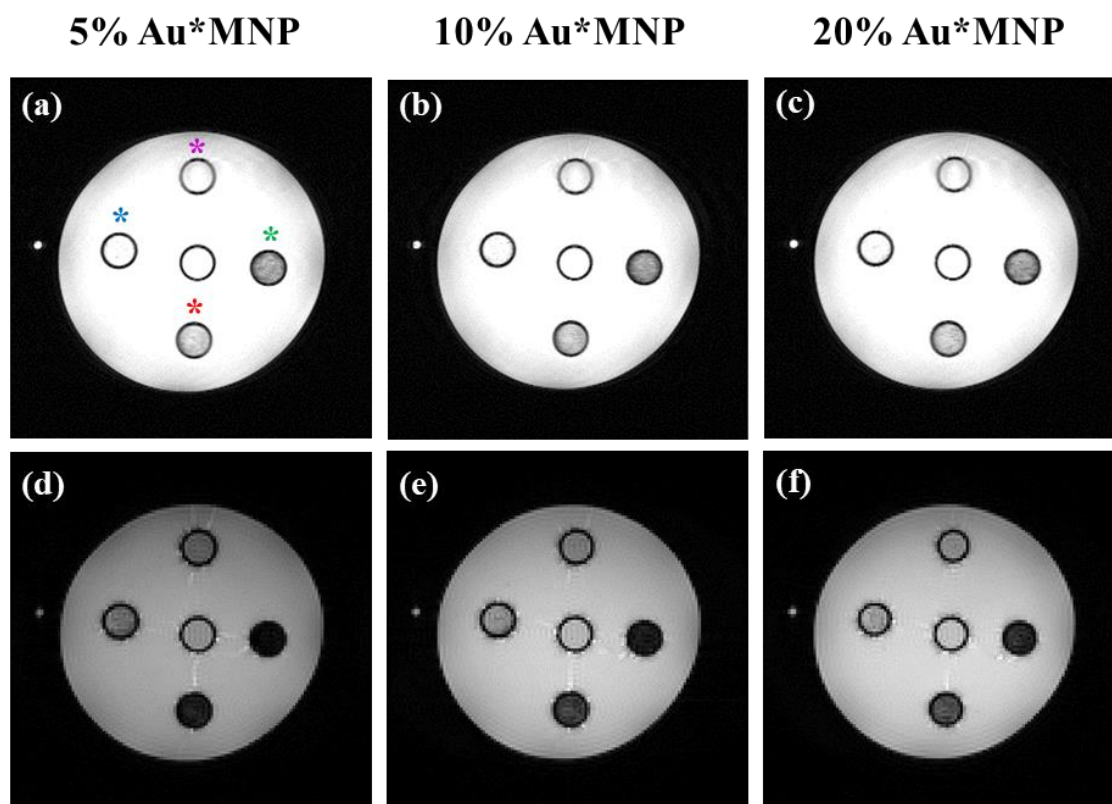
*Figure 2. 9: Different slice positions of Au*MNP samples in T_1-weighted MR imaging (a-c) and same slice positions of Au*MNP samples in T_2-weighted MR imaging (d-f). Note T_1 and T_2 "positive contrast" of Au*MNP samples as concentration increased across sample tubes, which is shown as increasing darkness of the individual samples. Blue, magenta, green and red stars denote 0.1, 0.2, 0.3, and 0.4 mM concentrations of Au*MNP, respectively. The central tube a-f are the pure Au reference samples.*

More importantly, the effect of the Au content on the MR contrast enhancement ability of MNPs was also studied. In Figure 2. 10, a and b, and Figure 2. 11, a and b, there was no systematic influence of the Au in the T_1 and T_2-weighted images across different Au*MNPs samples observed, which was consistent even for higher Au concentrations ($\geq$10% Au in MNP). This demonstrates that the Au component does not corrupt the MR signal modifications caused by Au*MNPs.
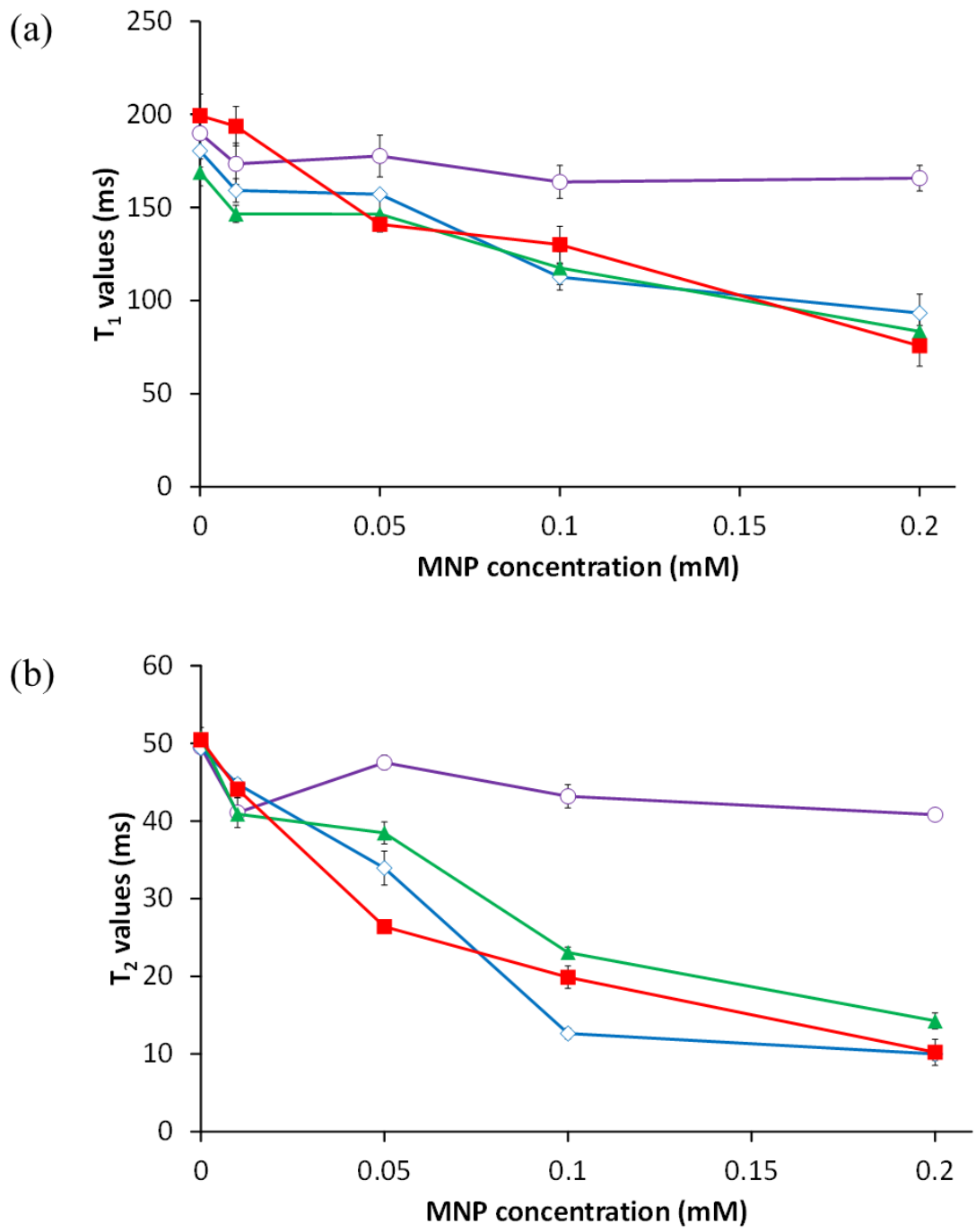
Figure 2. 10: MR T_1-weighted (a) and T_2-weighted (b) signal decreases quantified due to MNP concentration increase per sample (iron oxide only, purple; 5% Au*Fe₃O₄, blue; 10% Au*Fe₃O₄, green and 20% Au*Fe₃O₄, red).
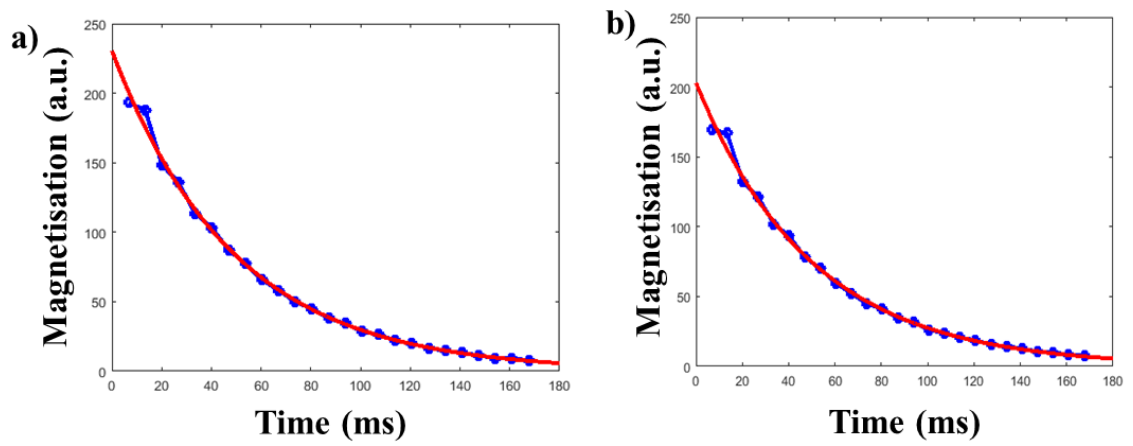
Figure 2. 11: T_2-weighted curves (blue) across all 25 T_2 images and transverse relaxation time model fit (red) from a sample tube with the lowest (a) and a sample tube with the highest (b) MNP concentration. Note that the exponential decay for the T_2 curve in (b) is shorter (curve decays faster) due to higher MNP concentration, compared to (a). Although visual differences between curves are relatively subtle, the T_2-values, calculated by the system after 3 repeating measurements, showed values of 50 ms in (a) and 12 ms in (b).

2.3.4. Contrast enhancement ability in CT

CT imaging was performed to separately assess a) the CT contrast enhancement ability of Au*MNPs and b) whether the MNPs and/ or PEG can affect the CT signal modifications caused by PEG-coated versus non-PEG-coated Au*MNPs. There are distinct increases shown in CT signal intensity as Au concentration was raised [from 0.1 mM to 0.4 mM Au]. This is consistent with a previous study assessing CT signal enhancement in the presence of Au on MNPs [2.18]. Moreover, there was no systematic signal enhancement observed on CT images due to MNP concentration increases across samples (from 0.1 to 0.4 mM Au, for all different 5% to 20% Au on MNP experiments, Figure 2. 12).
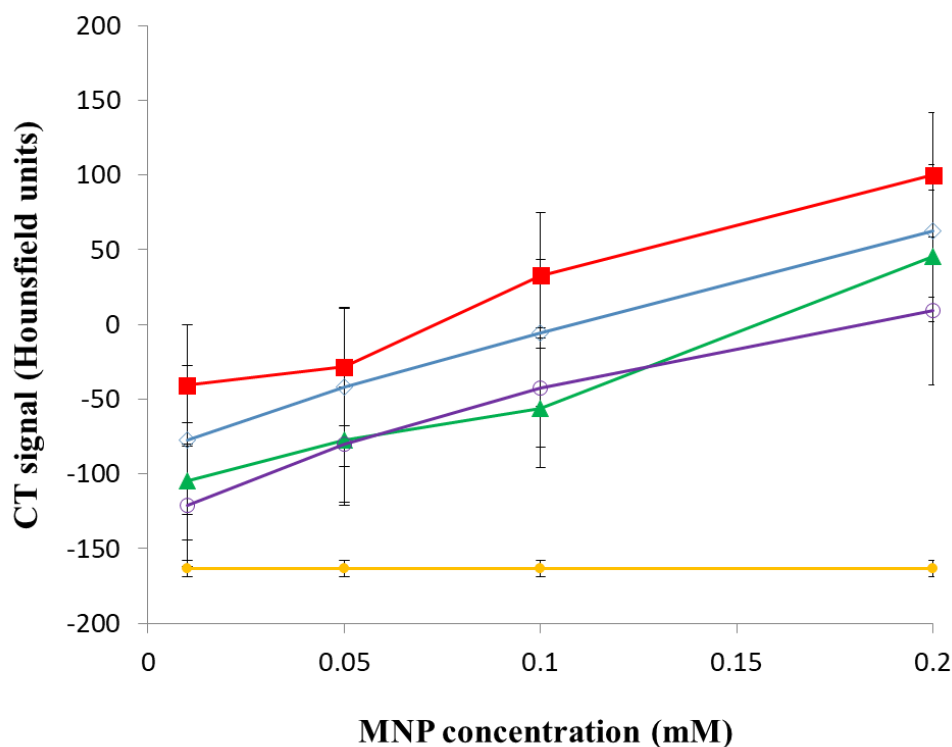
Figure 2. 12: The CT signals of iron oxide only (purple), 5% Au*Fe₃O₄ (blue), 10% Au*Fe₃O₄ (green), and 20% Au*Fe₃O₄ (red) increase with an increasing Au concentration per sample.

In contrast, a systematic reduction of HU in the CT signal was observed for PEG-coated Au*MNPs versus non-PEG-coated Au*MNPs (10% and 20% Au in MNP with PEG versus 5% and 10% Au in MNP with no PEG). Due to its low density, PEG has previously been used as a "negative" contrast agent in CT imaging [2.35], thus it is known that it can lower the signal intensity in CT imaging. However, this is the first study investigating PEG interaction across varying Au concentrations in CT imaging. As described above, PEG coating is commonly used to coat nanoparticles in biomedical research [2.17, 2.19-2.22], as it can avoid unwanted protein binding, leading to corona formations and eventually immune clearance [2.35]. It is therefore critical to examine to which degree PEG coating may alter the Au*MNP performance in CT imaging. Despite the PEG coating consistently reducing HU in the CT signal, it was still possible to obtain linear CT signal increases as Au*MNP concentration was raised (from 0.1 to 0.4 mM Au) within each of the PEG-coated experiments (10% and 20% Au in MNP with PEG) (Figure 2. 13). By increasing the concentration from 0.1 mM to 0.4 mM a stronger CT signal was achieved, improving the general signal performance as demonstrated in Figure 2. 12. This was an important assessment towards optimizing PEG-coated Au*MNPs for pre-clinical and clinical CT applications.
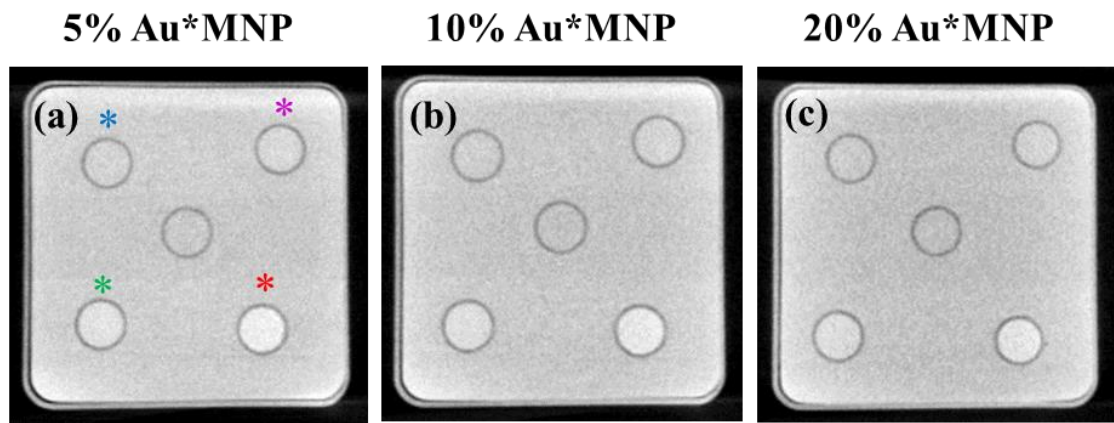
Figure 2. 13: Different slice positions of Au*MNP samples in CT imaging. Samples were re-positioned in an appropriately shaped radiolucent plastic container. Note that the CT signal increases with an increasing concentration per sample. Blue, magenta, green and red stars denote 0.1, 0.2, 0.3 and 0.4 mM concentrations of Au*MNP, respectively. The central tube a-c is the pure MNP reference sample. Changing the initial concentration of 0.1 mM (blue) to 0.4 mM (red) visibly increased the signal performance, represented as a lighter tone of gray across the concentrations.

2.3.5. Contrast enhancement assessment in Ultrasound

Figure 2. 14 shows typical images acquired from the IVUS scanner for all three Au*MNP concentrations. There was consistently increasing signal enhancement as Au concentration increased (from 1 mg/mL to 10 mg/mL Au*MNP concentration, and from 5% to 20% Au content on MNP). For low Au*MNP concentrations (1mg/mL) little enhancement was observed in the image but increasing Au*MNP concentrations resulted in an increase in enhancement. Figure 2. 15 illustrates the quantitative results from measuring the same sample 5 times, showing a four-fold increase in mean intensity between 1mg/mL and 5mg/mL Au*MNP concentration for 5% and 10% Au concentrations and a 2.5-fold increase for 20% Au concentration. The error bars result from the multiple measurements and represent the upper and lower limits measured, with no statistically significant differences between the samples ($p < 0.05$) These results are consistent with previous studies demonstrating enhancement of ultrasonic emission in photoacoustic imaging, whilst Au is known to have a high density and therefore high acoustic impedance [2.21, 2.22].

NP concentration	1 mg/mL	5 mg/mL	10 mg/mL
5 % Au*MNP			
10 % Au*MNP			
20 % Au*MNP			
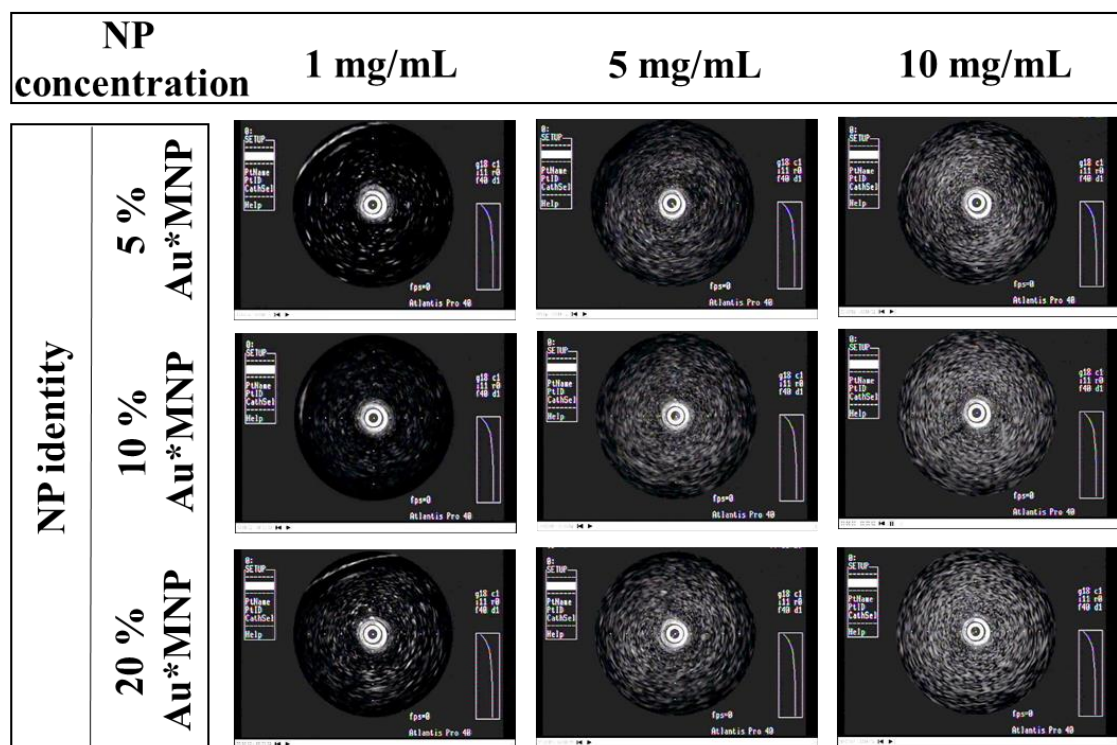
*Figure 2. 14: Qualitative signal differences in images acquired using the IVUS scanner, showing signal enhancement (more white noise), as Au*MNP concentration increased from 1 to 10 mg/mL and as Au content increased from 5 to 20%.*
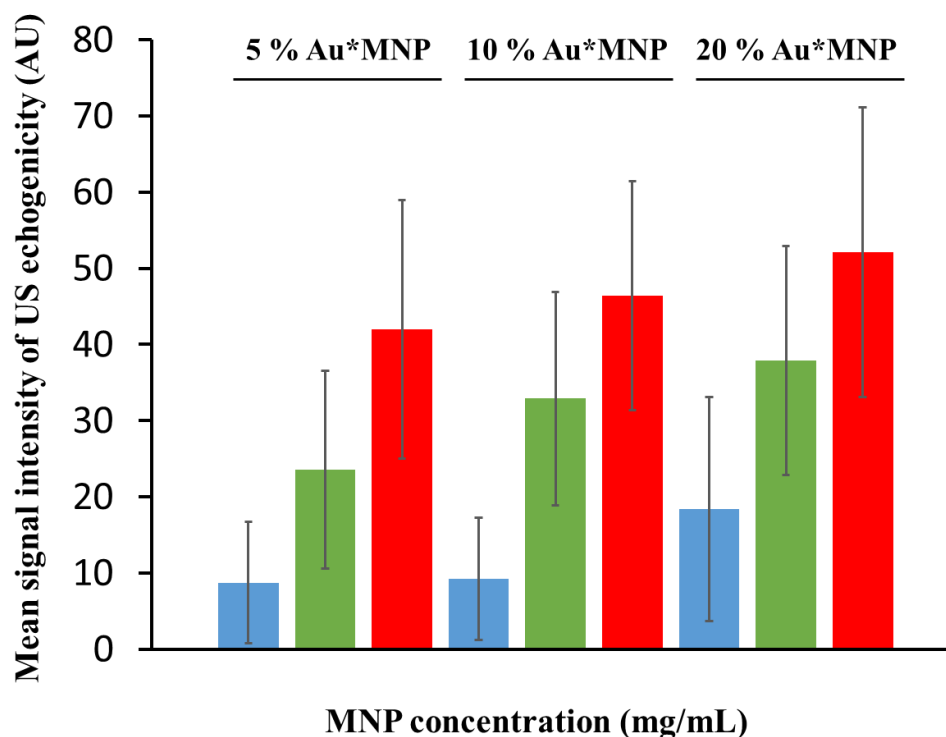
*Figure 2. 15: Quantitative signal differences across the same Au*MNP samples, where blue, green, and red represent concentrations of 1,5 and 10 mg/mL.*

This is the first study demonstrating increasing enhancement of ultrasonic emission from an IVUS scanner, due to Au concentrations increases within these Au*MNP samples. IVUS imaging is routinely used to invasively assess atherosclerotic plaque severity in coronary artery disease [2.38]. Furthermore, using MR imaging, our group has previously shown that MNPs are taken up in areas of cellular inflammation in the myocardium [2.14, 2.37]. Being able to monitor cellular inflammation in coronary artery disease is critically important for clinically assessing atherosclerotic plaque formation, development, and rupture [2.38]. Thus, it is suggested that Au*MNP can in principle support a novel imaging methodology to simultaneously assess atherosclerotic plaque development and inflammation, by using a single Au*MNP IVUS imaging setting.

2.4. Conclusions

In this chapter, the development of Au*MNPs which were synthesized using an impregnation method, leading to nanoparticles with pristine surfaces for either component. Pristine NP surfaces can be particularly important when functionalization needs to be engineered in molecularly targeted theragnostic applications. Moreover, the cytotoxicity of these Au*MNP was evaluated *in vitro* and showed that these were non-toxic to cells when a maximum concentration of 100 μg/mL was examined for 7 days. The contrasting capability of these Au*MNP was also shown to be concentration-dependent across all three (MR, CT, IVUS) imaging techniques. Most importantly, for the first time, it has been shown that larger diameter (20 - 30 nm) Au*MNPs can modify the MR signal in a T_1-weighted sequence which is routinely used for high spatial resolution anatomical imaging. This assessment supports the use of larger diameter Au*MNPs, beyond their well-established contrasting ability in T_2-weighted sequences. For the first time, it was finally shown that the Au content of the Au*MNP can lead to evident increases of the IVUS signal and suggest that Au*MNP can potentially support a novel IVUS imaging methodology to simultaneously assess atherosclerotic plaque development and inflammation. In conclusion, these materials have great potential where further developments and intensive studies in vitro and in vivo, can transform them into a powerful tool to enhance theragnostic applications and tri-modal imaging accuracy in the clinical setting.

2.5. References

[2.1.] S. D. Fihn, J. M. Gardin, J. Abrams, K. Berra, J. C. Blankenship, A. P. Dallas, P. S. Douglas, J. M. Foody, T. C. Gerber, A. L. Hinderliter, S. B. King, P. D. Kligfield, H. M. Krumholz, R. Y. K. Kwong, M. J. Lim, J. A. Linderbaum, M. J. Mack, M. A. Munger, R. L. Prager, J. F. Sabik, L. J. Shaw, J. D. Sikkema, C. R. Smith, S. C. Smith, J. A. Spertus, and S. V. Williams, 2012 ACCF/AHA/ACP/AATS/PCNA/SCAI/STS Guideline for the diagnosis and management of patients with stable ischemic heart disease: a report of the American College of Cardiology Foundation/American Heart Association Task Force on Practice Guidelines, and the American College of Physicians, American Association for Thoracic Surgery, Preventive Cardiovascular Nurses Association, Society for Cardiovascular Angiography and Interventions, and Society of Thoracic Surgeons; J. Am. Coll. Cardiol., **2012**, 60, 44–164.

[2.2.] L. J. Graham, M. P. Shupe, E. J. Schneble, F. L. Flynt, M. N. Clemenshaw, A. D. Kirkpatrick, C. Gallagher, A. Nissan, L. Henry, A. Stojadinovic, G. E. Peoples and N. M. Shumway; Current Approaches and Challenges in Monitoring Treatment Responses in Breast Cancer; J. Cancer, **2014**, 5, 58–68.

[2.3.] G. Montalescot, U. Sechtem, S. Achenbach, F. Andreotti, C. Arden, A. Budaj, R. Bugiardini, F. Crea, T. Cuisset, C. Di Mario, R. Ferreira, B. J. Gersh, A. K. Gitt, J.-S. Hulot, N. Marx, L. H. Opie, M. Pfisterer, E. Prescott, F. Ruschitzka, M. Sabate, R. Senior, D. P. Taggart, E. E. van der Wall, and C. J. M. Vrints; 2013 ESC guidelines on the management of stable coronary artery disease: The Task Force on the management of stable coronary artery disease of the European Society of Cardiology; Eur. Heart J., **2013**, 34, 2949–3003.

[2.4.] T. Murakami, Y. Imai, M. Okada, T. Hyodo, W.-J. Lee, M.-J. Kim, T. Kim, and B. I. Choi; A Bridge to a Consensus on Hepatocellular Carcinoma Management; Oncology, **2011**, 81, 86–99.

[2.5.] G. Papanastasiou, M. C. Williams, L. E. Kershaw, M. R. Dweck, S. Alam, S. Mirsadraee, M. Connell, C. Gray, T. MacGillivray, D. E. Newby, and S. I. Semple; Measurement of myocardial blood flow by cardiovascular magnetic resonance perfusion: comparison of distributed parameter and Fermi models with single and dual bolus; J. Cardiov. Magn. Reson., **2015**, 7, DOI:10.1186/s12968-015-0125-1.

[2.6.] R. T. George, A. Arbab-Zadeh, R. J. Cerci, A. L. Vavere, K. Kitagawa, M. Dewey, C. E. Rochitte, A. E. Arai, N. Paul, F. J. Rybicki, A. C. Lardo, M. E. Clouse, and J. A. C. Lima; Diagnostic Performance of Combined Noninvasive Coronary Angiography and Myocardial Perfusion Imaging Using 320-MDCT: The CT Angiography and Perfusion Methods of the CORE320 Multicenter Multinational Diagnostic Study; J. Roentgenol., **2011**, 197, 829–837.

[2.7.] H. Blessberger and T. Binder; NON-invasive imaging: Two-dimensional speckle tracking echocardiography: basic principles; Heart, **2010**, 96, 716–722.

[2.8.] G. Papanastasiou, V. González-Castro, C. D. Gray, R. O. Forsythe, Y. Sourgia-Koutraki, N. Mitchard, D. E. Newby and S. I. K. Semple; Multidimensional Assessments of Abdominal Aortic Aneurysms by Magnetic Resonance Against Ultrasound Diameter Measurements; in Medical Image Understanding and Analysis, Springer International Publishing, Cham, **2017**,723, 133–143.

[2.9.] G. Papanastasiou, M. C. Williams, M. R. Dweck, S. Mirsadraee, N. Weir, A. Fletcher, C. Lucatelli, D. Patel, E. J. R. van Beek, D. E. Newby, and S. I. K. Semple; Multimodality Quantitative Assessments of Myocardial Perfusion Using Dynamic Contrast Enhanced Magnetic Resonance and 15O-Labeled Water Positron Emission Tomography Imaging; IEEE TRPMS, **2018**, 2, 259–271.

[2.10.] E. Casals, S. Vázquez-Campos, N. G. Bastús, and V. Puntes; Distribution and potential toxicity of engineered inorganic nanoparticles and carbon nanostructures in biological systems; Trac-Trends Anal. Chem., **2008**, 27, 672–683.

[2.11.] N. Bertrand, J. Wu, X. Y. Xu, N. Kamaly and O. C. Farokhzad; Cancer nanotechnology: the impact of passive and active targeting in the era of modern cancer biology; Adv. Drug Deliv. Rev., **2014**, 66, 2–25.

[2.12.] C. Sun, J. S. H. Lee and M. Zhang; Magnetic nanoparticles in MR imaging and drug delivery; Adv. Drug Deliv. Rev., **2008**, 60, 1252–1265.

[2.13.] S. G. Ruehm, C. A. Corot, P. R. Vogt, S. E. Kolb, and J. F. Debatin; Magnetic resonance imaging of atherosclerotic plaque with ultrasmall superparamagnetic particles of iron oxide in hyperlipidemic rabbits; Circulation, **2001**, 103, 415–422.

[2.14.] C. G. Stirrat, S. R. Alam, T. J. MacGillivray, C. D. Gray, M. R. Dweck, J. Raftis, W. S. Jenkins, W. A. Wallace, R. Pessotto, K. H. Lim, S. Mirsadraee, P. A. Henriksen, S. I. Semple, and D. E. Newby; Ferumoxytol-enhanced magnetic resonance imaging assessing inflammation after myocardial infarction; Heart, **2017**, 103, 1528–1535.

[2.15.] G. Girardi, J. Fraser, R. Lennen, R. Vontell, M. Jansen and G. Hutchison; Imaging of activated complement using ultrasmall superparamagnetic iron oxide particles (USPIO) - conjugated vectors: an in vivo in utero non-invasive method to predict placental insufficiency and abnormal fetal brain development; Mol. Psychiatr., **2015**, 20, 1017–1026.

[2.16.] N. Lee, S. H. Choi, and T. Hyeon; Nano-Sized CT Contrast Agents; Adv. Mater., **2013**, 25, 2641–2660.

[2.17.] G. N. Wang, K. Qian, and X. F. Mei; A theranostic nanoplatform: magneto-gold@fluorescence polymer nanoparticles for tumor targeting T_1&T_2-MRI/CT/NIR fluorescence imaging and induction of genuine autophagy mediated chemotherapy; Nanoscale, **2018**, 10, 10467–10478.

[2.18.] H. Y. Zhao, S. Liu, J. He, C. C. Pan, H. Li, Z. Y. Zhou, Y. Ding, D. Huo, and Y. Hu; Synthesis and application of strawberry-like Fe_3O_4-Au nanoparticles as CT-MR dual-modality contrast agents in accurate detection of the progressive liver disease; Biomaterials, **2015**, 51, 194–207.

[2.19.] A. Kukreja, B. Kang, H.-O. Kim, E. Jang, H. Y. Son, Y.-M. Huh and S. Haam; Preparation of gold core-mesoporous iron-oxide shell nanoparticles and their application as dual MR/CT contrast agent in human gastric cancer cells; J. Ind. Eng. Chem., **2017**, 48, 56–65.

[2.20.] L. Han, Y. Zhang, Y. Zhang, Y. Shu, X. W. Chen and J. H. Wang; A magnetic polypyrrole/iron oxide core/gold shell nanocomposite for multimodal imaging and photothermal cancer therapy; Talanta, **2017**, 171, 32–38.

[2.21.] Y. Hu, R. Wang, S. Wang, L. Ding, J. C. Li, Y. Luo, X. L. Wang, M. W. Shen, and X. Y. Shi; Multifunctional Fe_3O_4 @ Au core/shell nanostars: a unique platform for multimode imaging and photothermal therapy of tumors; Sci Rep, **2016**, 6, 28325.

[2.22.] J. Reguera, D. Jiménez de Aberasturi, M. Henriksen-Lacey, J. Langer, A. Espinosa, B. Szczupak, C. Wilhelm and L. M. Liz-Marzán; Janus plasmonic–magnetic gold–iron oxide nanoparticles as contrast agents for multimodal imaging; Nanoscale, **2017**, 9, 9467–9480.

[2.23.] H. H. P. Yiu; Engineering the multifunctional surface on magnetic nanoparticles for targeted biomedical applications: a chemical approach; Nanomedicine, **2011**, 6, 1429–1446.

[2.24.] E. Beguin, L. Bau, S. Shrivastava, E. Stride; Comparing Strategies for Magnetic Functionalization of Microbubbles; ACS Appl. Mater. Interfaces, **2019**, 11, 1829-1840

[2.25.] S. Prabhu, S. Mutalik, S. Rai, N. Udupa, and B. S. S. Rao; PEGylation of superparamagnetic iron oxide nanoparticle for drug delivery applications with decreased toxicity: an in vivo study; J. Nanopart. Res., **2015**, 17, 412.

[2.26.] W. A. McDougald, R. Collins, M. Green and A. A. S. Tavares; High Dose MicroCT Does Not Contribute Toward Improved MicroPET/CT Image Quantitative Accuracy and Can Limit Longitudinal Scanning of Small Animals; Front. Physics, **2017**, 5, 50.

[2.27.] J. Huang, W. L. Dai, and K. N. Fan; Remarkable support crystal phase effect in Au/FeOx catalyzed oxidation of 1,4-butanediol to γ-butyrolactone; J. Catal., **2009**, 266, 228–235.

[2.28.] N. Gal, A. Lassenberger, L. Herrero-Nogareda, A. Scheberl, V. Charwat, C. Kasper and E. Reimhult; Interaction of Size-Tailored PEGylated Iron Oxide Nanoparticles with Lipid Membranes and Cells; ACS Biomater. Sci. Eng., **2017**, 3, 249–259.

[2.29.] T. Nissinen, S. Näkki, H. Laakso, D. Kučiauskas, A. Kaupinis, M. I. Kettunen, T. Liimatainen, M. Hyvönen, M. Valius, O. Gröhn and V.-P. Lehto; Tailored Dual PEGylation of Inorganic Porous Nanocarriers for Extremely Long Blood Circulation in Vivo; ACS Appl. Mater. Interfaces, **2016**, 8, 32723–32731.

[2.30.] E. Illés, M. Szekeres, E. Kupcsik, I. Y. Tóth, K. Farkas, A. Jedlovszky-Hajdú and E. Tombácz; PEGylation of surfacted magnetite core-shell nanoparticles for biomedical application; Colloid Surf. A-Physicochem. Eng. Asp., **2014**, 460, 429–440.

[2.31.] A. K. Gupta and A. S. G. Curtis; Surface modified superparamagnetic nanoparticles for drug delivery: interaction studies with human fibroblasts in culture; J. Mater. Sci.-Mater. Med., **2004**, 15, 493–496.

[2.32.] J. P. Ridgway; Cardiovascular magnetic resonance physics for clinicians: part Il; J. Cardiov. Magn. Reson., **2010**, 12, 71.

[2.33.] J. D. Biglands, A. Radjenovic, and J. P. Ridgway; Cardiovascular magnetic resonance physics for clinicians: part II; J. Cardiov. Magn. Reson., **2012**, 14, 66.

[2.34.] G. N. Wang, X. J. Zhang, Y. Liu, Z. J. Hu, X. F. Mei, and K. Uvdal; Magneto-fluorescent nanoparticles with high-intensity NIR emission, T_1- and T_2-weighted MR for multimodal specific tumor imaging; J. Mat. Chem. B, **2015**, 3, 3072–3080.

[2.35.] L. M. Minordi, A. Vecchioli, P. Mirk and L. Bonomo; CT enterography with polyethylene glycol solution vs CT enteroclysis in small bowel disease; Br. J. Radiol., **2011**, 84, 112–119.

[2.36.] S. I. Jenkins, D. Weinberg, A. F. al-Shakli, A. R. Fernandes, H. H. P. Yiu, N. D. Telling, P. Roach and D. M. Chari; 'Stealth' nanoparticles evade neural immune cells but also evade major brain cell populations: Implications for PEG-based neurotherapeutics; J. Control. Release, **2016**, 224, 136–145.

[2.37.] G. S. Mintz, S. E. Nissen, W. D. Anderson, S. R. Bailey, R. Erbel, P. J. Fitzgerald, F. J. Pinto, K. Rosenfield, R. J. Siegel, E. M. Tuzcu and P. G. Yock; American College of Cardiology Clinical Expert Consensus Document on standards for acquisition, measurement, and reporting of intravascular ultrasound studies (IVUS); ACC Clinical Expert Consensus Document, Eur. J. Echocardiogr., **2001**, 2, 299–313.

[2.38.] S. R. Alam, A. S. V. Shah, J.Richards, N. N. Lang, G. Barnes, N. Joshi, T. MacGillivray, G. McKillop, S. Mirsadraee, J. Payne, K. A. A. Fox, P. Henriksen, D. E. Newby, and S. I.K. Semple; Ultrasmall superparamagnetic particles of iron oxide in patients with acute myocardial infarction: early clinical experience; Circ.-Cardiovasc. Imaging, **2012**, 5, 559-565.

[2.39.] M. Fioranelli, A. G. Bottaccioli, F. Bottaccioli, M. Bianchi, M. Rovesti, and M. G. Roccia; Stress and Inflammation in Coronary Artery Disease: A Review Psychoneuroendocrineimmunology-Based; Front. Immunol., **2018**, 9, 2031.

CHAPTER 3

Impedance-based measurements and CARS imaging as advanced techniques to assess the cytotoxicity of nanomaterials on liver cells *in vitro*.

3.1. Introduction

To establish strategies for disrupting or circumventing the nanoparticle clearance mechanism by macrophages, a relevant, realistic liver model is required for evaluating the relationship between surface chemistry of nanoparticles and their uptake profile by macrophages. For this reason, iron oxide nanoparticles (Fe_3O_4) were coated with polyethylene glycol (PEG) using salinization, where the PEG polymers are grafted onto the nanoparticle surface by strong covalent bonding, ensuring long term stability of MNP coatings. Various methods (colorimetric assays, impedance measurements, TEM, and coherent anti-stokes Raman scattering) were used to study the MNP uptakes in liver cells in 2-D and 3-D models. Functionalized magnetic nanoparticles (e.g. SPIONs) have been widely used in research for various medical applications, namely targeted drug delivery, gene therapy, imaging and diagnosis, and hyperthermia [3.1, 3.2]. However, once they have served their purpose they need to be cleared from the system. Various factors can influence the time that the immune system needs to clear the nanoparticles, including particle size, surface chemistry, and charges. However, the same clearance time is a threat to the nanoparticles who have not fulfilled their intended purpose yet and premature clearance is threatening their efficiency, e.g., when a specific tissue or organ is targeted. Once the nanoparticles have been recognized by the system they are transported in vesicles to the liver or spleen, where they are likely to accumulate until excretion [3.3.]. Therefore, testing nanoparticle compatibility on a liver system becomes more relevant to assess the long-term effect on a human.

Conventionally, toxicity studies on magnetic nanoparticles (MNPs) in cancer cell lines are widely reported, but very few used liver cell models [3.4, 3.5]. A major issue for these toxicity assays is that they were designed for testing soluble substrates by measuring response via spectroscopy in the visible spectrum. Solid-state nanoparticles, in particular black Fe_3O_4, can absorb visible radiation effectively, leading to possible errors on color assays [3.6]. Moreover, most studies on liver cell models with MNPs focused on developing contrast agents for MRI imaging [3.7, 3.8], while others are on targeted drug delivery and hyperthermia to treat liver cancers [3.9, 3.10]. Few studies have been carried out on the interaction between MNPs and liver cells, possibly due to a lack of reliable models.

There are two approaches to assess the hazard of nanomaterials, 2D and 3D models. In general, 2D cultures refer to adherent cells that grow as a mono layer in a culture flask or petri dish. 3D culture models are prepared by growing cell lines in a concentrated media suspension, scaffolds, or gel-like substance without attaching to the culture dish surface [3.11]. The main reason for growing cells in 3D culture is, that they grow into spherical structures in which they form various cell layers. Both approaches have great advantages, but also certain limitations. 2D cultures are generally associated with simple and low-cost maintenance of the cell culture and tests are easy to perform according to the available test-kit s and protocols. However, cells cultured in 2D do not mimic the actual behavior as they would in the natural environment of tissues or tumors. 3D cultured cells mimic the physical and biochemical features of a solid tumor mass and therefore allow for a more accurate estimate of the cellular topology, gene expression, signaling, and metabolism [3.11, 3.12]. The limitations of a 3D model are, that the required nutrients might not necessarily penetrate through the whole 3D scaffold, causing cell apoptosis in the center of the spheroid [3.11]. Kapałczyńska et al. have published a table that compares the main features of 2D and 3D culture methods (Table 3.1.).

Table 3. 1: Comparison of 2D and 3D cell culture methods [3.11].

Type of culture	2D	3D	Ref.
Time of culture formation	Within minutes to a few hours	From a few hours to a few days	[3.13-3.15]
Culture quality	High performance, reproducibility, long-term culture, easy to interpret, simplicity of culture	Worse performance and reproducibility, difficult to interpret, cultures more difficult to carry out	[3.12.]
In vivo imitation	Do not mimic the natural structure of the tissue or tumor mass	*In vivo* tissues and organs are in 3D form	[3.17.]
Cell interactions	Deprived of cell-cell and cell-extracellular environment interactions, no *in vivo*-like microenvironment and no "niches"	Proper interactions of cell-cell and cell-extracellular environment, environmental "niches" are created	[3.18-3.22]
Characteristics of cells	Changed morphology and way of divisions; loss of diverse phenotype and polarity	Preserved morphology and way of divisions, diverse phenotype, and polarity	[3.23-3.29]
Access to essential compounds	Unlimited access to oxygen, nutrients, metabolites, and signaling molecules (in contrast to *in vivo*)	Variable access to oxygen, nutrients, metabolites, and signaling molecules (same as *in vivo*)	[3.30., 3.31.]
Molecular mechanisms	Changes in gene expression, mRNA splicing, topology, and biochemistry of cells	Expression of genes, splicing, topology, and biochemistry of cells as *in vivo*	[3.32-3.35.]
Cost of maintaining a culture	Cheap, commercially available tests and the media	More expensive, more time-consuming, fewer commercially available tests	[3.36]

For this chapter two liver cancer cell lines, Huh-7 and HepaRG were used to analyze the cytotoxicity of PEG-coated iron oxide nanoparticles in 2D and 3D cultures. Huh-7 is a well-established cell line that originates from a liver tumor taken from a 57-year-old Japanese male. It presents a highly heterogeneous cell culture with adherence to the surface of flasks or plates within hours and is typically grown as a 2D monolayer. The HepaRG cell line is an original human liver cancer cell line that comprises liver cells and cholangiocyte-like cells, which transport bile through the biliary system in the liver (*Figure 3. 1*) [3.36.]. The biliary system describes a network of the gall bladder, the liver, and bile ducts that clear waste products from the liver into the duodenum and aid the digestion with the controlled release of bile [3.36.]. Bile is made of cholesterol and bile salts and is secreted by the liver to carry away waste and break down fats during digestion. [3.36.]. Following a well-validated differentiation protocol, HepaRG cells grow to a uniquely stable, highly differentiated hepatocyte-cholangiocyte, co-culture system, in which liver-specific functions, such as drug efflux transporters and albumin and urea synthesis, are maintained for several weeks at levels, comparable to those found in primary human hepatocytes [3.37-3.39.]

In this chapter, the response of HepaRG liver cells to nanoparticles was examined by both methods (2D and 3D). Culturing the cells in 2D gives the cells room to stretch out and expand over the free surrounding area before cell assays were performed to assess their viability and proliferation. Furthermore, a wider spread of cells allows to analyze each part of the cell culture in more detail, e.g. cell morphology, viability as well as the nanoparticle settlement, internalization, and distribution within the cells [3.40]. The 3D cell culture was realized by culturing the HepaRG cells in a gel model that was modified to mimic a realistic liver environment.
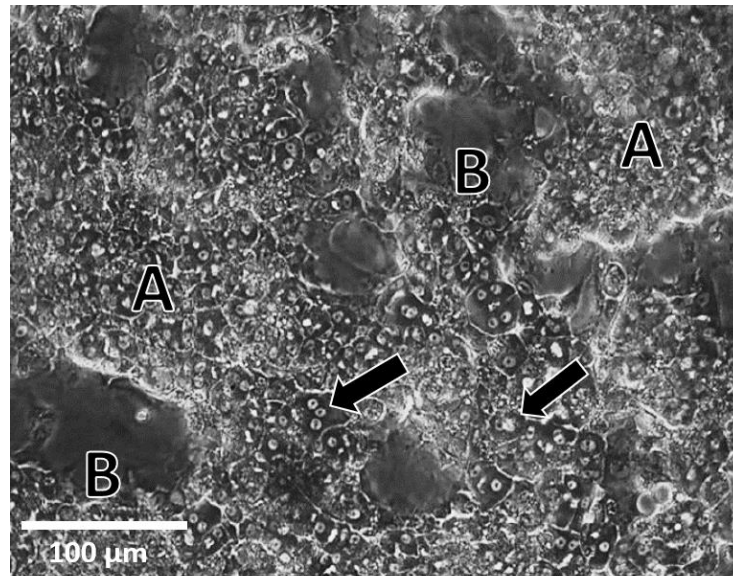
Figure 3. 1: Fully differentiated HepaRG culture imaged on a light microscope under 10x fold magnification, showing islands of hepatocytes (A, light structures), cholangiocyte-like cells (B, dark patches), and bile canaliculi (arrows, small spherical holes).

3.2. Colorimetric cell assays

Biochemical assays are analytical procedures that use various enzymatic or chemical activities within biological cells to detect, analyze and evaluate their behavior, response, and cellular processes. They are routinely used to characterize aims and targets but also to understand biomolecular functions [3.40]. Two-color assays have been chosen to assess the cell viability and proliferation (PrestoBlue®, Invitrogen™) and cell activity (CellTiter-Glo® 3D Cell Viability Assay, Promega®) of the cultured cell lines Huh-7 and HepaRG after nanoparticle exposure.

3.2.1. PrestoBlue® Cell Proliferation Assay

Viable cells possess the ability to reduce resazurin within their intracellular fluid (Cytosol) to red-fluorescent resorufin. The PrestoBlue® cell viability reagent targets that reducing environment to quantitatively measure cell proliferation and determines the relative viability of various reagents across many different cell types. The assay is based on a resazurin solution with a cell-permeant compound that is blue in color and non-fluorescent. Once the reagent is added to the cells, the reducing environment of viable cells changes the color of the solvent to a highly fluorescent red. The fluorescence can then be detected using fluorescence measurements, using the excitation (569 nm, green) and emission (586 nm, yellow) peaks for resorufin [Figure 3. 2]. Converting the fluorescent signal is proportional to the number of metabolically active cells, allowing for quantification of viable cells [3.40.].
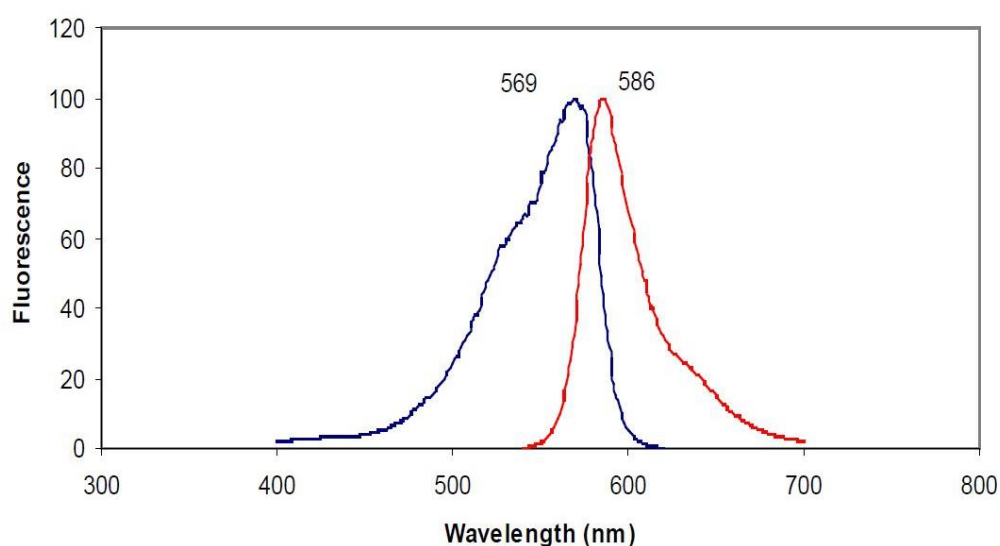
Figure 3. 2: Fluorescent measurement of resorufin with excitation and emission peaks at 569 nm and 586 nm. The fluorescence signal is proportional to the number of metabolically active cells and therefore allows for quantitative measurements of the cell viability [3.40.].

3.2.2. CellTiter-Glo® 3D Cell Viability Assay

The CellTiter-Glo® 3D Cell Viability Assay is a method to determine the number of viable cells in 2D and 3D cultures. It is based on the quantification of available adenosine triphosphate (ATP) after cell lysis. ATP is the source of energy for most cellular processes. The enzymatic removal of phosphate groups from ATP releases energy which is used by the cell in several metabolic processes as well as in the synthesis of macromolecules such as proteins. If there is no energy needed the phosphate groups are added back to form ATP storing the generated energy for the next time it is required [3.41.]. Once the assay solution is added to the cell culture, the cells undergo cell lysis and release their ATP. Luciferin, a light-emitting compound within the assay solution then reacts with the released ATP and generates a luminescent signal that can then be used to compare control cells to cells that have been treated with nanoparticles or other materials or substrates. The signal is equivalent to the amount of ATP present and therefore proportional to the number of viable cells within the culture [3.42.].

3.3. Techniques to evaluate cell viabilities after nanoparticle exposure

Biochemical assays can be very invasive and can mostly be performed only once one the same cell culture. Much preparation needs to be done to perform the assay and the cells can be severely damaged or useless for further experiments. When looking for long-term effects after nanoparticle exposure, several cell cultures need to be cultured for each time point (e.g. 1 day, 3 days, and 7 days, in triplicate) and large amounts of nanoparticles are needed for exposure. Furthermore, experiments showed that various biochemical assays interfere with iron oxide nanoparticles and can emit wrong or altered fluorescent, luminescent, and adsorption values [3.6.].

Non-invasive imaging techniques are a great alternative to avoid such errors and prevent wasting valuable resources as nanoparticles and biological samples when long-term studies are required. Once the cells are cultured only a single dose of nanoparticles is required to analyze the short- and long-term effects on the cell line. The same culture dish can be looked at and evaluated at any desired time point without harming or damaging the cells. Non-invasive imaging gives more insight into the cell behavior, response, and cellular processes, without harming or denaturing the cell and possible particle interference. The image capture acquisition times are reduced to a few seconds and give more insight into the cell culture's physiology than standard biochemical assays allow. In addition, shorter capturing times allow following biochemical reactions and cell responses in live cells in real-time [3.43.]. The two following microscopes have been

used to analyze the particle distribution and cell penetration of fluorescent-tagged and polyethylene glycol coated iron oxide nanoparticles (Meiji TC-5600 Epifluorescence microscope) and to determine how much PEG-coated nanoparticles influence the cell viability and study the cell expression in their lipid droplet formation (coherent anti-stokes Raman scattering, CARS).

A **Meiji TC-5600 Epifluorescence microscope** was used to analyze HepaRG cells in 2D culture. The cells were exposed to iron oxide nanoparticles functionalized with the fluorescent dye rhodamine B isothiocyanate (RITC) and finally coated with polyethylene glycol (Fe_3O_4-PEG-RITC). The PEGylation helped the nanoparticles to diffuse through the cell walls and distribute throughout the cell, while the RITC dye emitted a fluorescent signal that could be picked up on the fluorescence microscope. This allowed capturing images of the cell penetration and particle distribution within the cell.

Coherent Anti-Stokes Raman Scattering (CARS) is a minimally invasive and label-free imaging technique where image contrast is inherently generated from the molecular vibrations of the chemical bonds. Pulsed lasers excite molecular vibrations at various wavelengths and therefore make it possible to chemically select and image molecules within the cells (e.g. lipid droplets or organic functionalization on nanoparticle surfaces). This is especially useful as no fluorescent markers are needed that could affect or change the cells or nanoparticles surface and cause unwanted reactions. The CARS system offers a highly sensitive and three-dimensional digital imaging system using a Raman spectroscopy signal level that has been enhanced by 4-6 orders of magnitude [3.44., 3.45]. In general, the Stokes (1064 nm) and the pump (817 nm) beams are coupled and used to excite the Raman peak at the desired wavelength, e.g. at 2985 cm^{-1} (663 nm), corresponding to the CH_2 stretch in lipid droplets. Using this high magnitude, the image acquisition can be done within seconds enabling monitoring biochemical reactions and cell responses in liver cells in real-time.

An alternative method to evaluate the cytotoxicity of iron oxide nanoparticles (other than microscopy) is by **impedance-based measurements**. The xCELLigence system by ACEA Biosciences Inc. presents an analytical system, where sensor electrode arrays are integrated into the cell culture plate, measuring the local ionic environment (charge). When cells attach to the culture dish the ionic strength is altered, leading to an increase in electrode impedance. Therefore, the more cells are attached to the electrodes, the larger the increase in electronic impedance. This principle is depicted in Figure 3. 3.
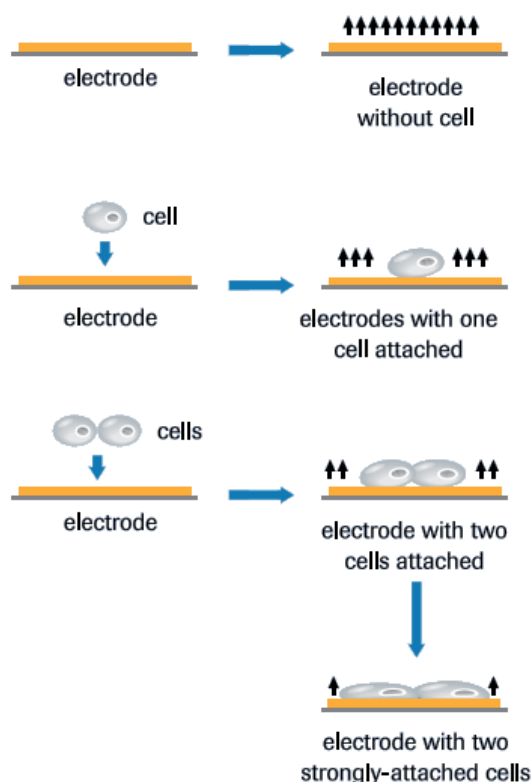
Figure 3. 3: Schematic drawing of impedance-based measurements, where the number of attached cells on the sensor electrode arrays results in an alteration of the impedance value [3.42.].

3.4. Experimental

3.4.1. Materials

Magnetite iron oxide nanoparticles (Fe_3O_4) with an average diameter of 30 nm were supplied by Alfa Aesar. 2-[Methoxy (poly-ethyleneoxy)$_{9-12}$ propyl]trimethoxysilane (PEG$_{9-12}$-silane) and 3-aminopropyltriethoxy silane were purchased from Fluorochem, U.K. Polyethylene glycol (BioUltra, M_w: 4000 g/mol and M_w: 400 g/mol), rhodamine B isothiocyanate (RITC) fluorescent dye and dimethyl sulfoxide (DMSO) were supplied from Sigma Aldrich, UK. Anhydrous sodium carbonate (reagent grade) and the solvents toluene (reagent grade) and methylated spirit (industrial 74 O.P) were purchased from Fisher Scientific UK Ltd. Toluene was dried using activated molecular sieves (type 4 Å, general-purpose grade, Fisher Scientific UK Ltd.) in a closed container for 24 hours. Phosphate buffered saline (Gibco™, PBS) was purchased from Thermofisher Scientific UK Ltd. All chemicals were used as received without further purification. All water used was deionized water.

3.4.2. PEG coating of Fe₃O₄-MNPs using salinization (Fe₃O₄-PEG)

To chemically graft polyethylene oxide chains onto iron oxide, 200 mg Fe_3O_4 MNPs were dispersed in 200 mL dry toluene (dried over activated 4Å molecular sieves) using sonication. After 30 min, the suspension was degassed with N_2 and mechanically stirred at 300 rpm for 45 min. Then, 1 mL of 2- [methoxy (poly-ethyleneoxy)₉₋₁₂ propyl] trimethoxysilane was injected into the reaction mixture, which was then heated up to 110ºC. The reaction mixture was kept under reflux with constant purging with N_2 gas and was stirred at 300 rpm for 4 hours. The resulting MNPs (Fe₃O₄-PEG) were then recovered using a rare earth NdFeB magnet and washed with ethanol (methylated spirit) at least 10 times to remove unreacted silane and toluene. After drying at room temperature overnight, the nanoparticles were dried at 80ºC under vacuum for 4 h. Figure 3. 4 shows the general synthetic pathway of PEGylating iron oxide nanoparticles (Fe₃O₄) using organosilane.
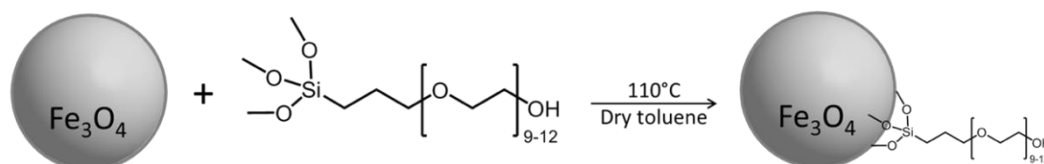
Figure 3. 4: Scheme illustrates the chemical grafting of 2- [methoxy (poly-ethyleneoxy)₉₋₁₂ propyl] trimethoxysilane (PEG-silane) onto the surface of iron oxide nanoparticles (Fe₃O₄).

The PEG-coated and unfunctionalized MNP samples were characterized using Fourier-transform infrared spectroscopy (FTIR), thermogravimetric analysis (TGA), and high-resolution transmission electron microscopy (HRTEM). The chemical nature of the PEG coating was identified using a Nicolet is5 FTIR spectrometer (Thermo Scientific), fitted with an iD7 ATR-Diamond (KBr). A total of 16 scans per sample between the wavelengths $500 cm^{-1}$ and $4000 cm^{-1}$ generated the final spectra. TGA for quantification of PEG coating was carried out using a TA Instrument STD600 thermobalance. In a typical experiment, ca. 5 mg of sample was heated to 800ºC under flowing air (100 mL min^{-1}) at a heating rate of 5°C min^{-1} and the sample was held isothermal for 60 min. The normalized weight loss against an unfunctionalized MNP sample was used to quantify the amount of organic material (PEG) on the particle surface. The nanoparticle morphology was captured using HRTEM. For this purpose, an FEI Tecnai TF20 microscope fitted with a field emission gun operating at 200 kV was used. The samples were suspended in ethanol before being dispersed on holey carbon sample grids (Agar Scientific Ltd.). The software ImageJ was used to measure the mean particle size.

3.4.3. Synthesis of fluorescent Fe₃O₄-PEG MNPs (Fe₃O₄-PEG-RITC)

Fluorescent iron oxide nanoparticles with PEG coating (Fe_3O_4-PEG-RITC) were synthesized by mixing a 95:5 ratio of polyethylene glycol (PEG, M_w: 400 g/mol, 38 mL) and 3-aminopropyl triethoxysilane (APTES, 2 mL) with 80 mg iron oxide MNPs. The mixture was then stirred at 300 rpm for 18 hours, using a mechanical overhead stirrer (IKA Eurostar 20 digital). This resulted in an MNP coating consisting of PEG and APTES silane groups. The resulting PEG-APTES coated MNPs were collected by centrifugation using an Eppendorf miniSpin centrifuge at 12.000 rpm for 10 minutes. Unreacted residues of PEG and APTES were removed by washing the resulting pellet of Fe_3O_4-PEG-APTES nanoparticles at least 10 times with ethanol and 5 times with deionized water. The amine groups in APTES were used as bonding sites for the fluorescent dye RITC (rhodamine B isothiocyanate). Fe_3O_4-PEG-APTES nanoparticles (50 mg) were mixed with 1 mL 0.5M sodium carbonate buffer solution and 100 µL RITC (1 mg RITC in 1 mL DMSO). The reaction mixture was covered in aluminum foil to prevent fluorescent bleaching and was well mixed on a rotator (Stuart rotator SB2) for 48 hours. The resultant nanoparticles (Fe_3O_4-PEG-RITC) were collected using a rare earth NdFeB magnet. Unreacted RITC was removed by washing the nanoparticles at least 50 times with phosphate-buffered saline (PBS) or until the supernatant did not show any residual fluorescence under UV light. All Fe_3O_4-PEG-RITC nanoparticles were stored in PBS and sterilized using γ-radiation for 5 minutes using a shielded irradiator that contained around 120 TBq of cesium-137 and operated at 5 µSvh^{-1}. In the first step amino propyl (3-aminopropyl triethoxysilane, APTES) and polyethylene glycol (PEG, M_w:400 g/mol) groups are grafted onto the iron oxide nanoparticles surface (salinization). The second step binds the fluorescent dye rhodamine B isothiocyanate (RITC) with the amine groups within the APTES coating. The resulting iron oxide nanoparticles are now PEG-coated and possess a fluorescent dye that can be viewed and monitored *in vitro*.

3.4.4. Culturing of Huh-7 breast cancer cells for cytotoxicity assays

The human liver cell line Huh-7 was cultured and maintained in 89 % low-glucose Dulbecco's Modified Eagles Medium (DMEM, Sigma-Aldrich) supplemented with 10 % fetal calf serum (FCS, GE Bioscience) and 1 % of a penicillin-streptomycin solution containing 10.000 units of penicillin and 10 mg streptomycin/mL (Sigma-Aldrich). The cells were incubated at 37°C in a 5 % CO_2 atmosphere for 7 days before nanoparticle exposure. All cultures were routinely screened for mycoplasma contamination. The control cells were cultured in the absence of any nanoparticles. When reaching confluency between 80-90 % the Huh-7 cells (passages 10-20) were seeded onto 96-well tissue culture plates (Costar, 3595) at a density of 3×10^3 cells per well.

The cells were exposed for 1, 3, and 7 days to either unfunctionalized iron oxide nanoparticles (Fe_3O_4; Ø30 nm) or polyethylene-glycol coated nanoparticles (Fe_3O_4-PEG) at concentrations of 125, 250, 500, and 1000 µg/mL. On the day of exposure, the nanoparticles were suspended in serum-free media (media without FCS or proteins), applied to culture dishes, and incubated for 24h. After the incubation period, the media was changed back to the original culture and maintenance media (incl. FCS). Before the performance of any cell assays, the cells were washed three times with Hank's Balanced Salt Solution (HBSS Ca^{2+}/Mg^{2+}) to remove any media and protein residuals that could interfere with the nanoparticle exposure. The cell viability was assessed using two colorimetric cell assays. The first assay evaluated the cell proliferation (PrestoBlue®, Fisher Scientific) and the second assay evaluated how active the cells were after nanoparticle exposure by quantification of available ATP after cell lysis (CellTiter Glo™, Promega). The assays were performed according to protocol and three PBS washes were carried out in between the assays.

3.4.5. Culturing HepaRG liver cells

To prepare the HepaRG cells for 2D experiments, the cells (HPR116-TA08; Cryopreserved HepaRG cells; Biopredic Int., Rennes, France) were cultured using specialized media and following the supplier's protocols. Each medium was made up using William's E Medium with GlutaMAX™ (Sigma Aldrich) as the basal medium and the appropriate additives (ADD). For each culture, format indicated, HepaRG cells were seeded (day 0) at $2.4 \times 10^5/cm^2$ initially in Thaw, Seed and General Purpose HepaRG® medium (GPS, ADD670) on either FluoroDish™ Cell Culture Dishes (35 mm, Fisher Scientific) or Corning 96-well tissue culture plates. On day 3, the medium was changed

to HepaRG^{TM} Maintenance and Metabolism Medium (MMM; ADD620) and cultured to confluence. The medium was renewed every 2–3 days with fresh MMM. On day 7, the cells were washed twice with Hank's Balanced Salt Solution (HBSS Ca^{2+}/Mg^{2+}) to prepare them for nanoparticle exposure.

A 3D culture was established by seeding and culturing HepaRG cells in a custom-designed gel phantom using a HyStem®-HP Hydrogel Kit (ESI BIO). The kit comprised of thiol-modified sodium hyaluronate with thiol-modified heparin (Heprasil®), thiol-modified gelatin (Gelin-S®), polyethylene glycol diacrylate (PEGDA, Extralink®), and degassed deionized water. The Heprasil and Gelin-S solutions form a transparent hydrogel when mixed with the Extralink solution. A liver-like gel phantom was formed by altering the ratios of Heprasil®:Gelin-S®:Extralink® according to protocols in previous but unpublished experiments by Leonard J. Nelson at Institute for Bioengineering, University of Edinburgh. The final gel phantom mimics a liver tissue sample not only through the added cell culture but also in its density and porosity. In brief, 1 mL of degassed and deionized water was added to each sample vial of Heprasil® and Gelin-S® and placed horizontally on a roller for 40 minutes to dissolve the reactants. In the meantime, the HepaRG cells were removed from the liquid nitrogen tank, placed immediately on dry ice, and then held into a warm water bath (37ºC) for a maximum of two minutes to defrost. The cell solution was then transferred into a 15 mL tube and mixed with 9 mL GPS media. After dispersing the cells, the cell solution was centrifuged at 320 g relative centrifugal force (RCF) for three minutes at room temperature. The dissolved Gelin-S® solution was then added to the Heprasil® solution and placed back on the roller. At this point, 0.25 mL of degassed deionized water was added to the Extralink® vial and the content dissolved through several inversions. Once all solutions were dissolved, the resulting supernatant from the cell solution was aspirated and the pellet dispersed in 10 mL of fresh GPS media. The final concentration now contained 1 million cells/ mL of which 1.3 mL were added to the Gelin-S® and Heprasil® mix. The chemical linker (Extralink®) was then injected, and the whole solution was left to gelate for 20 minutes. To nurture the cells overnight 1 mL GPS was added, which was then replaced by 1 mL MMM media on the following day. The cells were cultured at 37ºC, 5% CO$_2$ for 7 days when the cells were terminally differentiated and hepatic, and the cholangiocyte co-culture was fully developed. On the same day, the cells were washed twice with Hank's Balanced Salt Solution (HBSS Ca^{2+}/Mg^{2+}) and prepared for nanoparticle exposure.

On the day of exposure, both cell culture setups (2D and 3D) were treated with various dosages of unfunctionalized (Fe_3O_4) and polyethylene glycol coated iron oxide nanoparticles (Fe_3O_4-PEG). 2D cultures were exposed to 125, 250, 500, and 1000 µg/mL nanoparticles with exposure times of 1 – 7 days. 3D cultures were exposed to 50 µg/mL of unfunctionalized Fe_3O_4 and Fe_3O_4-PEG for 24 hours.

3.4.6. Colorimetric cell assays

All biochemical assays, including preparation, performing and evaluation of the assay, were carried out according to protocol and normalized to unexposed negative and lysed positive controls. Each experiment was performed in triplicate and three PBS washes were carried out before each assay. The order of performance was of importance, as some assays do not harm the cell culture and allow for further experiments and analysis, while others are so-called endpoint assays, where full cell lysis is required. For this analysis, we used two assays, PrestoBlue® and CellTiter-Glo®. PrestoBlue® solely reacts with dead cells or has a damaged cell wall. CellTiter-Glo® is a chemical endpoint assay and required full lyses of the cell culture for ATP quantification. The results of those assays determine the number of viable cells in culture, based on their metabolic activity.

PrestoBlue®

PrestoBlue® was prepared as a 10 % solution in a 3M culture medium. For a 96-well plate with a total volume of 100 µL/plate, the reagent consisted of 90 µL cell and 3M media (9.0×10^3 cells/well) with 10 µL PrestoBlue® Reagent. After incubation at 37℃ and under 5 % CO_2 atmosphere for 30 minutes the mixed solution was transferred to a white wall, clear bottom Corning 96-well tissue culture plate. The fluorescence was then measured at 570 nm with a reference wavelength for normalization at 600 nm. To evaluate the results, the fluorescence values of no-cell control wells were subtracted from the fluorescence values of each experimental well. To reduce any fluorescence caused by the nanoparticles, nanoparticles in 3M media only were measured and any occurring value was subtracted from each experimental well.

CellTiter-Glo® 3D Cell Viability Assay

The CellTiter-Glo® 3D Reagent was thawed at 4ºC overnight and equilibrated to room temperature by placing the reagent for approximately 30 minutes in a 22ºC water bath before use. The cells were washed again three times with PBS, and a volume of CellTiter-Glo® 3D Cell Reagent equal to the volume of cell culture medium was added to each well. For instance, a 96-well plate containing 100 µL CellTiter-Glo® Reagent was mixed with a 100 µL cell culture medium containing cells. Once the reagent was added, the culture plate was incubated at room temperature for 25 minutes to stabilize the luminescent signal and was then read on a microplate reader.

3.2.7. Techniques to evaluate cell viabilities after nanoparticle exposure
Meiji Techno TC-5600

2D cultures were established by seeding HepaRG cells onto FluoroDish™ Cell Culture Dishes (35mm, Fisher Scientific) at a density of 2.4 x 10^4 cells per dish and cultured for 7 days. 3D samples comprised of culturing HepaRG cells in a vial containing the HyStem®-HP Hydrogel and changing the 3M media every 2 days. On day 7, the 2D and 3D samples were exposed to 10 µg Fe_3O_4 nanoparticles. These nanoparticles were functionalized with the fluorescent dye rhodamine B isothiocyanate (RITC, Sigma Aldrich) and coated with polyethylene glycol (Fe_3O_4- PEG- RITC). The exposures were performed in serum-free media, where the media was changed back to the original 3M culture and maintenance media after 24 hours. Phase-contrast images were captured, using an inverted halogen/mercury epifluorescence microscope (Meiji Techno, TC-5600). Images were captured using an Andor ZYLA 5.5 MP camera combined with the Andor SOLIS software (Oxford Instruments) to highlight the fluorescent tag on the magnetic nanoparticles. The optical evaluation software ImageJ was used to highlight fluorescent nanoparticles using false color imaging.

CARS

CARS images were acquired using a custom-built multi-modal multiphoton microscope [3.43.]. The system used consisted of a mode-locked ND:YVO4 pump laser (PicoTrain, HighQ/ Spectra Physics) emitting 7ps pulses at 1064 nm. Part of the output beam was frequency-doubled to 532nm which was used to synchronously pump an optical parametric oscillator (OPO) (Levante Emerald, APE) generating a tunable output between 700-1000 nm. To match the CH_2 vibration of lipids at 2485cm^{-1}, the OPO was tuned to 817 nm to provide the pump beam, and the 1064 nm output was used as a stokes beam. The two beams were coupled into an inverted microscope (Eclipse TE2000U, Nikon) with a modified Nikon 'C1' scan head. Both beams were overlapped spatially and temporally onto the sample using a 25×/1.05 NA water-immersion objective lens (Olympus). All images were acquired with 125 mW (817 nm) and 85 mW (1064 nm) of excitation power at the sample plane. The forward directed CARS signal was collected using a 0.7 N.A condenser lens (Nikon) and fiber-coupled to a photomultiplier tube unit. The CARS signal was separated from the excitation beams using 700 nm and 785 nm short pass filters and a 660/13 nm band pass filter. Images were acquired with an exposure time of 64µs and averaged 3 times over 5 regions per sample. A schematic diagram of the multi-modal multiphoton microscope is presented in Figure 3. 5.
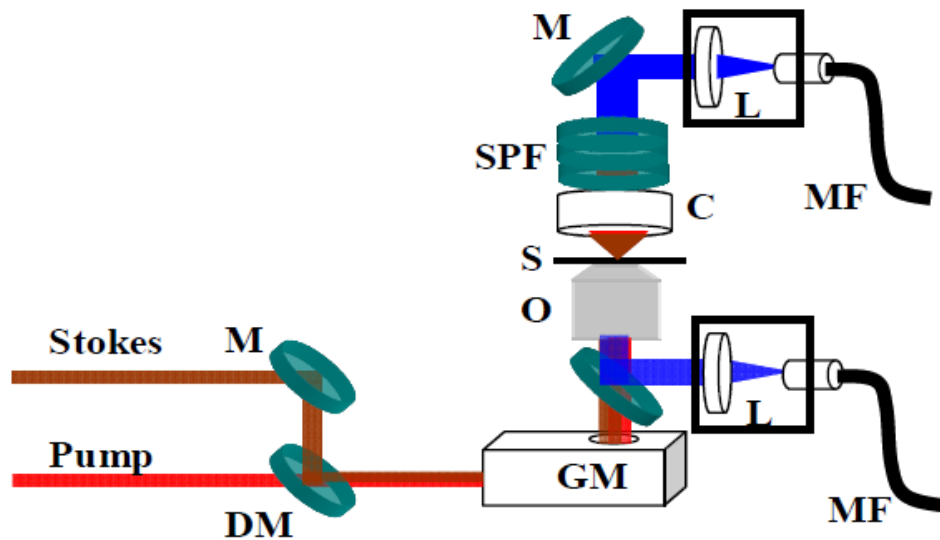
Figure 3. 5: Schematic diagram of the multi-modal multiphoton microscope setup. M, Mirror; DM, dichroic mirror; GM, Galvano mirrors; O, objective; S, sample; C, condenser; SPF, short pass filters set; L, focusing lens; MF, multimodal optical fibre [3.43.].

The number and size distribution of accumulated lipids were analyzed using the Spot Detector plugin for ICY, an open-access image analysis platform [3.46.]. The image analysis protocol operates by first thresholding the images to detect cell colonies in the image field of view. The area of the detected region of interest was then measured using the ROI statistics tool. The number of droplets within these defined ROIs was calculated by detecting bright spots over a dark background, using the undecimated wavelet transform detector. The results were manually checked for false positives and negatives and corrected accordingly. The number of lipid droplets per area of cell clusters was finally identified to compare between samples.

Transmission electron microscopy (TEM)

24 hours after exposing HepaRG cells to Fe_3O_4 nanoparticles the samples were fixed in 3 % glutaraldehyde in 0.1M sodium cacodylate buffer, pH 7.3, for 2 hours then washed in three 10- minute changes of 0.1M sodium cacodylate. Specimens were then post-fixed in 1 % osmium tetroxide in 0.1M sodium cacodylate for 45 minutes, then washed in three 10-minute changes of 0.1M sodium cacodylate buffer. These samples were then dehydrated in 50 %, 70 %, 90 %, and 100 % ethanol (X3) for 15 minutes each, then in two 10-minute changes in propylene oxide. Samples were then embedded in TAAB 812 resin. Sections, 1μm thick were cut on a Leica Ultracut ultramicrotome, stained with toluidine blue, and viewed in a light microscope to select suitable areas for investigation. Ultrathin sections, 60nm thick were cut from selected areas, stained in uranyl acetate and lead citrate then viewed in a JEOL JEM-1400 Plus TEM operated at 80kV to analyze particle distribution and cell adsorption. Representative images were collected on a GATAN OneView camera.

Impedance measurement (xCELLigence)

The cell viability was measured in real-time using the impedance-based xCELLigence system. HepaRG cells were seeded onto three 16 well plates at a density of 9.0×10^3 cells per well. The plates contained golden electrodes through which the electric current was measured continuously for 2 weeks. Once the cells were seeded the plates were connected to the xCELLigence system which was always kept in an incubator (37ºC and under 5 % CO_2 atmosphere). After culturing the cells for seven days, with a general-purpose culture medium (GPS) the cells were fully differentiated and ready for

nanoparticle exposure. On day 7, the cells were exposed to 125, 250, 500, and 1000 µg/mL of unfunctionalized and PEG-coated iron oxide nanoparticles in serum-free media. The impedance was measured for another 7 days while keeping the plates in an incubator and frequent media changes every two days.

3.5. Results and discussion

3.5.1. Characterization of PEG-coated Fe₃O₄ MNPs

PEG-coated Fe_3O_4 MNPs were fully characterized using Fourier-Transform Infrared Spectroscopy (FTIR), Thermogravimetric Analysis (TGA), and Transmission Electron Microscopy (TEM).

A successful polyethylene glycol functionalization (PEGylation) on the MNP surface was shown by comparing uncoated Fe_3O_4 nanoparticles with functionalized MNPs. The FTIR spectra of PEG-coated samples showed that the PEG coating on the nanoparticle surface had identical peaks of pure PEG-400 and PEG-4000 (Figure 3. 7). The characteristic peaks of the PEG repeating units (Figure 3. 6) occur at 1070, 1340, 1450, and 2860 cm⁻¹. The -C-O-C- band shows at 1070 cm⁻¹, whereas the three other peaks at 1350, 1470 and 2869 cm⁻¹ can be related to the carbon-hydrogen (-CH) bending (1350 and 1470 cm⁻¹) and stretching (2869 cm⁻¹) modes of the polymer (Figure 3. 8). These peaks were matched with spectra of the PEG-coated MNP samples, whereas the -CH peaks occurred at 1470, 1350, and 2869 cm⁻¹. However, the strong Si-O band from the organosilane (2-[methoxy (poly-ethyleneoxy)₉₋₁₂ propyl] trimethoxysilane) overlaps the -C-O-C- band at 1107 cm⁻¹. Figure 3. 8 shows a comparison of unfunctionalized Fe_3O_4 nanoparticles with PEG-coated MNP samples and their characteristic bonds.
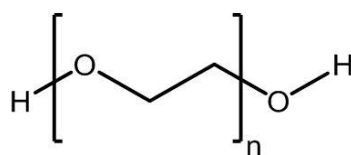
Figure 3. 6: Repeating unit of polyethylene glycol, showing the -O-C-C- group which will form -C-O-C- and -CH- chains within the polymer.
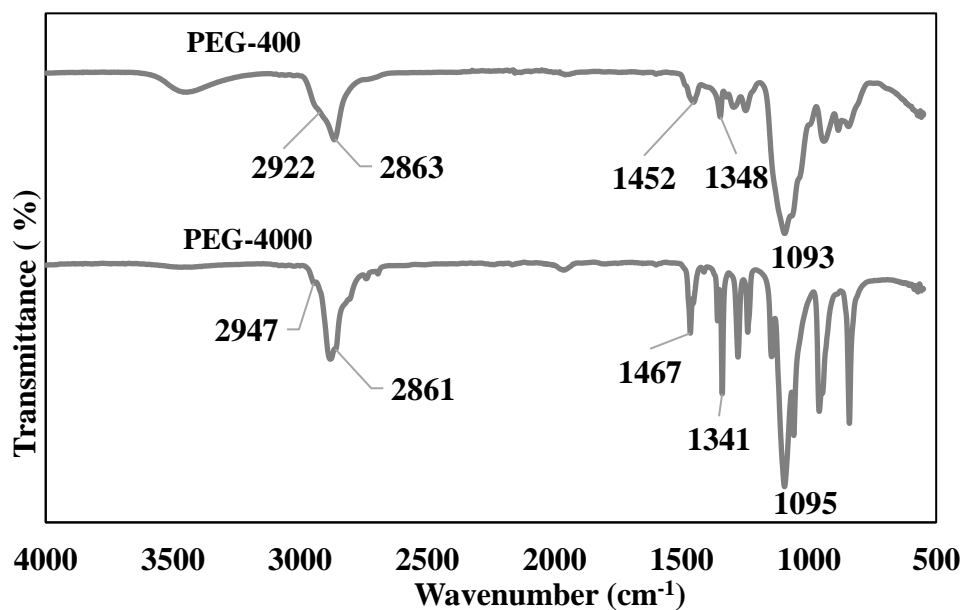
Figure 3. 7: FTIR spectra of polyethylene glycol M_w: 400 Da and M_w: 4000 Da, showing characteristic peaks for the repeating units of PEG (-C-O-C- at 1090 cm^{-1} and -CH at 1340, 1460, and 2860 cm^{-1}).
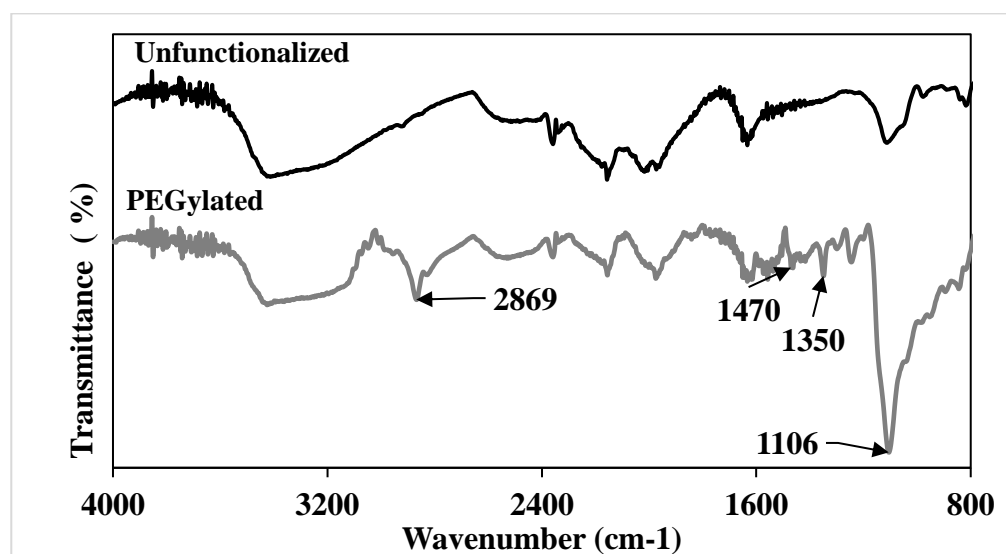
Figure 3. 8: Comparison of FTIR spectra of unfunctionalized and PEG-coated Fe_3O_4 nanoparticles. The PEG functionalization by silanization can be seen in the peaks of the Si-O group (1106 cm^{-1}) and -CH chains (1350, 1470, and 2869 cm^{-1}).

To quantify the amount of polyethylene glycol that has been bound onto the nanoparticle surface the PEG-coated samples were analyzed by thermogravimetric analysis (TGA). The resulting weight loss profiles allow a comparison of organic content that is burned over time and a temperature range up to 800ºC.

A typical thermogravimetric profile for a PEG-coated sample consisted of 3 major steps. The loss of residual solvents causes the first weight loss from around 50 to 200ºC. The

second step between 200-800ºC represents the loss of organic matter (PEG) on the MNP surface, which is then followed by the further combustion of the residuals in step three. The data range that has been considered in the weight loss evaluation is indicated by the dotted lines and any weight loss is related to the maximal temperature at 800ºC. The TGA weight loss profile of PEG-coated Fe_3O_4 nanoparticles in Figure 3. 9 shows a significant weight loss between 140 and 350ºC. This weight loss represents the amount of bound polyethylene glycol on the MNP surface that is being burnt off. The remaining weight percentage resembles the inorganic and therefore oxidized iron oxide residue (γ-Fe_2O_3). In comparison to the reference weight loss of unfunctionalized Fe_3O_4, the weight loss of the PEG-coated sample equals a total bound organic content of 3 %. This quantification indicates a successful PEG-coating on the Fe_3O_4 nanoparticle surface.
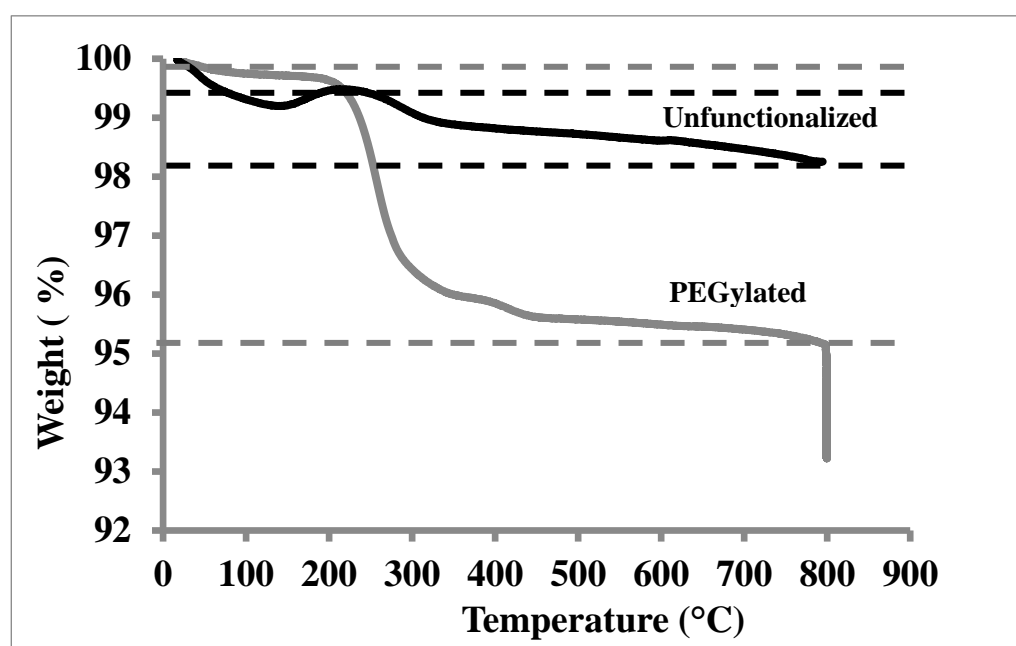
Figure 3. 9: TGA - weight loss profiles of unfunctionalized and PEG-coated iron oxide (Fe₃O₄). Due to the polymer coating being burnt the comparison shows a significant weight loss between 140 and 350ºC in the PEG-coated samples. All tested samples showed a significant weight loss in comparison to the unfunctionalized nanoparticles. This is in direct proportion to the amount of polyethylene glycol on the surface and how long the functionalization was allowed to run.

TEM images of PEG-silane$_{9-12}$ functionalized Fe_3O_4 MNPs were taken to determine the average particle size and their possible affection by the surface functionalization. Additionally, the TEM images allowed to determine the size distribution and shape of MNPs. The optical evaluation software ImageJ was used to manually measure the mean particle size (Figure 3. 10, a).

The results showed an average size of 30 ± 1 nm in diameter, calculated from a total of 423 labeled nanoparticles (Figure 3. 10, b). Originating from a mean nanoparticle's size of the commercially available Fe_3O_4 nanoparticles of 25-30 ± 1 nm, it can be said that the silanization with PEG-silane$_{9-12}$ did not cause any significant changes in the particle size or affected their homogeneity.
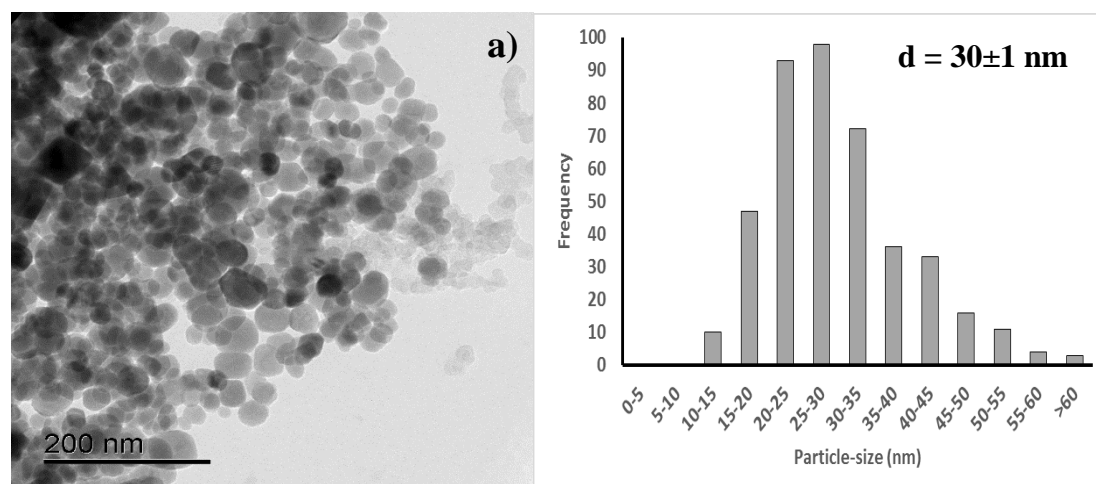
Figure 3. 10: (a) HRTEM microgram showing PEGylated iron oxide nanoparticles (PEG$_{9-12}$-MNPs) with an average nanoparticles size of 30±1 nm and (b) their particle size distribution calculated from 423 cells using ImageJ.

3.5.2. Colorimetric cell assays

Two cell assays were performed to determine the cell viability of Huh-7 and HepaRG cells after being exposed to unfunctionalized and PEG-coated Fe_3O_4 nanoparticles. The experiments were repeated in triplicates and a 95% confidence interval for data analysis (p-value < 0.05) was used to establish statistically significant results.

Starting with the PrestoBlue® cell viability assay, Huh-7 liver cancer cells were exposed to 4 different concentrations of unfunctionalized and PEG-coated Fe_3O_4 nanoparticles (125, 250, 500, and 1000 µg/mL). On days 1, 3, and 7 the cells were assayed using a PrestoBlue® cell viability assay. The results are shown in *Figure 3. 11*, where the cell graph suggests overall decreasing cell viability across the four concentrations of unfunctionalized iron oxide samples. Comparing that trend with the cell viability after being exposed to PEG-coated nanoparticles, the graph remained almost constant for 7 days. This confirms that the PEG coating made the iron oxide nanoparticle more biocompatible, decreased the cell stress during internalization, and therefore no significant cytotoxic effects on the cell culture.
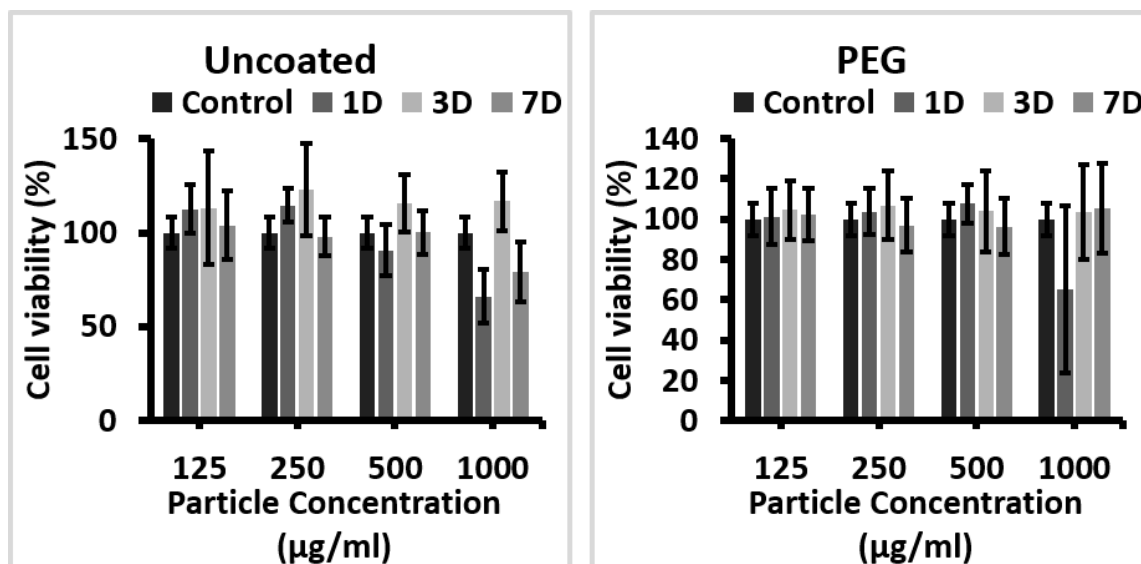
Figure 3. 11: Cell viability of Huh-7 breast cancer cells after exposure to 125, 250, 500, and 1000 µg/mL of unfunctionalized and PEG-coated Fe₃O₄ nanoparticles (p<0.05). Determined by PrestoBlue® Cell Viability Assay on day 1, 3, and 7 after exposure on day 0.

HepaRG cells were exposed to 4 different concentrations (125, 250, 500, and 1000 µg/mL) of unfunctionalized and PEG-coated Fe_3O_4 nanoparticles for 24 hours. The results depicted in Figure 3. 12, show that an increasing particle dose decreases cell viability.

The growing difference in cell viability between the unfunctionalized and coated samples suggests, that the higher the concentration of each sample, the higher is the difference in cell viability. With a difference of 8 % at a nanoparticle dose of 125 µg/mL and a difference of 60 % at 1000 µg/mL, it can be said that functionalization with polyethylene glycol reduces the negative effect on cells and decreases cell death.
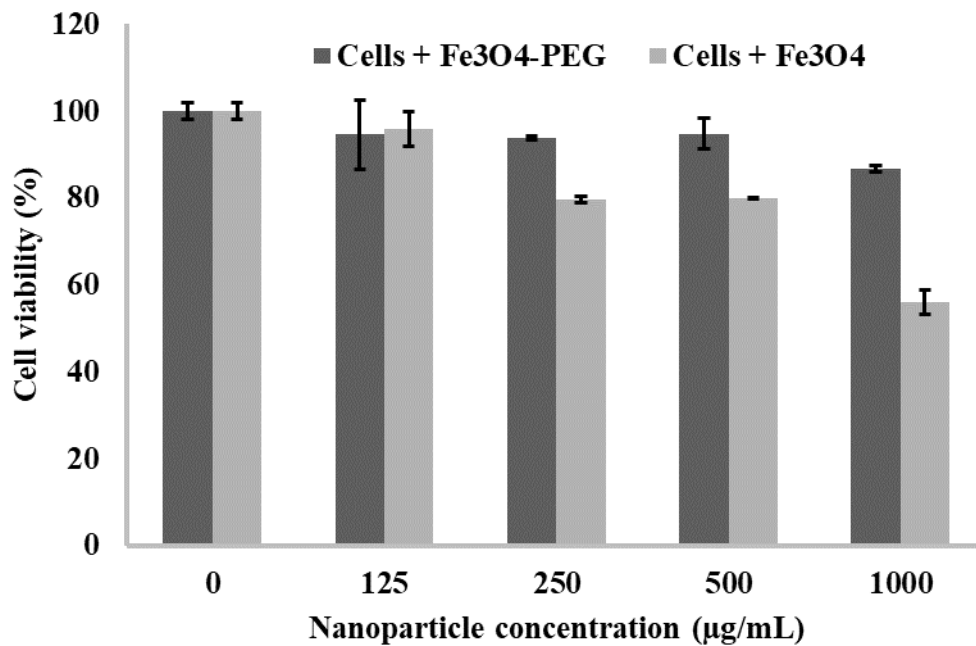
Figure 3. 12: Cell viability of HepaRG cells assayed by the PrestoBlue® cell viability assay. The cells were exposed to four doses (125, 250, 500, and 1000 µg/mL) of unfunctionalized and polyethylene glycol coated Fe_3O_4 nanoparticles for 24 hours (p<0.05).

The CellTiter-Glo® 3D Cell Viability Assay was used to further test the cell viability of Huh-7 cells after nanoparticle exposure. Similar to the results of the PrestoBlue® cell viability assay, the results depicted in *Figure 3. 13*, *Figure 3. 13* suggest similar decreasing viability for the unfunctionalized samples across all concentrations and over the whole exposure time of 1-7 days. The cell viability after being exposed to PEGylated samples remained almost constant and suggested no significant effect on cell health.
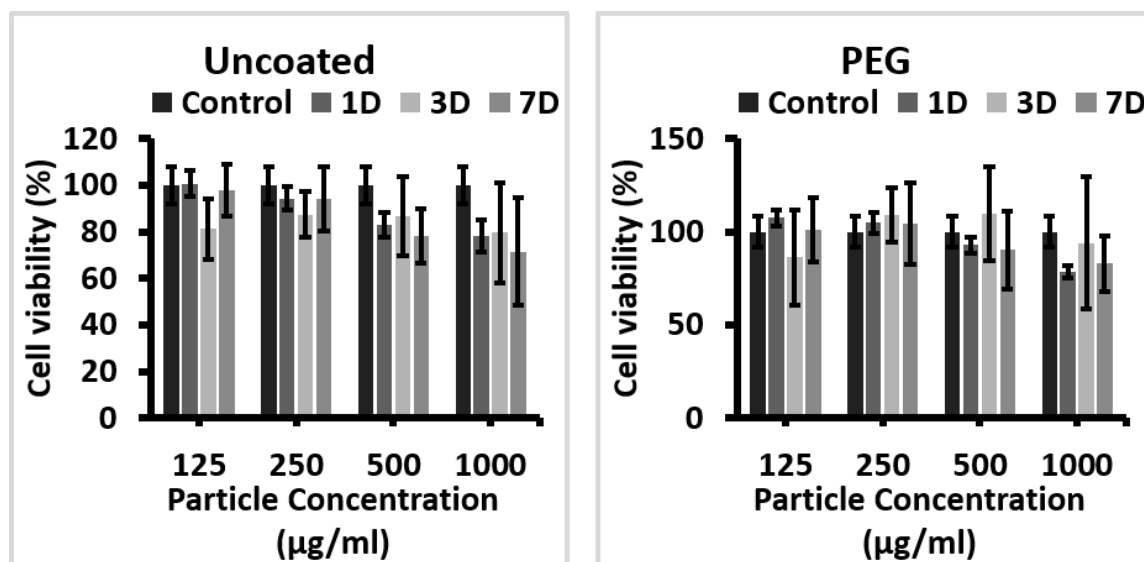
Figure 3. 13: Cell viability of Huh-7 breast cancer cells after being exposed to four concentrations (125, 250, 500, and 1000 μg/mL) of unfunctionalized and PEG-coated Fe₃O₄ nanoparticles (p<0.05). The cell viability was determined by performing a CellTiter-Glo® 3D Cell Viability Assay on days 1, 3, and 7 after exposure on day 0.

Additional to the other cell lines HepaRG liver cells were exposed to the same concentrations of unfunctionalized and PEG-coated nanoparticles and analyzed by the cell viability test CellTiter-Glo. The results are shown in Figure 3. 14 and showed that similar to the previous cell lines the PEG-coated samples had less effect on the cell viability of the MCF-7 cell culture than the unfunctionalized Fe_3O_4 nanoparticle samples.
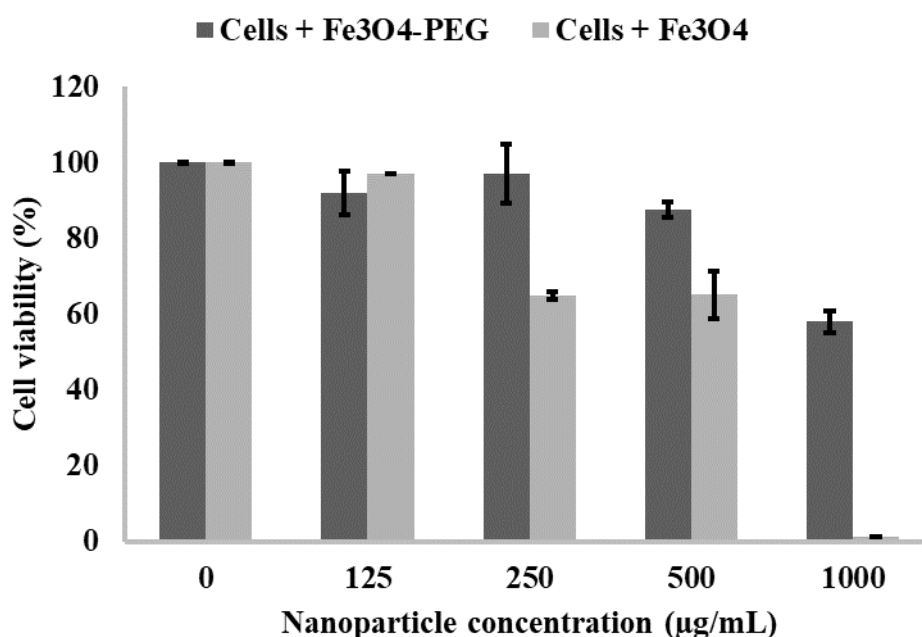
Figure 3. 14: Results of HepaRG cells after 24h exposure to 125, 250, 500 and 1000 µg/mL of unfunctionalized and polyethylene glycol coated Fe_3O_4 nanoparticles, using the CellTiter-Glo® cell viability assay (p<0.05).

A dropping cell viability after 250 µg of unfunctionalized Fe_3O_4 nanoparticles, however, was unexpected. It was found that a general dose-response experiment involving Fe_3O_4 iron oxide nanoparticles generally tends to show irregular behavior, especially at high dosages (>250 µg). Such behavior is often found in relation to when the emitted light signal (fluorescence, luminescence, etc.) is obstructed by the material. Data presented by Hoskins et al. strongly suggested that the interpretation of cell viabilities, using common commercial assays, can be affected by the nanoparticles. Depending on dosage and particle sizes, the light signal is changed to a signal that does not reflect the actual result (cell proliferation, cell viability, etc.). This makes any results gathered by colorimetric assays inaccurate and unreliable and therefore unusable. It is highly recommended to use different analytical approaches to determine cell reactions of any kind to the exposure of nanoparticles, such as impedance measurements or CARS [3.6.].

3.5.3. Alternative techniques to monitor cell viability after nanoparticle exposure

Two major issues of colorimetric assays are 1. the generation of false results when used in combination with light-absorbing materials such as iron oxide and 2. the requirement of partial or full cell lysis (cell death) for accurate results [3.6.]. To circumvent this, three alternative imaging methods were tested to determine the cell reaction to nanoparticle exposure; epifluorescence imaging (Meiji Techno TC-5600) for general cell penetration studies, Coherent Anti-Stokes Raman Scattering (CARS) to image the cell reaction in expressed lipid droplets and impedance measurement (xCELLigence) to determine the cell viability. All results suggest increased cell viability and cell acceptance towards PEG-coated iron oxide nanoparticles.

Fluorescence imaging

The fluorescence of RITC functionalized Fe_3O_4 was measured using a Meiji Techno TC-5600 microscope. The results were compared to a control dish without any nanoparticles (Figure 3. 15) and are displayed in Figure 3. 16 and Figure 3. 17. The difference can be seen in the debris of nanoparticles that have spread over the whole HepaRG culture dish (2D). Particle agglomerations in and around the cells prove that the nanoparticles not only penetrate the cell surface but are also ingested by the cells through endocytosis, thus suggesting good biocompatibility and cell viability. Allowing nanoparticles to penetrate through the cell membrane and disperse within the cell is essential for an effective particle delivery and therefore the potential drug that might be carried on the surface of the nanoparticles.

HepaRG cell cultures seeded into a HyStem®-HP Hydrogel showed similar results to the 2D culture. However, the 3D culture showed a limited amount of PEG-RITC functionalized nanoparticles, as no mechanism helps them to fully diffuse through the liver-gel model (Figure 3. 17). Therefore, most of the particle dose remained on the gel surface. Images of the 3D model showed nanoparticle internalization identified by the fluorescent tags on the nanoparticle surface (Figure 3. 18). However, one of the main issues using a 3D model is that there is no cell or enzymatic activity present, which could support the diffusion of liquids and nanoparticles through the gel phantom. This in return only allows performing experiments and assays on the surface of the gel. For this reason, any following biochemical assays and imaging techniques were performed in 2D culture.
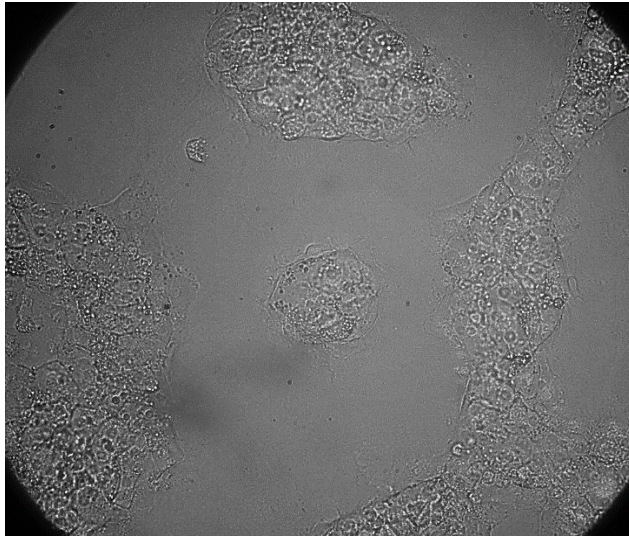
Figure 3. 15: Control image of HepaRG cells on a 2D cell culture dish (large structures), cultured at 37ºC in 5 % CO_2 atmosphere for 7 days before nanoparticle exposure.
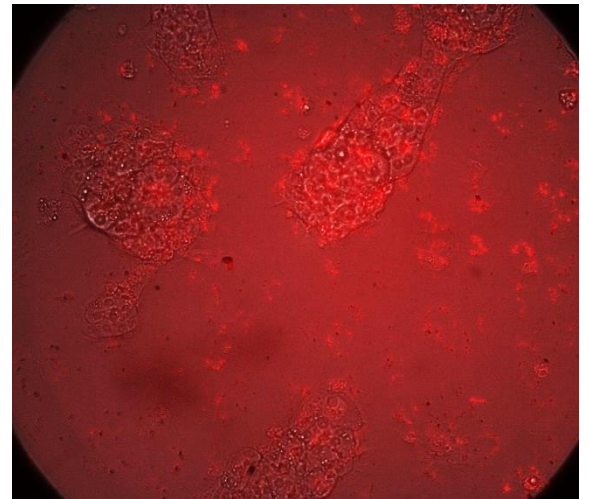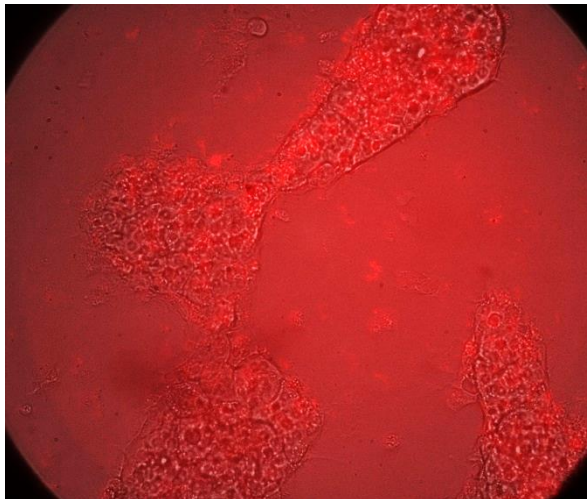
Figure 3. 16: False-color images of HepaRG cells exposed to Fe_3O_4 functionalized with PEG and the fluorescent dye RITC (bright red spots) after 24 hours in 2D cell culture. The images show a higher occurrence of nanoparticles in and around the cells, suggesting a successful internalization by the cells.
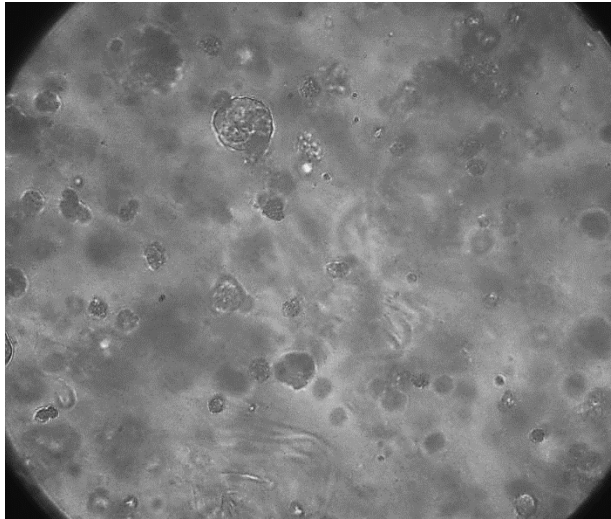
Figure 3. 17: Control image of HepaRG cells in 3D cell culture (spherical spots) highlighting the cell culture droplets within the gel matrix (arrows).
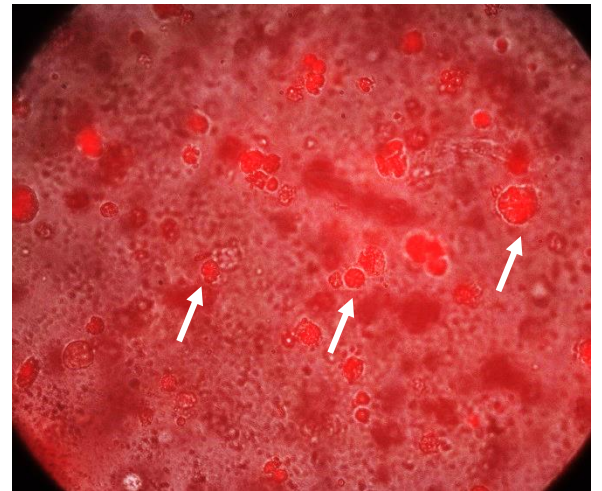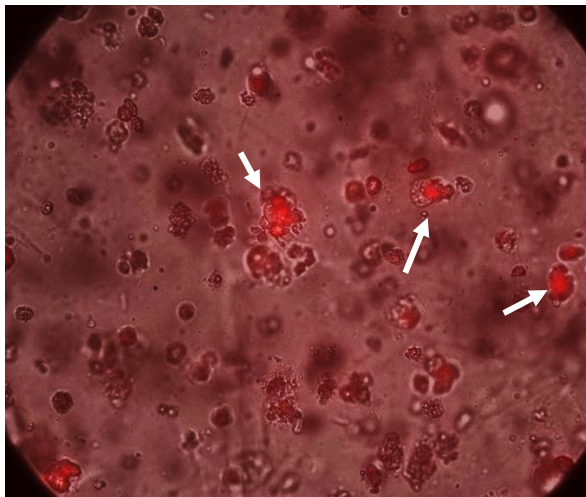
Figure 3. 18: False-color images of 3D HepaRG cell cultures (arrows) exposed to 10 µg Fe$_3$O$_4$ functionalized with PEG and RITC (bright red) for 24 hours., displaying the internalization of nanoparticles into the 3D cell culture. Bright red spots are detected in the 3D cultures, suggesting a successful penetration of the MNPs (arrows).

Coherent Anti-Stokes (CARS)

Following the analysis of lipid droplet accumulation in live HepaRG cells, PEG-coated MNPs showed the least amount of lipid droplets in comparison to unfunctionalized Fe_3O_4 nanoparticles. The CARS system was tuned to a wavelength of 2985 cm-1 to only highlight lipid droplets and their aggregates in the cell cultures. Both samples were compared to the control samples after an incubation period of 24 hours (*Figure 3. 19*, a). While it is normal for the control cells to form small lipid droplets (300-800 nm diameter) for metabolic energy and other bodily functions, it was noticeable that the size distribution of lipid droplets changed after the exposure to unfunctionalized and PEG-coated MNPs (Figure 3. 20). Within the focus area of 100 µm, PEG-coated MNPs induced larger lipid droplets with diameters larger than 2 µm, than unfunctionalized Fe_3O_4 nanoparticles with averages below 1 µm. This could be due to several factors that stimulate the intracellular metabolism into an overexpression of lipids by affecting the lipogenesis, the esterification, and down-regulation of free fatty acids or the expression of proteins involved in the retention of lipids [3.47.]. It can also be seen that the lipids induced by PEG-coated Fe_3O_4 nanoparticles spread wider across the cells than the unfunctionalized samples. This again, not only confirms the stimulated cell metabolism but also that the nanoparticles can penetrate deeper into the cell culture than the unfunctionalized samples. Even though the lipid droplet sizes increased, a reduced amount of lipid droplets generally suggest that the nanoparticle exposure with PEG-coated iron oxide did not induce as much cellular stress as the unfunctionalized Fe_3O_4 samples.
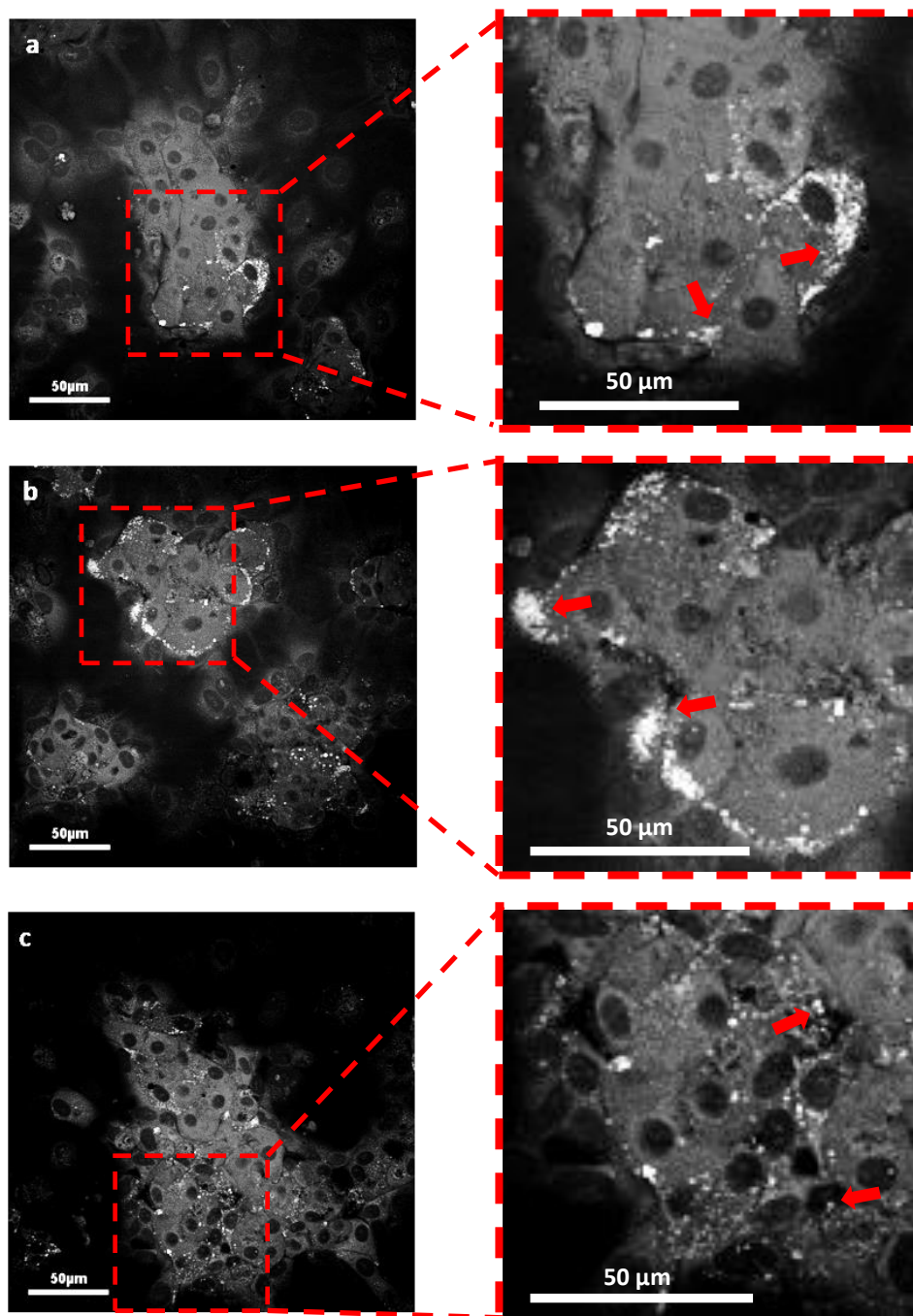
Figure 3. 19: The CARS system was tuned to a wavelength of 2985 cm^{-1} to highlight the lipid droplets in control cells (a), showing enhanced lipid expression after exposure to unfunctionalized iron oxide (b), but no visible increase of lipid droplet numbers for the PEG-coated samples (c). The arrows point out the occurring lipid droplets.
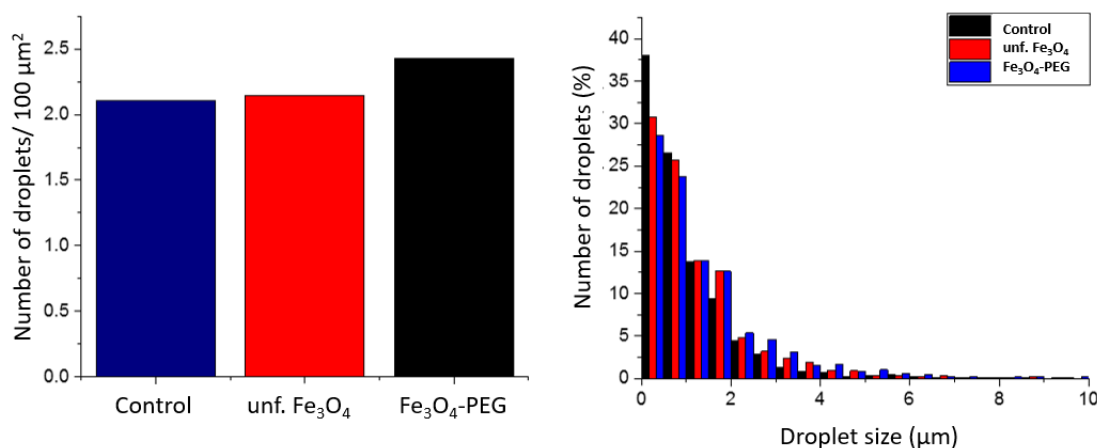
Figure 3. 20: Analysis of lipid distribution in 2D HepaRG cultures after 24h exposure with 50 µg of magnetic iron oxide (Fe_3O_4) nanoparticles. The number of lipid droplets were detected per $100µm^2$ over 5 regions of interest on each sample (left) and the size distribution of droplets displayed with (n=1) on the right.

TEM imaging

The cell samples of iron oxide exposed HepaRG cells were also analyzed by Transmission Emission Microscopy (TEM) to determine the particle diffusion and distribution within the cell samples (Figure 3. 21). The TEM images show the cell culture (grey) with the internalized iron oxide nanoparticles (black). The nanoparticles are internalized by phagocytosis, where the particles undergo the natural process of solid intake (attachment, engulfment, and fission) and are then stored in vacuoles (light circles within the cell), a space within the cell that is filled with enzymes and other fluids, performing functions such as storage, ingestion, digestion, excretion and expulsion of excess water [3.48.].

The results show clear differences between unfunctionalized (Figure 3. 21, a) and PEG-coated (Figure 3. 21, b) nanoparticles, compared to the control (Figure 3. 21, c). The unfunctionalized nanoparticles tend to agglomerate in a much shorter time than PEG-coated samples. Even though both nanoparticles showed deep cell penetration and distribution within the cell, unfunctionalized Fe_3O_4 nanoparticles appear to agglomerate much denser than their polyethylene glycol functionalized counterpart. This can be seen when comparing the magnifications (red boxes) of Figure 3. 21, a with that of Figure 3. 21, b. The PEGylation prevented the nanoparticles from agglomerating as dense as unfunctionalized MNPs, confirming that the coating supports the nanoparticles to maintain their sizes. Therefore, and extended particle distribution within the cell sample

is ensured, as smaller nanoparticles penetrate deeper into the cell and spread further without getting retained by membranes or intracellular activities. A wider spread of nanoparticles means that the nanoparticles diffuse further than unfunctionalized nanoparticles, increases the imaging area, and show more detail through extended particle distribution within the cell and their high contrast. This allows for highly detailed pictures and clearer differentiation from their surrounding tissue.
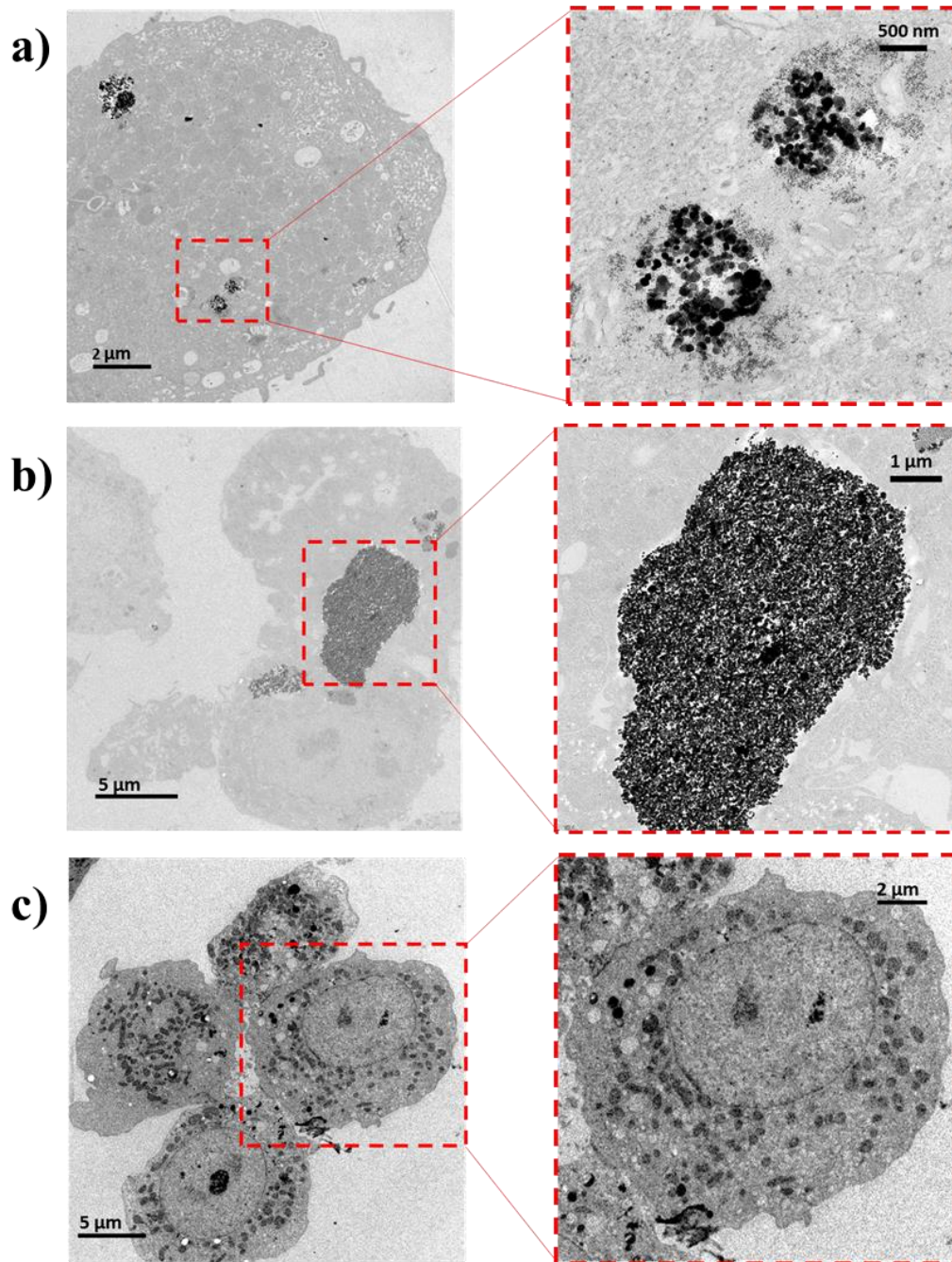
Figure 3. 21: TEM images of HepaRG cells (grey) and their uptake of unfunctionalized (a) and polyethylene glycol coated Fe_3O_4 nanoparticles (b). Highlighted are the areas of interest, where the nanoparticles (black dots) have successfully been engulfed by the HepaRG cells and are stored in vacuoles (light grey circles). Unexposed control cells are depicted in picture (c), where the nucleus (large circle) takes up most of the space and is surrounded by various vacuoles (dark spots).

Impedance measurements using the xCELLigence system

Impedance measurements using the xCELLigence equipment over 14 days were recorded to analyze the cell response to three concentrations (250, 500, and 1000 µg/mL) of unfunctionalized Fe_3O_4 nanoparticles (Figure 3. 22), PEG-coated Fe_3O_4 nanoparticles (Figure 3. 23) and Co_3O_4 nanoparticles as negative sample (Figure 3. 24). Each experiment underwent the same setup, where seeding the HepaRG cells caused the initial high impedance measurement (high cell viability) as none of the cells have now attached and a high current flowed through the cell plates. The results shown are the averaged values generated automatically by the system, based on three simultaneous measurements of the triplicates. Over the next 7 days, the cells are attaching to the cell plate and start growing, causing the impedance to drop and then rise again. The impedance peaks (▼) occur due to media changes every two days, where the plates are disconnected from the system and reattached, as the system requires a few moments to adjust to the actual cell viability again. After 7 days the HepaRG cells are fully differentiated (fully grown) and exposed to the three concentrations of nanoparticles (★). The exposure was done in serum-free media (culture medium without fetal bovine serum (FBS), as protein can react with the nanoparticle surfaces and therefore alter the results [3.49.]. A constant decrease in cell viability can be seen 24 hours after the exposure, as the media did not contain FBS in the following two media changes. The steady decline of cell viability after the following media change (▼) is caused by the lack of FBS in the culture medium, which functions as the food source for the cultured cells. Each media change causes a peak, as the system needs to be paused and reactivated between the changes. The system immediately starts measuring after reactivation and needs a minute to adjust the actual cell viability. This is visible through the sharp jump after reactivation and the amount of measuring points thereafter (Error! Reference source not found., c).
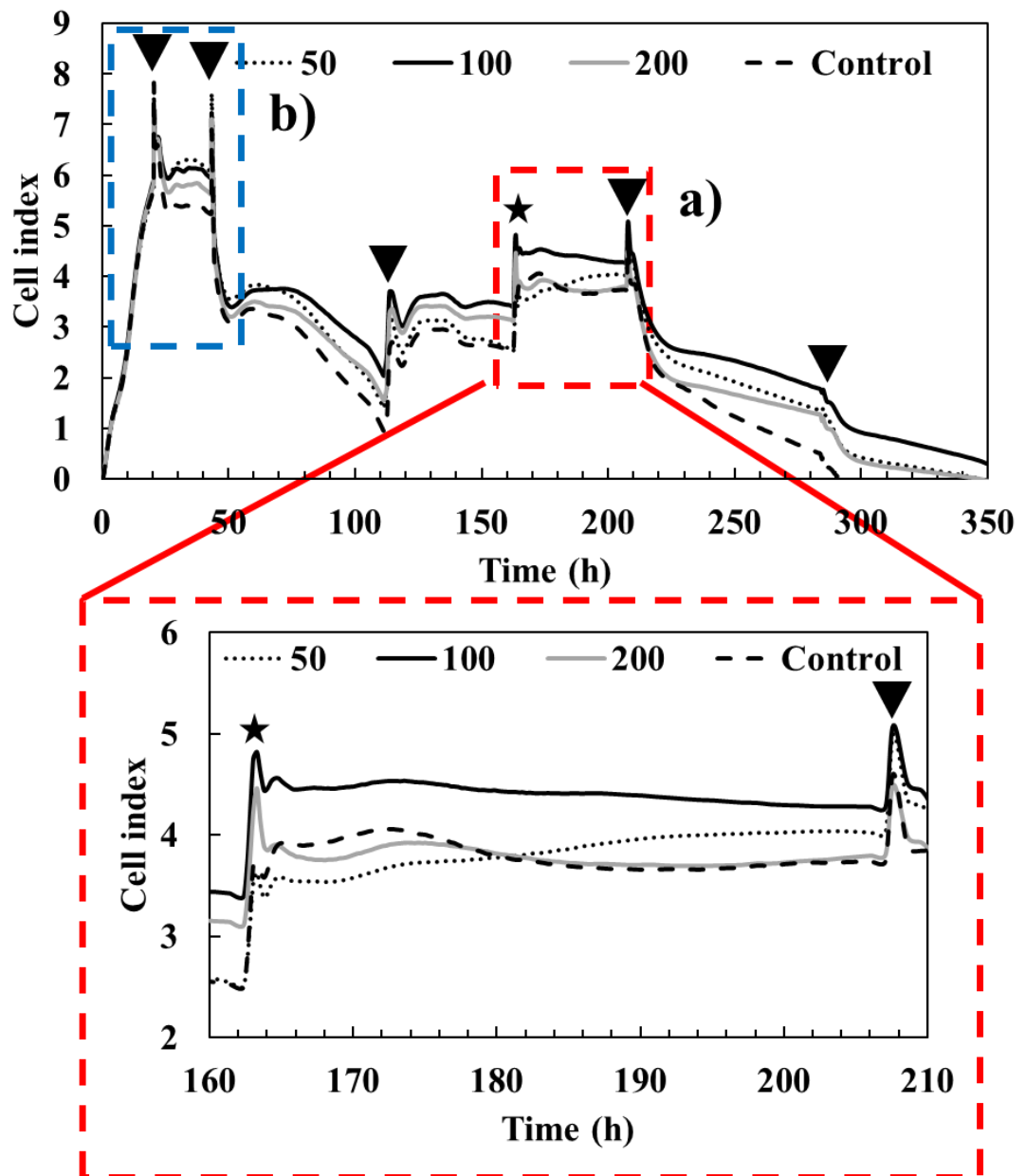
Figure 3. 22: xCELLigence reading over 14 days (350 h), where HepaRG cells were exposed to three concentrations of unfunctionalized Fe₃O₄ nanoparticles (★) on day 7. All other peaks resemble media changes (▼).
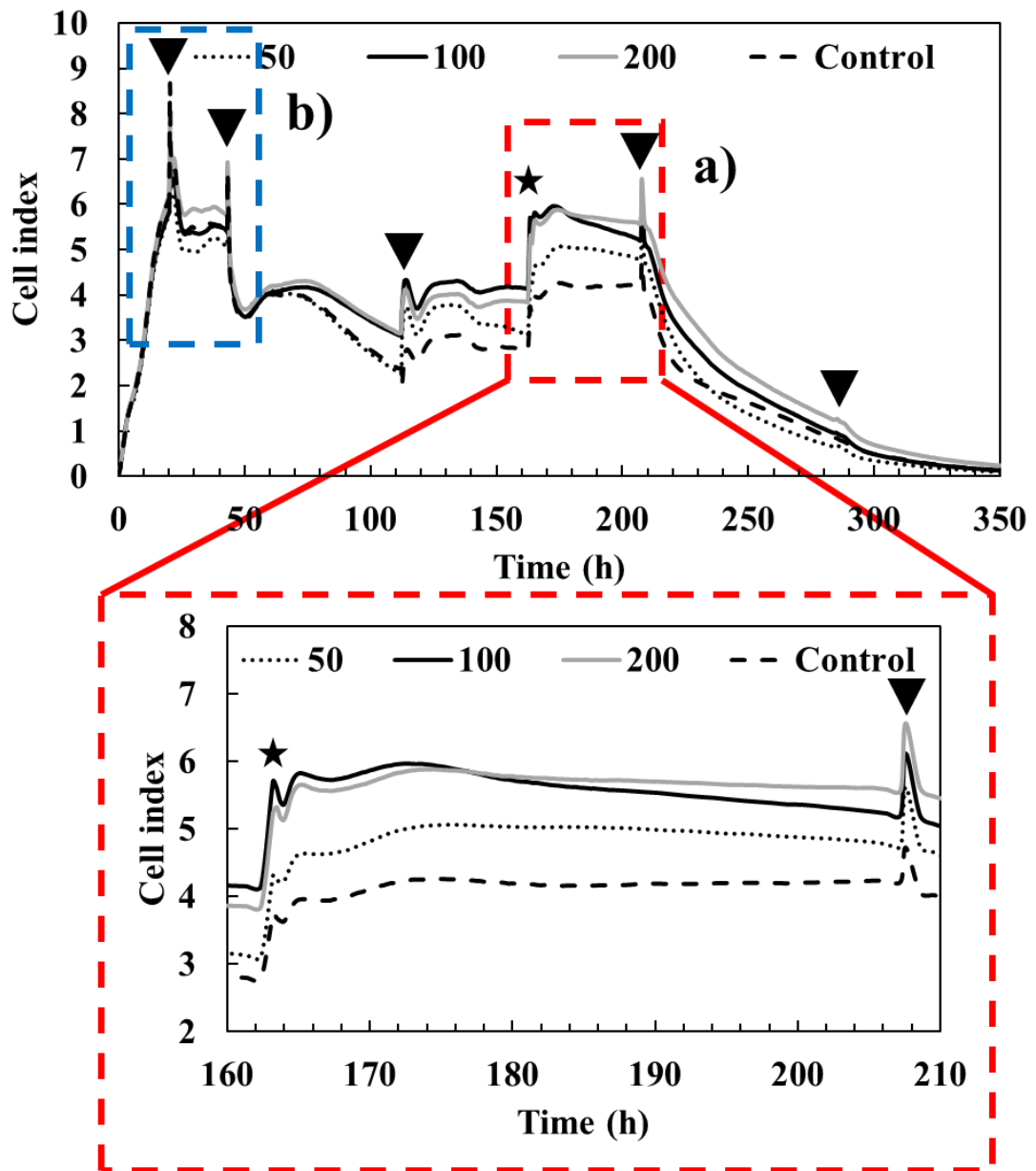
Figure 3. 23: xCELLigence reading over 14 days (350 h), where HepaRG cells were exposed to three concentrations of PEG-coated Fe₃O₄ nanoparticles (★) on day 7. All other peaks resemble media changes (▼).
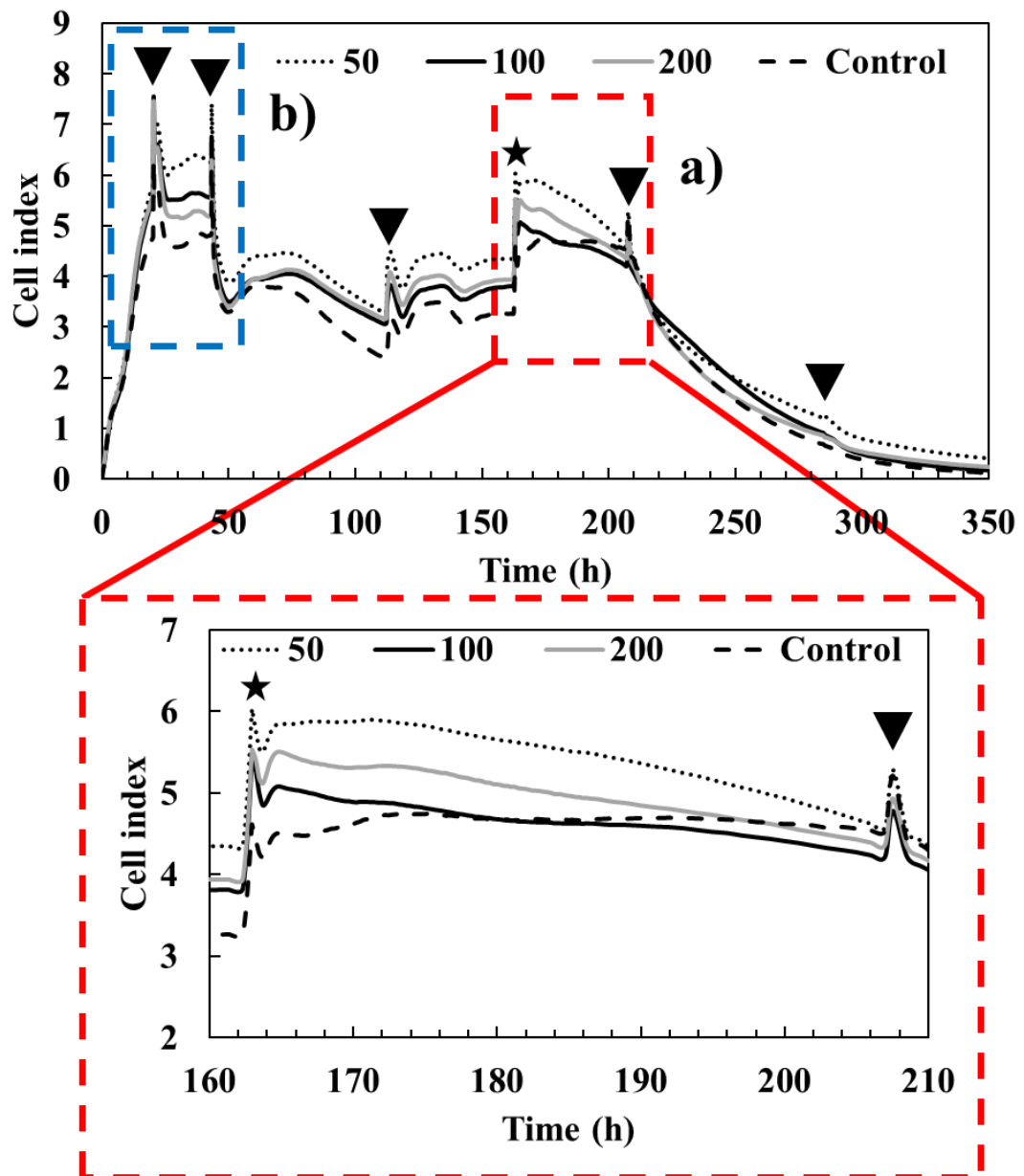
Figure 3. 24: xCELLigence reading over 14 days (350 h), where HepaRG cells were exposed to three concentrations of Co₃O₄ nanoparticles (★) on day 7. All other peaks resemble media changes (▼).

Comparing the effects of unfunctionalized and PEG-coated Fe_3O_4 nanoparticles on HepaRG cells showed a clear difference in cell viability (Error! Reference source not found.). The unfunctionalized Fe_3O_4 samples showed to affect the cell viability more than the PEG-coated nanoparticles (Error! Reference source not found., a), which generally presented more consistent cell viability throughout the experiment (Error! Reference source not found., b). Around 5 hours after nanoparticle exposure (★) in serum-free media (culture medium without fetal bovine serum (FBS) unfunctionalized iron oxide the cell viability of the HepaRG culture started to show a continuous decline (Error! Reference source not found., a). Almost the opposite happened with the PEG-coated samples of iron oxide (Error! Reference source not found., b), where the cell viability is stimulated within the first 5 hours and then plateaued without any further effects. This is due to the polyethylene coating which is known to reduce cell stress through reactive oxygen species (ROS) as the cell does not recognize the nanoparticles as foreign bodies [3.50.].
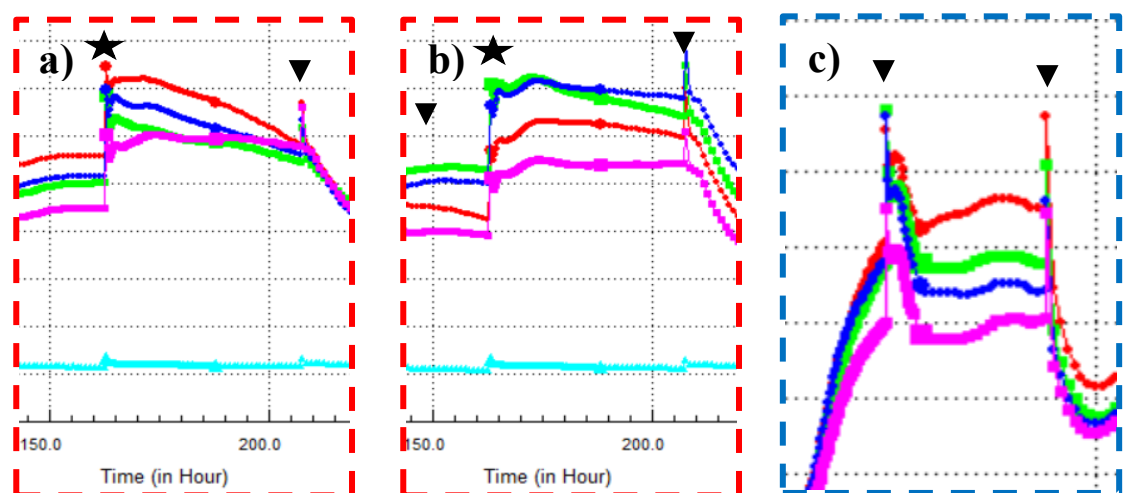
Figure 3. 25: Extract of xCELLigence a) unfunctionalized and b) PEGylated nanoparticle exposure to HepaRG cells, highlighting the time complete nanoparticle exposure time of 24 hours. Shown are the viabilities of the control (purple)and after exposure to 50 (red), 100 (green), 200 µg/mL (blue) of each sample. Shown in figure c) is the initial adjustment to the actual cell viability after reconnecting the cell culture plate to the impedance measurement system.

Comparing the three samples (unfunctionalized Fe_3O_4, PEG-coated Fe_3O_4, and unfunctionalized Co_3O_4) by the three concentrations of 250 µg (Figure 3. 26), 500 µg (Figure 3. 27) and 1000 µg/mL (Figure 3. 28), the PEGylates samples showed the highest cell viability across all concentrations. Constant cell viability after the exposure with

PEGylated nanoparticles, suggests that the polyethylene coating did indeed reduce cell stress and ultimately cell death. The unfunctionalized Fe_3O_4 samples showed lower cell viability than the Co_3O_4 samples in the beginning, but the cell viability remained constant thereafter at any concentration. While the Co_3O_4 nanoparticles did not cause the cell viability to drop immediately, a constant decrease was observed over the exposure time of 24 hours. It is notable that the initial cell viability, after exposure to 1000 µg/mL of unfunctionalized Fe_3O_4, showed a substantial drop within the first 2 hours and then remained constant throughout the rest of the exposure time. This could be the cell's response to iron-mediated toxicity, induced by the high concentration of free radicals. Free radicals are generated by interconverting between ferrous (Fe^{2+}) and ferric (Fe^{3+}) forms [1.51]. However, this needs further investigation and can be covered in the future work of this project.
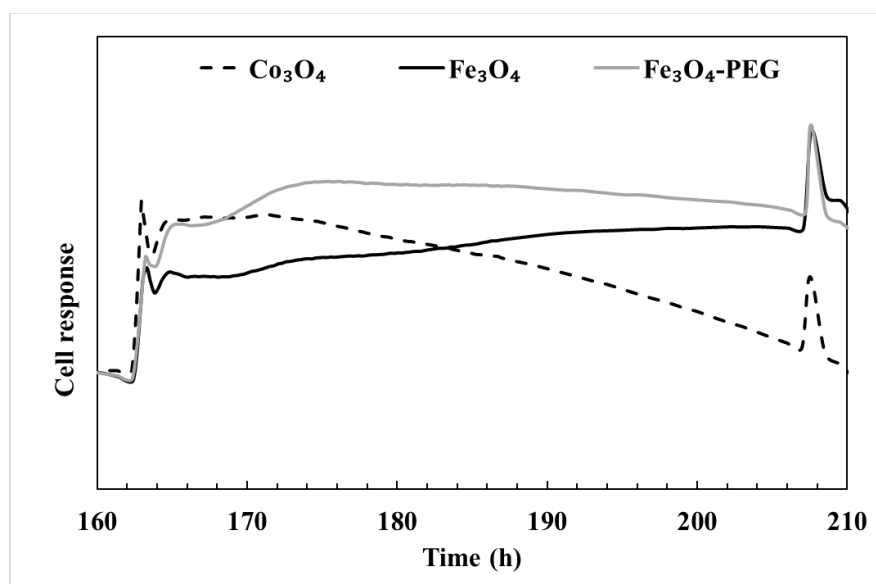
Figure 3. 26: Extract of xCELLigence reading of HepaRG cells after exposure to 50 µg of unfunctionalized Fe_3O_4, unfunctionalized Co_3O_4, and PEG-coated Fe_3O_4 nanoparticles. Both peaks show media changes, where only the first one included a dose of nanoparticles and therefore represents the nanoparticle exposure. The cell viability after exposure to PEGylated and unfunctionalized nanoparticles remained stable, while toxic Co_3O_4 nanoparticles induced a constant decrease within 24 hours.
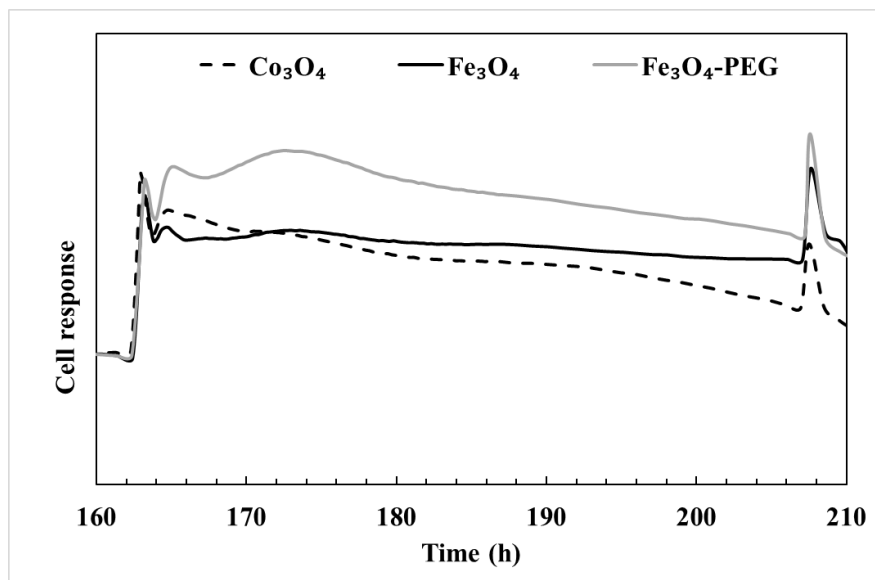
Figure 3. 27: Extract of xCELLigence reading of HepaRG cells after exposure to 100 μg of unfunctionalized Fe_3O_4, unfunctionalized Co_3O_4, and PEG-coated Fe_3O_4 nanoparticles. Both peaks show media changes, where only the first one included a dose of nanoparticles and therefore represents the nanoparticle exposure. The cell viability after exposure to PEGylated and unfunctionalized nanoparticles remained stable, while toxic Co3O4 nanoparticles induced a constant decrease within 24 hours.
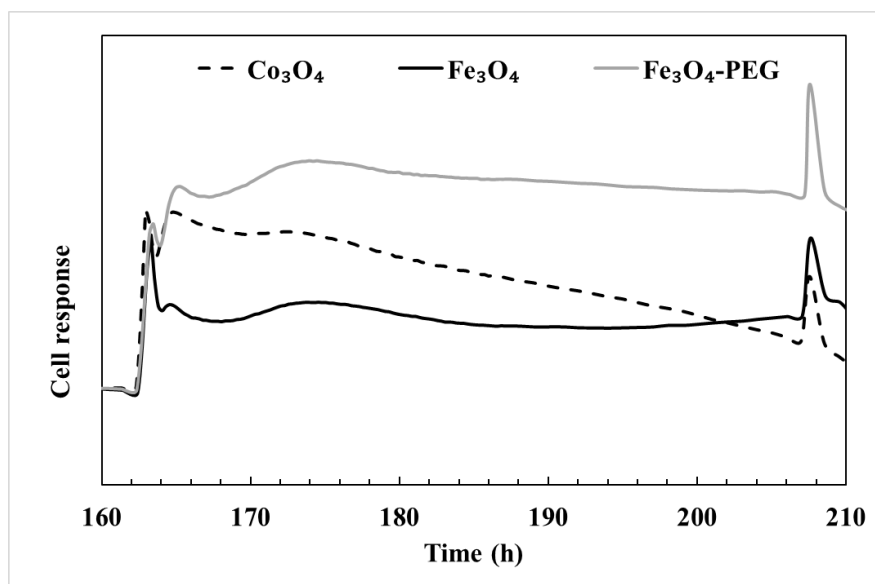
Figure 3. 28: Extract of xCELLigence reading of HepaRG cells after exposure to 1000 μg/mL of unfunctionalized Fe_3O_4, unfunctionalized Co_3O_4, and PEG-coated Fe_3O_4 nanoparticles. Both peaks show media changes, where only the first one included nanoparticles and therefore represents the nanoparticle exposure. The cell viability after exposure to PEGylated and unfunctionalized nanoparticles remained stable, while toxic Co_3O_4 nanoparticles induced a constant decrease within 24 hours.

3.6. Conclusion and future work

Since the liver is one the most important organs for blood purification, detoxification of chemicals, and metabolization of drugs, studying the effects of nanoparticles on liver cells is crucial to understand how the liver and especially liver cells behave after exposure to Fe_3O_4 iron oxide nanoparticles. Even though colorimetric assays such as CellTiter-Glo and PrestoBlue have been established as valuable cell assays all over the world, some restrictions, such as the absorption of light, can alter the data and produce inaccurate results and estimates. By analyzing the liver functions and the cell response in 2D and 3D cultures an accurate estimation of the toxicity of nanoparticles can be made. The results suggest that impedance-based measurements (xCELLigence system) and Coherent Anti-Stokes Raman Scattering (CARS) are powerful tools to analyze the cell viability of liver cells. Measuring the effects of nanoparticles on the cell cultures through an electrical current does not only provide valuable data on the immediate effects in real-time but also allows for long-term exposures.

Liver cells in 2D cultures *in vitro* do not necessarily represent an accurate behavior of liver cells, future work will focus on the further development of the 3D liver tissue model to mimic the liver's behavior more accurately. While cells are easily analyzed in a 2D culture, where the cells have enough space to spread, a realistic liver model presents a much more complex environment, where cells are forming lumps and therefore pose a much more difficult matrix to penetrate by nanoparticles.

Additionally, further investigations into the cell response to free iron radicals are required to develop an understanding of the acute toxicity of ferrous nanoparticles at high concentrations.

3.7. References

[3.1.]   S. A. Meenach, J. Z. Hilt, K. W. Anderson; Poly(ethylene glycol)-based magnetic hydrogel nanocomposites for hyperthermia cancer therapy; Acta Biomaterialia, **2010**, 6, 1039-1046.

[3.2.]   F. Sonvico, S. Mornet, S. Vasseur; Folate-conjugated iron oxide nanoparticles for solid tumor targeting as potential specific magnetic hyperthermia mediators: synthesis, physicochemical characterization, and *in vitro* experiments. Bioconjugate Chem., **2005**, 16, 1181 – 1188.

[3.3.]   B.   Yin; Toward Understanding *in vivo* Sequestration of nanoparticles at the Molecular Level; *ACS Nano*, **2018**, 12, 2088–2093.

[3.4.]   J. Marquez, I. Fernandez-Piñeiro, M. J. Araúzo-Bravo, G. Poschmann, K. Stühler, A-M Khatib, A. Sanchez, F. Unda, G. Ibarretxe, I. Bernales, I. Badiola; Targeting liver sinusoidal endothelial cells with miR-20a-loaded nanoparticles reduces murine colon cancer metastasis to the liver; International Journal of Cancer, **2018**, 143, 709-719.

[3.5.]   Ahamed, Maqusood; Akhtar, Mohd Javed; Alhadlaq, Hisham A.; Khan, M.A. Majeed; Alrokayan, Salman A., Comparative cytotoxic response of nickel ferrite nanoparticles in human liver HepG2 and breast MFC-7 cancer cells, Chemosphere, **2015**, 135, 278.

[3.6.]   C. Hoskins, L. Wang, W. P. Cheng and A. Cushieri; Dilemmas in the reliable estimation of the *in vitro* cell viability in magnetic nanoparticle engineering: which tests and what protocols?; Nanoscale Res. Lett., **2012**, 7, 77.

[3.7.]   D. Hogemann, L. Josephson, R. Weissleder, JP Basilion; Improvement of MRI probes to allow efficient detection of gene expression; Bioconjugate Chem., **2000**, 11, 941 – 946.

[3.8.]   EH Kim, HS Lee, BK Kwak, BK Kim; Synthesis of ferrofluid with magnetic nanoparticles by sonochemical method for MRI contrast agent; J. Magnet. Magnet. Mater., **2005**, 289, 328 – 330.

[3.9.] Z. Q. Lei, L. Li, G. J. Li, C. W. Leung, J. Shi, C. M. Wong, K. C. Lo, W. K. Chan, C. S. K. Mak, S. B. Chan, N. M. M. Chan, C. H. Leung, P. T. Lai, P. W. T. Pong; Liver cancer immunoassay with magnetic nanoparticles and MgO-based magnetic tunnel junction sensors, Proceedings Of The 55th Annual Conference On Magnetism And Magnetic Materials, Atlanta, Georgia; Journal of Applied Physics, **2012**, 111, 7.

[3.10.] Q Wang, Y Sun, ZR Zhang, YR Duan; Targeted polymeric therapeutic nanoparticles: Design and interactions with hepatocellular carcinoma, Biomaterials, **2015**, 55, 229.

[3.11.] M. Kapałczyńska, T. Kolenda, W. Przybyła, M. Zajączkowska, A. Teresiak, V. Filas, M. Ibbs, R. Bliźniak, K. Łuczewski, and K. Lamperska; 2D and 3D cell cultures – a comparison of different types of cancer cell cultures; Arch Med Sci., **2018**, 14, 910–919.

[3.12.] H. Marushima, S. Shibata, T. Asakura; Three-dimensional culture promotes reconstitution of the tumor-specific hypoxic microenvironment under TGFβ stimulation.; Int J Oncol, **2011**, 39, 1327-36.

[3.13.] B. Baker, C. Chen; Deconstructing the third dimension – how 3D culture microenvironments alter cellular cues; J Cell Sci, **2012**, 125, 3015-3024.

[3.14.] S. Chen, Y. Chang, S. Nieh; Nonadhesive culture system as a model of rapid sphere formation with cancer stem cell properties.; PLoS One, **2012**, 7, 31864

[3.15.] S. Khetan, JA Burdick; Patterning network structure to spatially control cellular remodeling and stem cell fate within 3-dimensional hydrogels.; Biomaterials, **2010**; 31, 8228-34.

[3.16.] JA Hickman, R. Graeser, R. de Hoogt; Three-dimensional models of cancer for pharmacology and cancer cell biology: capturing tumor complexity *in vitro*/ex vivo.; Biotechnol J, **2014**, 9, 1115-28.

[3.17.] LG Griffith, MA Swartz; Capturing complex 3D tissue physiology *in vitro*; Nat Rev Mol Cell Biol, **2006**, 7, 211-24.

[3.18.] MJ Bissell, A. Rizki, IS Mian; Tissue architecture: the ultimate regulator of breast epithelial function; Curr Opin Cell Biol 2003; 15, 753-62.

[3.19.] PM Gilbert, KL Havenstrite, KE Magnusson; Substrate elasticity regulates skeletal muscle stem cell self-renewal in culture; Science, **2010**; 329, 1078-81.

[3.20.] A. Engler, S. Sen, HL Sweeney, DE Discher; Matrix elasticity directs stem cell lineage specification; Cell, **2006**; 126, 677-89.

[3.21.] D. Cawkill, SS Eaglestone; Evolution of cell-based reagent provision.; Drug Discov Today, **2007**; 12, 820-5.

[3.22.] J. Lee, MJ Cuddihy, NA Kotov; Three-dimensional cell culture matrices: state of the art; Tissue Eng Part B Rev 2008; 14, 61-86

[3.23.] K. Yamada and E. Cukierman; Modeling tissue morphogenesis and cancer in 3D. Cell, **2007**; 130, 601-10.

[3.24.] K. von der Mark, V. Gauss, H. von der Mark, P. Müller; Relationship between cell shape and type of collagen synthesised as chondrocytes lose their cartilage phenotype in culture; Nature, **1977**; 26, 531-2.

[3.25.] OW Petersen, L. Rønnov-Jessen, AR Howlett, MJ Bissel; Interaction with basement membrane serves to rapidly distinguish growth and differentiation pattern of normal and malignant human breast epithelial cells; Proc Natl Acad Sci USA, **1992**; 89, 9064-8.

[3.26.] G. Mahmud, CJ Campbell, KJM Bishop; Directing cell motions on micropatterned ratchets; Nat Phys, **2009**; 5, 606-12. 17.

[3.27.] K. Kilian, B. Bugarija and BT Lahn; Geometric cues for directing the differentiation of mesenchymal stem cells; Proc Natl Acad Sci USA, **2010**, 107, 4872-7.

[3.28.] T. Mseka, JR Bamburg and LP Cramer; ADF/cofilin family proteins control formation of oriented actin-filament bundles in the cell body to trigger fibroblast polarization; J Cell Sci, **2007**; 120, 4332-44.

[3.29.] PD Benya and JD Shaffer; Dedifferentiated chondrocytes reexpress the differentiated collagen phenotype when cultured in agarose gels; Cell, **1982**; 30, 215-24

[3.30.] S. Breslin and L. O'Driscoll; Three-dimensional cell culture: the missing link in drug discovery; Drug Discov Today, **2013**; 18, 240-9.

[3.31.] HBFrieboes, BR Smith, Y. Chuang; An integrated computational/experimental model of tumor invasion; Cancer Res, **2006**; 66, 1597-604.

[3.32.] A. Birgersdotter, R. Sandberg and I. Ernberg; Gene expression perturbation *in vitro* – a growing case for three-dimensional (3D) culture systems; Semin Cancer Biol, **2005**; 15, 405-12.

[3.33.] C. Li, M. Kato, L. Shiue, JE Shively, M. Ares, RJ Lin; Cell type and culture condition-dependent alternative splicing in human breast cancer cells revealed by splicing-sensitive microarrays; Cancer Res, **2006**; 66, 1990-9.

[3.34.] E. Fuchs, T. Tumbar, G. Guasch; Socializing with the neighbors: stem cells and their niche; Cell, **2004**; 116, 769-78.

[3.35.] M. Gomez-Lechon, R. Jover and T. Donato; Long-term expression of differentiated functions in hepatocytes cultured in three-dimensional collagen matrix; J Cell Physiol, **1998**; 77, 553-62.

[3.36.] B. Aggarwal, D. Danda, S. Gupta, P. Gehlot; Models for prevention and treatment of cancer: problems vs promises; Biochem Pharmacol, **2009**; 78, 1083-94.

[3.36.] M.D., Cecilia & M.D.; F.A.C.S.. (2015). Biliary System Anatomy, Physiology, and Embryology. 10.1007/978-3-319-22273-8_1.

[3.37.] R. Jossé, C. Aninat, D. Glaise, J. Dumont, V. Fessard, F. Morel, JM Poul, C. Guguen-Guillouzo, A. Guillouzo; Long-term functional stability of human HepaRG hepatocytes and use for chronic toxicity and genotoxicity studies; Drug Metab Dispos., **2008**; 36(6),1111-8.

[3.38.] S. Anthérieu, C. Chesné, R. Li, S. Camus, A. Lahoz, L. Picazo, M. Turpeinen, A. Tolonen, J. Uusitalo, C. Guguen-Guillouzo, A. Guillouzo; Stable expression, activity, and inducibility of cytochromes P450 in differentiated HepaRG cells; Drug Metab Dispos., **2010**; 38, 516-25.

[3.39.] R. Parent, MJ Marion, L. Furio, C. Trépo, MA Petit; Origin and Characterization of a Human Bipotent Liver Progenitor Cell Line; Gastroenterology, **2004**; 126, 1147–1156.

[3.40.] N. Hoshyar, S. Gray, HB Han, and G. Bao; The effect of nanoparticle size on *in vivo* pharmacokinetics and cellular interaction; Nanomedicine (Lond)., **2016**; 11, 673–692.

[3.40.] Invitrogen, PrestoBlue® Cell Viability Reagent, Frequently Asked Questions, Version No.: 21Mar12

[3.41.] S. Baljit Khakh and Geoffrey Burnstock; The double life of ATP; Sci. Am., **2009**, 301, 84-92.

[3.42.] CellTiter-Glo® 3D Cell Viability Assay, Technical Manual, TM412 Revised 11/15

[3.43.] Mouras; Nonlinear optical microscopy of adipose-derived stem cells induced towards osteoblasts and adipocytes, **2011**, DOI: 10.1117/12.889780

[3.44.] M. Müller and J. Schins; Imaging the Thermodynamic State of Lipid Membranes with Multiplex CARS Microscopy; J. Phys. Chem. B, **2002**,106, 3715-3723.

[3.45.] A. Kachynski, A. Kuzmin, P. Prasad, I. Smalyukh; Realignment-enhanced coherent anti-Stokes Raman scattering and three-dimensional imaging in anisotropic fluids; Opt. Express, **2008**,16, 10617-10632.

[3.46.] J.-C. Olivo-Marin; Extraction of spots in biological images using multi scale products; Pattern recognition, **2002**, 35, 1989-1996.

[3.47.] E. Przybytkowski, M. Behrendt, D. Dubois, and Dusica Maysinger; Nanoparticles can induce changes in the intracellular metabolism of lipids without compromising cellular viability; FEBS Journal, **2009**, 6204-6217.

[3.48.] Y. Wada; Vacuoles in mammals - A subcellular structure indispensable for early embryogenesis; Bioarchitecture., **2013** Jan 1; 3, 13–19.

[3.49.] H. T. R. Wiogo, M. Lim, V. Bulmus, J. Yun, and R. Amal; Stabilization of Magnetic Iron Oxide Nanoparticles in Biological Media by Fetal Bovine Serum (FBS); Langmuir, **2011**, 27, 2, 843–850.

[3.50.] V. Patsula, D. Horák, J. Kučka; Synthesis and modification of uniform PEG-neridronate-modified magnetic nanoparticles determines prolonged blood circulation and biodistribution in a mouse preclinical model; Sci Rep, **2019**, 9, 10765.

[3.51.] R. Eid, N. T. T. Arab, and M. T. Greenwood; Iron mediated toxicity and programmed cell death: A review and a re-examination of existing paradigms; Biochimica et Biophysica Acta 1864, **2017**, 399-430.

CHAPTER 4

Monitoring the cell internalization of iron oxide nanoparticles using a holographic imaging system

4.1. Introduction

The internalization process of PEG-coated iron oxide nanoparticles was monitored continuously using a new holography technique. It was found that the internalization of MNPs completed in 35 minutes, presenting an online study on internalization that has not been found in the literature. The system is based on taking a series of pictures of a selection of cells under a microscope over time and thus generating a time-lapse video. The frequency of captures can be optimized to ensure the desired process is precisely measured and in focus. A long long-term exposure would require a lower frame capture rate (frequency) than for example a short exposure, such as the internalization process presented in this chapter.

In contrast to a single cell observation, a time-lapse video allows interpreting the cell dynamics, cell morphologies, and cell reactions to nanoparticles (e.g., toxicity and apoptosis). Information about the cell surface and its properties is highly essential to analyze the cell-substrate interactions and possible cellular effects that result from the exposure to the substrates. For example, loading a cell with nanoparticles and monitor the cell proliferation over time helps to identify the cellular uptake of MNPs and their toxicity. In the literature, cell monitoring usually focuses on the effects on a single cell [4.1.-4.3.]. The HoloMonitor M4 (Phase Holographic Imaging), however, is one of the first microscopes that allows to monitor and average of multiple cells for evaluation. A possible toxic effect and other properties can therefore be identified with higher precision.

One of the most significant cellular processes for drug delivery and contrasting is cellular uptake (internalization). This can occur through cellular activities such as endocytosis, where the particle or substrate is internalized in form of a vesicle. Figure 4. 1 illustrates the three major steps of a nanoparticle internalization through endocytosis. The first step is the MNP adhesion to the cell surface (membrane). From here, the membrane bends until the particle is fully encapsulated (engulfment). The final step is the detachment of the newly built vesicle from the cell membrane (fission) and its uptake into the cell [4.4.]. Understanding the mechanism and kinetics of the internalization is highly important for the design and optimization of nanoparticles for drug delivery and contrast enhancement.

Monitoring MCF-7 breast cancer cells with the HoloMonitor M4 microscope did not only present valuable data about the cell proliferation but also allowed study on the roughness

of the cell surface, which presented the key factors for this chapter. Focusing on the shape parameters skewness and kurtosis a surface profile of the monitored cell can be created. The surface roughness expressed in skewness shows if the surface is generally porous or peaked, whereas the kurtosis indicates how "peaked" the measured surface is. This means that negative values would refer to a rather porous surface with a lot of valleys, whilst positive values indicate a surface with peaks and asperities.
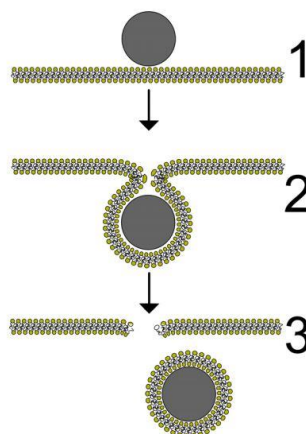
Figure 4. 1: The three steps of nanoparticle internalization by endocytosis:- adhesion (1), engulfment (2), and fission (3) [52]

For this experiment, MCF-7 breast cancer cells were loaded with PEG_{9-12}-silane nanoparticles (Chapter 3) and continuously monitored under a HoloMonitor M4 microscope for 72 hours to test the toxicity and cell response. The results not only suggested that the nanoparticles did not cause cell death and improved the cell distribution, but also allowed for a novel way of monitoring each step of the internalization process of nanoparticles into the cell (adhesion, engulfment, and fission).

4.2. Experimental

4.2.1. Culturing MCF-7 breast cancer cells

For this experiment, MCF-7 breast cancer cells were seeded and cultured in a T25 cell culture flask (25 mL). The cell culture medium (Medium I) contained 88% Dulbecco's Modified Eagles Medium (DMEM), 10% fetal bovine serum (FBS), 1% antibiotics (penicillin-streptomycin), and 1% L-glutamine. The medium was changed every two days until a sufficient number of cells was obtained (80k cells/ dish or around 20% confluency). The cell cultures were incubated at 37ºC with a 5% CO_2 atmosphere. To acquire enough cells for the planned experiments the MCF-7 cell cultures were split several times when they reached confluency between 80% -90%. At first, the exhausted medium (5 mL) had

to be removed from the flask. The cells were then washed with 1 mL phosphate-buffered saline (PBS), followed by trypsinization using 1 mL trypsin solution to dissociate the adherent cells from the flask. After the trypsin was removed, the cells were incubated for 7 minutes at 37 ºC in a 5% CO_2 atmosphere. After that, the cells were mixed with 5 mL of fresh media (medium I), split in the desired ratio, and topped up with the necessary amount of media to reach a total volume of 5 mL.

4.2.2. Loading the cell line with nanoparticles and monitoring the cell internalization process using the HoloMonitor M4 microscope

First MCF-7 cancer cells were seeded on a petri dish (Ø 25 mm) at a density of 1 x 10^5 cells per dish with 2 mL medium I. Two different media were used during this exposure experiment; medium (I) was prepared as the standard culture medium (4.2.1. Cell culturing); medium (II) is of the same composition as medium (I) except for any fetal bovine serum (FBS). The missing amount of FBS in medium (II) was compensated by adding an equivalent amount of DMEM. The serum-free medium (II) was used during particle loading to avoid any possible interactions between proteins and nanoparticles. After 48 h of incubation (37ºC, 5% CO_2 atm.), the medium was changed to medium (II), which included 150 µL of a sterile filtrated 5 µg/mL PEG_{9-12}-silane nanoparticle solution. The serum-free medium II, used during monitoring of the MNP-loaded cells, was changed to medium I (containing proteins) after 48h to provide fresh nourishment for the cells.

The viability of cells was then digitally monitored using a HoloMonitor M4 time lap microscope (Phase Holographic Imaging, Sweden). Cells loaded with PEG_{9-12}-silane MNPs were incubated at 37 ºC and 5% CO_2 atmosphere. The frame capture rate was set to take an image every minute, with a total imaged area of 1.558 mm^2. The captured frames generated a time lap video showing the cell proliferation and recorded the surface roughness in skewness and kurtosis.

4.3. Results and discussion

In this study, MCF-7 breast cancer cells were loaded with polyethylene glycol coated MNPs (Chapter 3, Fe_3O_4-PEG-silane$_{9-12}$) and monitored for 72 hours. This is depicted in Figure 4. 2, a and Figure 4. 2, b which are images taken during the recorded time. One frame was taken on Day 1 of the internalization (cell loading) and the other 72 hours later (Day 4). The pictures presented here are only two frames out of a very large collection of timepoints, where a time-lapse analysis was generated by capturing an image every minute for 72 hours. Collating those images produces a time-laps video and dataset, which allows monitoring the cell behavior, movement, and response to the particle loading and viability of each cell. The images demonstrate the detail at which the system produces the holographic images. Each peak in the system (green) represents a living cell. When the highlighted cells (circled in white) between the two images are compared, it can be seen that more peaks have developed in the exposure time of 72 hours. This shows that cell splitting and proliferation took place, and thus no extraordinary damages or cell death was caused by the internalization of the particles.

This experiment was repeated three times and compared to control images to ensure accuracy. Agglomerations of nanoparticles only are displayed as white noise between the cells (arrows). No distinguishable differences were determined in the images of the individual exposure samples (control, PEG-silane-9-12, and uncoated Fe_3O_4). However, clear differences became apparent when the kurtosis and skewness of the samples were compared.
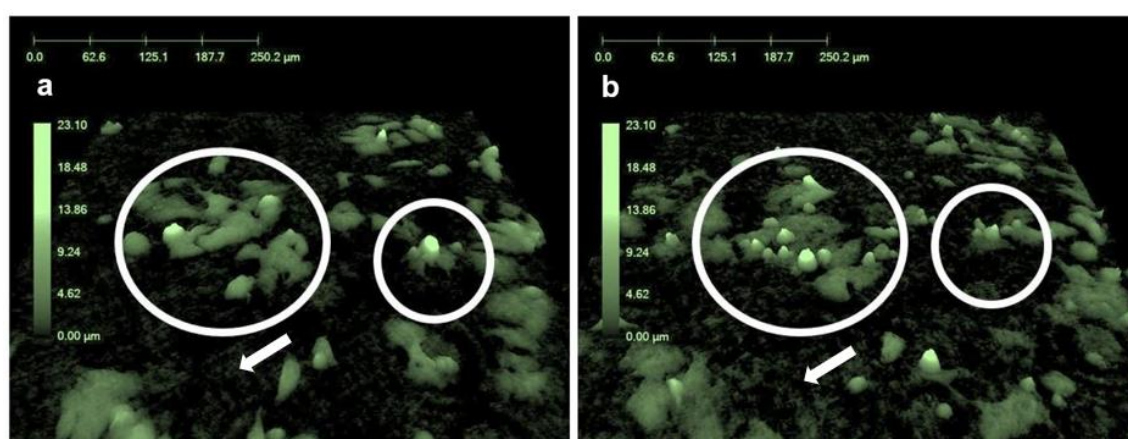
Figure 4. 2: MCF-7 breast cancer cells (green) on the first day of MNP internalization (a) and 72 hours after internalization (b). The highlights (peaks circled in white) point out that cell proliferation took place and was not significantly affected by nanoparticle exposure (arrows).

Kurtosis and skewness

Figure 4. 3 and Figure 4. 4 show the kurtosis and skewness of two MCF-7 breast cancer cells that were monitored for 60 minutes at a frame capture rate of 1 image/ minute. Since the cells are alive and constantly in motion, the graphs display up and down peaks, rather than smooth and straight lines. The roughness profiles display a clear difference between the control cells, which were grown in absence of any iron oxide nanoparticles, and cells that were loaded with MNPs.

It is visible that both shape parameters (kurtosis and skewness) change between 10 and 30 minutes after the exposure. This is presumed to represent the extracellular stages of the MNP internalization as shown in Figure 4. 1:

Step 1,   the attachment of MNPs to the cell surface, causing the values to peak

Step 2,   the cell reaction and recognition of adherent nanoparticles

Step 3,   the internalization of the particles, causing the values to normalize again

To illustrate that this process did not only apply to single cells the average roughness values for kurtosis and skewness of 156 MCF-7 control cells (no MNPs) and 88 MCF-7 cells loaded with PEG-silane$_{9-12}$ nanoparticles were averaged and shown in Figure 4. 5 and Figure 4. 6. The average roughness values for kurtosis did not show a significant change in the "peakedness" of the cell surface. Averaging the surface skewness revealed a much rougher cell surface than the single control cell in Figure 4.6. It is presumed that cell activity such as cell proliferation and cell movement cause surface changes. However, these changes can still be distinguished from external events as the internalization process.

This project revealed that the endocytosis process can be monitored by measuring the cell roughness in kurtosis and skewness. However, additional studies of potential cell function inhibitors during the exposures are required to develop a further understanding of the individual steps during the internalization process of iron oxide nanoparticles.
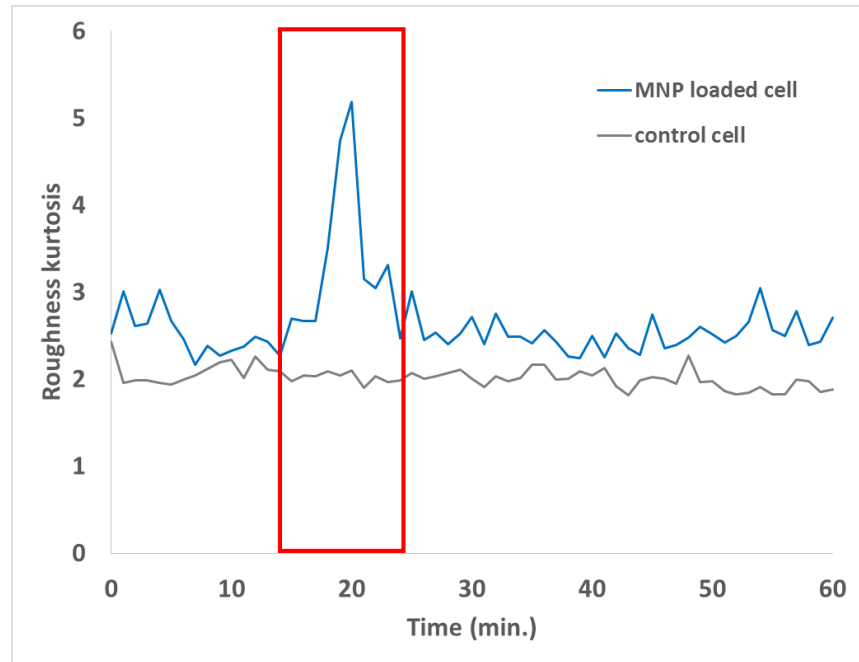
Figure 4. 3: Roughness (kurtosis), compared by MNP loaded (PEG-silane$_{9-12}$) and unloaded (control) MCF-7 breast cancer cells. The highlighted section displays the physical internalization of MNPs through the cell membrane.
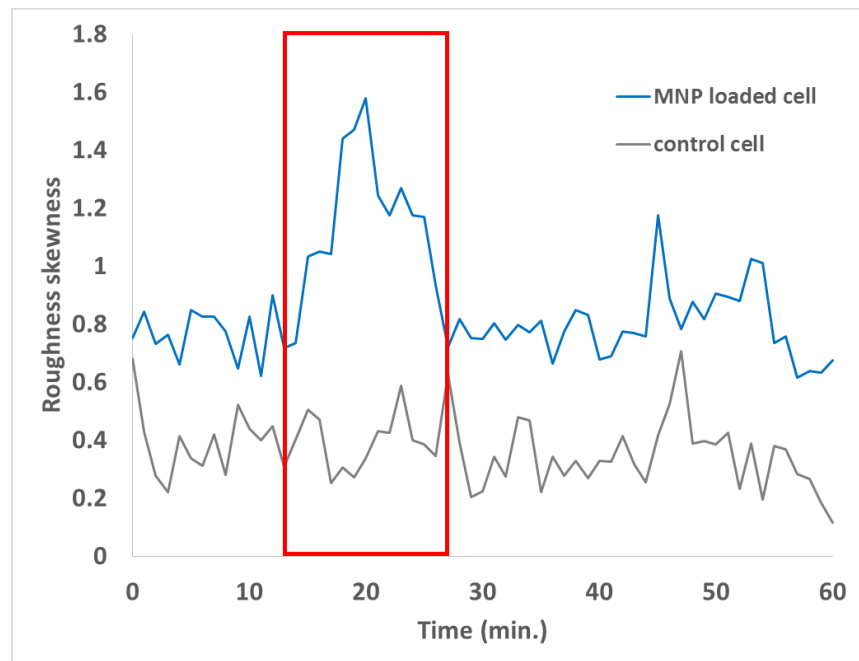
Figure 4. 4: Roughness (skewness), compared by MNP loaded (PEG-silane$_{9-12}$) and unloaded (control) MCF-7 breast cancer cells. The highlighted section displays the physical internalization of MNPs through the cell membrane.
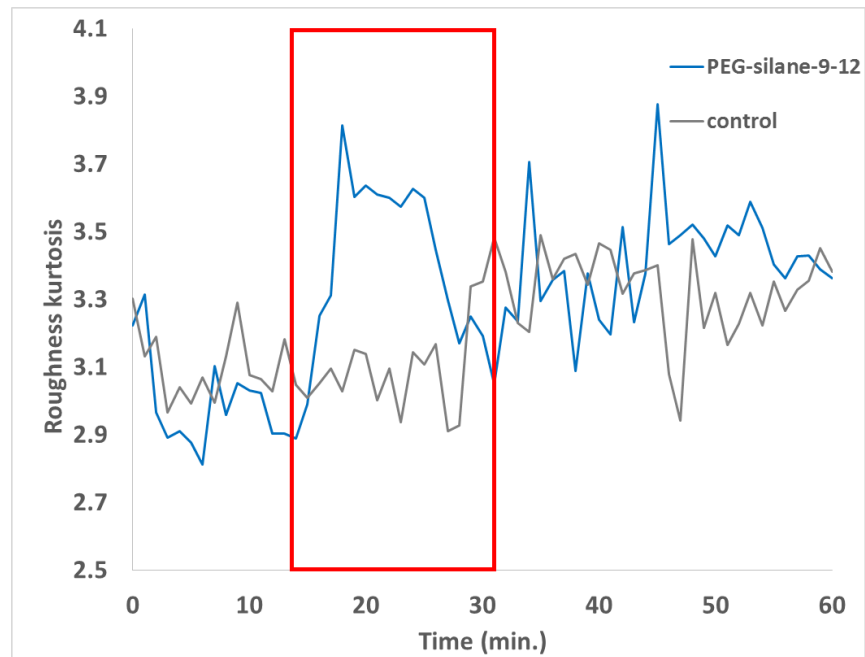
Figure 4. 5: Average Roughness (kurtosis) of MCF-7 breast cancer cells. The highlighted section displays the physical internalization of MNPs through the cell membrane.
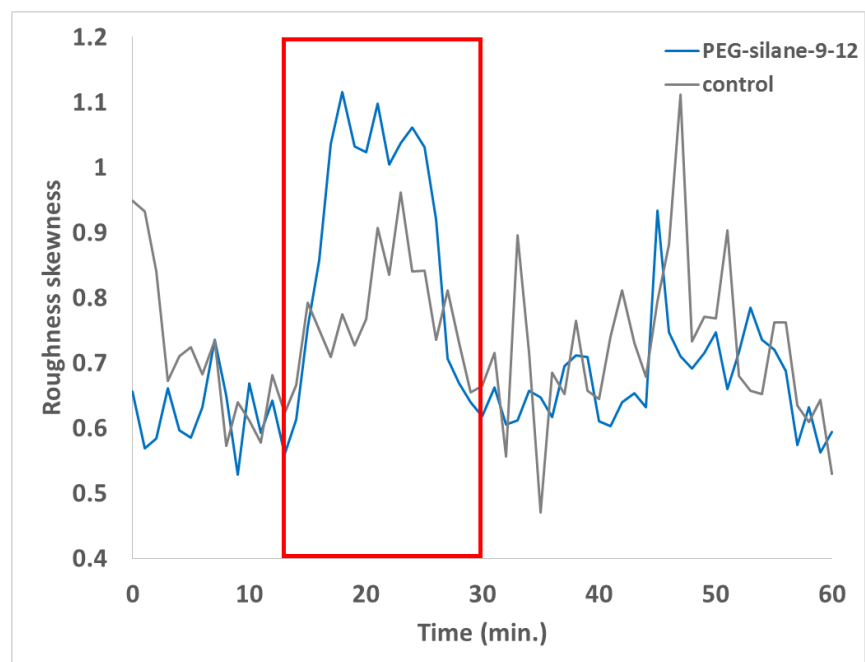
Figure 4. 6: Average Roughness (skewness) of MCF-7 breast cancer cells. The highlighted section displays the physical internalization of MNPs through the cell membrane.

4.4. Future work

The next stage focuses on further toxicity tests of PEG-coated magnetic iron oxide nanoparticles studying the internalization kinetics of particles based on the roughness on cell surfaces. To use nanoparticles for biomedical applications, for instance as contrast agents, several aspects must be considered and addressed up front. MTT color assays and impedance measurements will provide further information about the impact and effects of PEG-coated MNPs on MCF-7 breast cancer cells. Moreover, the use of toxic nanoparticles presents negative controls for comparison. These will be prepared by replacing the Fe_3O_4 core particle with toxic Co_3O_4 nanoparticles and changing the biocompatible polyethylene glycol coating with different surface functionalization that are known to be toxic to living cells. The toxicity of these MNPs will be monitored over MCF-7 cancer cells using a HoloMonitor M4 microscope. This digital imaging method will generate further information about the cell internalization process of nanoparticles and therefore help to optimize the cell uptake of functionalized nanoparticles into cell and tissue cultures and improve their intended purposes such as drug delivery and contrast enhancement.

4.5. References

[4.1.] I. Ojea-Jiménez, P. Urbán, F. Barahona, M. Pedroni, R. Capomaccio, G. Ceccone, A. Kinsner-Ovaskainen, F. Rossi, D. Gilliland, Douglas; Highly Flexible Platform for Tuning Surface Properties of Silica Nanoparticles and Monitoring Their Biological Interaction; ACS Appl. Mater. Interfaces, **2016**, 8, 4838–4850.

[4.2.] Y. Shan, N. Panday, Y. Myoung, M. Twomey, X. Wang, W. Li, E. Celik, V. Moy, H. Wang, J. H. Moon, J. He; Scanning Ion Conductance Microscopic Study for Cellular Uptake of Cationic Conjugated Polymer Nanoparticles; Macromol. Biosci., **2016**, 599–607.

[4.3.] C. W. Lee, L. L. Jang, H. J. Pan, Y. R. Chen, C. C. Chen, and C. H. Lee; Membrane roughness as a sensitive parameter reflecting the status of neuronal cells in response to chemical and nanoparticle treatments; J. Nanobiotechnology, **2016**, 1–7.

[4.4.] F. G. Strobl, F. Seitz, C. Westerhausen, A. Reller, A. A. Torrano, C. Bräuchle, A. Wixforth, M. F. Schneider; Intake of silica nanoparticles by giant lipid vesicles: influence of particle size and thermodynamic membrane state; Beilstein J. Nanotechnol., **2014**, vol. 5, 2468–78.

CHAPTER 5

Magnetic molecularly imprinted polymer networks and spheres (MMIPs) for the selective binding of antibiotics

5.1. Introduction

Molecular imprinting is a technique where monomers polymerize around a template molecule that is later recognized as the substrate. This process forms a polymer mold of the template molecule, adapting the characteristic shape and binding sites complementary to the template into the polymer matrix (molecularly imprinted polymer, MIP) [5.1.]. The addition of cross-linking agents creates additional bonds between the monomer units and so strengthen the polymer structure furthermore. After removing the template molecule, the chemical binding sites, and cavities of the template molecule, imprinted into the structure of the polymer, are retained and now active for recognition and selective binding of the target molecule. Figure 5. 1 shows the general formation of molecularly imprinted polymers (MIPs).
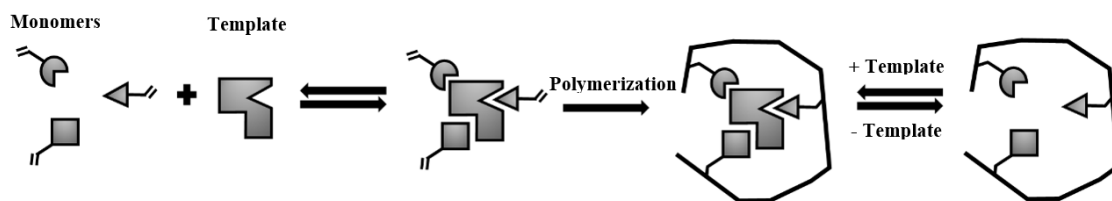
Figure 5. 1: A basic illustration of the formation of molecularly imprinted polymers. Selected monomers and template molecules undergo polymerization, creating an imprint of the template molecule. The imprint contains binding sites of the template molecule that become active after removing the template and makes the polymer highly selective.

Intermolecular forces form the basis of molecular imprinting and are achieved by. covalent and non-covalent bonding. Wulff et al. first reported the covalent approach by developing a covalent bond between the template molecule (acrylic acid) and the polymer mold. He found that, once he removed the template, its specific functionalities imprinted on the polymer became active [5.2.]. The binding sites did show not only high through molecular recognition towards the template molecule but also developed a selectivity for other similar molecules. However, the lack of suitable template molecules available for covalent binding and the general strength of covalent bonds make it difficult to remove the template and reuse the molecularly imprinted polymers. This led to the conclusion that the

covalent approach was not optimal for the intention when recovery and recyclability are required.

Instead of using rather strong covalent bonds, Wulff et al. then reported a non-covalent approach by focusing on temporary and reversible reactions between monomers and the template molecule [5.3.]. Binding and removing the template molecule is of importance for the functionality of the molecularly imprinted polymer as no active binding sites and cavities for molecular recognition would otherwise be created. The main reversible reactions between the monomers and the template molecule are based on their electrostatic charge, followed by smaller but relevant Van der Waal's Forces and hydrophobic interactions. Van der Waal's forces are the result of movements in electrons which induce temporary dipoles by forming electrostatic attractions between the atoms and molecules [5.4.]. Hydrophobic interactions hold molecules together by intermolecular forces reaction (e.g., the agglomeration of micelles to reduce the contact of hydrophobic lipids with water) [5.5.].

When a swift recovery and recyclability of the polymer are required, a quick binding and release mechanism becomes essential. In addition to the reversible interactions between the polymer network and the template molecule, the non-covalent approach allows the synthesis of homogenous MIP structures [5.6.]. A homogenous shape of the polymeric structure is highly desirable to maintain a consistent result in drug binding and release, e.g., where swelling of the polymer network is induced to release the drug from the polymer structure, an irregular shaped network could result in uncontrolled expansion and therefore inconsistent drug release [5.6.].

The most common mechanism to release the target molecule from MIP systems is based on the swelling and collapsing of the polymer network. This mechanism can be triggered by changes in pH, temperature, ionic strength, electric fields, and irradiation by ultraviolet or visible light [5.7.]. Changes in pH can cause swelling of the polymer as ionizable groups within the MIP system can accept or donate hydrogen ions at specific pH levels, inducing the polymer to collapse or expanded (swollen). This could be achieved by adding acidic or alkaline solutions to the mixture for quick changes in the pH environment or by applying an electric field. Temperature changes can be used to collapse the polymer when hydrophobic groups form at the lower critical solution temperature, breaking the weaker hydrogen bonds that have built when the polymer reached its upper critical solution temperate and started swelling. Ultraviolet (UV) and visible light is another possibility to stimulate the polymer into swelling but, the procedure would be time-consuming,

laborious, and would not provide the required amount of energy to trigger the polymer [5.8.]. Whichever release method is applied, a quick release of the target molecule from the MIP system is essential for a quick recovery and recyclability of the polymer.

Since molecularly imprinted polymers are produced by molding them around the targeted template molecule, they become highly selective. This selectivity has gained much attention for separation techniques and purification systems, especially in water purification [5.9.]. In the past decades, water security became a global issue, especially in developing countries where the lack of clean water supplies affects their health and lives. Polluted water sources take their toll on humanity, wildlife, and the environment while presenting new global challenges like Pharmaceuticals Emerging Contaminants (PECs). PECs can origin in agricultural activities like poultry and cattle farming [5.10.-5.13], where the excessive usage of antibiotics and other drugs find their way into freshwater sources, such as rivers, lakes, and underground water sources [5.14, 5.15.]. Even though those pollutants usually occur in concentrations below ppm levels, the available amounts are high enough to develop catastrophic problems, including Antimicrobial Resistance (AMR). As per the definition of the World Health Organization (WHO), "Antimicrobial resistance (AMR) is the ability of a microorganism (like bacteria, viruses, and some parasites) to stop an antimicrobial (such as antibiotics, antivirals, and antimalarials) from working against it. As a result, standard treatments become ineffective, infections persist and may spread to others." [5.16.]. The WHO made it one of their top priorities to tackle the global problem of developing AMRs [5.16.-5.20], as such low concentrations are difficult to detect with conventional analytical methods such as spectrophotometry. [5.17.], mass spectrometry [5.18.], liquid chromatography [5.19.], solid-phase extraction[5.20.], capillary electrophoresis [5.21.], and electrochemical techniques [5.22.]. All those methods have the disadvantages of being time-consuming, expensive, laborious, and requiring experienced/skillful analysts. Moreover, few methods are currently available for the selective removal of PECs from water and food produce [5.23.-5.25]. It is essential to develop methods for the detection of antibiotic pollution below the ppb level that are selective, reproducible, cost-effective, and have a quick recovery time. Wei et al. developed a magnetic mesoporous polymer that was imprinted with two different template molecules (florfenicol and chloramphenicol) and showed binding capacities of 190.1 mg/g and 146.5 mg/g, respectively.

A recently developed molecular imprinting technique for the detection and removal of PECs, including antibiotic pollutants, was developed by Sari et al., where the synthesized MIPs showed quick and highly selective binding of the imprinted target molecules, have a long shelf life, and are economical to prepare when compared with antibodies and natural receptors [5.26.-5.29]. Most MIPs reported in the literature are based on the synthesis of bulk polymers and usually show a low surface area for active sites and, therefore, a low binding capacity [5.30., 5.31.]. The synthesis of nano and micro-sized MIPs presents a solution to this problem by enhancing the surface area, fast binding kinetics, binding capacity, and stability [5.32, 5.33.].

However, one of the biggest disadvantages of micron-sized MIPs is the inefficient recovery rate. The recovery of MIPs by centrifugation or filtration usually results either in a significant loss of materials or is time-consuming and laborious. The addition of magnetic nanoparticles (e.g., iron oxide, Fe_3O_4) into the polymeric structure can help to overcome the issue of MIP recovery from media, as the application of a magnetic field will induce immediate magnetic separation.

Magnetic iron oxide nanoparticles (MNPs) have been functionalized for separation, isolation, and purification of proteins, and showed various promising features, such as a rapid recovery rate and recyclability. The combination of MNPs and MIPs allows to utilize the high selectivity of the polymer with the fast recovery rate of the nanoparticles during magnetic separation. Despite such advantages, few published pieces of research on the development of MMIPs for antibiotic detection were found [5.34-5.36]. Solid-phase extraction of fluoroquinolone antibiotics (ciprofloxacin, lomefloxacin, enoxacin, and norfloxacin), presented by Tong et al., who used magnetic imprinted polymers made of the functional monomer acrylic acid, N, N′-methylene bis(acrylamide) as a crosslinker, and a Fe_3O_4/SiO_2 core. In combination with an HPLC, the detection limits measured from 4.1 to 21.3 µg/L (ppb) [5.34]. Chen et al. prepared a monomer matrix of styrene and divinylbenzene with MAA as the functional monomer and used the MIPs for the separation of the antibiotic tetracycline contamination from egg and tissue samples [5. 35]. After a combination with an LC-MS system, the detection limit was found to be < 0.2 ng/g (ppb) [5. 36]. Table 5. 1 shows a comparison of MIPs that have been combined with other materials to utilize the high selectivity and sensitivity for the extraction of analytes from real-world samples, such as milk, blood, tap water, fish, and eggs.

Table 5. 1: Comparison of reported methods with our proposed method [5.36.].

Analyte	Forms of matrices	Binding capacity (mg/g)	Imprinting factor (MIP/MNIP)	Magnetic (Yes/No)	Real sample	Ref.
Ampicillin	MIP microspheres on silica	13.5	3.2	N	Milk, Blood	[5.37.]
Cephalexin	MIP with magnetic yeast composite	36.9	2.5	Y	Tap water, Milk	[5.38.]
Cephalexin	Not reported	3.6	3.0	N	Milk	[5.39.]
Cephalexin	polymer shell with iron particle core	11.0	2.0	Y	Marine sediments, Sea water	[5.40.]
Chloramphenicol	Magnetic mesoporous dual template MIP	146.5	2.9	Y	Blood, Egg	[5.41.]
Enrofloxacin	Hollow MIP with $K_2Ti_4O_9$ component	2.4	2.3	Y	Fish	[5.42.]
Erythromycin	Magnetic molecularly imprinted microspheres	38.4	1.6	Y	Not reported	[5.43.]
Florfenicol	Magnetic mesoporous dual template MIP	190.1	4.3	Y	Blood, Egg	[5.39.]
Ofloxacin	Spherical MIPs	80.7	1.9	N	Not reported	[5.44.]
Tulathromycin	MIP microspheres	54.1	2.4	N	Pork	[5.44.]
Erythromycin	Porous MIP network with magnetic Fe_3O_4 component	70.0	5.5	Y	Milk	Present work *[5.36.]*
Ciprofloxacin	Porous MIP network with magnetic Fe_3O_4 component	32.0	4.3	T	Milk	Present work *[5.36.]*

This chapter focuses on the selective binding of antibiotics using magnetic molecular imprinted polymer networks and spheres (MMIPs) prepared from vinyl-functionalized magnetic nanoparticles. MMIPs are prepared using a microemulsion technique to selectively bind the model antibiotics erythromycin (ERY) and ciprofloxacin (CPX). The magnetic MIPs structures showed high selectivity for the chosen template molecules, which was further proven by additional cross-binding experiments.

5.2. Experimental

5.2.1. Materials

Ethylene glycol dimethacrylate (EGDMA, 98 %), 2-hydroxyethyl methacrylate (HEMA, 98 %), methacrylic acid (MAA, 99 %), erythromycin (ERY, BioReagent), polyvinyl alcohol (PVA, Mw = 13,000-23,000, 87-89 % hydrolyzed), sodium dodecyl sulfate (SDS, 99 %), ammonium persulfate ($(NH_4)_2S_2O_8$, 98 %), and sodium hydrogen sulfite ($NaHSO_3$, ACS reagent), ciprofloxacin (CPX), tetracycline, kanamycin sulfate, and neomycin sulfate were all purchased from Sigma-Aldrich, UK. 3-Butenyltriethoxysilane (vinyl silane, 95 %) was supplied by Fluorochem UK, while Alfa Aesar supplied magnetite Fe_3O_4 nanoparticles (20-30 nm). The solvents methylated spirit (industrial 74 O.P.), toluene (reagent grade), and methanol (lab reagent grade) were purchased from Fisher Scientific UK Ltd. Toluene was dried by mixing the solvent with activated molecular sieves (type 4A, general-purpose grade, Fisher Scientific UK Ltd.) in a closed container for 24 h. All other chemicals were used as received without further purification. All water used was deionized water. All binding and cross-binding measurements were performed in triplicate, and the standard deviations were calculated and plotted in graphs as error bars.

5.2.2. Synthesis of a magnetic molecular imprinted polymer network (MMIP)

Surface functionalization of Fe₃O₄ magnetic nanoparticles with vinyl silane

Vinyl silane (3-butenyltriethoxysilane) coated magnetic nanoparticles (vinyl-MNPs) were prepared using a polymerization method published by Yiu et al. [5.45.]. In a typical experiment, Fe_3O_4 nanoparticles (1 g) were suspended in dry toluene (125 mL) using an ultrasonic bath. 3-Butenyltriethoxysilane (1.0 mL) was then added to the Fe_3O_4 nanoparticle suspension; this reaction mixture was heated to reflux (110°C) under mechanical stirring at 300 rpm (IKA overhead stirrer). After 24 h, the solid was recovered

using a rare earth NdFeB magnet and washed with acetone at least ten times to remove residual toluene and unreacted vinyl silane. The vinyl-MNPs were then dried under vacuum at 80ºC. A general scheme of the synthetic method is described in Figure 5. 2.
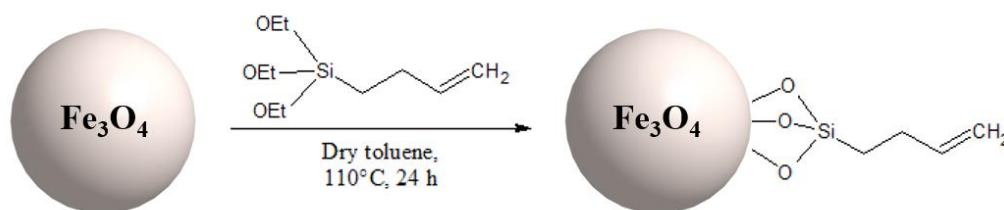
Figure 5. 2: Silanization of iron oxide (Fe₃O₄) using 3-Butenyltriethoxysilane (vinyl silane; -VS).

Synthesis of magnetic erythromycin (ERY) imprinted polymers (ERY-MMIPs)

MMIP samples with an ERY template and embedded magnetic Fe_3O_4-VS nanoparticles were synthesized using a two-phase microemulsion polymerization method [5.45., 5.46]. The polymer network enclosed the vinyl-MNPs by co-polymerizing the two monomers MAA and HEMA (Figure 5. 3). EGDMA was added as an additional crosslinker for a more rigid polymer structure.
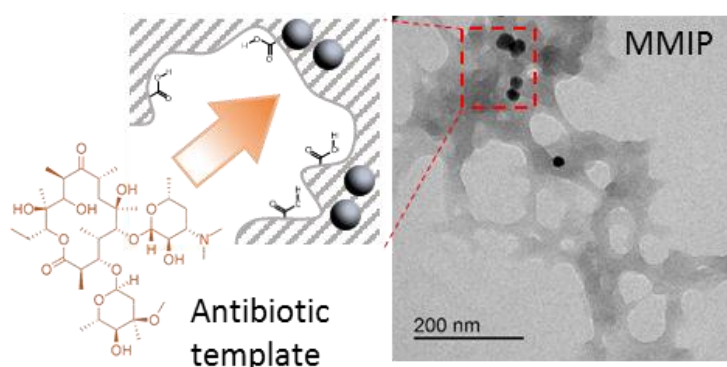
Figure 5. 3.: Illustration to highlight the binding sites of the antibiotic template (ERY) and the polymer network (left). Magnetic molecular imprinted polymer network (MMIP) showing vinylsilane coated magnetic Fe₃O₄ nanoparticles embedded into the polymer network (black dots) (right).

Three solutions were prepared to synthesize ERY-MMIP, two aqueous solutions, and one organic phase. The first aqueous solution was prepared by dissolving polyvinyl alcohol (PVA, 94 mg), sodium dodecyl sulfate (SDS, 14 mg), and sodium bicarbonate (12 mg) in 5 mL of deionized water. The second aqueous phase consisted of PVA (50 mg) and SDS (100 mg) in 100 mL deionized water. The organic phase was prepared by mixing the co-monomers methacrylic acid (MAA, 2.17 mmol) and (hydroxyethyl) methacrylate (HEMA, 1.85 mmol) with the crosslinker ethylene glycol dimethacrylate (EGDMA, 5.56 mmol) and 50 mg of vinyl-MNPs. The template molecule erythromycin (136 µmol) was added to the organic phase to establish a ratio between the monomers MAA and HEMA and the template in a 16:13.6:1 (MAA:HEMA:ERY) mole ratio. The organic phase was then mixed with the first aqueous phase and homogenized using an ISOLAB homogenizer at 30,000 rpm (Laborgeräte GmbH). The resultant microemulsion was then added to the second aqueous phase while stirring at 600 rpm using a mechanical stirrer (IKA Eurostar 20 digital). The final mixture was slowly heated to the polymerization temperature of 40°C. When the polymerization temperature was reached, sodium bisulfite (125 mg) and ammonium persulfate (125 mg) was added to initiate the polymerization process. After 24 h, the polymerized sample was recovered using a magnet, and the magnetic solid was denoted as ERY-MMIP. The collected ERY-MMIP emulsion was washed five times with a 50 % v/v ethanol in water solution and then three times with deionized water. The ERY-MMIP sample was then dispersed in deionized water and stored at 4°C. The synthetic pathway of (a) ERY imprinted MMIPs and (b) CPX imprinted MMIPs can be seen in Figure 5. 4.
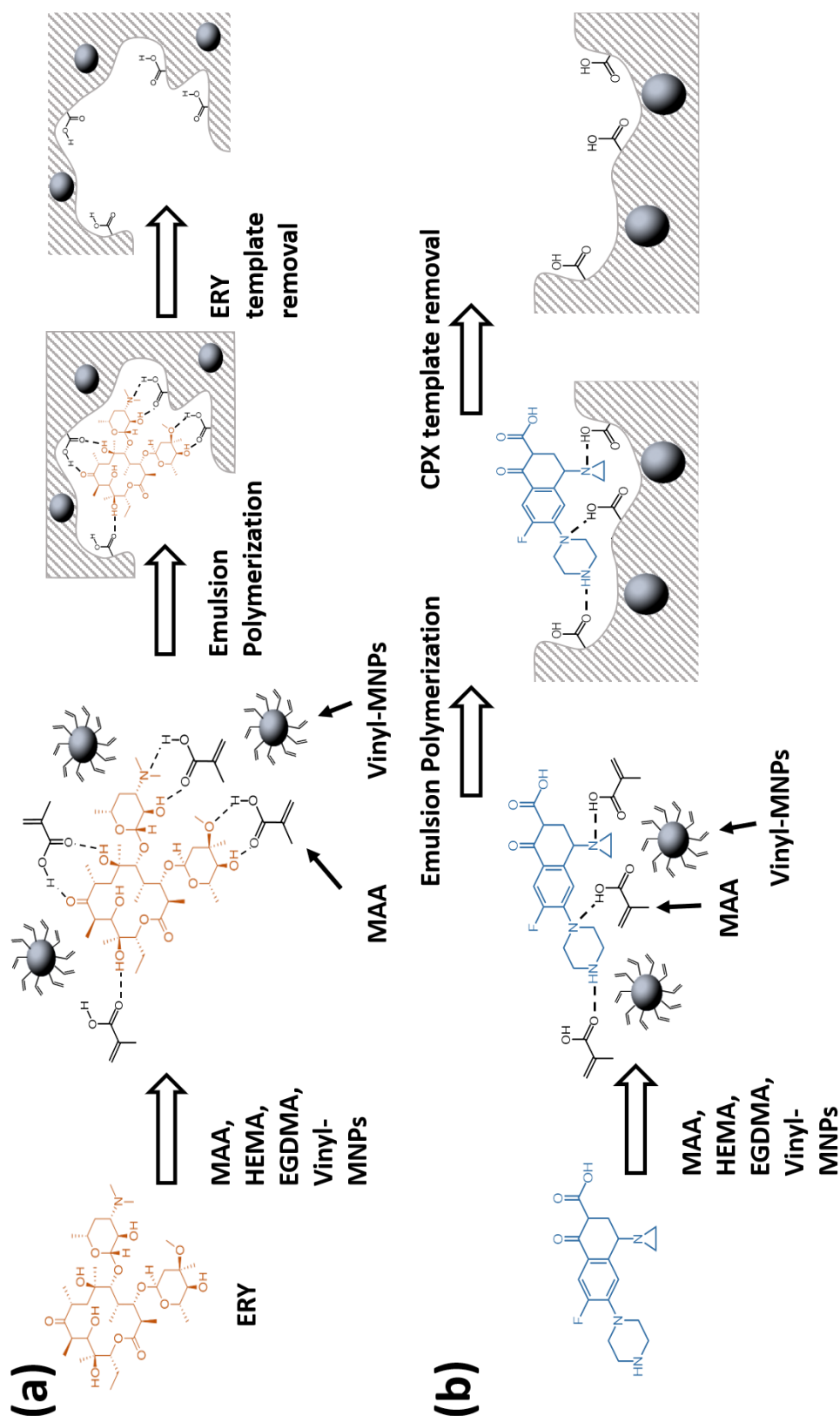
Figure 5. 4: An illustration for the formation of (a) ERY-MMIPs and (b) CPX-MMIPs. Displayed are the steps of mixing the template molecule with the co-monomers, cross-linkers, and nanoparticles (step 1), emulsion polymerization (step 2), and the template removal (step 3).

Synthesis of magnetic ciprofloxacin (CPX) imprinted (CPX-MMIP) and non-imprinted polymers (MNIP)

Magnetic CPX imprinted polymer networks (CPX-MMIPs) were synthesized using the ERY-MMIP method above. However, the erythromycin template was replaced by a mixture of ciprofloxacin (33.13 mg, 100 µmol) and the functional monomer MAA (260 mg, 255 µL, 3 mmol), allowing a molar ratio of 1:30 (CPX:MAA).

Non-imprinted magnetic polymers (MNIP) were prepared following the same procedure except for voiding the antibiotic template.

5.2.3. Synthesis of spherical magnetic molecular imprinted polymers (MMIP spheres)

MMIP spheres were synthesized following the same ERY-MMIP protocol as described above, with the only difference of using a TissueRuptor II homogenizer from Qiagen at a reduced homogenization speed of 25,000 rpm. Changing the homogenizer speed resulted in the formation of spherical polymer particles rather than a polymer network.

Characterization of magnetic molecularly imprinted polymers (MMIPs)

A Bruker Fourier transform infrared spectrometer (Vertex 70v) in the range of 500–4000 cm^{-1} with a 2 cm^{-1} resolution was used to identify a successful silanization of vinyl-MNPs and define the polymer components of MMIPs, MNIPs, and MMIP spheres. TEM images of the spheres and the polymer network were taken on a Tecnai T20 (FEI) operating at 120 kV (Kelvin Nanocharacterization Centre, University of Glasgow, UK) to examine the structure of MMIPs and MNIPs. Thermogravimetric analysis (TGA) was performed using a Thermobalance Q500 system (TA Instruments), where the resulting weight loss profile was used to determine the organic content in the magnetic polymer network and spheres. In a typical experiment, a heating rate of 10°C/min was used to heat a sample to a final temperature of 800°C. The temperature was held isothermal for 60 minutes at 800°C and finally cooled down to room temperature. The mean particle size and size distribution were measured by Dynamic Light Scattering (DLS) using a Mastersizer 2000 system (Malvern Panalytical Ltd.). The polymers were dispersed in water at a concentration of 10 mg/300 mL and measured under a beam length of 2.35 mm.

5.3. Antibiotic binding tests

5.3.1. Determination of binding capacity

The binding capacity of MMIP and MNIP on ERY and CPX was studied by analyzing a range of concentrations, ranging from 8 to 100 mg/mL of the template/target molecules (ERY and CPX) in a 4:1 methanol to water solution. The absorbance values (A_i) for ERY and CPX at 280 nm and 275 nm respectively were first measured using a Cary 100 Bio UV-Vis Spectrophotometer (Agilent) before incubating the solution (3 mL) with 28.8 mg of the corresponding MMIP sample for two hours. The MMIP and MNIP samples were then removed using a magnet, and the absorbance values of the supernatants (A_f) were measured again at 280 nm and 275 nm. Concentration values (C_i and C_f) were derived from the calibration curve. The binding capacity (Q) values were then calculated from the equation [5. 36].

$$Q = (C_i - C_f)\frac{V}{m}$$

where Q is the Binding Capacity (in mg/g of MMIP), C_i and C_f are the initial and final concentration of the template molecule (in mg/mL), V is the volume of the incubated solution (in mL), and m is the mass of the MMIP used (in g).

5.3.2. Time studies (binding kinetics) and recycling

A time study was set out to determine the minimum time for a maximum adsorption capacity of ERY and CPX by the MMIP samples. The lowest concentrations with the highest binding capacities for ERY-MMIP and CPX-MMIPs were measured at 40 mg/mL and 10 mg/mL. For each MMIP sample, the minimum concentration value for maximum binding capacity was chosen, i.e., 40 mg/mL for ERY-MMIP and 10 mg/mL for CPX-MMIP. A similar measurement procedure to binding capacity measurement was carried out by recording the initial absorbance (A_i), before adding the corresponding MMIP samples. The absorbance values of the supernatant were then measured again after removing the MMIPs, using a magnet at time intervals of 10, 20, 40, 60, 90, 120, 150, 180 min (A_f). Concentrations (C_i and C_f) and Q values were calculated, as mentioned previously. A recycling experiment was performed to test the reusability of the imprinted magnetic nanoparticles in an ERY solution with a concentration of 40 mg/mL. A NdFeB magnet was used to recover the MMIP networks after each cycle. Four cycles in total were performed for both ERY-MMIP and CPX-MMIP samples.

5.3.3. Selectivity tests in methanol/water media and milk matrices

The selective binding capacity of MMIP was tested in the presence of three other competing antibiotics (tetracycline, kanamycin sulfate, and neomycin sulfate). Each antibiotic was used at a concentration of 40 mg/mL, using the derived concentration from the antibiotic template that established an optimal binding capacity and incubation time in the previous time studies. The selectivity studies were performed with the optimized concentration of ERY (40 mg/mL) and CPX (10 mg/mL). A selectivity test using ERY-MMIPs comprised of two different solutions, methanol/water (4:1 v/v mixture) and skimmed milk. Each test solution contained 40 mg/mL of the antibiotics and was stirred for 40 min after the addition of ERY-MMIPs. Before the incubation period, the absorbance values (A_i) of each emulsion for the specific wavelengths of neomycin sulfate (304 nm), tetracycline (365 nm), kanamycin sulfate (527 nm), and ERY (280 nm) were determined from a full UV analysis. After incubation and extraction of the MMIPs from the binding samples, the absorbance values (A_f) of the supernatants were measured again to detect any differences. The binding capacities (Q) were established by using the same method, as stated previously. All experiments were repeated in triplicate. Selectivity tests using CPX-MMIP were performed in the same manner as the ERY-MMIP studies, but with a concentration of 10 mg/mL for each antibiotic (ciprofloxacin, tetracycline, kanamycin sulfate, and neomycin sulfate) and an incubation time of 60 minutes. The absorbance value of ciprofloxacin (A_i) was analyzed at 275 nm.

Due to the similar wavelength of absorbance between ERY and CPX (280 nm vs. 275 nm), a separate set of cross-binding experiments was set out to assess the selectivity towards the other template. In this experiment, only the other antibiotic template was dissolved in solution at the concentration achieving the binding capacity for the MMIP sample. For instance, in an experiment using ERY-MMIP to bind CPX, 28.8 mg of ERY-MMIP sample was suspended in methanol/water or milk matrix at a concentration of 40 mg/mL of CPX. The absorbance of CPX was measured at 275 nm before and after the 40-minute incubation. The data were treated, as mentioned previously. The binding of ERY by CPX-MMIPs was carried out with the same protocol, but at a wavelength of 280 nm.

5.4. Results and Discussion

5.4.1. Characterization of vinyl-MNPs

Iron oxide nanoparticles (Fe_3O_4) were functionalized with 3-butenyltriethoxysilane to attach a vinyl group to the surface of the particles (vinyl-MNPs) using silanization. The vinyl group shall create a chemical bond between the polymer network and the particle. A successful silanization was identified by analyzing vinyl-MNPs by Fourier Transform Infrared Spectroscopy (FTIR). The FTIR spectrum of vinyl-functionalized Fe_3O_4 (Figure 5. 3), shows peaks at 550 cm^{-1}, 1400 cm^{-1}, 2950 cm^{-1} and 3020 cm^{-1}. The peak at 550 cm^{-1} represents a Si-O bond, while the peaks at 2950 cm^{-1} and 3020 cm^{-1} are allocated to -CH groups, and the bond at 1400 cm^{-1} is due to a vinyl (C=C) bond. All four peaks confirm the presence of 3-butenyltriethoxysilane and, therefore a successful silanization.
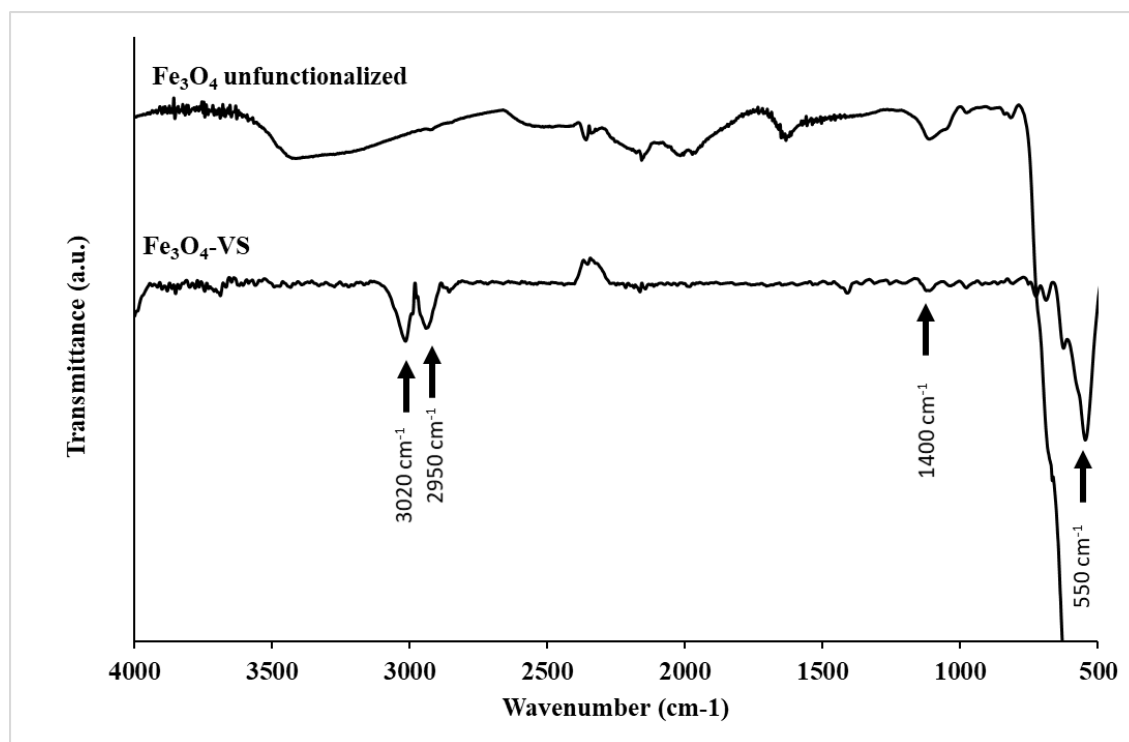
Figure 5. 3: FTIR spectra of magnified unfunctionalized Fe_3O_4 and vinylsilane functionalized Fe_3O_4, showing peaks at 550 cm^{-1}, 1400 cm^{-1}, 2950 cm^{-1}, and 3020 cm^{-1}, which can be allocated to the vinyl (C=C)group and the Si-O bond of 3-butenyltriethoxilane that has been bound to the surface of the particles. There is no transmittance recorded below 800 nm for the unfunctionalized iron oxide samples due to the lack of organic groups on the inorganic surface.

Both samples were analyzed by thermogravimetric analysis (TGA) to quantify the iron content and amount of organic matter (3-butenyltriethoxysilane) on the surface of the particles.   A typical thermogravimetric profile of molecularly imprinted polymers consisted of two significant steps: the loss of residual solvents between 50 to 200ºC and the loss of organic matter on the MNP surface between 250-450ºC. The TGA weight loss profile of unfunctionalized Fe_3O_4 nanoparticles in Figure 5. 4 shows a notable increase in weight percentage between 140 and 350ºC; this is the result of Fe_3O_4 being oxidized to γ-Fe_2O_3. The weight-loss profile of vinyl-MNPs shows an additional difference of 1.7 % in weight between 250-450ºC compared to the unfunctionalized Fe_3O_4 sample. The weight loss profile of vinyl-MNPs confirms the presence of added organic matter (3-butenyltrietoxysilane) and, therefore a successful silanization.
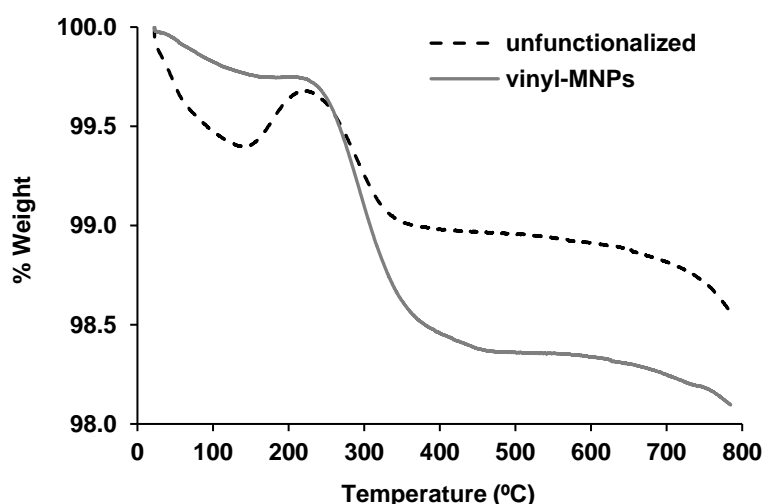
Figure 5. 4: TGA- weight loss profile of unfunctionalized and vinylsilane functionalized Fe₃O₄ nanoparticles. The additional weight loss of 1.7 % in weight between 250ºC and 450ºC of vinyl-MNPs compared to the unfunctionalized sample suggested a successful silanization.

5.4.2. Characterization of MMIP networks

The chemical structures of imprinted (MMIP) and non-imprinted (MNIP) network samples were analyzed using FTIR spectroscopy. The spectra of the MMIP and MNIP networks, shown in Figure 5. 5, are almost identical as they are both PMAA-based materials. The characteristic bands in the spectra were found at 2950 cm^{-1}, 1720 cm^{-1}, 1250 cm^{-1} and 1150 cm^{-1}. Broad bands at 3100 - 3500 cm^{-1} are typically due to –OH groups from both MAA and HEMA units. The peaks at around 3020 cm^{-1} and 2950 cm^{-1} were attributed to –CH groups. Carbonyl (–C=O) bands were shown at 1720 cm$^{-1,}$ while bands at 1450 and 1380 cm^{-1} were due to –CH$_3$ and –CH$_2$– groups. The -C-O- single bond around 1250 cm^{-1} was assigned to the carboxyl group (-COO$^-$) of MAA and HEMA, while the -C-O- bands around 1130 cm^{-1} refer to the ester group of EGDMA. Bands at 1635 cm^{-1} were attributed to the C=C bonds from residual monomers. Adsorption peaks at around 550 cm^{-1} were due to Fe$_3$O$_4$ particles. The results suggested that all four samples have a PMAA-HEMA backbone with EDGMA crosslinking units.
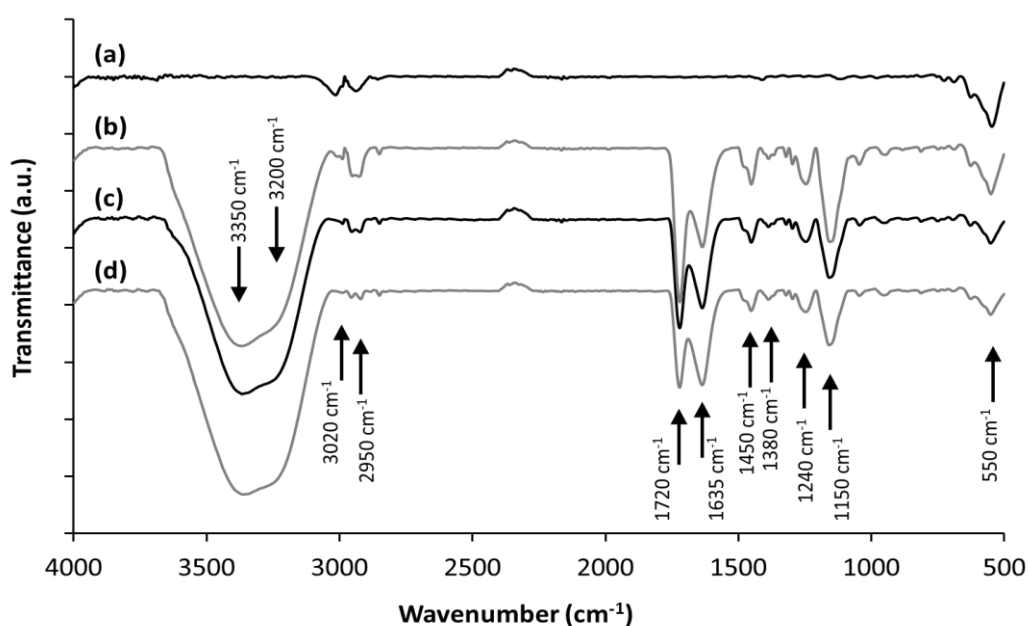
Figure 5. 5: FTIR spectra of (a) vinyl-MNPs, (b) erythromycin imprinted MMIPs (ERY-MMIPs), (c) ciprofloxacin imprinted MMIPs (CPX-MMIPs), and (d) non-imprinted MMIPs (MNIPs).

The morphology of the ERY-MIP and CPX-MIP network samples were examined using transmission electron microscopy (TEM). In both cases, the TEM images show the structure of a porous network and the embedded magnetic nanoparticles (Figure 5. 6, a and Figure 5. 6, b). The nanoparticles show a constant average diameter of 20-30 nm, whereas the polymer networks show pore sizes between 10 and 100 nm. The high porosity and network structure are regulated by the speed at which the emulsion is homogenized. The higher the porosity of a network or sphere is, the higher is the surface area that can potentially bind antibiotics and other template molecules. It also allows for a higher drug diffusion throughout the network towards more recognition sites. The non-imprinted sample (MNIP, Figure 5. 6, c) showed a similar structure, suggesting that the addition of a template molecule did not alter the porous morphology of the polymer.
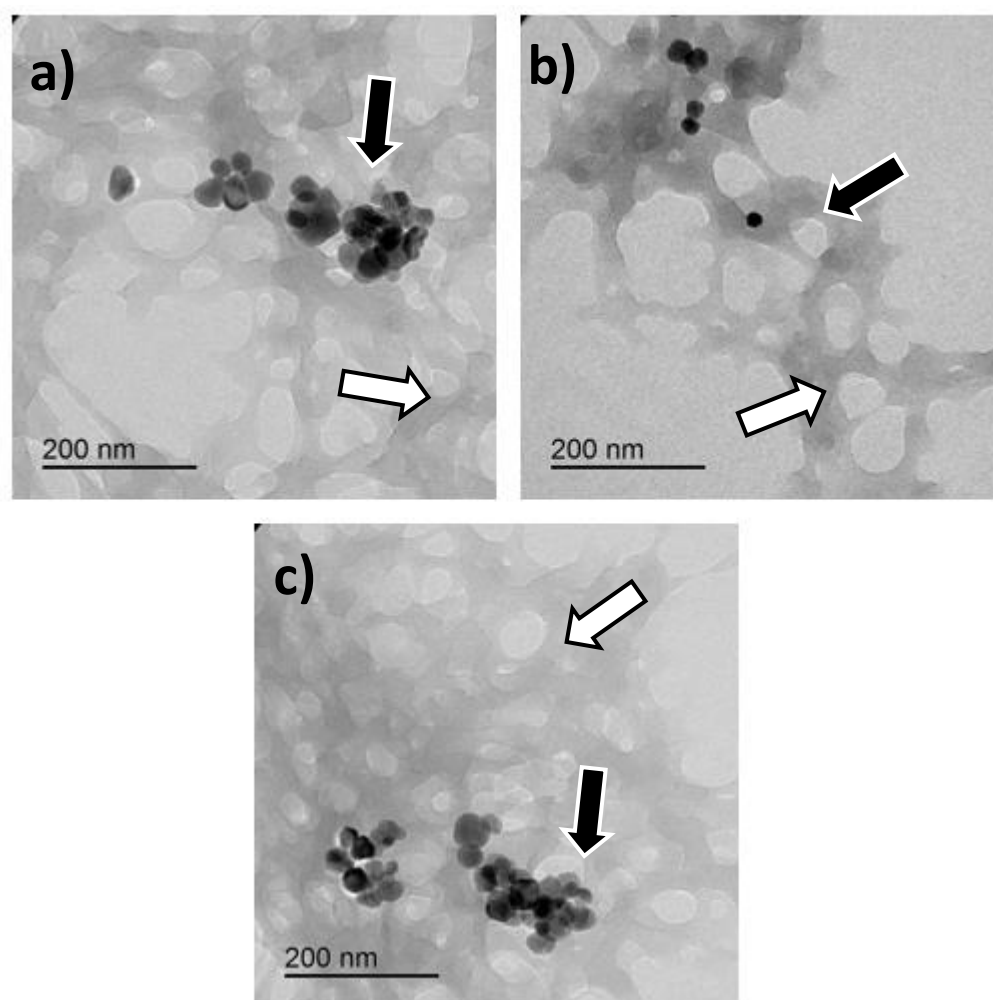
Figure 5. 6: TEM images of a) ERY-MMIP, b) CPX-MMIP, and c) MNIP, showing the morphology of the porous polymer network (white arrows) with fully engulfed Fe$_3$O$_4$ nanoparticles (black arrows).

The thermographic profiles of ERY-MMIP, CPX-MMIP, and MNIP samples can be seen in Figure 5. 7 and show a very similar TGA weight loss profile. Most of the weight loss was recorded between 250 and 450°C and is caused by the combustion of the PMAA polymer. The remaining weight percentages are due to Fe_2O_3 residuals from oxidized Fe_3O_4. The ERY-MMIP and CPX-MMIP samples showed a total remaining Fe_3O_4 content of 16 % and 21 %. The non-imprinted MNIP sample showed a similar weight loss profile, with a final residual weight of 14 %. Applying a magnetic field to these amounts of magnetic nanoparticles can be used to separate the polymer from matrices at a high recovery rate and recycle them for further use.
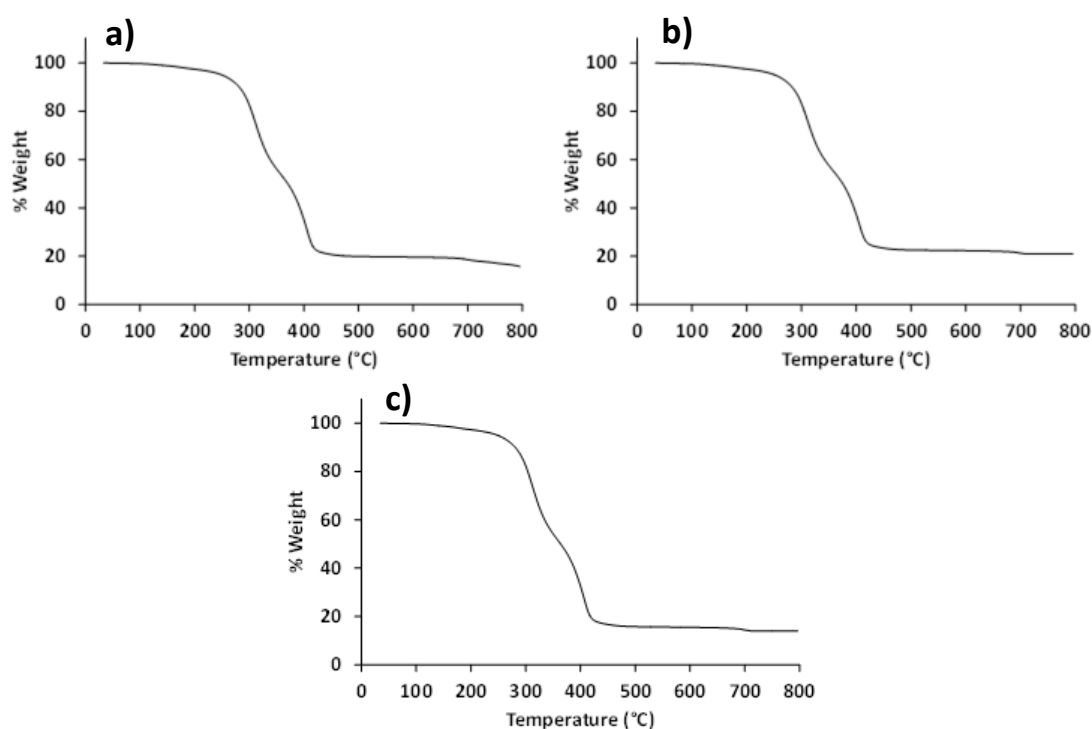
Figure 5. 7: TGA weight loss profiles of a) ERY-MMIP, b) CPX-MMIP, and c) MNIP showing residual weights of 16 %, 21 %, and 14 %, respectively. The residual weight is caused by residual Fe_2O_3 from the oxidized magnetic Fe_3O_4 component.

The average hydrodynamic size and size distribution of ERY-MMIP, CPX-MMIP, and MNIP samples were analyzed using dynamic light scattering (DLS). The results are shown in Figure 5. 8 and highlight the differences between the imprinted and non-imprinted polymer samples. Both imprinted samples (ERY and CPX) showed an average hydrodynamic size of around 33 µm, whereas the non-imprinted polymer network showed a broader size distribution and an average particle size of 105 µm. This could be due to the polymer network polymerizing without a template molecule and the altered steric hindrance of the missing template allowing a broader size distribution. This can also be seen when comparing the peak sharpness of the imprinted and non-imprinted networks. The imprinted polymers show sharper peaks and have a definite maximum, whereas the non-imprinted polymer sample has a broader size distribution and a less defined hydrodynamic particle size. Additionally, non-imprinted networks tend to have larger hydrodynamic particle sizes. However, it is also noticeable that the size distribution of ERY-MMIP peaks again at around 330 µm, indicating the additional synthesis of bulk material within the polymerization process.
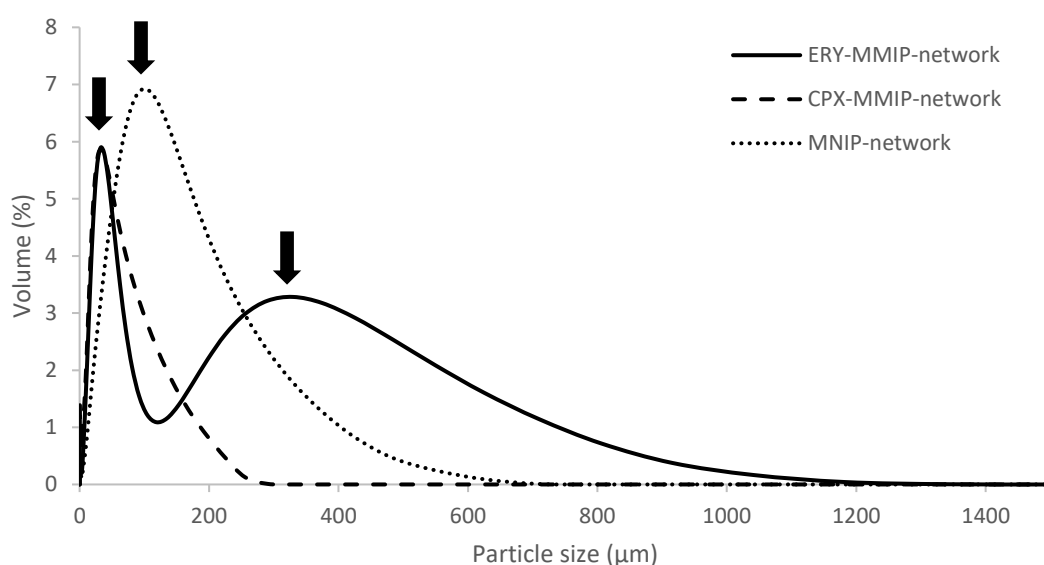
Figure 5. 8: DLS spectra of ERY-MMIP, CPX-MMIP, and MNIP network samples, indicating mean hydrodynamic particle sizes of 33 µm, 33.1 µm, and 105 µm, respectively. Both imprinted samples showed a similar hydrodynamic particle size, whereas the non-imprinted polymer had a significantly larger hydrodynamic particle size with a broader particle distribution. The second peak at 330 µm of the ERY-MMIP sample indicates the additional synthesis of bulk material within the polymerization process.

5.4.3. *Binding capacity and recycling of MMIP samples*

The binding capacities of ERY and CPX imprinted MMIP samples for their respective target molecule was determined by binding experiments with concentrations ranging from 8 mg/mL to 100 mg/mL. The experiments were repeated in triplicates and a 95% confidence interval for data analysis (p-value < 0.05) was used to establish statistically significant results. The maximum binding capacities were found to be 70 mg/g for ERY-MMIPs (Figure 5. 9, a) and 32 mg/g for CPX-MMIPs (Figure 5. 9, b). While CPX-MMIPs reached their maximum adsorption at the lowest concentration of 10 mg/mL, the binding capacity of ERY-MMIPs peaked at 40 mg/mL. Performing the same binding experiment with the non-imprinted polymer samples showed a maximum binding capacity of 20 mg/mL for ERY-MNIPs and 10 mg/mL for CPX-MNIPs. Despite the same synthetic method and a similar structure and porosity, MNIPs show only 25 % of the maximum capacities compared to imprinted MIPs. This suggests that the imprinting method is successful, and the functional binding sites have been established on the MMIP network.

How fast the maximum binding capacity was achieved was analyzed by performing time studies with the previously determined optimal template concentrations of 40 mg/mL for ERY-MMIPs and 10 mg/mL for CPX-MMIPs. The established time curves are shown in Figure 5. 9 (c and d) and suggest that both MMIP networks establish their maximum binding capacity saturation after 40 – 60 minutes.
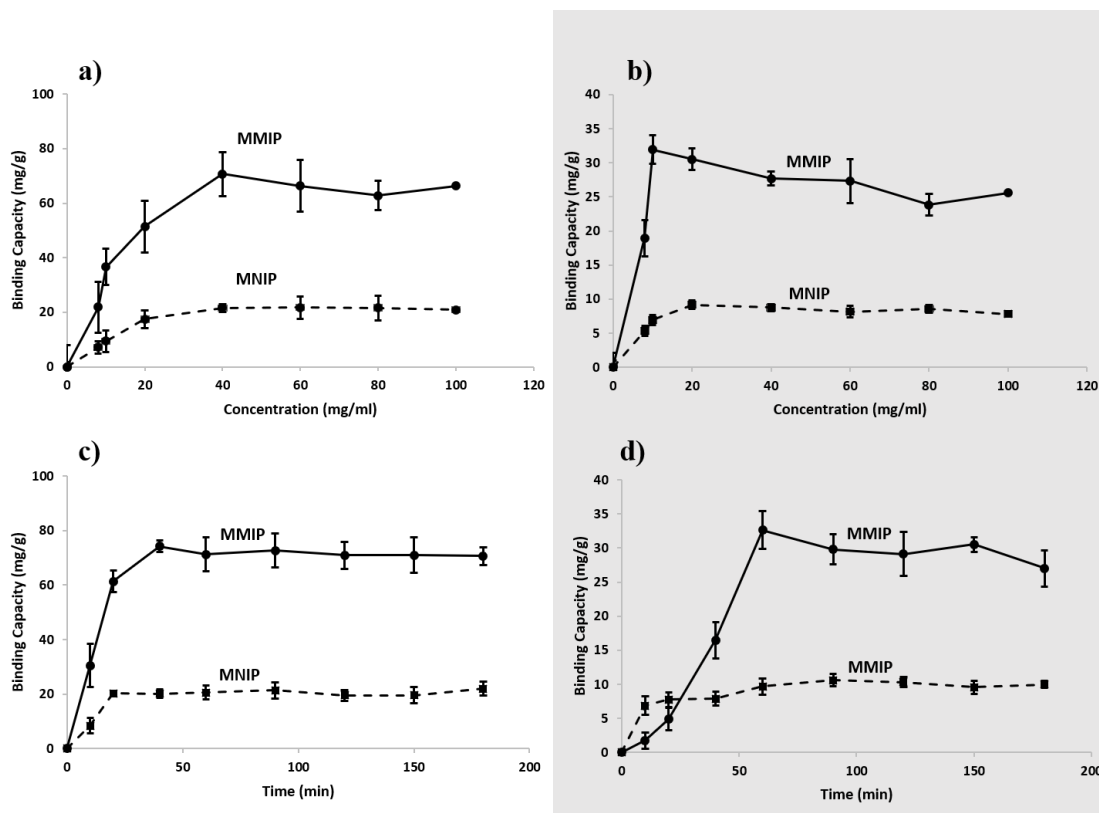
Figure 5. 9: Determination of the maximum binding capacity of (a) ERY-MMIPs and (b) CPX-MMIPs and time studies on how fast the maximum binding capacity was established for (c) ERY-MMIPs and (d) CPX-MMIPs (p<0.05).

Combining magnetic nanoparticles with the imprinted polymer helps to overcome specific disadvantages in joint separation and recycling techniques, such as filtration and centrifugation. Filtration systems generally retain everything of a certain width and could potentially bind the polymer to the filtration mesh itself. This mostly results in either unwanted contaminants or reduced yield, especially when using nano-scaled materials. An additional issue is the application of the right mesh size as bulk polymers can have a broad size distribution. Once a filter is applied, everything below the mesh size cannot be retrieved and therefore counts directly as loss of recyclable material. Centrifugation has the benefit of separating light solids from solids with a higher density. However, since only small batches can be spun down and recovered at a time, this method is time-consuming and laborious. Additionally, the resulting pellet will contain all contaminants from the solution as well, as there is no differentiation between the MIP and other substances and the whole batch will be centrifuged at the same time. The polymer would have to be separated from the contaminants again, adding extra steps to the recycling process. Besides that, general centrifugation can be laborious, extremely time-consuming,

and can only be done in small batches. The magnetic polymer network can quickly be recovered and recycled by applying a simple magnetic field. The reusability of MMIP samples was analyzed by running a series of recycling experiments. Both MMIP networks (ERY and CPX) showed their recycling potential and retained 75 % and 68 % of their binding capacity for their respective template molecules after four cycles (Figure 5. 10). The fact that not 100 % of the polymer could be recovered is related to the strength of the applied magnet and its efficiency when used for magnetic separation, and the regeneration of binding sites within the polymer network after the template (or target) molecule has been removed.
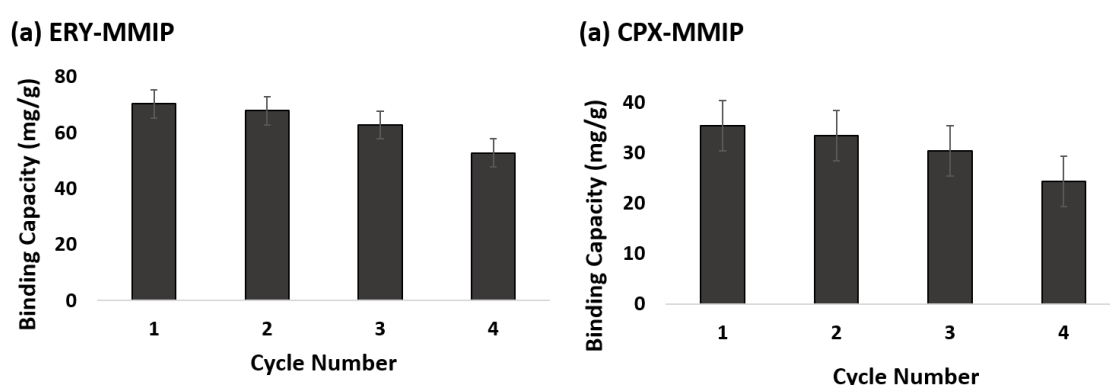
Figure 5. 10: Recycling experiment of (a) ERY-MMIP and (b) CPX-MMIP showing their binding capacity after repeated exposure and extraction of their respective target molecules after four cycles. After each cycle, all MMIP samples were recovered using a NdFeB magnet. This experiment was repeated three times ($p < 0.05$).

5.4.4. Selective binding and cross-binding in methanol-water and milk matrices

Imprinting MIPs with a template molecule can create specific cavities in the polymer structure that precisely identify a molecule by its shape and surface functionalities. This selective recognition is demonstrated in Figure 5. 11, where ERY-MMIPs and CPX-MMIPs were exposed to their imprinted target molecule in the presence of three other competing antibiotics (neomycin sulfate, tetracycline, and kanamycin sulfate) in a methanol/water medium. The ERY- (Figure 5. 11, a) and CPX-imprinted (Figure 5. 11, b) polymer networks show a clear preference towards their imprinted target/template molecules, 4 - 7 times higher than binding capacity towards the competing antibiotics. The non-imprinted polymer samples (MNIPs) did not show any molecular recognition or selectivity towards any of the used antibiotics.

The same experiment was performed three times in milk matrix to test the MMIP selectivity for their template molecules in a more challenging environment. Here, other factors such as proteins and fats could interfere with the selectivity and potentially block those template molecule-specific binding sites. However, results in Figure 5. 11 c and d show that both MMIP networks remained highly selective towards their template (or target) molecule.
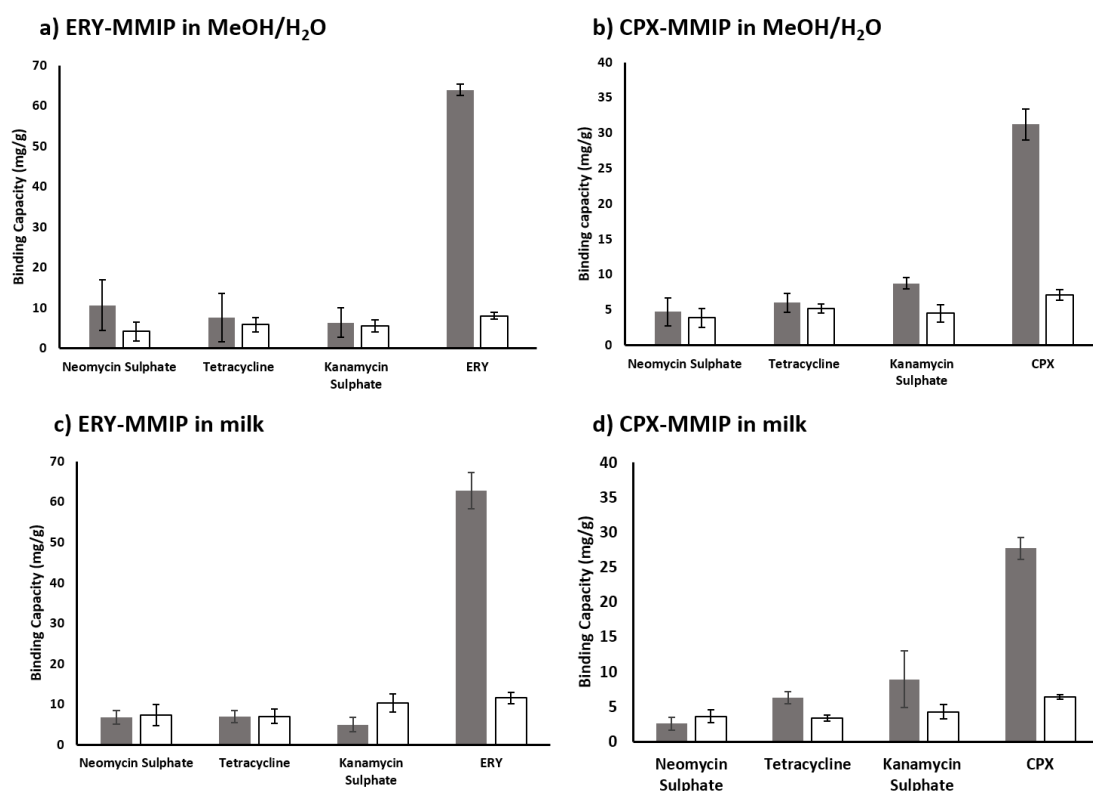
Figure 5. 11: Selectivity of ERY-MMIP and CPX-MMIP for their template molecules in a methanol/water (a, b) and milk matrix (c, d). Both matrices contained the respective template antibiotic molecule (erythromycin and ciprofloxacin) and three other competing antibiotics (neomycin sulfate, tetracycline, and kanamycin sulfate). All graphs show the selectivity of the MMIP (■) and non-imprinted MNIP (□) samples (p<0.05).

These results suggested that both ERY-MMIP and CPX-MMIP networks were indeed imprinted with template-specific binding sites and can be used for highly selective binding and removal of antibiotics from different media. Using milk to test the selectivity in a challenging environment was of significance as one primary source of antibiotic pollution originates in agricultural activities, such as cattle and poultry farming. The exposure of livestock to excessive amounts of antibiotics (e.g., in their feed) leaves traces of residues in their produce, for example, eggs on a poultry farm and meat and milk products on a

cattle farm. Detecting and monitoring traces of antibiotics below the ppb level require sensitive and selective recognition. The selectivity tests of MMIPs showed that pre-concentration of antibiotic residues in various media is possible and could be used in other animal products. This work confirms that using MMIPs for selective detection of antibiotic pollutants helps to enhance their monitoring in farmed animals, safeguarding food security, and, most importantly, tackle the global problem of developing "antimicrobial resistance" (AMR).

A separate experiment was carried out three times to test the cross-binding of ERY-MMIP and CPX-MMIP networks in methanol/water media and milk matrices. The experiment could not be performed simultaneously as the absorbance maximum of ERY (280 nm) would interfere in the UV-vis spectrum with the absorbance maximum of CPX (275 nm). Results of the cross-binding experiment in methanol:water media (Figure 5. 12, a) show that CPX-MMIPs bind ciprofloxacin over 5-fold higher than the competitor template erythromycin. ERY-MMIPs displayer an even higher selectivity with the nearly 8-fold higher binding of erythromycin than ciprofloxacin. Performing the same cross-binding experiment in milk matrices (Figure 5. 12, b) showed similar results, where CPX-MMIPs had a 3-fold selectivity of CPX over ERY and ERY-MMIPs a 9-fold higher binding preference of ERY over CPX. These results further affirmed the selectivity of both ERY-MMIP and CPX-MMIP samples.
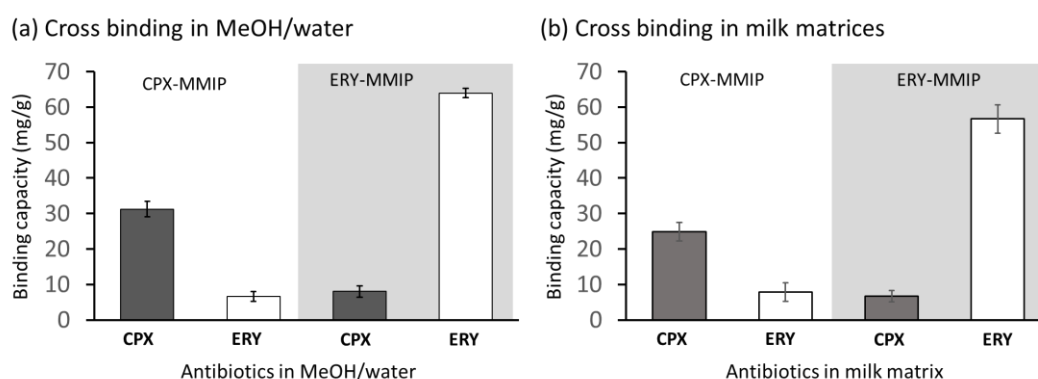
Figure 5. 12: Cross-binding experiments of ERY and CPX imprinted MIP samples to determine their selectivity for their opponents' target molecule (ERY vs. CPX) within (a) methanol/water media and (b) milk matrices. CPX and ERY were measured separately due to overlapping adsorption maxima of ERY (□) (280 nm) and CPX (■) (275 nm) in the UV-vis spectra (p<0.05).

The studies on selectivity and cross-binding showed that both MMIP networks are capable of detecting and binding their imprinted target molecule. Even after repeated removal of the target molecule, they retained their binding capacity. This potential is essential for the effective detection of trace amounts of antibiotics, specifically in challenging environments where other molecules could interfere with the selectivity. Furthermore, those networks allow pre-concentration of antibiotic contaminants from samples and therefore, further enhance downstream detection.

5.4.5. *Characterization of MMIP spheres*

Except for the different homogenization speed of 25,000 rpm, the synthesis of MMIP spheres used the same co-polymerization technique as for the synthesis of the MMIP network. Hence, a similar PMMA based composition was expected. FTIR spectroscopy was used to identify the polymer structure based on MAA, HEMA, and the crosslinker EGDMA. The FTIR spectra of vinyl-MNPs, MIP networks, and MMIP spheres are shown in Figure 5. 13. The spectra of the ERY imprinted polymers show identical bonds for MAA, HEMA, and EGDMA to those of the MMIP networks. The results confirmed that the composition of all spherical MMIP samples is based on the same PMMA-HEMA backbone as the MMIP networks with EGDMA crosslinking units.
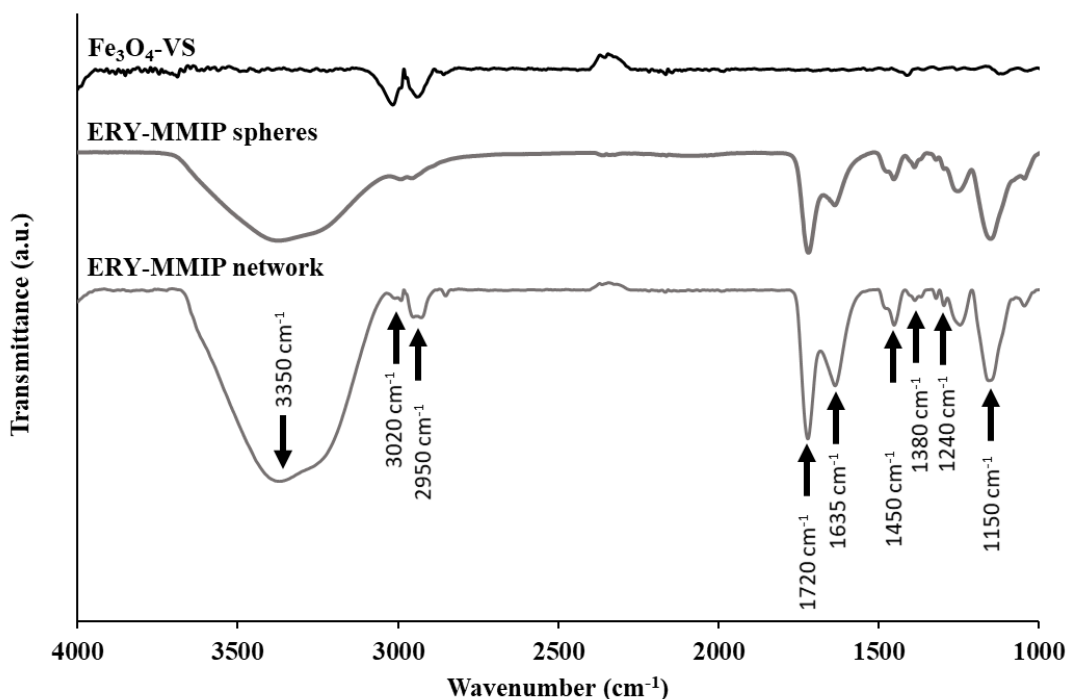
Figure 5. 13: FTIR spectra of vinyl-MNPs and erythromycin imprinted MMIP spheres and networks, showing the individual bonds for the same polymer backbone based on MAA, HEMA, and EGDMA crosslinking units.

The morphology of ERY and CPX imprinted MMIP spheres were examined using transmission electron microscopy (TEM) and showed that the homogenization at 25,000 rpm resulted in spherical MMIPs (*Figure 5. 14*) rather than the previously described MMIP network which was homogenized at 30.000 rpm. The TEM images show vinyl-MNPs with an average particle size of around 20 – 30 nm embedded into the polymer sphere. The spheres showed an average particle size of around $1 \pm 0.3 \mu m$.
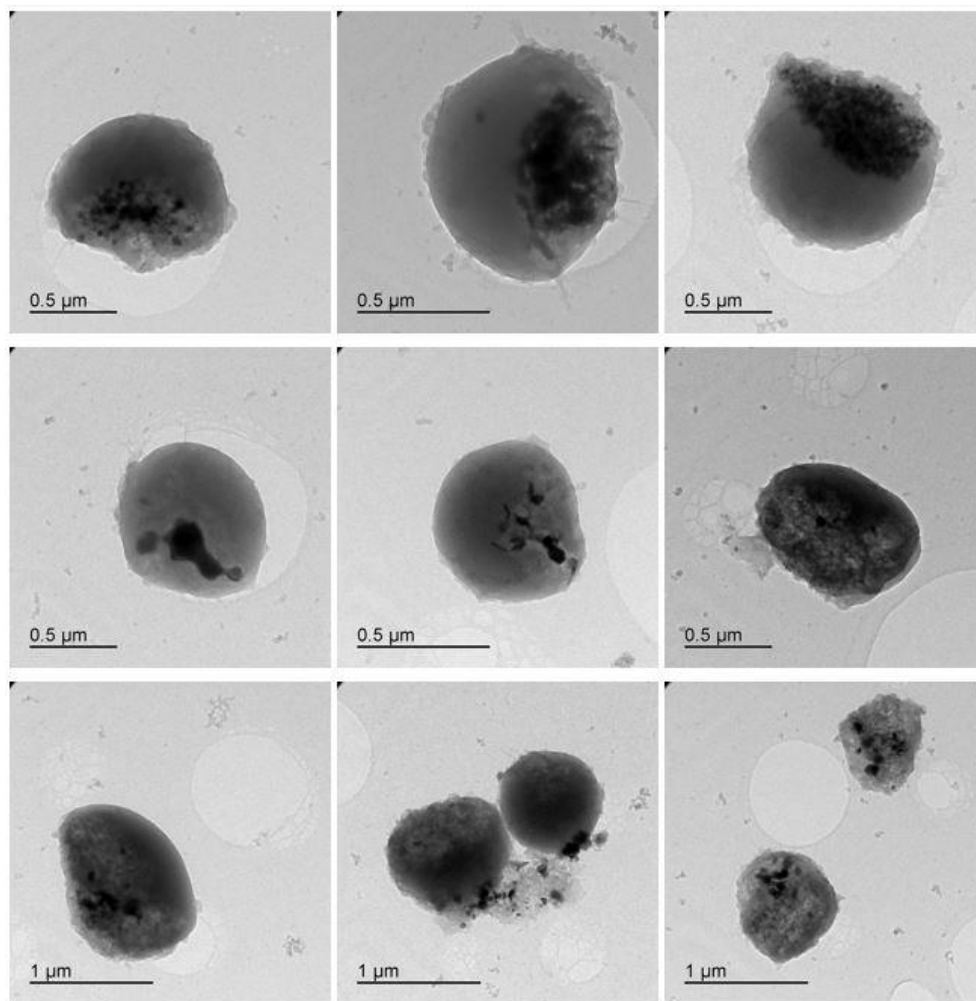
Figure 5. 14*: Display of MMIP spheres, showing the successful embedding of vinylsilane coated magnetic Fe₃O₄ particles (vinyl-MNPs) into the polymeric sphere. The spheres are a direct result of a reduced homogenization speed at 25,000 rpm and have an average particle size of 1 ± 0.3μm*

ERY imprinted MMIP spheres and networks were analyzed using dynamic light scattering (DLS) to determine their average hydrodynamic particle size. The results in Figure 5. 15, show the MMIP samples in the water matrix and present them with hydrodynamic average particle sizes ranging from 35 µm for the MMIP network to 33 µm for the MMIP sphere. This significant difference in particle size compared to dried MMIP samples in the TEM analysis could be due to the limitations of dynamic light scattering when measuring dark materials, such as iron oxides. Dark materials tend to absorb most of the laser beam, which can lead to inconsistent measurements and distorted results. Despite their increased particle size, their size distributions are very similar but have one distinct difference, the distribution of the ERY-MMIP networks peaks again at around 330 µm. This could be due to the network nature of the polymer that is slightly spread than the spherical and compact polymer structure of the ERY-MMIP spheres.
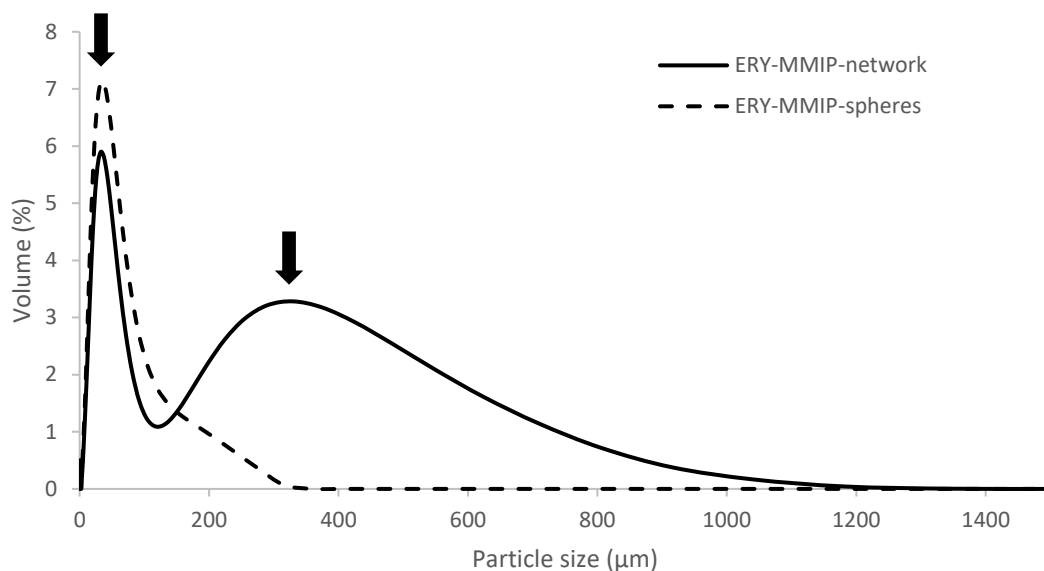
Figure 5. 15: DLS result of ERY MMIP network and spheres with an average particle size of 33 μm and 35 μm, respectively. It is noticeable that the size distribution of the MMIP network samples peaks again at 330 μm, this could be due to the shape and structure of the network being spread, rather than the less porous polymeric sphere.

5.4.6. Antibiotic binding tests

Binding capacity and selectivity of MMIP spheres

The binding capacities of erythromycin imprinted polymeric spheres were determined by performing binding experiments. In these experiments, the same concentrations of 8 – 100 mg/mL were used as previously described in the method for the analysis of the MMIP network. The experiments were repeated in triplicates and a 95% confidence interval for data analysis (p-value < 0.05) was used to establish statistically significant results. The results showed that erythromycin-imprinted and non-imprinted MIP spheres have a maximum binding capacity of 70 mg/g and 40 mg/g, respectively (Figure 5. 16, a). This equals a difference of 55 % and proved that the co-polymerization technique indeed established functional binding sites for the desired target molecules in the polymer structure.

Time studies were performed at the optimal template concentrations of 40 mg/mL to determine the binding kinetics towards the target molecule erythromycin. Both polymers achieved their maximum binding capacity within 40 to 60 minutes after exposure (Figure 5. 16, b).
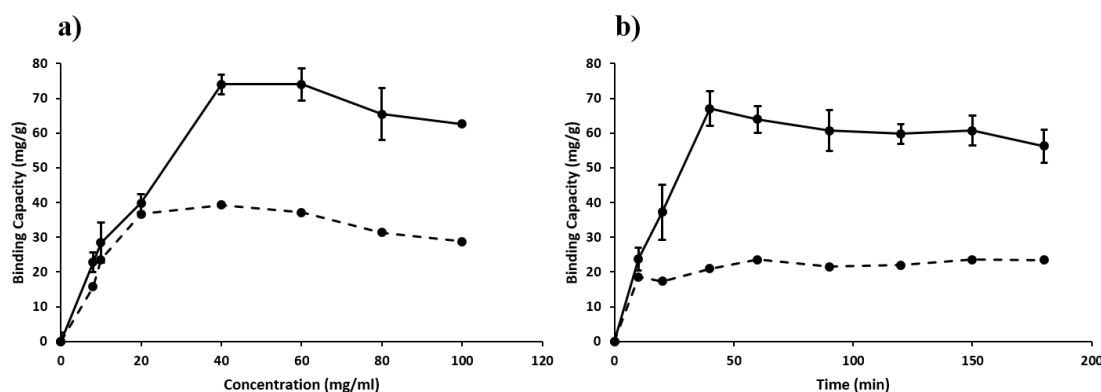
Figure 5. 16: a) Binding capacities and b) time studies of ERY imprinted and non-imprinted polymeric spheres for the template molecule erythromycin. Imprinted samples are displayed with solid lines and non-imprinted samples with dotted lines (p<0.05).

The selectivity of MMIP spheres was determined in the presence of three other antibiotics neomycin sulfate, tetracycline, and kanamycin sulfate (Figure 5. 17). The ERY- imprinted polymer spheres showed a clear preference towards their imprinted target/template molecules, up to 5-6 times higher than the binding capacity towards the competing antibiotics. Non-imprinted MNIP samples showed only a slight selectivity towards ERY but not significantly towards any of the other used antibiotics. This result suggested that ERY-MMIP was imprinted with template-specific binding sites and can be used for highly selective binding.
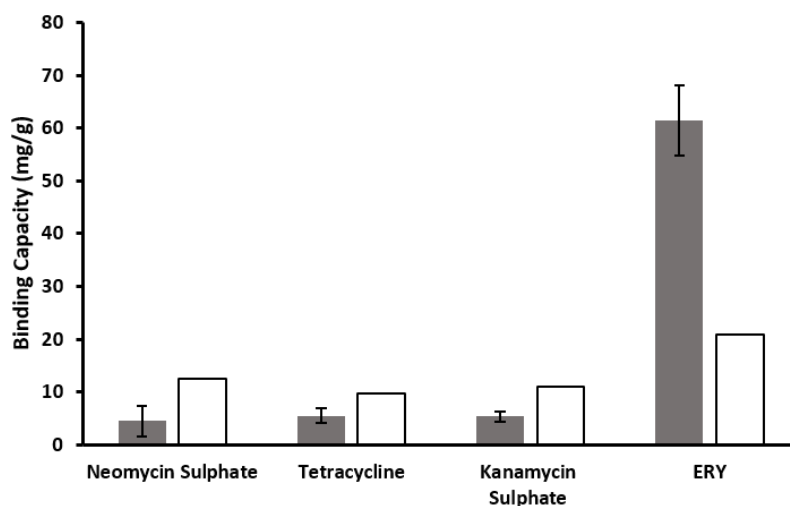
Figure 5. 17: Selectivity of ERY-MMIP for their template molecules in milk matrix containing the target molecule (erythromycin) and three competing antibiotics (neomycin sulfate, tetracycline, and kanamycin sulfate). All graphs show the selectivity of the MMIP (■) and non-imprinted MNIP (□) samples (p<0.05).

5.5. Comparison of the MMIP network to MMIP spheres

A comparison of the binding capacity and selectivity of MMIP networks against the corresponding spheres is depicted in Figure 5. 18. The result shows that the MMIP network has a 15 % higher binding capacity at lower concentrations than the MMIP spheres. At a template concentration of 40 mg/g, the MMIP structures show a maximum binding capacity of 70 mg/g for MMIP networks and 75 mg/g for MMIP spheres. The time curves suggested that a maximum binding capacity can be achieved from both MMIP samples within 40 minutes after exposure. When analyzing the concentration to binding capacity trend, the MMIP network binds more erythromycin at lower concentrations (<40 mg/ mL) and less when reaching above 40 mg/ mL (Figure 5. 18, a). However, these results remain within the error values of MMIP spheres. It is presumed that the MMIP spheres are not as porous as the corresponding MMIP network and cannot allow a drug diffusion rate as high as the polymer structure of MMIP networks. A high drug diffusion rate allows the network to establish more functional binding sites and therefore present an increased maximum binding capacity towards the template molecule. Comparing the time studies (Figure 5. 18, b) illustrates that both MMIP structures (network and spheres) have a similar binding capacity and reach their highest binding capacity between 40 -60 minutes.
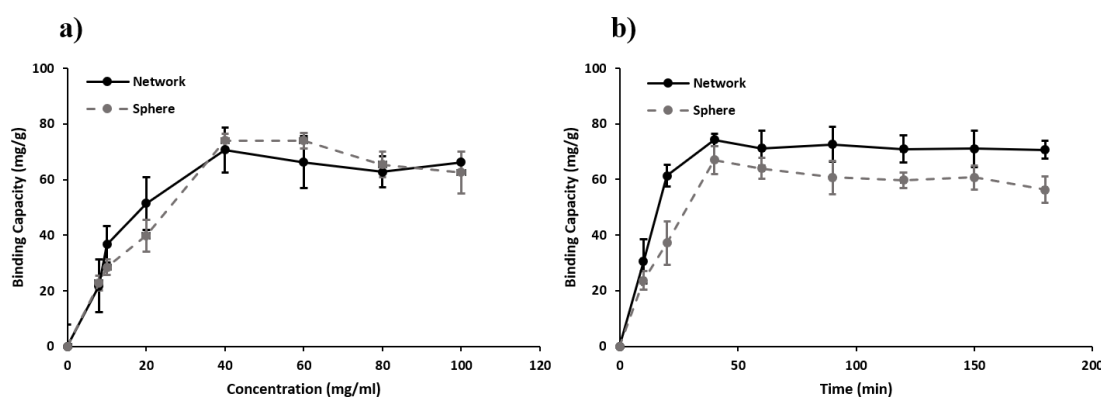
Figure 5. 18: Comparison of ERY imprinted MMIP networks and MMIP spheres based on their a) binding capacity vs. concentration and b) binding kinetics of the template molecule (ERY). The dotted lines depict the binding capacity of MMIP spheres.

A comparison of the selectivity from MMIP networks and MMIP spheres towards the target molecule erythromycin shows high similarity in their preferences (Figure 5. 19). Both MMIP structures have a clear binding preference of up to 5-6 times higher for ERY rather than for any of the other competing antibiotics (neomycin sulfate, tetracycline, and kanamycin sulfate). It is noticeable that the general selectivity of MMIP spheres tends to be marginally smaller than the MMIP network. As previously mentioned, this could be due to the reduced amount of functional binding sites in the MMIP spheres and a lower drug diffusion rate through the structure. The results present that despite their different structures, both magnetic molecular imprinted polymers can be used for highly selective binding.
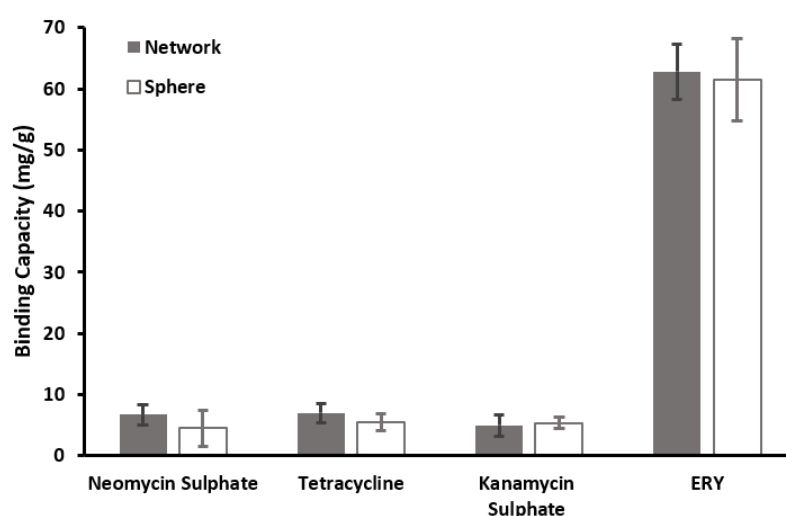
Figure 5. 19: Comparison of erythromycin imprinted MMIP networks and MMIP spheres based on their selectivity for the template molecule (ERY). In addition to the template molecule (ERY), all solutions contained the three competing antibiotics neomycin sulfate, tetracycline, and kanamycin sulfate. The graphs show the selectivity of MMIP networks (■) and MMIP spheres (□).

5.6. Conclusion

This chapter presented the successful synthesis of magnetic molecular imprinted (MMIPs), with the antibiotics erythromycin (ERY) and ciprofloxacin (CPX) as template molecules, and non-imprinted polymers (MNIPs) without template molecules. Both imprinted samples showed high binding capacities of 70 mg/g and 32 mg/g and established their maximum binding capacity within 40-60 minutes after exposure. The imprinted samples were tested on their recovery rates using magnetic separation and retained 68 – 75 % of their binding capacity after 4 cycles. The high selectivity of all MMIPs towards their respective template molecule (ERY or CPX) was demonstrated in methanol:water and milk matrices. A reduced homogenization speed at 25,000 rpm resulted in the synthesis of spherical polymers rather than a porous network. The ERY-MMIP spheres showed a similar binding capacity of 70 mg/g for imprinted and 40 mg/g for non-imprinted samples, which was established after 40-60 minutes. The selectivity of ERY-MMIP spheres was determined in the milk matrix and showed a clear binding preference for the target molecule erythromycin. The comparison of the two different MMIP samples (network and sphere) shows that despite their different structures, both polymers have similar binding capacities and selectivity. The combination of a highly selective polymer structure towards antibiotic pollutants and the magnetic property of iron oxide (Fe_3O_4) can be a useful tool to monitor and remove antibiotic pollutants from freshwater sources and food products. While the polymer binds the target molecules, the whole system can be recovered by simply applying a magnetic field rather than time-consuming and laborious centrifugation and filtration processes. Further modifications and interchangeable template molecules allow the use of a magnetic MIP system for a broad range of applications and can help to tackle the global problem of pharmaceutical and chemical pollution in aquatic environments.

5.7. References

[5.1.] S. Banerjee and B. König; Molecular Imprinting of Luminescent Vesicles; J. Am. Chem. Soc., **2013**, 135, 2967–2970.

[5.2.] G. Wulff and A. Sarhan; The use of polymers with enzyme-analogous structures for the resolution of racemates; Angew. Chem. Int., **1972**, 11, 341–346.

[5.3.] G. Wulff and K. Knorr; Stoichiometric noncovalent interaction in molecular imprinting; Bio separation, **2001**, 10, 257, DOI: 10.1023/A:1021585518592

[5.4.] Jacob N. Israelachvili; The nature of van der Waals forces; Contemporary Physics, **1974**,15, 159-178.

[5.5.] E. E. Meyer, K. J. Rosenberg, and J. Israelachvili; Recent progress in understanding hydrophobic interactions; PNAS, **2006**, 103, 15739-15746.

[5.6.] E. Caro, M. Masque, R.M. Marce, F. Borrull, P.A.G. Cormack, D.C.Sherrington; Non-covalent and semi-covalent molecularly imprinted polymers for selective on-line solid-phase extraction of 4-nitrophenol from water samples; Journal of Chromatography A, **2002**, 963 (1-2). pp. 169-178. ISSN 0021-9673.

[5.6.] RN Liang, TT Wang, H. Zhang, RQ Yao, and W. Qin1; Soluble Molecularly Imprinted Nanorods for Homogeneous Molecular Recognition; Front Chem., **2018**, 6, 81.

[5.7.] K. Lee, D.S. Kim and B.S. Kim; Biodegradable molecularly imprinted polymers based on poly(ε-caprolactone); Biotechnol. Bioprocess Eng., **2007**, 12, 152–156.

[5.8.] O.I. Parisi, M. Ruffo, R. Malivindi, A. F. Vattimo, V. Pezzi, and F. Puoci; Molecularly Imprinted Polymers (MIPs) as Theranostic Systems for Sunitinib Controlled Release and Self-Monitoring in Cancer Therapy; Pharmaceutics, **2020**, 12, 41.

[5.9.] DL Huang, RZ Wang, YG Liu; Application of molecularly imprinted polymers in wastewater treatment: a review; Environ Sci Pollut. Res Int.; **2015**; 22, 963-977.

[5.10.] The United Nations World Water Development Report 2019: Leaving No One Behind; United Nations Educational, Scientific and Cultural Organization, Paris, **2019**; ISBN 978-92-3-100309-7

[5.11.] Industrial wastewater treatment – pressures on Europe's environment; EEA Report No 23/2018; European Environment Agency, Luxembourg, **2019**; DOI: 10.2800/496223

[5.12.] European water – Assessment of status and pressures 2018; EEA Report No 7/2018; European Environment Agency, Luxembourg, **2018**; DOI: 10.2800/303664

[5.13.] Water pollution from agriculture: A global review; I7754EN/1/08.17; Food and Agriculture Organization of the United Nations, Rome, 2017, and the International Water Management Institute on behalf of the Water Land and Ecosystems research program Colombo, **2017**; www.fao.org/3/a-i7754e.pdf

[5.14.] D. G. J. Larsson; Antibiotics in the Environment; Ups. J. Med. Sci., **2014**, 119, 108–12.

[5.15.] J. Bengtsson-Palme and D. G. J. Larsson; Concentrations of Antibiotics Predicted to Select for Resistant Bacteria: Proposed Limits for Environmental Regulation. Environ. Int; **2016**, 140–49.

[5.16.] **2017** WHO GAP AMR Newsletter No.32 – Implementation of the global action plan on antimicrobial resistance.

[5.17.] Monitoring and evaluation of the global action plan on antimicrobial resistance: framework and recommended indicators; World Health Organization (WHO), Food and Agriculture Organization of the United Nations (FAO) and World Organization for Animal Health (OIE), Geneva, **2019**; ISBN 978-92-4-151566-5

[5.18.] Tackling antimicrobial resistance (AMR) together. Working Paper 1.0: Multisectoral coordination, WHO/HWS/AMR/2018.2, World Health Organization, Geneva, **2018**; www.who.int/antimicrobial-resistance/publications/Tackling-AMR-multisectoral-coordination-june2018.pdf

[5.19.] Turning plans into action for antimicrobial resistance (AMR). Working Paper 2.0: Implementation and coordination, WHO/WSI/AMR/2019.2, World Health Organization, Geneva, **2019**; www.who.int/antimicrobial-resistance/publications/AMR-Turning-plans-into-action-working-paper-march-2019.pdf

[5.20.] R. L. Finley, P. Collingnon, D. G. J. Larsson, S. A. McEwen, X. Z. Li, W. H. Gaze, R. Reid-Smith, M. Timinouni, D. W. Graham and E. Topp; The Scourge of Antibiotic Resistance: The Important Role of the Environment; Clin. Infect. Dis., **2013**, 57, 704–10.

[5.16.] F. Baquero, J. L. Martínez, and R. Cantón; Antibiotics and Antibiotic Resistance in Water Environments; Curr. Opin. Biotechnol., **2008**, 260–65.

[5.17.] M. Samia, M. El-Sadek, and E. A. Alla; Spectrophotometric Determination of Ciprofloxacin, Enrofloxacin, and Pefloxacin through Charge Transfer Complex Formation.; Journal of J. Pharm. Biomed. Anal., **2002**, 27, 133–42.

[5.18.] E. Caro, R. M. Marcé, P. A. G. Cormack, D. C. Sherrington, and F. Borrull; Direct determination of ciprofloxacin by mass spectrometry after a two-step solid-phase extraction using a molecularly imprinted polymer. J. Sep. Sci., **2006**, 29, 1230–1236.

[5.19.] J. L. Urraca, M. Castellari, C. A. Barrios, and M. C. Moreno-Bondi; Multiresidue analysis of fluoroquinolone antimicrobials in chicken meat by molecularly imprinted solid-phase extraction and high performance liquid chromatography; J. Chromatogr. A, **2014**, 1343.

[5.20.] X. L. Sun, J. C. Wang, Y. Li, J. J. Yang, J. Jin, S. M. Shah, and J. P. Chen; Novel dummy molecularly imprinted polymers for matrix solid-phase dispersion extraction of eight fluoroquinolones from fish samples; J. Chromatogr. A., **2014**, 1359, 1–7.

[5.21.] X. M. Zhou, D. Xing, D. B. Zhu, Y. B. Tang, and L. Jia; Development and application of a capillary electrophoresis–electrochemiluminescent method for the analysis of enrofloxacin and its metabolite ciprofloxacin in milk; Talanta, **2008**, 75, 1300–1306.

[5.22.] R. E. Ionescu, N. Jaffrezic-Renault, L. Bouffier, C. Gondran, S. Cosnier,; D. G. Pinacho, M.-P. Marco, F. J. Sánchez-Baeza, T. Healy, and C. Martelet; Impedimetric immunosensor for the specific label free detection of ciprofloxacin antibiotic; Biosens. Bioelectron., **2007**, 23, 549–555.

[5.23.] O. M. Rodriguez-Narvaez, J. M. Peralta-Hernandez, A. Goonetilleke, and E. R. Bandala; Treatment technologies for emerging contaminants in water: A review; Chem. Eng. J., **2017**, 323, 361-380

[5.24.] A. A. Basheer; New generation nano-adsorbents for the removal of emerging contaminants in water; J. Mol. Liq., **2018**, 261, 583-593.

[5.25.] M. Cantarella, S.C. Carroccio, S. Dattilo, R. Avolio, R. Castaldo, C. Puglisi, and V. Privitera; Molecularly imprinted polymer for selective adsorption of diclofenac from contaminated water; Chem. Eng. J., **2019**, 367, 180-188.

[5.26.] E. Sari, R. Üzek, M. Duman and A. Denizli; Detection of ciprofloxacin through surface plasmon resonance nanosensor with specific recognition sites; J. Biomater. Sci.-Polym. Ed., **2018**, 29, 1302–1318.

[5.27.] M. Okan, and M. Duman; Functional polymeric nanoparticle decorated microcantilever sensor for specific detection of erythromycin; Sens. Actuator B-Chem., **2018**, 256, 325–333.

[5.28.] H. Y. Yan, X. L. Cheng, and N. Sun; Synthesis of Multi-core–shell Magnetic Molecularly Imprinted Microspheres for Rapid Recognition of Dicofol in Tea; J. Agric. Food Chem., **2013**, 61, 2896–2901.

[5.29.] S. Banerjee and B. König; Molecular Imprinting of Luminescent Vesicles; J. Am. Chem. Soc., **2013**, 135, 2967–2970.

[5.30.] C. Armutcu, N. Bereli, E. Bayram, L. Uzun, R. Say, and A. Denizli; Aspartic acid incorporated monolithic columns for affinity glycoprotein purification; Colloid Surf. B-Biointerfaces, **2014**, 114, 67–74.

[5.31.] M. K. Yoshikawa, K. Tharpa, and S.-O. Dima; Molecularly Imprinted Membranes: Past, Present, and Future; Chem. Rev., **2016**, 116, 11500–11528.

[5.32.] Y. Hoshino; T. Kodama, Y. Okahata and K. J. Shea; Peptide Imprinted Polymer Nanoparticles: A Plastic Antibody; J. Am. Chem. Soc., **2008**, 130, 15242–15243.

[5.33.] G. J. Guan, R. Y. Liu, Q. S. Mei, and Z. P. Zhang; Molecularly Imprinted Shells from Polymer and Xerogel Matrices on Polystyrene Colloidal Spheres; Chem. Eur. J., **2012**, 18, 4692–4698.

[5.34.] Y. Tong, Y. Hu, Q. Xia, W. Huang, and M. Tian; Preparation of a novel magnetic molecularly imprinted polymer and its application for the determination of fluoroquinolone antibiotics; Chin. J. Chromatogr., **2017**, 35, 291.

[5.35.] L. G. Chen, J. Liu, Q. L. Zeng, H. Wang, A. Yu, H. Q. Zhang, and L. Ding; Preparation of magnetic molecularly imprinted polymer for the separation of tetracycline antibiotics from egg and tissue samples; J. Chromatogr. A, **2009**, 1216, 3710–3719.

[5.36.] S. Comber, M. Gardner, P. Sörme, D. Leverett and B. Ellor; Active pharmaceutical ingredients entering the aquatic environment from wastewater treatment works: A cause for concern?; Sci. Total Environ., **2018**, 613–614, 538–547.

[5.36.] J. Kuhn, G. Aylaz, E. Sari, M. Marco, H. H. P. Yiu, and M. Duman; Selective binding of antibiotics using magnetic molecular imprint polymer(MMIP) networks prepared from vinyl-functionalized magnetic nanoparticles; J. Hazard. Mater., **2020**, 387, 121709.

[5.37.] N.L. Wu, Z.M. Luo, Y.H. Ge, P.Q. Guo, K.L. Du, W.L. Tang, W. Du, A.G. Zeng, C. Chang, and Q. Fu; A novel surface molecularly imprinted polymer as the solid-phase extraction adsorbent for the selective determination of ampicillin sodium in milk and blood samples; J. Pharm. Anal., **2016**, 6, 157-164.

[5.38.] XX Li, JM Pan, JD Dai, XH Dai, LC Xu, X Wei, H Hang, CX Li, Y Liu; Surface molecular imprinting onto magnetic yeast composites via atom transfer radical polymerization for selective recognition of cefalexin; **2012**. 198, 503-511.

[5.39.] K. Lata, R. Sharma, L. Naik, Y.S. Rajput and B. Mann; Synthesis and application of cephalexin imprinted polymer for solid phase extraction in milk; Food Chem., **2015**, 184, 176-182.

[5.40.] D. Qin, J.T. Wang, C. G. Ge, and Z. Lian; Fast extraction of chloramphenicol from marine sediments by using magnetic molecularly imprinted nanoparticles; Microchim. Acta., **2019**, 186, 428.

[5.41.] SL Wei, JW Li, Y Liu, and JK Ma; Development of magnetic molecularly imprinted polymers with double templates for the rapid and selective determination of amphenicol antibiotics in water, blood, and egg samples; **2016**. 1473, 19-27.

[5.42.] YW Tang, M Li, X Gao, XY Liu, Y Ma, Y Li, YX Xu, JR Li; Preconcentration of the antibiotic enrofloxacin using a hollow molecularly imprinted polymer, and its quantitation by HPLC; Microchimica Acta, **2016**, 183, 589-596.

[5.43.] HX Ou, QH Chen, JM Pan, YL Zhang, Y Huang, XY Qi; Selective removal of erythromycin by magnetic imprinted polymers synthesized from chitosan-stabilized Pickering emulsion; **2015**, 289, 28-37.

[5.44.] J.M. Li, L.J. Zhao, C.L. Wei, Z.A. Sun, S.W. Zhao, T.P.Cai and B.L. Gong; Preparation of restricted access media molecularly imprinted polymers for efficient separation and enrichment of ofloxacin in bovine serum samples; J. Sep. Sci., **2019**, 42, 2491-2499.

[5.44.] X.Q. Song, T. Zhou, J.F. Li, Y.J. Su, J.M. Xie, and L. He; Determination of macrolide antibiotics residues in pork using molecularly imprinted dispersive solid-phase extraction coupled with LC–MS/MS; J Sep Sci., **2018**, 41, 1138-1148.

[5.45.] H. H. P. Yiu, L. Bouffier, P. Boldrin, J. Long, J. B. Claridge, and M. J. Rosseinsky; Comprehensive Study of DNA Binding on Iron(II, III) Oxide Nanoparticles with a Positively Charged Polyamine Three-Dimensional Coating; Langmuir, **2013**, 29, 11354–11365.

[5.46.] M. Okan, E. Sari, and M. Duman; Molecularly imprinted polymer based micromechanical cantilever sensor system for the selective determination of ciprofloxacin; Biosens. Bioelectron., **2017**, 88, 258–264.

[5.47.] E. Sari, R. Üzek, M. Duman, and A. Denizli; Fabrication of surface plasmon resonance nanosensor for the selective determination of erythromycin via molecular imprinted nanoparticles; Talanta, **2016**, 150, 607–614.

CHAPTER 6

Zebrafish larvae as *in vivo* model system for the characterization of iron oxide supported gold nanoparticles with polyethylene glycol coating

6.1. Introduction

In the previous chapters, the cell viability and response of various cell lines were tested *in vitro* by exposing MCF-7, Huh-7, and HepaRG cells to a range of concentrations of various iron oxide nanoparticles. The cell proliferation rates and cell viability were analyzed using the colorimetric cell assays Celltiter-Glo® and PrestoBlue®. The results showed no adverse effects on the cells after nanoparticle exposure. Colorimetric assays for nanoparticles *in vitro* are fast, easy, and cheap in comparison to *in vivo* setups. However, their results are highly dependent on the particles being tested and the testing method, such as fluorescence or luminescence. The fluorescent or luminescent signal is produced by the metabolization of resazurin to resorufin or other chemicals (See "Chapter 3) The emitted signal can then be converted to a proportional number of metabolically active cells, allowing to calculate the toxicity of the tested nanomaterial [6.1.]. However, due to the darkness of materials such as iron oxide (Fe_3O_4), the fluorescence and luminescence signals can be absorbed. This could lead to altered signals that cause considerable error within the results [6.2.]. To circumvent this problem and obtain more precise and reliable results, the cells were analyzed using impedance measurement (xCELLigence) and Coherent Anti-Stokes Raman Scattering (CARS) microscopy in Chapter 3. Similar to the colorimetric results, the microscopy analyses showed no adverse effects on the cell viability at any of the tested concentrations and exposure periods.

Testing the effect of nanoparticles *in vitro* is a general method to gather toxicologic data quickly and easily, but the translational values are limited, and the link between *in vitro* and *in vivo* is sometimes questionable due to the complexity of the organism [6.3.]. However, running large-scale *in vivo* experiments requires extensive amounts of preparation, maintenance, and can be too large for the actual intent. Gene expression analyses like the amplification of a targeted DNA, or the analysis of a potential dermal uptake of nanoparticles by direct exposure generally require a large amount of tissue, making mice and other rodents rather laborious and expensive. Therefore, after thorough characterization and *in vitro* testing, zebrafish embryos (Danio rerio) are assessed for their response to various nanoparticle doses.

Zebrafish embryos and larvae have been used as an "intermediate" method for *in vivo* experiments throughout the literature [6.4.-6.6]. Different from large-scale *in vivo* test setups, such as rabbits, rats, and mice, zebrafish reach adulthood and become sexually mature within 2-3 months after fertilization. A single female zebrafish can spawn about 200-300 eggs per week, which can generate an extensive data set from a small-scale experimental setup [6.6.]. Zebrafish have a unique developmental process, as the embryo fully develops most of its organs within 48 hours post-fertilization (hpf) and remains almost transparent during embryogenesis. This allows to monitor the development of the organs, their physiology, and detect the development of any potential diseases until adulthood [6.6.]. This transparency and fast embryogenesis made them highly attractive for toxicology assessments of nanoparticles as each step can be viewed, captured, and analyzed by microscopy.

Matos et al. exposed zebrafish embryos to amino-functionalized silica nanoparticles, with an average diameter of 165 nm and a green fluorescence protein tag for 96 hours and at concentrations reaching from 0.04 mg/mL - 0.7 mg/mL. The fluorescent nanoparticles were successfully tracked *in vivo*, using a fluorescence microscope, and data on biodistribution showed no cytotoxic effect. In addition to this, mortality and developmental endpoints of the zebrafish embryos were studied and showed no toxic effects on the exposed zebrafish eggs [6.7.]. Jurewicz et al. exposed zebrafish larvae to iron oxide nanoparticles with an average particle size of 40 nm and a fluorescent tag of Congo red for 96 hours post-fertilization (hpf). Monitoring the mortality and hatching rate showed that the exposed nanoparticles did not build up any toxicity during the embryonic and larval stages of the zebrafish [6.8.].

In both studies the zebrafish embryos were exposed to nanoparticles by dispersing them in culture water, this is the only non-invasive method for nanoparticle exposure at the larval stage. During embryogenesis and the larval stage, the zebrafish has not developed a mouth for ingestion [6.9.]. However, once the larvae reach 5 – 6 days post fertilization (dpf), a mouth has developed, and the fish can eat small algae particles. The larvae in the next stage should be fed with brown shrimp at 9 dpf and finally should receive crushed adult food one month after fertilization [6.9.]. At this final stage, the adult food can be spiked with nanoparticles to test the effects on zebrafish after ingestion [6.7., 6.10.]. The fish will then naturally ingest the nanoparticles or absorb them through their skin and gradually release them into the body during digestion. Subsequently, the organs can then be dissected and analyzed by in-situ hybridization, immunohistochemistry, histology, RNA extraction, or other common molecular techniques to assess the effects of

nanoparticles on zebrafish. This chapter focuses on the effects of polyethylene glycol coated Fe_3O_4 (PEG-coated, Fe_3O_4-PEG) and iron oxide supported gold nanoparticles in a 10% weight to weight ratio and polyethylene glycol coating (10% Au:Fe_3O_4-PEG) on zebrafish larvae. Both types of nanoparticles were magnetic and had an average diameter of 30 ± 5 nm. Possible adverse effects on zebrafish health after exposure were analyzed by monitoring the survival rate over 96 hours past fertilization.

6.2. Experimental

6.2.1. Materials

ZM small granular fish food, TetraMin Baby food for baby fish, and artemia cysts were purchased from Zebrafish Management Ltd. All adult zebrafish were bred from larvae of previous generations. Artemia were hatched in seawater for 36 hours under constant aeration. The seawater was sourced from the North Berwick Harbour Trust Association, UK.

Ethyl 3-aminobenzoate methanesulfonate (MS222) was purchased from Sigma Aldrich and potassium chloride (KCl) was sourced from MP Biomedicals Inc. Calcium chloride dihydrate ($CaCl_2 \cdot 2H_2O$), sodium chloride (NaCl), and magnesium chloride heptahydrate ($MgCl_2 \cdot 6H_2O$) were purchased from VWR International. Magnesium sulfate heptahydrate ($MgSO_4 \cdot 6H_2O$) and sodium hydrogen carbonate ($NaHCO_3$) were supplied by Fisher Scientific. Two functionalized iron oxide (Fe_3O_4) nanoparticles, introduced in Chapter 2, were used for this experiment: 1) polyethylene glycol coated Fe_3O_4 (PEG-coated, Fe_3O_4-PEG) and 2) iron oxide supported gold nanoparticles in a 10% weight to weight ratio and polyethylene glycol coating (10% Au:Fe_3O_4-PEG). Both types of nanoparticles had an average diameter of 30 ± 5 nm.

6.2.2. Husbandry of zebrafish

Any experiments in this project were performed within the framework of the OECD guidelines and under the personal license of Prof. Theodore Henry (License no. 1E09E49E).

The general maintenance media for zebrafish husbandry (OECD water) was prepared by dissolving 29.4 g calcium chloride dihydrate ($CaCl_2 \cdot 2H_2O$), 12.32 g magnesium sulfate heptahydrate ($MgSO_4 \cdot 7H_2O$), 6.47 g sodium hydrogen carbonate ($NaHCO_3$), and 0.57 g of potassium chloride (KCl) in 100 liters of reverse osmosis water. A breeding solution including methylene blue (E3 media) was used to add additional protections for freshly spawned zebrafish embryos. Methylene blue is an antifungal agent that induces mitochondrial dysfunction and membrane homeostasis [6.11.]. A concentrated 60x stock solution of E3 media consisted of 34.8 g NaCl, 1.6 g KCl, 5.8 g $CaCl_2 \cdot 2\,H_2O$, and 9.78 g $MgCl_2 \cdot 6\,H_2O$ dissolved in a final volume of 2 liters of reverse osmosis water. The solution was adjusted to pH 7.2 using NaOH and then autoclaved. Experiments were performed using a 1x solution, which was prepared by diluting 16.5 mL of the 60x stock solution to 1 liter. Then, 100 µL of 1% methylene blue was added as an antifungal agent [6.12.].

Adult zebrafish were fed twice a day, once in the morning at around 9 am and once in the afternoon at around 3 pm, with a minimum of 6 hours between the feeding times. Before every feeding time, the tanks were cleaned by sucking accumulated dirt, feces, and old food out of the tank and refilling the tank with fresh OECD water. While letting the fish tanks rest for 10 minutes, the fish were checked for injuries or signs of discomfort. Any fish with serious damages or signs of severe and permanent discomfort were euthanized in ethyl 3-aminobenzoate methanesulfonate (MS222) for 15 minutes and decapitated to ensure quick and painless relief.

After this cleaning and general check-up procedure, the fish were fed twice with three grams of ZF small granular fish food (Zebrafish Management Ltd.) for every 10 adult zebrafish, with approximately 20 minutes between the feedings. After the morning feed, artemia (brine shrimp) were set up for the afternoon feed on the next day. This was done by mixing approximately 0.5 g of artemia cysts with 1.5 liters of seawater and aerating the solution with an air pump for 36 hours. Twice a year, a food-grade tanker from TP Niven Ltd (Palnackie, UK) supplied fresh seawater sourced by the North Berwick Harbour Trust Association, UK. Once the seawater was delivered on campus, the water was filtered through an ASME VIII, Div. 1 boiler and pressure vessel (Swinney Engineering Ltd.) with a 100-micron particle filter and was cooled to 9°C using an M6-MFM heat exchanger (Alfa Laval Ltd.) until further use.

The afternoon feeding session followed the same cleaning procedure, but instead of dry adult food, the fish were fed with hatched artemia, which were set up 36 hours before. Artemia were collected sieved into a fine mesh container and rinsed with OECD water to remove any residual seawater. Then, the artemia were dispersed in 250 mL OECD water and set aside to rest for 10 minutes. Finally, the adult zebrafish were fed with a 5 ml artemia solution for every 10 fish in the tank. Attention was paid to not stirring up the beaker while extracting the required amount of artemia and that only artemia from the middle of the beaker were used. This was done to avoid feeding unhatched artemia cysts from the water surface or bottom of the beaker since those could potentially cause indigestion and discomfort to the fish.

Adolescent zebrafish (<2 months post-fertilization) were fed with approximately 3g of crushed adult food (crushed using mortar and pestle) for every 20 fish in the morning and 5 mL artemia for every 10 fish in the afternoon.

Freshly hatched zebrafish larvae (72hpf) were fed at the same time points as the adult fish stock. However, an algae-based baby food (TetraMin Baby food) was used instead of the standard ZF small granular fish food. After using a 5 ml pipette to remove leftover food and accumulated dirt from the fish tanks, a mixture of 0.2 g algae-based baby food (1 measuring spoon) was mixed with OECD water and added dropwise to the tanks.

6.2.3. General spawning of zebrafish

An adult female zebrafish can spawn about 200 – 300 eggs each week, but to reach the highest fertility, male and female zebrafish need to be separated for at least 3-4 weeks before the eggs are of consistent quality and ready to be used for experiments. Once the fish are separated by sex, the fish need to be mated once a week until a consistent number of eggs is produced, and the survival rate of 80-90% is accomplished.

In general, zebrafish eggs are spawned for experiments on 5 consecutive days. On the first day of fertilization (day 1), the required number of spawning tanks were filled with OECD water. Then 2 female and 2 male zebrafish were transferred into tanks, which were then covered with a lid and left in the dark overnight. The fish started spawning the next day as soon as the lights were switched on by the automated light/dark cycle of 16:8 hours and at constant room temperature between 27 - 30ºC.

On the next day (day 2, 24hpf = 24 hours past fertilization), the fish were separated and returned to their original tanks. The eggs were then collected and washed with a sieve and OECD water. Once all eggs were collected, unfertilized eggs were separated from fertilized eggs. This is a crucial step since unfertilized eggs start to rot and develop egg fungi (oomycetes) which then spread and infect otherwise healthy eggs. Figure 6. 1 shows two zebrafish eggs 24 hours (a) and 48 hours (b) after spawning. The egg with a dark core is unfertilized and already started to rot and grew toxic fungi on its surface (arrow). The light egg shows a fertilized egg with an early-stage zebrafish embryo in its core. After 48 hours, the fungi on the rotting egg have grown so much that it now starts to affect the healthy neighboring egg.

All other fertilized eggs were counted and placed into petri dishes at 50 healthy eggs per dish and covered with OECD water. In the afternoon, the eggs were sorted again (unfertilized eggs from fertilized) and washed with OECD water, where about 60% of the petri dish water was replaced. For better fertility and to simulate a natural environment, the petri dishes were covered with aluminum foil to create a semi-dark environment overnight.
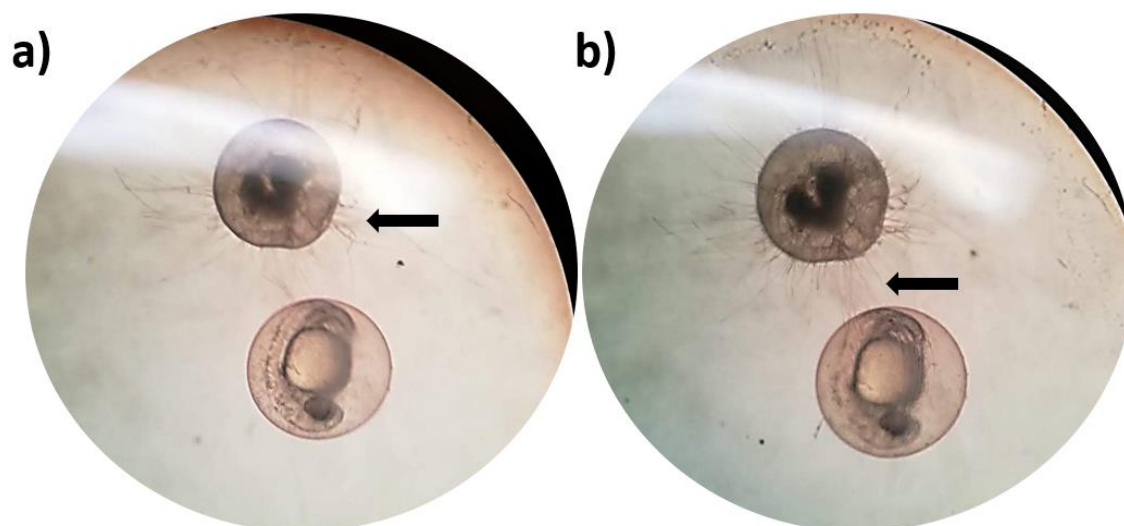
Figure 6. 1: Two zebrafish eggs 24 hours (a) and 48 hours (b) after spawning. The unfertilized and rotting egg (dark) is growing fungi on its surface (arrow), which then starts to affect the fertilized and healthy neighboring egg (light strings).

The sorting and washing process was repeated on days three and four. However, larvae that hatched during that time are either discarded or used for other experiments. This is necessary as most eggs will hatch on the fifth day, allowing for a broader exposure experiment and comparison.

Every day the number of fertilized, dead, and unhealthy eggs were noted down to assess the viability of the spawn and evaluate the egg quality of the fish culture. Monitoring the egg quality is essential, so the test results remain reliable and comparable with other experiments.

6.2.4. Spawning zebrafish larvae for nanoparticle exposure

New zebrafish larvae were spawned by setting up 10 breeding tanks, each containing 3 female and 3 male zebrafish from the tank systems 3 and 4. Before spawning, both systems were maintained under the same conditions. The light was turned off overnight and switched on, on the following morning, triggering the fish to begin spawning and fertilization of the eggs. After 1 hour, the fish were separated again and returned to their respective systems. The eggs were then collected and siphoned from the spawning aquaria into petri dishes containing 50 mL OECD water. Each dish was filled at a density of 50 eggs/dish and dead eggs were removed.

On the following three days, the petri dishes were kept between 27 - 30°C and photoperiod at 14 hours of light per day and covered with aluminum foil to only allow for partial darkness. Additionally, 50% of the culture water was replaced and the embryos were examined for the presence of dead eggs/embryos using a Meiji compound microscope (ML 2000 Microscope, Meiji Techno Co. Ltd). Any dead eggs or embryos were counted and discarded. Larvae that had hatched before 72 hpf were separated and euthanized by placing them on crushed ice for a minimum of 1 hour or until no heartbeat was detected under a microscope.

Approximately 72 hours post-fertilization (72 hpf), most embryos had hatched and were placed out individually into a 96-well plate. The culture water was then replaced by 300 µL of media (Milli-Q water). After preparing and sonicating the media containing nanoparticles (Milli-Q + nanoparticles) for at least 30 minutes, the respective volume of water was then replaced within each well.

6.2.5. Zebrafish larvae exposure to iron (II, III) oxide-based magnetic nanoparticles

Two experiments were set out to test the effects of Fe_3O_4-PEG and 10% $Au:Fe_3O_4$-PEG nanoparticles on the viability of zebrafish larvae that hatched 72 hours past fertilization (72 hpf). The first experiment determined the most suitable zebrafish culture media to be used for assessing Fe_3O_4-PEG and 10% $Au:Fe_3O_4$-PEG nanoparticles. Five different culture media were compared by their effects on the mortality of zebrafish larvae in combination with 1mM concentration of both nanoparticles after 24 hours. The larvae were bred in Milli-Q water, OECD water, seawater, and E3 medium (12 larvae/medium) and exposing them to a 1mM solution of 10% $Au:Fe_3O_4$-PEG nanoparticles. Finally, the zebrafish larvae were assessed under a compound microscope (ML 2000 Microscope, Meiji Techno Co. Ltd), and their viability was recorded after 24 and 48 hours. Control larvae were bred in E3 media and in the absence of any nanoparticles. E3 media is a culture media commonly used especially for zebrafish larvae as it contains the antifungal additive methylene blue for extra protection [6.11.]. The experiment was run in triplicates. Once the most suitable medium for the exposure of 10% $Au:Fe_3O_4$-PEG and Fe_3O_4-PEG nanoparticles were determined. In triplicate, 12 zebrafish larvae (72 hpf) per concentration were exposed to a range of six concentrations of 10% $Au:Fe_3O_4$-PEG nanoparticles (0.1, 1, 1.25, 1.5, 1.75, 2mM or 23.1, 231.5, 289.4, 347.4, 405.2, 463.1 mg/L), one concentration of Fe_3O_4-PEG (1 mM, 231.5 mg/L), and one concentration of uncoated Fe_3O_4 (1mM, 231.5 mg/L). The endpoint of this experiment was the mortality of the larvae, where the potential absence of a heartbeat was checked under a brightfield microscope every 24 hours for three days (24, 48, 72 hours). The statistical significance was set at a P-value of <0.05. Images of the exposed zebrafish were taken by a MicrOkular Full HD telescope digital camera (Bresser GmbH).

6.3 Results

6.3.1. *Spawning of zebrafish*

The fertility of zebrafish can be measured by the survival rate of their spawn. A healthy female zebrafish can spawn about 200-300 eggs each week, of which approximately 80 - 90% survive until adulthood. The survival rate divided by the total amount of eggs resembles the fertility of the spawn [Equation 6. 1].

Equation 6. 1: Calculation of the fertility rate of a zebrafish spawn.

$$\frac{Alive\ zebrafish\ larvae\ at\ 72\ hpf\ (survival\ rate)}{Total\ amount\ of\ eggs} = Fertility\ rate$$

Figure 6. 2 shows the fertility of the spawn that was used for the experiments depicted in this chapter. The fertility of 30% was calculated from the data shown in Table 6.1., suggesting that the fish cultures needed to be replaced by a younger generation of zebrafish. This is acceptable for testing the survival rate of zebrafish larvae solely, as the fish are still at 100% health at the point of exposure. This means the mortality is not be affected by the low fertility of the parent zebrafish. However, when in-depth analysis is required, i.e., when performing experiments that analyze the gene expression in zebrafish after exposure to nanoparticles, the fertility rate becomes relevant. More zebrafish would be required to gather enough tissue samples for the amplification of a targeted DNA molecule using quantitative polymerase chain reaction (qPCR) [6.13.].

Table 6. *1: Four-day spawning information of zebrafish larvae, where the amount of healthy, fertilized, dead, and discarded eggs were regularly monitored.*

Date	System 3		System 4	
Day 1	healthy	Unfertilized and discarded	healthy	Unfertilized and discarded
	616	6	238	18
Day 2	healthy	dead	healthy	dead
	218	398	153	85
Day 3	healthy	hatched	healthy	hatched
	181	37	68	85
Day 4	healthy	unhatched/dead	healthy	unhatched/dead
	179	2	66	2
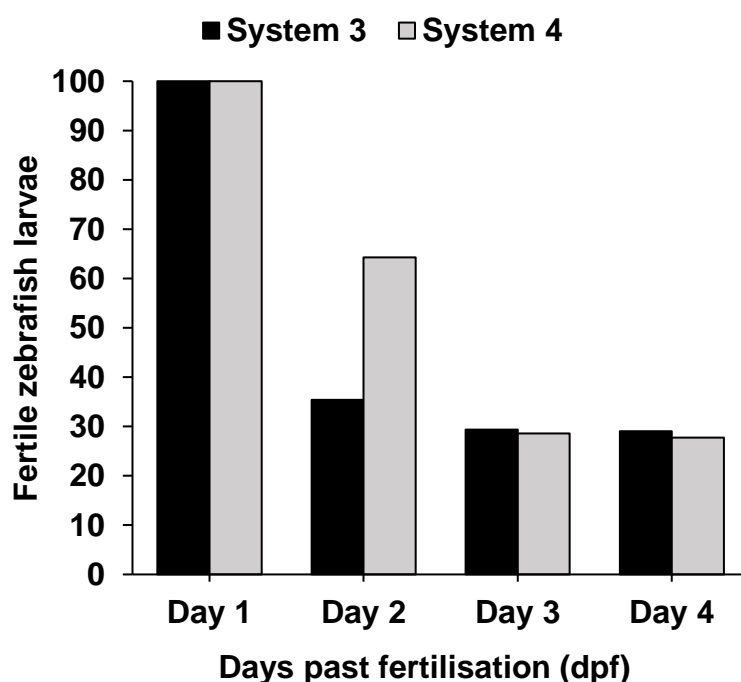
Figure 6. 2: The fertility rate of zebrafish larvae over four consecutive days from fish tank systems 3 and system 4. A final survival rate of 30% is recorded on day 4 post-fertilization.

6.3.2. *Exposure of zebrafish larvae to iron oxide nanoparticles*

The first part of this experiment focused on finding the most suitable culture media for the exposure of 10% $Au:Fe_3O_4$-PEG and Fe_3O_4-PEG nanoparticles with an average diameter of 30 ± 5 nm to zebrafish larvae. A survival rate of 100% for all test samples was confirmed by the presence of a heartbeat in all tested zebrafish larvae at both time points (24 and 48 hours) past exposure to 10% $Au:Fe_3O_4$-PEG, Fe_3O_4-PEG, and uncoated Fe_3O_4 nanoparticles. All zebrafish were active and responsive to touch, showing that a 1 mM concentration of 10% $Au:Fe_3O_4$-PEG, Fe_3O_4-PEG, and Fe_3O_4 did not kill any zebrafish larvae after 48 hours of exposure. Figure 6. 3 shows a zebrafish larva resting next to an agglomeration of nanoparticles, not showing any signs of physical damage or respiratory issues. The presence of a heartbeat confirmed that the fish was alive and well after 48 hours of exposure.

Since none of the culture media showed distinctive reactions with the two types of functionalized iron oxide nanoparticles, the most generic culture media (OECD water) was used for all further experiments.

Figure 6. 3: Zebrafish larva resting next to an agglomeration of 10% Au:Fe₃O₄-PEG nanoparticles, showing no sign of distress or visible deformations to the body structure.

The second half of this experiment consisted of exposing zebrafish larvae to six concentrations (0.1 - 2mM / 23.1 - 463.1 mg/L) of 10% $Au:Fe_3O_4$-PEG, one concentration of Fe_3O_4-PEG, and one concentration of Fe_3O_4 in OECD water for 72 hours at 12 zebrafish larvae for each concentration. At time points (24/48/72h) the presence of a heartbeat, and visual activity when the larvae were touched with a pipette tip, confirmed the viability of all zebrafish larvae. Therefore, a 100% survival rate throughout the experiment was determined.

The results showed that none of the 10% Au:Fe$_3$O$_4$-PEG, Fe$_3$O$_4$-PEG, or Fe$_3$O$_4$ nanoparticle concentrations (0.1 - 2mM / 23.1 - 463.1 mg/L) induced any apparent signs of physical damage to any of the exposed zebrafish larvae. Figure 6. 4 shows three pictures of control larvae, highlighting the fins (a), eyes (b), spine (c), and gills (d) of the zebrafish larvae at 96 hpf. These four body parts of the zebrafish can be analyzed to determine physical and health damages when exposed to any concentrations of iron oxide nanoparticles. This could be expressed through deformations in the bone structure, unhealed wounds and cracks in the skin, mucus membrane or eyes, and other abnormal growth of tissue or bones.

Figure 6. 4: Unexposed (control) zebrafish larvae after 72 hours in OECD media, highlighting the fins (a), eyes (b), spine (c), and gills (d). All zebrafish were healthy, had a visual heartbeat, and showed no signs of deformation or damage.

Comparing the pictures of the control zebrafish larvae, with larvae that were exposed to 10% Au:Fe_3O_4-PEG, Fe_3O_4-PEG, and Fe_3O_4 (0.1 - 2mM / 23.1 - 463.1 mg/L) for 72 hours showed healthy physical development and no signs of deformation or damage. Figure 6. 5 shows the upper body (a) and the tail (b) of a zebrafish larva that was exposed to 100 mg/L of 10% Au:Fe_3O_4-PEG nanoparticles for 72 hours. It is noticeable that in both images, the nanoparticles are agglomerated and attached to the skin and gills of the larvae (see white rings). This was evident in all tested zebrafish larvae of that concentration and is most likely due to the mucus membrane that covers the whole larvae [6.14.]. The mucus membrane is a primary barrier to defend the fish from pathogenic microbes and contains antimicrobial peptides, lysozymes, lectins, proteases, and other substances that provide further protection from environmental exposures [6.15.]. It is likely that the nanoparticles are attaching to the mucus membrane and its components to later be stripped off the skin, along with other contaminants. However, further investigation must be done to identify the exact interactions of iron oxide nanoparticles with the mucus membrane.
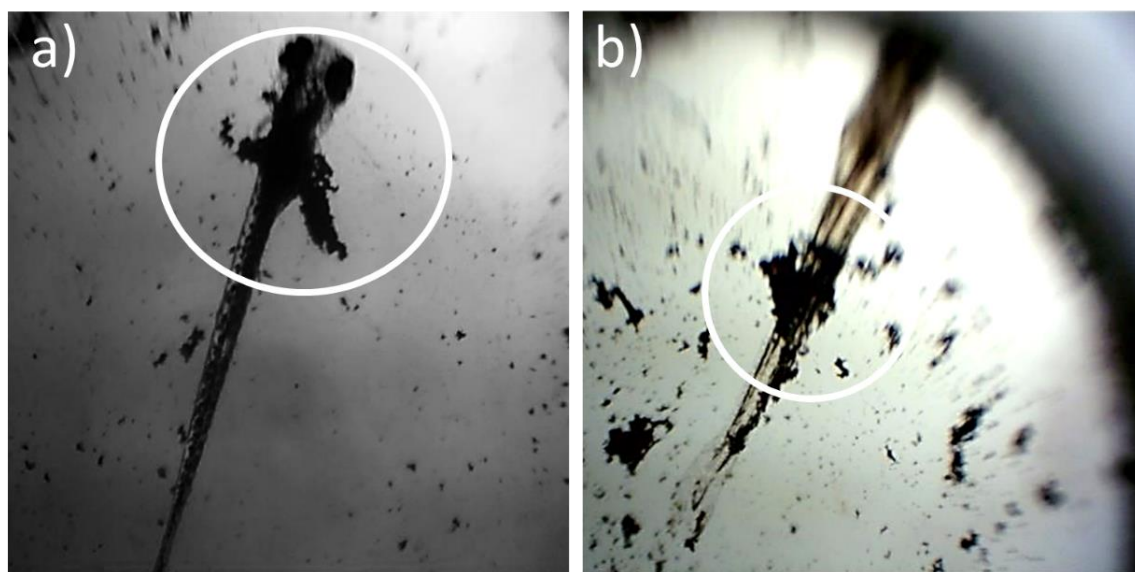
Figure 6. 5: Zebrafish larva exposed to 10% Au:Fe₃O₄-PEG nanoparticles at a concentration of 100 mg/L for 72 hours. The white circles show nanoparticles agglomerating at the gills (a) and the tail (b) of the fish.

After 72 hours, after exposure, the zebrafish were euthanized on an ice bath for at least three hours or until no heartbeat was detected under a brightfield microscope. The euthanized zebrafish larvae were then collected in a 15 mL falcon tube to further test the attachment of the uncoated Fe_3O_4, Fe_3O_4-PEG, and 10% Au:Fe_3O_4-PEG nanoparticles to the fish. This was done by applying an external magnetic field to the falcon tube, using a rare earth NdFeB magnet. It was observed that all zebrafish larvae, which were exposed

to the magnetic Fe_3O_4, Fe_3O_4-PEG, and 10% Au:Fe_3O_4-PEG nanoparticles, were collected on the magnet within three seconds (Figure 6. 6). It was observed that some larvae were faster attracted to the magnet than others, while other larvae showed no attraction at all. This allowed for the hypothesis that the dose-response was also visible by the agglomeration time, where a fast agglomeration represents a higher number of nanoparticles. This response to a magnetic field confirms the hypothesis that the magnetic Fe_3O_4, Fe_3O_4-PEG, and 10% Au:Fe_3O_4-PEG nanoparticles are attached to the fish. Whether this attachment occurs solely on the surface membrane (mucosal attachment) or through internalization of the nanoparticles into the fish, requires further experiments. Figure 6. 6 shows images of the euthanized zebrafish larvae being attracted to the applied magnet over a time of three seconds.
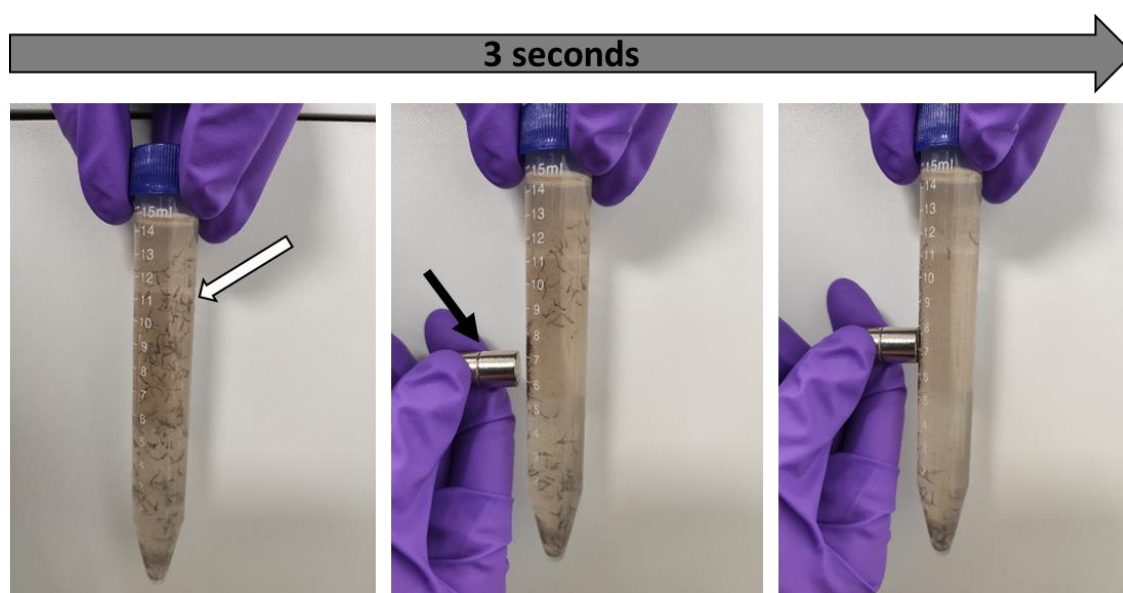
Figure 6. 6: Euthanized zebrafish larvae (white arrow) collecting on a NdFeB magnet (black arrow) within 3 seconds, after they were exposed to magnetic 10% Au:Fe₃O₄-PEG and Fe₃O₄-PEG and uncoated Fe₃O₄ nanoparticles for 72 hours in OECD water.

6.4. Conclusion and prospects

From the gathered results, it can be said that all zebrafish larvae survived the exposure to 10% $Au:Fe_3O_4$-PEG, Fe_3O_4-PEG nanoparticles, and Fe_3O_4 (0.1 - 2mM / 23.1 - 463.1 mg/L) and showed a 100% survival rate even at high concentrations of up to 2mM. At the same time, it is evident that the magnetic iron oxide nanoparticles agglomerated on the body of the fish and made it responsive to an external magnetic field.

Future work includes testing the hypothesis of monitoring the dose-response of magnetic Fe_3O_4 iron oxide nanoparticles by agglomeration time and identifying the physical barriers that avoid the internalization of the nanoparticles into the zebrafish.

6.5. References

[6.1.]   Invitrogen, PrestoBlue® Cell Viability Reagent, Frequently Asked Questions, Version No.: 21Mar**2012**

[6.2.]   C. Hoskins, L. Wang, W. P. Cheng and A. Cushieri; Dilemmas in the reliable estimation of the *in vitro* cell viability in magnetic nanoparticle engineering: which tests and what protocols?; Nanoscale Res. Lett.; **2012**, 7, 77.

[6.3.]   L. Y. Rizzo, S. K. Golombek, M. E. Mertens, Y. Pan, D. Laaf, J. Broda, J. Jayapaul, D. Moeckel, V. Subr, W. E. Hennink, G. Storm, U. Simon, W. Jahnen-Dechent, F. Kiessling and T. Lammers; *In vivo* nanotoxicity testing using the zebrafish embryo assay; J. Mater. Chem. B, **2013**, 3918.

[6.4.]   J D Best and W. K Alderton; Zebrafish: An *in vivo* model for the study of neurological diseases; Neuropsychiatr Dis Treat., **2008**, 4, 567–576.

[6.5.]   A, M. Vacaru, G. Unlu, M. Spitzner, M. Mione, E. W. Knapik, K. C. Sadle; *In vivo* cell biology in zebrafish – providing insights into vertebrate development and disease; Journal of Cell Science, **2014** 127: 485-495

[6.6.]   P. Antinucci, R. Hindges; A crystal-clear zebrafish for *in vivo* imaging; Sci Rep., 6, **2016**, 29490.

[6.7.]   J. C. Matos, A. R. Soares, I. Domingues, G. A. Monteiro, and M. C. Goncalves; ORMOPLEXEs for gene therapy: *In vitro* and *in vivo* assays; Mater. Sci. Eng. C-Mater. Biol. Appl., **2016**, 63, 546-553.

[6.8.] A. Jurewicz, S. Ilyas, J. K. Uppal, I. Ivandic, S. Korsching, and S. Mathur; Evaluation of Magnetite Nanoparticle-Based Toxicity on Embryo–Larvae Stages of Zebrafish (Danio rerio); ACS Appl. Nano Mater., **2020**, 3, 1621-1629.

[6.9.] D. M. Parichy, M. R. Elizondo, M. G. Mills, T. N. Gordon, and R. E. Engeszer; Normal Table of Post-Embryonic Zebrafish Development: Staging by Externally Visible Anatomy of the Living Fish; Dev Dyn., **2009**, 238, 2975–3015.

[6.10.] E. Haque and A. C. Ward; Zebrafish as a Model to Evaluate Nanoparticle Toxicity; Nanomaterials, **2018**, 8, 561.

[6.11.] A. Moiz; Antifungal action of methylene blue involves mitochondrial dysfunction and disruption of redox and membrane homeostasis in C. Albicans.; Open Microbiol J., **2016**, 10, 12-22.

[6.12.] Cold Spring Harb Protoc., E3 medium (for zebrafish embryos); **2011**, Cold Spring Harbor Laboratory Press doi:10.1101/pdb.rec066449

[6.13.] F.C.P. Freitas, T.S. Depintor, L.T. Agostini, D. Luna-Lucena, F. M. F. Nunes, M. M. G. Bitondi, Z. L. P. Simoes and A.P. Lourenco; Evaluation of reference genes for gene expression analysis by real-time quantitative PCR (qPCR) in three stingless bee species (Hymenoptera: Apidae: Meliponini); Sci Rep., **2019**, 9, 17692

[6.14.] HR Jia, YX Zhu, KF Xu, GY Pan, XY Liu, Y Qiao, and FG Wu; Efficient cell surface labeling of live zebrafish embryos: wash-free fluorescence imaging for cellular dynamics tracking and nanotoxicity evaluation; Chem. Sci., **2019**, 10, 4062-4068.

[6.15.] S. Dash, S. K. Das, J. Samal, and H. N. Thatoi; Epidermal mucus, a major determinant in fish health: a review; Iran J. Veterinary Res., **2018**, 19, 72-81.

CHAPTER 7

Key findings and developments, future work, possible applications

7.1. Introduction

This thesis displayed the broad spectrum of applications for iron oxide. Each chapter showed its unique way to functionalize, optimize and utilize iron oxide for their respective project aims. The key findings and developments are summarized in the following paragraphs.

7.1.1. Iron oxide-gold nanoparticles for multimodal contrast enhancement in magnetic resonance, computed tomography, and intravascular ultrasound imaging

In this chapter, the development of Au*MNPs which were synthesized using an impregnation method, leading to nanoparticles with pristine surfaces for either component. Pristine NP surfaces can be particularly important when functionalization needs to be engineered in molecularly targeted theragnostic applications. Moreover, the cytotoxicity of these Au*MNP was evaluated *in vitro* and showed that these were non-toxic to cells when a maximum concentration of 100 μg/mL was examined for 7 days. The contrasting capability of these Au*MNP was also shown to be concentration-dependent across all three (MR, CT, IVUS) imaging techniques. Most importantly, for the first time, it has been shown that larger diameter (20-30 nm) Au*MNPs can modify the MR signal in a T_1-weighted sequence which is routinely used for high spatial resolution anatomical imaging. This assessment supports the use of larger diameter Au*MNPs, beyond their well-established contrasting ability in T_2-weighted sequences. For the first time, it was finally shown that the Au content of the Au*MNP can lead to evident increases of the IVUS signal and suggest that Au*MNP can potentially support a novel IVUS imaging methodology to simultaneously assess atherosclerotic plaque development and inflammation. In conclusion, these materials can be developed further into a powerful tool to enhance theragnostic applications and tri-modal imaging accuracy in the clinical setting.

7.1.2. Impedance based measurements and CARS imaging as advanced techniques to assess the cytotoxicity of nanomaterials on liver cells *in vitro*

Since the liver is one the most important organs for blood purification, detoxification of chemicals, and metabolization of drugs, studying the effects of nanoparticles on liver cells is crucial to understand how the liver and especially liver cells behave after exposure to Fe_3O_4 iron oxide nanoparticles. Even though colorimetric assays such as CellTiter-Glo and PrestoBlue have been established as valuable cell assays all over the world, some restrictions, such as the absorption of light, can alter the data and produce inaccurate results and estimates. By analyzing the liver functions and the cell response in 2D and 3D cultures an accurate estimation of the toxicity of nanoparticles can be made. The results suggest that impedance-based measurements (xCELLigence system) and Coherent Anti-Stokes Raman Scattering (CARS) are powerful tools to analyze the cell viability of liver cells. Measuring the effects of nanoparticles on the cell cultures through an electrical current does not only provide valuable data on the immediate effects in real-time but also allows for long-term exposures. Liver cells in 2D cultures *in vitro* do not necessarily represent an accurate behavior of liver cells, future work will focus on the further development of the 3D liver tissue model to mimic the liver's behavior more accurately.

7.1.3. Monitoring the cell internalization of iron oxide nanoparticles using a holographic imaging system

The next stage focuses on further toxicity tests of PEG-coated magnetic iron oxide nanoparticles studying the internalization kinetics of particles based on the roughness on cell surfaces. To use nanoparticles for biomedical applications, for instance as contrast agents, several aspects must be considered and addressed upfront. MTT color assays and impedance measurements will provide further information about the impact and effects of PEG-coated MNPs on MCF-7 breast cancer cells. Moreover, the use of toxic nanoparticles presents negative controls for comparison. These will be prepared by replacing the Fe_3O_4 core particle with toxic Co_3O_4 nanoparticles and changing the biocompatible polyethylene glycol coating with different surface functionalization that are known to be toxic to living cells. The toxicity of these MNPs will be monitored over MCF-7 cancer cells using a HoloMonitor M4 microscope. This digital imaging method will generate further information about the cell internalization process of nanoparticles and therefore help to optimize the cell uptake of functionalized nanoparticles into cell and tissue cultures and improve their intended purposes such as drug delivery and contrast enhancement.

7.1.4. Magnetic molecularly imprinted polymer networks and spheres (MMIPs) for the selective binding of antibiotics

This chapter presented the successful synthesis of magnetic molecular imprinted (MMIPs), with the antibiotics erythromycin (ERY) and ciprofloxacin (CPX) as template molecules, and non-imprinted polymers (MNIPs) without template molecules. Both imprinted samples showed high binding capacities of 70 mg/g and 32 mg/g and established their maximum binding capacity within 40-60 minutes after exposure. The imprinted samples were tested on their recovery rates using magnetic separation and retained 68 – 75 % of their binding capacity after 4 cycles. The high selectivity of all MMIPs towards their respective template molecule (ERY or CPX) was demonstrated in methanol:water and milk matrices. A reduced homogenization speed at 25,000 rpm resulted in the synthesis of spherical polymers rather than a porous network. The ERY-MMIP spheres showed a similar binding capacity of 70 mg/g for imprinted and 40 mg/g for non-imprinted samples, which was established after 40-60 minutes. The selectivity of ERY-MMIP spheres was determined in the milk matrix and showed a clear binding preference for the target molecule erythromycin. The comparison of the two different MMIP samples (network and sphere) shows that despite their different structures, both polymers have similar binding capacities and selectivity. The combination of a highly selective polymer structure towards antibiotic pollutants and the magnetic property of iron oxide (Fe_3O_4) can be a useful tool to monitor and remove antibiotic pollutants from freshwater sources and food products. While the polymer binds the target molecules, the whole system can be recovered by simply applying a magnetic field rather than time-consuming and laborious centrifugation and filtration processes. Further modifications and interchangeable template molecules allow the use of a magnetic MIP system for a broad range of applications and can help to tackle the global problem of pharmaceutical and chemical pollution in aquatic environments. Future work includes the determination of the lower binding and detection limits of the MMIP networks and spheres

7.1.5. Zebrafish larvae as *in vivo* model system for the characterization of iron oxide supported gold nanoparticles with polyethylene glycol coating

This chapter summarizes that all zebrafish larvae survived the exposure to 10% Au:Fe_3O_4-PEG, Fe_3O_4-PEG, and uncoated Fe_3O_4 nanoparticles with concentrations ranging from 0.1 - 2mM or 23.1 - 463.1 mg/L. The results showed a 100% survival rate, even at high concentrations of up to 2mM. At the same time, it was evident that the magnetic iron oxide nanoparticles agglomerated on the body of the fish and made it responsive to an external magnetic field.

Future work includes testing the hypothesis of monitoring the dose-response of magnetic Fe_3O_4 iron oxide nanoparticles by agglomeration time and identifying the physical barriers that avoid the internalization of the nanoparticles into the zebrafish.

7.2. Concluding remarks

In this thesis, various applications of functionalized iron oxide nanoparticles are demonstrated and display their great potential for future use in biomedical sciences. Their unique properties in size, shape, and magnetism can be selectively modified and utilized for a broad range of applications. Constant research and development of these nanoparticles show that their prospective use empowers researchers to valuable analytical and investigative insight, leading to never seen innovation and development in the biomedical sector.

CHAPTER 8

Journal publications produced from this thesis

8.1.   Selective binding of antibiotics using magnetic molecular imprint polymer(MMIP) networks prepared from vinyl-functionalized magnetic nanoparticles

J. Kuhn, G. Aylaz, E. Sari, M. Marco, H. H. P. Yiu, and M. Duman

J. Hazard. Mater., 2020, 387, 121709.

Selective binding of antibiotics using magnetic molecular imprint polymer (MMIP) networks prepared from vinyl-functionalized magnetic nanoparticles

Joel Kuhn[a,1], Gülgün Aylaz[b,1], Esma Sari[c], Mariano Marco[a], Humphrey H.P. Yiu[a,*], Memed Duman[b,*]

[a] Chemical Engineering, School of Engineering and Physical Sciences, Heriot-Watt University, Edinburgh, EH14 4AS, UK
[b] Nanotechnology and Nanomedicine Division, Institute of Science, Hacettepe University, Ankara, Turkey
[c] Vocational School of Health Services, Medical Laboratory Techniques, Yüksek İhtisas University, Ankara, Turkey

GRAPHICAL ABSTRACT
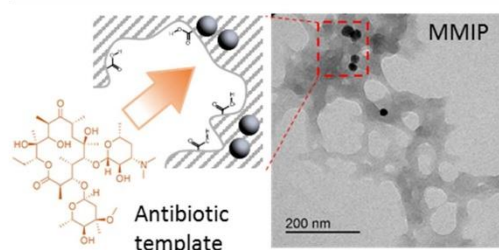
ARTICLE INFO

ABSTRACT

Adverse effects of pharmaceutical emerging contaminants (PECs), including antibiotics, in water supplies has been a global concern in recent years as they threaten fresh water security and lead to serious health problems to human, wildlife and the environment. However, detection of these contaminants in water sources, as well as food products, is difficult due to their low concentration. Here, we prepared a new family of magnetic molecular imprinted polymer (MMIP) networks for binding antibiotics via a microemulsion polymerization technique using vinyl silane modified Fe_3O_4 magnetic nanoparticles. The cross-linked polymer backbone successfully integrated with $20-30$ nm magnetic nanoparticles and generated a novel porous polymeric network structure. These networks showed a high binding capacity for both templates, erythromycin and ciprofloxacin at 70 and 32 mg/g. Both MMIPs were also recyclable, retaining 75 % and 68 % of the binding capacity after 4 cycles. These MMIPs have showed a clear preference for binding the template molecules, with a binding capacity 4- to 7-fold higher than the other antibiotics in the same matrix. These results demonstrate our MMIP networks, which offered high binding capacity and selectivity as well as recyclability, can be used for both removal and monitoring hazardous antibiotic pollutants in different sources/samples and food products.

---

* Corresponding authors.
   E-mail addresses: h.h.yiu@hw.ac.uk (H.H.P. Yiu), memi@hacettepe.edu.tr (M. Duman).
   [1] These authors contributed equally.

1. Introduction

Water security is now a global issue to humanity as poor supply of clean water in developing countries affect the health and lives of over one billion of people, as well as the wildlife and the environment. Water pollution can come from industrial and agricultural activities (Anon, 2019a, b; Anon, 2018a, 2017). One class of pollutants being a major hazard to human lives is Pharmaceuticals Emerging Contaminants (PECs), including antibiotics and other drugs present in fresh water sources (rivers, lakes, underground water sources) (Larsson, 2014; Bengtsson-Palme and Larsson, 2016). These pollutants usually exist in an ultralow concentration (e.g. < ppm level), making them difficult to detect with conventional methods (e.g. colorimetric methods), but high enough to cause catastrophic problems including Antimicrobial Resistance (AMR), which is now one of the top priority in the WHO agenda (Anon, 2019c, b; Anon, 2019d; Finley et al., 2013; Baquero et al., 2008). Conventional analytical methods including spectrophotometry (Samia et al., 2002), mass spectrometry (Caro et al., 2006), liquid chromatography (Urraca et al., 2014), solid phase extraction (Sun et al., 2014), capillary electrophoresis (Zhou et al., 2008) and electrochemical techniques (Ionescu et al., 2007) have all been used for the detection of antibiotic pollutants. These methods all have some disadvantages, e.g. being time-consuming, expensive, laborious, and requiring experienced/skillful analysts. Moreover, few methods are currently available for selective removal of PECs from water sources (Rodriguez-Narvaez et al., 2017; Basheer, 2018; Cantarella et al., 2019). Research on new detection systems for antibiotic pollutants needs to focus on developing methods that are sensitive at sub-ppm level, specific, reproducible, cost effective, and having fast response time.

Recently, molecular imprinting technique has been developed for the detection and removal of these hazardous PECs including antibiotic pollutants (Sari et al., 2018; Okan and Duman, 2018). Molecularly imprinted polymers (MIPs) allow rapid and highly selective adsorption on target analytes (Yan et al., 2013). MIPs are polymers built around the target analytes and the final polymer matrix are printed with specific cavities with a three-dimensional structure complementary to the shape, size and binding sides of the analytes (Banerjee and König, 2013). These MIPs are chemical and mechanical stable, have long shelf life and are economical to prepare when compared with antibodies and natural receptors. However, many MIP examples reported in the literature are based on the preparation of a bulk polymer (e.g. monoliths), which usually associates with a low surface area and therefore a low binding capacity (Armutcu et al., 2014; Yoshikawa et al., 2016). Recently, MIP nanoparticles have been a solution for this problem by enhancing surface area, fast binding kinetics, binding capacity and stability (Hoshino et al., 2008; Guan et al., 2012). Unfortunately, using MIP nanoparticles still has a major obstacle, namely inefficient recovery via filtration (significant loss of materials) and centrifugation (time consuming and laborious).

Incorporation of a magnetic component to an MIP system will help separation using an external magnetic field. Functionalized magnetic nanoparticles (MNPs) have been used for separation, isolation and purification of proteins (Chang et al., 2018, 2019; Konwar et al., 2019; Guo et al., 2019; Sun et al., 2019). However, in order to enhance selective binding, more sophisticated methods such as immunobinding may be required but this is not applicable to most antibiotics. Magnetic MIP systems, or MMIPs, can be used for binding biomolecules with high specificity and enhanced recovery. Despite such advantages, few published research works on the development of MMIPs for antibiotic detection were found (Tong et al., 2017; Chen et al., 2009; Comber et al., 2018). For example, Tong et al. demonstrated magnetic imprinted polymers for the solid phase extraction of fluoroquinolone antibiotics (ciprofloxacin, lomefloxacin, enoxacin and norfloxacin). The MMIP was made using acrylic acid as functional monomer and N,N′-Methylenebis (acrylamide) as cross-linker with an Fe_3O_4/SiO_2 core. In combination with a HPLC, a detection limit of 4.1–21.3 µg/L (ppb) was reported (Tong et al., 2017). Chen et al. also prepared MMIPs using a monomer matrix of styrene and divinylbenzene with methacrylic acid (MAA) as the functional monomer for the separation of tetracycline antibiotics from egg and tissue samples (Chen et al., 2009). The detection limit was found to be < 0.2 ng g^{-1} (or ppb) (Comber et al., 2018) when used in tandem with a LC–MS system. In our work presented here, we demonstrated the synthesis of MMIP networks for binding erythromycin (ERY) and ciprofloxacin (CPX), chosen as model PECs, via a microemulsion pathway. The resultant MMIP materials showed a highly porous structure and are capable of selective binding of the target antibiotics. Cross binding tests have also been carried out to demonstrate the selectivity of MMIPs.

2. Experimental section

2.1. Materials

Ethylene glycol dimethacrylate (EGDMA, 98 %), 2-hydroxylethyl methacrylate (HEMA, 98 %), methacrylic acid (MAA, 99 %), erythromycin (ERY, BioReagent), polyvinyl alcohol (PVA, Mw = 13,000–23,000, 87–89 % hydrolyzed), sodium dodecyl sulfate (SDS, 99 %), ammonium persulfate ($(NH_4)_2S_2O_8$, 98 %), and sodium bisulfite ($NaHSO_3$, ACS reagent), ciprofloxacin (CPX), tetracycline, kanamycin sulfate and neomycin sulfate were all purchased from Sigma-Aldrich, UK. 3-Butenyltriethoxysilane (vinyl silane, 95 %) was supplied by Fluorochem UK while magnetite Fe_3O_4 nanoparticles (20 – 30 nm) were supplied by Alfa Aesar. The solvents methylated spirit (industrial 74 O.P.), toluene (reagent grade), acetic acid (glacial) and methanol (lab reagent grade) were purchased from Fisher Scientific UK Ltd. Toluene was dried by mixing the solvent with activated molecular sieves (type 4A, general purpose grade, Fisher Scientific UK Ltd.) in a closed container for 24 h. All other chemicals were used as received without further purification.

2.2. Synthesis of magnetic molecular imprinted particles (MMIPs)

Vinyl silane (3-butenyltriethoxysilane) coated magnetic nanoparticles (vinyl-MNPs) were prepared using a standard silanization protocol published elsewhere (Yiu et al., 2013). The synthesis of magnetic MIPs (MMIPs) with erythromycin as antibiotic template molecule was carried out using a two-phase microemulsion polymerization method (Okan et al., 2017; Sari et al., 2016). Three solutions were prepared; two aqueous solutions and one organic phase. The first aqueous phase was prepared by dissolving polyvinyl alcohol (PVA, 94 mg), sodium dodecyl sulphate (SDS, 14 mg) and sodium bicarbonate (12 mg) in 5 mL of deionized water. The second aqueous phase was a solution of PVA (50 mg) and SDS (50 mg) in 100 mL water. The organic phase was prepared by mixing the co-monomers methacrylic acid (MAA, 2.17 mmol) and (hydroxyethyl) methacrylate (HEMA, 1.85 mmol) with the cross-linker ethylene glycol dimethacrylate (EGDMA, 5.56 mmol) and 50 mg of vinyl-MNPs. The template molecule erythromycin (136 µmol) was added to the organic phase to establish a ratio between the monomers MAA and HEMA and the template in a 16:13.6:1 (MAA:HEMA:ERY) mole ratio. This optimized ratio was set based on our prior work (Sari et al., 2016).

The organic phase was then mixed with the first aqueous phase and homogenized using an ISOLAB homogenizer at 30,000 rpm (Laborgeräte GmbH). The resultant microemulsion was then added to the second aqueous phase while stirring at 600 rpm using a mechanical stirrer (IKA Eurostar 20 digital). The final mixture was slowly heated to the polymerization temperature of 40 °C. When the polymerization temperature was reached, sodium bisulfite (125 mg) and ammonium persulfate (125 mg) were added to initiate the polymerization process. After 24 h, the polymerized sample was recovered using a magnet and the magnetic solid was denoted as ERY-MMIP. The collected ERY-MMIP emulsion was washed five times with a 50 % v/v ethanol in water solution and then three times with deionized water. The template was removed using 20 % v/v acetic acid in water. The ERY-MMIP sample was then dispersed in deionized water and stored at 4 °C.

2

Magnetic CPX imprinted polymer (CPX-MMIP) was synthesized using the ERY-MMIP method above but ciprofloxacin (33.13 mg, 100 μmol) was used as the template with a molar ratio of 1:30 (CPX:MAA). Non-imprinted magnetic polymers (MNIP) were prepared following the same procedure except for voiding the antibiotic template.

2.3. Characterization of magnetic molecularly imprinted polymers (MMIPs)

FTIR spectra of vinyl-MNPs, MMIPs and MNIPs were recorded using a Bruker Fourier transform infrared spectrometer (Vertex 70v) in the range of 500–4000 cm^{-1} with a 2 cm^{-1} resolution. All samples were washed, dried and without template molecules. TEM images of the particles and polymer network were taken on a Tecnai T20 (FEI) operating at 120 kV (Kelvin Nanocharacterization Centre, University of Glasgow, UK) to examine the morphologies of MMIPs and MNIP. SEM images were acquired using a TESCAN GAIA 3 microscope with an accelerating voltage of 5.0 kV. Thermogravimetric analysis (TGA) was performed using a thermobalance (Q500, TA Instruments). In a typical experiment, a heating rate of 10 °C/min was used to heat up a sample to a final temperature of 800 °C. The temperature was held isothermal for 60 min at 800 °C and then cooled down to room temperature. The resulting weight loss profile was used to determine the organic content in the magnetic polymer network.

2.4. Antibiotic binding tests

2.4.1. Determination of binding capacity

The binding capacity of MMIP and MNIP on ERY and CPX was studied by analyzing a range of concentrations, ranging from 8 to 100 mg/mL of the template/target molecules (ERY and CPX) in a 4:1 methanol:water solution. The absorbance values (A_i) for ERY and CPX at 280 nm and at 275 nm respectively were first measured using a Cary 100 Bio UV–vis Spectrophotometer (Agilent) before incubating the solution (3 mL) with 28.8 mg of the corresponding MMIP sample for 2 h. The MMIP and MNIP samples were then removed using a magnet and the absorbance values of the supernatants (A_f) were measured again at 280 nm and 275 nm. Concentration values (C_i and C_f) were derived from the calibration curve. The binding capacity (Q) values were then calculated from the equation (Comber et al., 2018)

$$Q = (C_i - C_f)\frac{V}{m}$$

where Q is the Binding Capacity (in mg/g of MMIP), C_i and C_f are the initial and final concentration of the template molecule (in mg/mL), V is the Volume of the incubated solution (in mL), and m is the mass of the MMIP used (in g). The imprinting factor (IF) is calculated as

$$IF = \frac{Q_{MMIP}}{Q_{MNIP}}$$

where Q$_{MMIP}$ and Q $_{MNIP}$ is the binding capacity using MMIP and non-imprinted MNIP samples respectively (Nantasenamat et al., 2007). All binding and cross-binding measurements were triplicated and the standard deviations were calculated and plotted in graphs as error bars.

2.4.2. Time studies (binding kinetics) and recycling

A time study was also set out to determine the minimum time for a maximum adsorption capacity of ERY and CPX by the MMIP samples. The lowest concentration (40 mg/mL and 10 mg/mL) showing the maximum binding capacity for ERY-MMIP and CPX-MMIPs respectively were used for this study. A similar measurement procedure to binding capacity measurement was carried out. The absorbance values of the supernatant were measured after removing the MMIPs at time intervals of 10, 20, 40, 60, 90, 120, 150, 180 min (A_f). Concentrations (C_i and C_f) and Q values were calculated as mentioned previously. In order to test the reusability of the imprinted magnetic nanoparticles, a recycling test was performed using 40 mg/mL ERY solution and an NdFeB magnet for

recovering the MMIP particles after each cycle. The binding sites were regenerated with 20 % v/v acetic acid in water. Four cycles in total were performed for both ERY-MMIP and CPX-MMIP samples.

2.4.3. Selectivity tests in methanol/water media and milk matrices

The selective binding capacity of MMIP was tested in the presence of three other competing antibiotics (tetracycline, kanamycin sulfate and neomycin sulfate), each at a concentration of 40 mg/mL. These three competing antibiotics were selected because they are widely used as prescription medicine. Using the derived concentration of the template antibiotic for achieving optimal binding capacity and the incubation time from the previous time studies, the selectivity studies were performed with the optimized concentration of ERY (40 mg/mL) and CPX (10 mg/mL). A selectivity test using ERY-MMIPs comprised of two different solutions, methanol/water (4:1 v/v mixture) and skimmed milk. Each test solution contained 40 mg/mL of the antibiotics and was stirred for 40 min after the addition of ERY-MMIPs. Before the incubation period, the absorbance values (A_i) of each emulsion for the specific wavelengths of neomycin sulfate (304 nm), tetracycline (365 nm), kanamycin sulfate (527 nm) and ERY (280 nm) was determined from a full UV analysis. After incubation and extraction of the MMIPs from samples, the absorbance values (A_f) of the supernatants were measured again to detect any differences. The binding capacities (Q) were established by using the same method as stated previously. All experiments were repeated in triplicate. Selectivity tests using CPX-MMIP were performed in the same manner as the ERY-MMIP studies, but with a concentration of 10 mg/mL for each antibiotic (ciprofloxacin, tetracycline, kanamycin sulfate and neomycin sulfate) and an incubation time of 60 min. The absorbance value of ciprofloxacin (A_i) was analyzed at 275 nm. The selectivity factor (SF) is calculated as

$$SF = \frac{Q_{template}}{Q_{competitor}}$$

where $Q_{template}$ and $Q_{competitor}$ is the binding capacity for the template molecules (ERY or CPX) and that for the competitive molecules respectively using MMIP.

Due to the similar wavelength of absorbance between ERY and CPX (280 nm vs 275 nm), a separate set of cross-binding experiments was set out to assess the selectivity towards the other template. In this experiment, only the other antibiotic candidate was dissolved in solution at the concentration achieving the binding capacity for the MMIP sample. For instance, in an experiment using ERY-MMIP for binding CPX, 28.8 mg of ERY-MMIP sample was suspended in methanol/water or milk matrix with a concentration of 40 mg/L of CPX. Absorbance at 275 nm for CPX was measured before and after incubation for 40 min. The data was treated as mentioned previously. A reverse experiment, CPX-MMIP for binding ERY, was also carried out with the same protocol but at 280 nm.

3. Results and discussion

3.1. Characterization of MMIPs

The formation of MMIPs is based on the co-polymerization of MAA and HEMA around the template molecules (ERY or CPX), as shown in Fig. 1. The vinyl-MNPs became part of the polymer network by co-polymerizing with monomers MAA and HEMA. EGDMA served as a cross-linker to provide a more rigid polymer structure.

The chemical structures of the imprinted (MMIP) and non-imprinted (MNIP) samples were analyzed using FTIR spectroscopy. The spectra of the MMIP and MNIP particles, shown in Fig. 2, are almost identical as they are both PMAA-based materials. The characteristic bands in the spectra were found at 2950 cm^{-1}, 1720 cm^{-1}, 1250 cm^{-1} and 1130 cm^{-1}. Broad bands at 3100–3500 cm^{-1} are typically due to −OH stretching from both MAA and HEMA units. The peaks at around
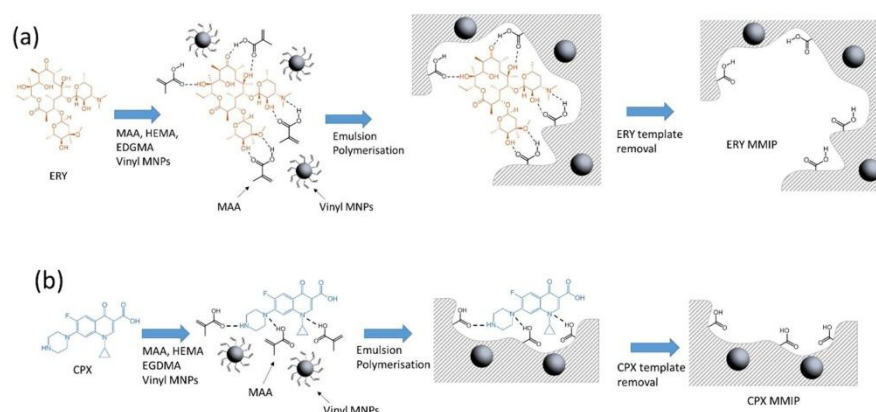
3

Fig. 1. An illustration for the formation of (a) ERY-MMIP and (b) CPX-MMIP.
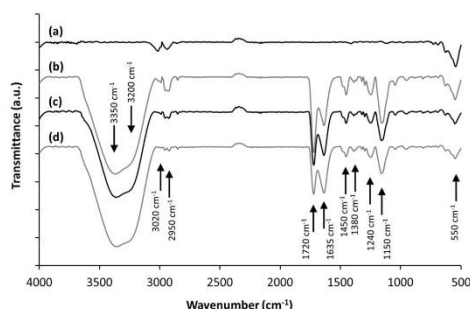

Fig. 2. FTIR spectra of (a) vinyl-MNP, (b) erythromycin imprinted MMIP (ERY-MMIP), (c) ciprofloxacin imprinted MMIP (CPX-MMIP) and (d) non-imprinted MMIP (MNIP).

$3020\,cm^{-1}$ and $2950\,cm^{-1}$ were attributed to $-CH$ stretching from alkenes and alkanes respectively. Carbonyl $-C=O$ stretching bands were shown at $1720\,cm^{-1}$ while bands at 1450 and $1380\,cm^{-1}$ were due to $-CH_3$ and $-CH_2-$ deformation vibrations (Rufino and Monteiro, 2003). The $-C-O-$ single bond stretching bands around $1250\,cm^{-1}$ were assigned to the carboxyl group ($-COO^-$) of MAA and HEMA, while the $-C-O-$ stretching bands around $1130\,cm^{-1}$ refer to the ester group of EGDMA. Bands at $1620\,cm^{-1}$ were attributed to the $C=C$ stretching from residual monomers. Adsorption peaks at around $550\,cm^{-1}$ were due to Fe_3O_4 particles. The spectra confirmed that all three samples have a PMAA-HEMA backbone with EGDMA crosslinking units.

The morphology of the ERY-MIP and CPX-MIP were examined using transmission electron microscopy (TEM) and scanning electron microscopy (SEM). TEM images shown in Fig. 3a.i and a.ii depicted the porous network nature of both MMIP materials. While the magnetic nanoparticles of around 20–30 nm were embedded in the polymer, there are pores ranging from 10 - > 100 nm in the polymer structure. This is likely to be caused by homogenizing the emulsion. Such a porous structure indeed provides a higher surface area for antibiotic binding and facilitating drug diffusion towards the recognition sites. The non-imprinted material (MNIP, Fig. 3a.iii) showed a remarkably similar structure, suggesting that the addition of a template (target) molecule did not alter the porous morphology of the polymer. Fig. 3b.i, b.ii and

b.iii are SEM images for ERY-MMIP, CPX-MMIP and MNIP respectively. No significant difference was observed in morphology.

In order to quantify the polymer content in MMIP and MNIP samples, thermogravimetric analyses (TGA) were carried out in flowing air; the results are shown in Fig. 3c. All three samples showed a very similar TGA weight loss profile, with the main weight loss recorded between 250 and 450 °C. This weight loss is caused by the combustion of the PMAA polymer. The remaining weight percentage are due to the Fe_3O_4 remains that have been oxidized to Fe_2O_3. The results suggested that a total content of 16 % and 21 % of Fe_3O_4 in the ERY-MMIP and CPX-MMIP samples. The non-imprinted MNIP sample showed a similar weight loss profile, with a final residual weight of 14 %. These amounts of magnetic nanoparticles in the MIP polymer network allow the materials to get separated, recovered, and recycled through the application of a magnetic field.

3.2. Binding capacity and recycling of MMIP samples

The binding capacities for the template (or target) molecules (ERY and CPX) were established by performing binding experiments in a concentration range from 8 to 100 mg/mL. Results depicted in Fig. 4a and b showed that ERY-MMIP and CPX-MMIP networks have a maximum binding capacity of 70 mg/g and 32 mg/g respectively. These binding capacities showed a considerable improvement when comparing with a bulk polymer material imprinted with roxithromycin, which showed a binding capacity of around 12 mg/g (Yu et al., 2010). While CPX-MMIP achieved a maximum adsorption at the lowest concentration of 10 mg/mL, the binding capacity of ERY-MMIP peaked at 40 mg/mL. In the same experimental setup non-imprinted polymers showed a max binding capacity of 20 mg/mL and 10 mg/mL respectively. This equals to only 30 % of their imprinted counterpart, or imprinting factors of 3.28 and 3.37, and is proved that functional binding sites for the desired target molecules were printed on the MMIP networks. Since the same synthesis method was used to prepare imprinted and non-imprinted MIPs albeit use of a template, both polymer networks showed a similar structure and porosity. The binding kinetics were examined by conducting the time study on binding the target molecules at the optimal template concentrations of 40 mg/mL (ERY) and 10 mg/mL respectively (CPX). The time curves shown in Fig. 4c and d suggested that a maximum binding capacity can be achieved from both MMIP samples within 40–60 min after exposure. In all curves, after the binding capacity reaching a peak, there is a small reduction on binding capacity at a higher concentration, which causes a higher error in absorbance. Nonetheless, we have observed the maximum binding that each set of
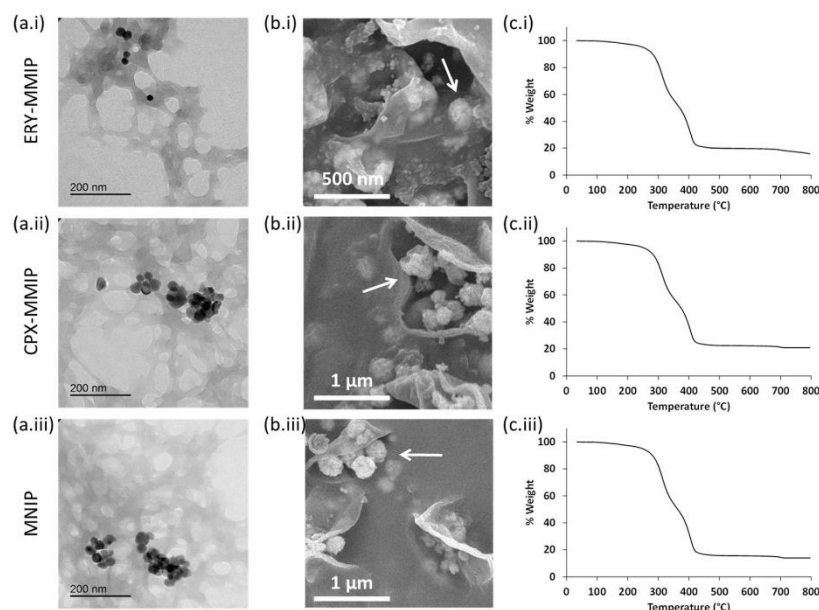
4

Fig. 3. TEM images of (a.i) ERY-MMIP, (a.ii) CPX-MMIP and (a.iii) MNIP. All showed the morphology of a porous polymer network. SEM images of (b.i) ERY-MMIP, (b.ii) CPX-MMIP and (b.iii) MNIP. The white arrows depict the magnetic nanoparticle aggregates embedded in a polymer matrix. The TGA weight loss profiles of (c.i) ERY-MMIP, (c.ii) CPX-MMIP and (c.iii) MNIP are shown with residual weight caused by the magnetic Fe_3O_4 component (14–21%).

experiments can achieve. The binding capacity of the ERY-MMIP and CPX-MMIP prepared in this work is compared with other related studies from the literature in Table 1. Data from the literature showed that the binding capacity of an antibiotic-templated MIP ranges from 2.4 to 190.1 mg/g for various antibiotics. In a related study, an MIP system showing 18.7 mg/g of binding capacity for enrofloxacin, followed by an HPLC-MS/MS analysis, recorded a detection limit 5–1000 μg/kg, which is at ppb level (Urraca et al., 2014). However, the detection limit is highly dependent on the complimentary technique for quantifying the target antibiotics. Since our MMIP networks have a binding capacity a comparable level, we expect the same range of detection limit if a similar quantification system (HPLC-MS/MS) is used.

In order to compare the imprinting property of the MMIP networks, the imprinting factor (IF) of ERY-MMIP and CPX-MMIP against the MNIP was presented in Table 1 and 2. Both materials showed an IF 3.28–5.45, which are comparable with values reported in the literature (see Table 1). Incorporation of magnetic nanoparticles into the MIP networks did not affect the imprinting property. In general, the binding capacity and imprinting factor can be affected by the measuring conditions such as pH and temperature of the medium. From related studies in the literature, the optimum pH for binding is around neutral (Javanbakht et al., 2012). This is because at an extreme pH environment, acid groups will be protonated (at low pH) while basic groups will be deprotonated (at high pH). As such electrostatic interaction between template molecules and binding sites will diminished, leading to a lower binding capacity. Regarding the effect of temperature, a higher solution temperature will increase the kinetic energy of molecules, leading to an increase in non-specific interaction and binding (Sánchez-Polo et al., 2015). Therefore, a lower specificity will be recorded (imprinting factor and selectivity factor). Also, at an elevated temperature, the polymer networks are expected to be less rigid and

more relaxed. The shape recognition property may reduce and non-specific binding can therefore increase.

The key feature of MMIPs over non-magnetic MIP materials is that they can be recovered and reused using a magnetic field. Common separation techniques of bulk MIPs include filtration or centrifugation, but of both them have their drawbacks. Filtration can cause a significant loss of materials, in particular for nano-scaled materials, while centrifugation is usually laborious and time consuming. Magnetic separation can circumvent these problems. A series of recycling experiments using magnetic separation had been carried out to establish the reusability of MMIP samples. Fig. 4e and f show that both ERY-MMIP and CPX-MMIP are recyclable and retained 75 % and 68 % of the binding capacity for their corresponding template molecules after 4 cycles. Reduction in binding capacity can be attributed to two reasons: (1) < 100 % recovery efficiency from a simple magnetic separation, and (2) < 100 % regeneration of binding sites. The former can be improved by developing a more sophisticated magnetic separation system with a stronger magnetic field, e.g. use of an electromagnet. The latter depends on the regeneration method and the MIP structure. In this work, we use a mild acid (acetic acid) to remove bound antibiotic in order to avoid damages on the delicate MMIP network structures. In theory, a stronger acid such as HCl may improve the regeneration efficiency, but this may also increase non-selective binding upon damaging the shape of the binding sites.

3.3. Selective binding and cross-binding in methanol-water and milk matrices

One distinct advantage of MIPs is their specific recognition of molecules based on their shape and surface functionalities. To demonstrate this on our MMIP networks, a series of experiments were set out using

5
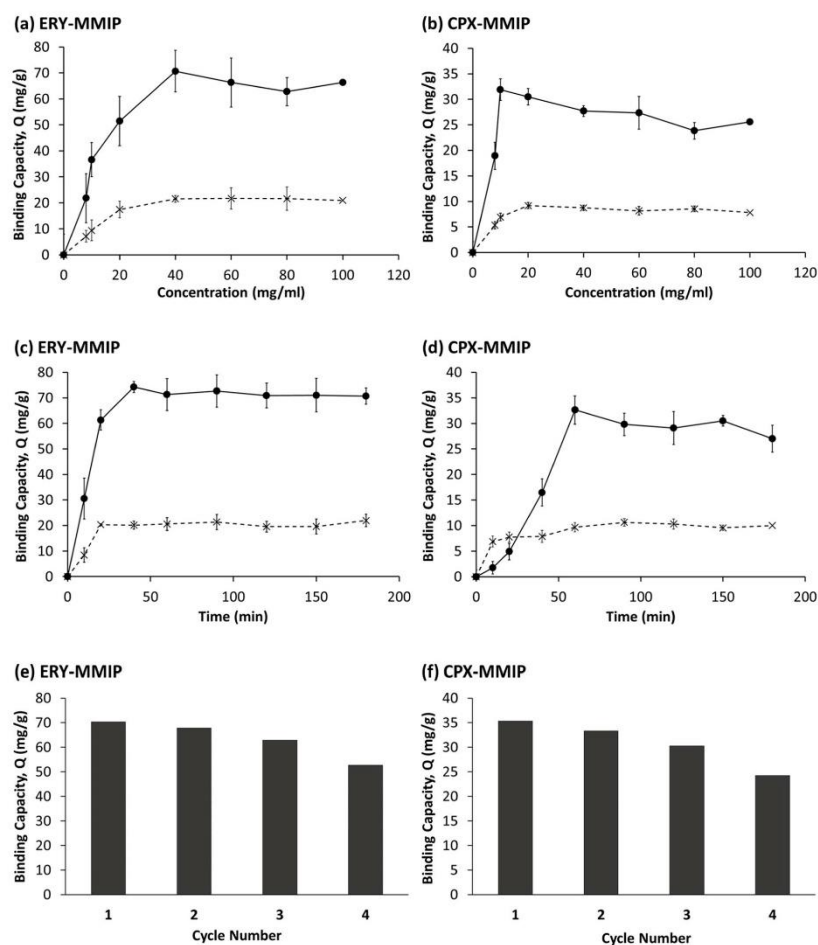
Fig. 4. Binding capacity (*Q*) vs concentration of template molecules for (a) ERY-MMIP and (b) CPX-MMIP and time studies on binding capacity for (c) ERY-MMIP and (d) CPX-MMIP. The dotted lines depict the binding capacity of non-imprinted MNIP materials vs template concentration (a and b) and time (c and d). Recycling of (e) ERY-MMIP and (f) CPX-MMIP in binding the template molecule. MMIP samples were recovered using an NdFeB magnet after each cycle.

ERY-MMIP and CPX-MMIP to selectively bind the target antibiotic molecules in a methanol/water medium in the presence of three other antibiotics (neomycin sulfate, tetracycline and kanamycin sulfate), which are selected because they are widely prescribed in medicine and likely to be a pollutant. The ERY- (Fig. 5a) and CPX-imprinted (Fig. 5b) polymer networks show a clear preference towards their imprinted target/template molecules with a selectivity factor of 3.59–10.06 against the competing antibiotics. Among these competing antibiotics, two possess structural similarity (with two glycosides) to erythromycin but no specific improvement was observed, compared with selectivity factors against other competing antibiotics. Non-imprinted MNIP samples showed no particular selectivity or binding affinity to any of the used antibiotics. This result suggested both ERY-MMIP and CPX-MMIP were imprinted with template specific binding sites and can be used for highly selective binding.

More importantly, such selective binding property was not limited to the simple methanol/water medium. Fig. 5c and d showed the results of similar experiments carried out in a milk matrix and the selectivity of both ERY-MMIP and CPX-MMIP was retained. Milk was selected for two reasons; (1) its complexity allows us to validate the selective binding property of MMIP networks in a realistic environment, and (2) it can be used as a model food product since antibiotic contamination in food is a growing concern. This shows the versatility and practicality of these MMIP samples in binding and removal of antibiotics from different media. Results from the experiments in a milk matrix were also significant. One major source of antibiotic pollution was due to misuse of antibiotic in agricultural activities, such as cattle and poultry farming. Excessive use of antibiotics to these animals will leave traces of residues in their meat, eggs (for poultry) and milk products (for cattle). Since these traces can be in a very small amount (< ppb level), detection and

6

Table 1
A summary of binding capacity and imprinting factor for key antibiotic-templated MIP systems reported in the literature. (PMDETA = N,N,N′,N′,N″-pentamethyl diethylenetriamine, TFMAA = 2-(Trifluoromethyl)acrylic acid, GMA = Glycidyl methacrylate).

Analyte	Monomers/Cross-linkers	Binding capacity (mg/g)	Imprinting factor (MIP/MNIP)	Magnetic (Yes/No)	Real sample	Ref.
Ampicillin	MAA, EGDMA	13.50	3.2	N	Milk, Blood	(Wu et al., 2016)
Cephalexin	MAA, EGDMA, PMDETA	36.86	2.5	Y	Tap water, Milk	(Li et al., 2012)
Cephalexin	TFMAA, EGDMA	3.62	2.6	N	Milk	(Lata et al., 2015)
Cephalexin	MAA, EGDMA	11.89	2.0	Y	Marine sediments, Sea water	(Qin et al., 2019)
Chloramphenicol	MAA, EGDMA	146.50	2.9	Y	Blood, Egg	(Wei et al., 2016)
Enrofloxacin	MAA, EGDMA	2.36	2.3	Y	Fish	(Tang et al., 2016)
Erythromycin	MAA, EGDMA	38.39	1.6	Y	No real sample tested	(Ou et al., 2015)
Florfenicol	MAA, EGDMA	190.10	4.3	Y	Blood, Egg	(Wei et al., 2016)
Ofloxacin	GMA, MAA, EGDMA	80.67	1.9	N	Bovine serum	(Li et al., 2019)
Tulathromycin	MAA, EGDMA	54.10	2.4	N	Pork	(Song et al., 2018)
Erythromycin	MAA	70.0	5.5	Y	Milk	Present work
Ciprofloxacin	MAA	32.0	4.3	Y	Milk	Present work

Table 2
A summary of imprinting factors (IF) and selectivity factors (SF) for ERY-MMIP and CPX-MMIP networks. The numbers were calculated as IF $= Q_{MMIP}/Q_{MNIP}$ and SF $= Q_{template}/Q_{competitor}$.

MMIP network sample	ERY-MMIP		CPX-MMIP	
Testing medium	MeOH/H$_2$O	milk	MeOH/H$_2$O	milk
Imprinting factor (IF) vs MNIP	3.28	5.45[a]	3.37	4.32[a]
Selectivity factor (SF) vs				
Erythromycin (ERY)	–	–	7.93	9.43
Ciprofloxacin (CPX)	4.71	3.53	–	–
Tetracycline (TET)	8.37	8.99	6.55	4.39
Kanamycin sulfate (KAN)	10.06[b]	12.66[b]	3.59	3.10
Neomycin sulfate (NM)	5.99[b]	9.34[b]	6.62	10.69

[a] Imprinting factors measuring with competitive antibiotics.

[b] Selectivity factors against the competitive antibiotics are possessing structural similarity (with two glycosides) but not in the same structural analogue as the template antibiotic.

monitoring can be difficult. The selective binding of these MMIP samples showed that pre-concentration of antibiotic residues from milk, as well as other animal products, can be possible. This will enhance monitoring of antibiotic pollutants in farmed animals, safe-guarding the food security, and hence helping to tackle the global problem of "antimicrobial resistance" AMR.

A separate experiment set was carried out to test cross-binding of the ERY-MMIP and CPX-MMIP networks in methanol/water media and milk matrices. This could not be performed simultaneously with the other antibiotics because the absorbance of ERY and CPX in the UV–vis spectra overlaps, with maxima at 280 nm and 275 nm respectively. Results in Fig. 6a show that, in MeOH/water media, CPX-MMIP binds CPX over 5-fold higher than ERY while ERY-MMIP has a shown a selectivity nearly 8-fold towards ERY. Similar results were observed in milk matrices (Fig. 6b) where CPX-MMIP has a 3-fold selectivity towards CPX and ERY-MMIP is 9-fold more selective towards its template ERY. These results further affirmed the selectivity of both ERY-MMIP and CPX-MMIP samples.

Results from selectivity and cross-binding studies show that both ERY- and CPX-MMIPs are capable for binding, detecting and removing the target template molecules. The high selectivity is crucial as antibiotic contamination can be complex and difficult to detect. These two network materials also allow pre-concentration of antibiotic contaminants from samples, enhancing downstream detection. Unlike bulk MIPs, our "MIP network structures" offer a high surface area and hence elevated binding capacities and accessibility for the target molecules. More importantly, these magnetic MIPs enable simple magnetic separation and recycling. In the literature, MIP nanoparticles have been reported with enhanced binding capacity (Sánchez-Polo et al., 2015; Gao et al., 2010; Ashley et al., 2017) but separation (using

centrifugation for example) and recycling can be problematic. Particularly if the water samples for detection is full of silt or other solid particulates, magnetic separation for precious MIP materials offer a viable solution for recycling.

To further improve the performance of these MMIP systems, two possible further developments could be seen in future. As discussed earlier, materials recovery using a simple magnet is likely to be below 100 %. More advanced recovery set up (e.g. circulation) with a stronger magnetic field, possibly with a high gradient magnetic separation (or HGMS) system could improve percentage of recovery (Leong et al., 2016). The second direction is to enhance the production of this MMIP materials to a commercial scale. Currently, the synthesis requires a high-speed homogenization and the batch size is limited to a level < 1 g. Large-scale high-pressure homogenization (HPH) (Hakansson et al., 2009; Silva et al., 2011) may be a possible solution but was never tested in MIP synthesis.

Water pollution due to PECs, including antibiotics, has been a challenging issue and highlighted in recent reports (Comber et al., 2018). Existing water treatment facilities seem to be inadequate to deal with these emerging hazardous pollutants and their concentrations are usually at sub-ppm level, making them difficult to be detected. Such a problem is likely to be much more severe in countries with strong agricultural sectors where mass use of antibiotics is a common practice and can be poorly regulated. Antibiotic pollutants in aquatic environment had already been identified as a major contributor to Antimicrobial Resistance (AMR). Detection and removal of antibiotic pollutants must be improved in order to effectively tackle AMR. The MMIP network materials developed from this work could help to enhance both detection and removal of antibiotic pollutants, making an impact on the global catastrophe of AMR.
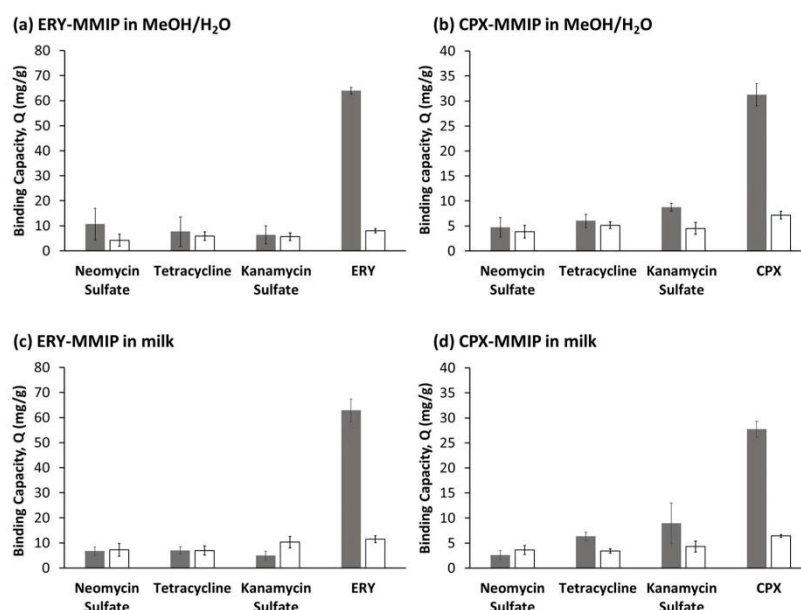
Fig. 5. Selectivity of ERY-MMIP and CPX-MMIP for their respective template molecules in a methanol/water (a, b) and milk matrix (c, d). In addition to the target molecules (erythromycin and ciprofloxacin), all solutions contained the three competing antibiotics neomycin sulfate, tetracycline and kanamycin sulfate. All graphs show the selectivity of the MMIP (■) and non-imprinted MNIP (□) samples.
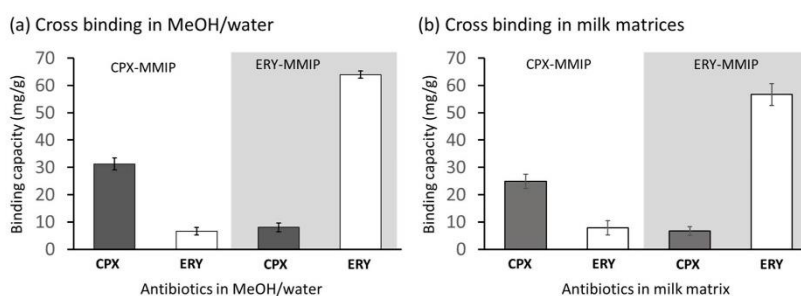
Fig. 6. Cross-binding of ERY and CPX target molecules with CPX-MMIP and ERY-MMIP samples in (a) methanol/water media and (b) milk matrices. Measurements on samples spiked with CPX (■) and ERY (□) were carried out separately.

4. Conclusion

In this work, magnetic MIP networks were successfully prepared using erythromycin (ERY) and ciprofloxacin (CPX) as templates. Both MMIP networks show high binding capacity (70 and 32 mg/g) and achieve maximum capacity within 60 min. Moreover, both samples are recyclable via magnetic separation/recovery and retained 68–75 % binding capacity after 4 cycles. More importantly, both MMIPs showed high selectivity towards the template molecules, in both methanol/water media and milk matrices. These MMIP networks can be used for removal and monitoring hazardous antibiotic pollutants in fresh water sources/samples and food products. The unique magnetic property allows separation using an external magnetic field instead of laborious centrifugation. The protocol of synthesis can be adapted for other antibiotic pollutants and pharmaceuticals, helping to tackle the problem of pharmaceutical pollution in aquatic environments.

Author contributions section

JK initiated the study, designed the experiment, carried out synthesis and functionalization of magnetic nanoparticles, interpreted the results and contributed to writing the manuscript. GA carried out synthesis of MMIPs and MNIPs, binding capacity measurements and recycling, and interpreted the results. ES designed the original experiment for MMIP synthesis. MM contributed to the synthesis of magnetic nanoparticles. HHPY coordinated the study, interpreted the results, wrote and organized the manuscript. MD coordinated the study, interpreted the results, and wrote the manuscript.

Declaration of Competing Interest

There is no conflict of interest to declare.

Acknowledgements

References

Anon, 2017. Water Pollution From Agriculture: a Global Review. I7754EN/1/08.17. Food and Agriculture Organization of the United Nations, Rome, 2017, and the International Water Management Institute on behalf of the Water Land and Ecosystems research program Colombo. www.fao.org/3/a-i7754e.pdf.

Anon, 2019a. The United Nations World Water Development Report 2019: Leaving No One Behind. United Nations Educational, Scientific and Cultural Organization, Paris ISBN 978-92-3-100309-7.

Anon, 2019b. Industrial Waste Water Treatment – Pressures on Europe's Environment. EEA Report No 23/2018. European Environment Agency, Luxembourg. https://doi.org/10.2800/496223.

Anon, 2018a. European Water – Assessment of Status and Pressures 2018. EEA Report No 7/2018. European Environment Agency, Luxembourg. https://doi.org/10.2800/303664.

Anon, 2018b. Tackling Antimicrobial Resistance (AMR) Together. Working Paper 1.0: Multisectoral Coordination. WHO/HWS/AMR/2018.2. World Health Organization, Geneva. www.who.int/antimicrobial-resistance/publications/Tackling-AMR-multisectoral-coordination-june2018.pdf.

Anon, 2019c. Monitoring and Evaluation of the Global Action Plan on Antimicrobial Resistance: Framework and Recommended Indicators. World Health Organization (WHO), Food and Agriculture Organization of the United Nations (FAO) and World Organisation for Animal Health (OIE), Geneva ISBN 978-92-4-151566-5.

Anon, 2019d. Turning Plans Into Action for Antimicrobial Resistance (AMR). Working Paper 2.0: Implementation and Coordination. WHO/WSI/AMR/2019.2. World Health Organization, Geneva. www.who.int/antimicrobial-resistance/publications/AMR-Turning-plans-into-action-working-paper-march-2019.pdf.

Armutcu, C., Bereli, N., Bayram, E., Uzun, L., Say, R., Denizli, A., 2014. Aspartic acid incorporated monolithic columns for affinity glycoprotein purification. Colloid Surf. B Biointerfaces 114, 67–74.

Ashley, J., Shahbazi, M.-A., Kant, K., Chidambara, V.A., Wolff, A., Bang, D.D., Sun, Y., 2017. Molecularly imprinted polymers for sample preparation and biosensing in food analysis: progress and perspectives. Biosens. Bioelectron. 91, 606–615.

Baquero, F., Martínez, J.L., Cantón, R., 2008. Antibiotics and antibiotic resistance in water environments. Curr. Opin. Biotechnol. 260–265.

Basheer, A.A., 2018. New generation nano-adsorbents for the removal of emerging contaminants in water. J. Mol. Liq. 261, 583–593.

Bengtsson-Palme, J., Larsson, D.G.J., 2016. Concentrations of antibiotics predicted to select for resistant Bacteria: proposed limits for environmental regulation. Environ. Int. 140–149.

Cantarella, M., Carroccio, S.C., Dattilo, S., Avolio, R., Castaldo, R., Puglisi, C., Privitera, V., 2019. Molecularly imprinted polymer for selective adsorption of diclofenac from contaminated water. Chem. Eng. J. 367, 180–188.

Caro, E., Marcé, R.M., Cormack, P.A.G., Sherrington, D.C., Borrull, F., 2006. Direct determination of ciprofloxacin by mass spectrometry after a two-step solid-phase extraction using a molecularly imprinted polymer. J. Sep. Sci. 29, 1230–1236.

Chang, M., Chang, Y.J., Chao, P.Y., Yu, Q., 2018. Exosome purification based on PEG-coated Fe$_3$O$_4$ nanoparticles. PLoS One 13. https://doi.org/10.1371/journal.pone.0199438.

Chang, M.M., Qin, Q., Wang, B.H., Xia, T., I.v, W.J., Sun, X.S., Shi, X.Z., Xu, G.W., 2019. Carboxymethylated polyethylenimine modified magnetic nanoparticles specifically for purification of His-tagged protein. J. Sep. Sci. 42, 744–753.

Chen, L.G., Liu, J., Zeng, Q.L., Wang, H., Yu, A., Zhang, H.Q., Ding, L., 2009. Preparation of magnetic molecularly imprinted polymer for the separation of tetracycline antibiotics from egg and tissue samples. J. Chromatogr. A 1216, 3710–3719.

Comber, S., Gardner, M., Sörme, P., Leverett, D., Ellor, B., 2018. Active pharmaceutical ingredients entering the aquatic environment from wastewater treatment works: a cause for concern? Sci. Total Environ. 613–614, 538–547.

Finley, R.L., Collignon, P., Larsson, D.G.J., McEwen, S.A., Li, X.Z., Gaze, W.H., Reid-Smith, R., Timinouni, M., Graham, D.W., Topp, E., 2013. The scourge of antibiotic resistance: the important role of the environment. Clin. Infect. Dis. 57, 704–710.

Gao, R.X., Zhang, J.J., He, X.W., Chen, L.X., Zhang, Y.K., 2010. Selective extraction of sulfonamides from food by use of silica-coated molecularly imprinted polymer nanospheres. Anal. Bioanal. Chem. 398, 451–461.

Guan, G.J., Liu, R.Y., Mei, Q.S., Zhang, Z.P., 2012. Molecularly imprinted shells from polymer and xerogel matrices on polystyrene colloidal spheres. Chem. Eur. J. 18, 4692–4698.

Guo, X.Y., Wang, W.J., Yang, Y., Tian, Q.H., Xiang, Y., Sun, Y., Bai, Z.M., 2019. Magnetic nano capture agent with enhanced anion internal layer diffusion performance for removal of arsenic from human blood. Appl. Surf. Sci. 470, 296–305.

Hakansson, A., Tragardh, C., Bergenstahl, B., 2009. Dynamic simulation of emulsion formation in a high pressure homogenizer. Chem. Eng. Sci. 64, 2915–2925.

Hoshino, Y., Kodama, T., Okahata, Y., Shea, K.J., 2008. Peptide imprinted polymer nanoparticles: a plastic antibody. J. Am. Chem. Soc. 130, 15242–15243.

Ionescu, R.E., Jaffrezic-Renault, N., Bouffier, L., Gondran, C., Cosnier, S., Pinacho, D.G., Marco, M.-P., Sánchez-Baeza, F.J., Healy, T., Martelet, C., 2007. Impedimetric immunosensor for the specific label free detection of ciprofloxacin antibiotic. Biosens. Bioelectron. 23, 549–555.

Javanbakht, M., Pishro, K.A., Nasab, A.H., Akbari-adergani, B., 2012. Extraction and purification of penicillin G from fermentation broth by water-compatible molecularly imprinted polymers. Mater. Sci. Eng. C Mater. Biol. Appl. 32, 2367–2373.

Konwar, A., Chowdhury, D., Dan, A., 2019. Chitosan based in situ and ex situ magnetic iron oxide nanoparticles for rapid endotoxin removal from protein solutions. Mater. Chem. Front. 3, 716–725.

Larsson, D.G.J., 2014. Antibiotics in the environment. Ups. J. Med. Sci. 119, 108–112.

Lata, K., Sharma, R., Naik, L., Rajput, Y.S., Mann, B., 2015. Synthesis and application of cephalexin imprinted polymer for solid phase extraction in milk. Food Chem. 184, 176–182.

Leong, S.S., Yeap, S.P., Lim, J.K., 2016. Working principle and application of magnetic separation for biomedical diagnostic at high- and low-field gradients. Interface Focus 6, 20160048.

Li, X., Pan, J.M., Dai, J.D., Xu, L.C., Wei, X., Hang, H., Li, C.X., Liu, Y., 2012. Surface molecular imprinting onto magnetic yeast composites via atom transfer radical polymerization for selective recognition of cefalexin. Chem. Eng. J. 198, 503–511.

Li, J.M., Zhao, L.J., Wei, C.L., Sun, Z.A., Zhao, S.W., Cai, T.P., Gong, B.L., 2019. Preparation of restricted access media molecularly imprinted polymers for efficient separation and enrichment ofloxacin in bovine serum samples. J. Sep. Sci. 42, 2491–2499.

Nantasenamat, C., Isarankura-Na-Ayudhya, C., Naenna, T., Prachayasittikul, V., 2007. Quantitative structure-imprinting factor relationship of molecularly imprinted polymers. Biosens. Bioelectron. 22, 3309–3331.

Okan, M., Duman, M., 2018. Functional polymeric nanoparticle decorated microcantilever sensor for specific detection of erythromycin. Sens. Actuator B-Chem. 256, 325–333.

Okan, M., Sari, E., Duman, M., 2017. Molecularly imprinted polymer based micro-mechanical cantilever sensor system for the selective determination of ciprofloxacin. Biosens. Bioelectron. 88, 258–264.

Ou, H.X., Chen, Q.H., Pan, J.M., Zhang, Y.L., Huang, Y., Qi, X.Y., 2015. Selective removal of erythromycin by magnetic imprinted polymers synthesized from chitosan-stabilized Pickering emulsion. J. Hazard. Mater. 289, 28–37.

Qin, D., Wang, J.T., Ge, C.G., Lian, Z., 2019. Fast extraction of chloramphenicol from marine sediments by using magnetic molecularly imprinted nanoparticles. Microchim. Acta. 186, 428.

Rodriguez-Narvaez, O.M., Peralta-Hernandez, J.M., Goonetilleke, A., Bandala, E.R., 2017. Treatment technologies for emerging contaminants in water: a review. Chem. Eng. J. 323, 361–380.

Rufino, E.S., Monteiro, E.E.C., 2003. Infrared study on methyl methacrylate–methacrylic acid copolymers and their sodium salts. Polymer 44, 7189–7198.

Samia, M., El-Sadek, M., Alla, E.A., 2002. Spectrophotometric determination of ciprofloxacin, enrofloxacin and pefloxacin through charge transfer complex formation. Journal J. Pharm. Biomed. Anal. 27, 133–142.

Sánchez-Polo, M., Velo-GalaJesús, I., López-Peñalver, J., Rivera-Utrilla, J., 2015. Molecular imprinted polymer to remove tetracycline from aqueous solutions. Microporous Mesoporous Mater. 203, 32–40.

Sari, E., Üzek, R., Duman, M., Denizli, A., 2018. Detection of ciprofloxacin through surface plasmon resonance nanosensor with specific recognition sites. J. Biomater. Sci. Polym. Ed. 29, 1302–1318.

Sari, E., Üzek, R., Duman, M., Denizli, A., 2016. Fabrication of surface plasmon resonance nanosensor for the selective determination of erythromycin via molecular imprinted nanoparticles. Talanta 150, 607–614.

Silva, A.C., González-Mira, E., García, M.L., Egea, M.A., Fonseca, J., Silva, R., Santos, D., Souto, E.B., Ferreira, D., 2011. Preparation, characterization and biocompatibility

9

studies on risperidone-loaded solid lipid nanoparticles (SLN): high pressure homogenization versus ultrasound. Colloid Surf. B Biointerfaces 86, 158–165.

Song, X.Q., Zhou, T., Li, J.F., Su, Y.J., Xie, J.M., He, L., 2018. Determination of macrolide antibiotics residues in pork using molecularly imprinted dispersive solid-phase extraction coupled with LC–MS/MS. J. Sep. Sci. 41, 1138–1148.

Sun, X.L., Wang, J.C., Li, Y., Yang, J.J., Jin, J., Shah, S.M., Chen, J.P., 2014. Novel dummy molecularly imprinted polymers for matrix solid-phase dispersion extraction of eight fluoroquinolones from fish samples. J. Chromatogr. A 1359, 1–7.

Sun, Z.Y., Cheng, K., Yao, Y.Y., Wu, F.Y., Fung, J., Chen, H., Ma, X.W., Tu, Y.F., Xing, L., Xia, L.M., Cheng, Z., 2019. Controlled Nano–Bio interface of functional nanoprobes for *in vivo* monitoring enzyme activity in tumors. ACS Nano 13, 1153–1167.

Tang, Y.W., Li, M., Gao, X., Liu, X.Y., Ma, Y., Li, Y., Xu, Y.X., Li, J.R., 2016. Preconcentration of the antibiotic enrofloxacin using a hollow molecularly imprinted polymer, and its quantitation by HPLC. Microchim. Acta 183, 589–596.

Tong, Y., Hu, Y., Xia, Q., Huang, W., Tian, M., 2017. Preparation of a novel magnetic molecularly imprinted polymer and its application for the determination of fluoroquinolone antibiotics. Chin. J. Chromatogr. 35, 291.

Urraca, J.L., Castellari, M., Barrios, C.A., Moreno-Bondi, M.C., 2014. Multiresidue analysis of fluoroquinolone antimicrobials in chicken meat by molecularly imprinted solid-phase extraction and high performance liquid chromatography. J. Chromatogr. A 1343.

Wei, S.L., Li, J.W., Ma, J.K., 2016. Development of magnetic molecularly imprinted polymers with double templates for the rapid and selective determination of amphenicol antibiotics in water, blood, and egg samples. J. Chromatogr. A 1473, 19–27.

Wu, N.L., Luo, Z.M., Ge, Y.H., Guo, P.Q., Du, K.L., Tang, W.L., Du, W., Zeng, A.G., Chang, C., Fu, Q., 2016. A novel surface molecularly imprinted polymer as the solid-phase extraction adsorbent for the selective determination of ampicillin sodium in milk and blood samples. J. Pharm. Anal. 6, 157–164.

Yan, H.Y., Cheng, X.L., Sun, N., 2013. Synthesis of multi-core–shell magnetic molecularly imprinted microspheres for rapid recognition of dicofol in tea. J. Agric. Food Chem. 61, 2896–2901.

Yiu, H.H.P., Bouffier, L., Boldrin, P., Long, J., Claridge, J.B., Rosseinsky, M.J., 2013. Comprehensive study of DNA binding on Iron(II,III) oxide nanoparticles with a positively charged polyamine three-dimensional coating. Langmuir 29, 11354–11365.

Yoshikawa, M.K., Tharpa, K., Dima, S.-O., 2016. Molecularly imprinted membranes: past, present, and future. Chem. Rev. 116, 11500–11528.

Yu, J., Hu, X., Li, D., Wang, H., 2010. In: 4th International Conference on Bioinformatics and Biomedical Engineering. Chengdu, China, June 18–20. https://doi.org/10.1109/ICBBE.2010.5515319.

Zhou, X.M., Xing, D., Zhu, D.B., Tang, Y.B., Jia, L., 2008. Development and application of a capillary electrophoresis–electrochemiluminescent method for the analysis of enrofloxacin and its metabolite ciprofloxacin in milk. Talanta 75, 1300–1306.

10

8.2. Tri-modal imaging of gold-dotted magnetic nanoparticles for magnetic resonance imaging, computed tomography, and intravascular ultrasound: an in vitro study

J. Kuhn, G. Papanastasiou, C-W. Tai, CM Moran, MA, Jansen, AAS Tavares, RJ Lennen, CA Corral, CJ Wang, AJW Thomson, CC Berry, HHP Yiu

Tri-modal imaging of gold-dotted magnetic nanoparticles for magnetic resonance imaging, computed tomography and intravascular ultrasound: an *in vitro* study

Joel Kuhn[‡,1], Giorgos Papanastasiou[‡,2,3], Cheuk-Wai Tai[4], Carmel M Moran[3,5], Maurits A Jansen[3,5], Adriana AS Tavares[3,5], Ross J Lennen[3,5], Carlos Alcaide Corral[3,5], Chengjia Wang[3], Adrian JW Thomson[3,5], Catherine C Berry[6] & Humphrey HP Yiu[*,1]

[1]Chemical Engineering, School of Engineering & Physical Sciences, Heriot-Watt University, Edinburgh, EH14 4AS, UK
[2]School of Computer Science & Electronic Engineering, University of Essex, Colchester, CO4 3SQ, UK
[3]Edinburgh Imaging, Queen's Medical Research Institute, University of Edinburgh, Edinburgh, EH16 4TJ, U.K.
[4]Department of Materials & Environmental Chemistry, Arrhenius Laboratory, Stockholm University, Stockholm, SE-106 91, Sweden
[5]Centre for Cardiovascular Science, Queen's Medical Research Institute, University of Edinburgh, Edinburgh, EH16 4TJ, UK
[6]Centre for Cell Engineering, IMCSB, Joseph Black Building, University Avenue, University of Glasgow, Glasgow, G12 8QQ, UK
*Author for correspondence: Tel.: +44 131 4518145; h.h.yiu@hw.ac.uk
‡Sharing first authorship.

Aim: To examine the multimodal contrasting ability of gold-dotted magnetic nanoparticles (Au*MNPs) for magnetic resonance (MR), computed tomography (CT) and intravascular ultrasound (IVUS) imaging. **Materials & methods:** Au*MNPs were prepared by adapting an impregnation method, without using surface capping reagents and characterized (transmission electron microscopy, x-ray diffraction and Fourier-transform infrared spectroscopy) with their *in vitro* cytotoxicity assessed, followed by imaging assessments. **Results:** The contrast-enhancing ability of Au*MNPs was shown to be concentration-dependent across MR, CT and IVUS imaging. The Au content of the Au*MNP led to evident increases of the IVUS signal. **Conclusion:** We demonstrated that Au*MNPs showed concentration-dependent contrast-enhancing ability in MRI and CT imaging, and for the first-time in IVUS imaging due to the Au content. These Au*MNPs are promising toward solidifying tri-modal imaging-based theragnostics.

Medical imaging techniques are extensively used for the non-invasive diagnosis for various diseases [1,2]. Among medical imaging techniques, MRI, computed tomography (CT) and ultrasound (US) are widely available and commonly used in the clinical setting [3,4]. Due to intrinsic technical disparities, these imaging techniques have different advantages and limitations, which determine their diagnostic performance across clinical specialties. MRI benefits from non-ionizing radiation exposure, high soft-tissue contrast and high spatial and temporal resolution, and is capable of molecular and functional multi-parametric imaging [1–5]. However, it is limited by long imaging times, and is not suitable for patients with claustrophobia or MR contraindications [4,5]. CT provides a physical representation of the tissue attenuation properties, high spatial and temporal resolution and fast imaging, but is associated with ionizing radiation exposure and lower soft-tissue contrast compared with MRI [1–4,6]. US is often used for early disease assessment and compared with other imaging modalities is an inexpensive, real-time imaging technique with no non-ionizing radiation exposure [1,3,4,7]. The main limitations of US are that it is sub-optimal for imaging obese patients and air-filled organs, and requires a trained and skilled operator to achieve clinically relevant images [7]. Among important US applications, intravascular US (IVUS) is used in cardiology to determine the hemodynamic significance of atherosclerotic plaques [1,3]. The development of multimodal imaging protocols

Future Medicine

aims to capitalize on the advantages and overcome the limitations of individual imaging techniques, and helps to derive clinically relevant complementary diagnostic information [1–4]. Importantly, multimodal diagnostic imaging workflows are essential in cardiology, where complementary information is critical due to the clinical urgency of cardiac diseases [1–4,8,9].

Contrast agents are commonly employed in MRI, CT and US scans to enhance the qualitative diagnostic information acquired, and to obtain quantitative diagnostic information through the extraction of dynamic measurements and image-derived biomarkers [3,5,7,9]. Since the above imaging modalities are based on different physical principles, the development of contrast agents is usually modality-specific. Moreover, the surface properties of different contrast agents vary considerably, leading to significant disparities in terms of biodistribution and tissue uptake. This compromises the design, optimization and cross-validation of multimodal imaging protocols [10]. Thus, one single agent carrying multimodal contrast ability is required for multimodal imaging.

Various nanoparticles (inorganic, organic and hybrid) have been developed as contrast agents for diagnostic imaging techniques [11]. Among these, iron oxide (Fe_3O_4) magnetic nanoparticles (MNPs) have been commercialized for clinical MRI [12], as they benefit from low toxicity and are detectable by MR even at low concentrations [13–15]. Gold (Au) NPs are among the most promising for CT, since they have high atomic number (abundant electrons for CT contrasting), good biocompatibility, controllable synthesis and easy modification [16,17]. In the context of multimodal imaging, previous studies have developed several methodologies for synthesizing Au/Fe_3O_4 hybrids with different morphologies [17–26]. These morphologies include Au clusters on Fe_3O_4 to form 'strawberry-like' NPs [17,18], Au shell structures with an Fe_3O_4 core [19,20], Au encapsulated Fe_3O_4 star-shaped particles and Janus dumbbell-like particles [21,22]. However, all previous synthetic routes have used stabilizers before or after the reaction of the MNP component with Au and thus, have not focused on keeping either component surface pristine. If possible, pristine NP surfaces could support functionalization of Au/Fe_3O_4 hybrids, which is widely needed in molecularly targeted diagnosis and therapy [11].

Synthesis of multimodal contrast-enhancing agents with combined NP properties is not straightforward, due to different chemical criteria that need to be satisfied for each component (such as in formation chemistry, pH control and/or when specific functional groups are needed for coupling) [18,22]. Possible interference between the NP precursors and/or between chemical functional groups on the NP surface will result in undesirable assembly, such as in agglomeration and/or in deactivation of functional groups and NP surfaces [27]. Hence, developing a direct deposition route while aiming to keep either component pristine for further functionalization, could contribute toward optimizing the next generation of multimodal/multifunctional contrast agents.

In terms of imaging assessments, previous studies have mainly examined the MR and CT contrasting ability of Au/Fe_3O_4 hybrids [18–20], while some have demonstrated signal changes in photoacoustic imaging due to the presence of the Au component [21,22]. Investigating the contrast-enhancing ability of Au/Fe_3O_4 hybrids across MR, CT and IVUS would support multimodal assessments in the clinical setting. To our knowledge, there is no previous work examining whether the Au component of Au/Fe_3O_4 hybrids can modify the IVUS signal in a concentration-dependent mode. Our group has previously shown that MNPs are taken up (through macrophage activity) in areas of cellular inflammation in the myocardium [14]. It is known that cellular inflammation within atherosclerotic plaques is associated with plaque progression and rupture, which can lead to acute myocardial infarction [28]. Demonstrating that Au/Fe_3O_4 hybrids could modify the IVUS signal is therefore clinically important, as it would enable to measure cellular inflammation and plaque size in a single (IVUS) imaging setting, through localizing the uptake of Au/Fe_3O_4 hybrids.

We demonstrate for the first-time the synthesis of Au-dotted magnetic nanoparticles (Au*MNPs) via a direct sono-deposition route, with variable Au/Fe mass ratios. In the literature, synthesis pathways for other Au/Fe_3O_4 nanoparticles usually result in individual particle surfaces covered with stabilizers before or after the reaction with Au [17–22]. In contrast, our method allowed the surface of both components to be kept pristine for further functionalization, which can efficiently support molecularly targeted diagnosis and therapy. In addition, we demonstrate prominent results when these Au*MNP were assessed in multimodal imaging techniques. We have extensively assessed for the first-time tri-modal signal changes, due to concentration increases of these Au*MNPs on MRI, on CT and on IVUS B-mode scans. Our finding on IVUS scans for different Au*MNP concentrations suggested that this has the potential to be used in assessing cardiovascular disease, using a single Au*MNP/IVUS setting. We finally evaluated the toxicity of these Au*MNPs in breast cancer cells hence, fully assessing whether they have potential to be optimized as a tri-modal contrast agent for clinical research and diagnosis.

Materials & methods

Materials

Magnetite nanoparticles (Fe_3O_4 MNPs, 98%, 20–30 nm) and chloroauric acid tetrahydrate ($HAuCl_4 \cdot 4H_2O$, 99.9%) were purchased from Alfa Aesar (Heysham, UK). Urea (AR grade) was supplied by Thermo Fisher Scientific (Loughborough, UK). PEG (Mw = 400) was purchased from Sigma-Aldrich (Gillingham, UK). All water used was deionized water. DMEM growth medium with 10% FBS and 1% penicillin–streptomycin (D5671) was supplied by Sigma-Aldrich. Ethidium homodimer (EthD-1) and Calcein AM (0.1% in DMEM) were purchased as a kit (LIVE/DEAD™ Viability/Cytotoxicity Kit) supplied by Invitrogen™ (Renfrew, UK). Glutaraldehyde (25% EM grade 1 (G5882), Sigma-Aldrich) and sodium cacodylate buffer (0.1 M, AGR1104) were supplied by AGAR Scientific Ltd (Stansted, UK). Tannic acid was purchased from TAAB Laboratory and Microscopy Ltd (Aldermeston, UK). Methanol and ethanol were purchased from VWR BDH Chemicals (Lutterworth, UK). Uranyl acetate and osmium tetraoxide were purchased from OXKEM Ltd (Reading, UK). Hexamethyldisilazane (HMDS, 99%) was supplied by (Sigma-Aldrich). All chemicals were used as supplied without further purification.

Preparation of Au*MNP nanoparticles & characterization

Au was deposited onto Fe_3O_4 MNPs using a method adapted from the preparation of Au/Fe_3O_4 catalyst [29]. Au*MNPs with three Au/Fe mass ratios (0.15, 0.19 and 0.25) were prepared. These ratios were chosen based on prior experience in gold on iron oxide catalysts, where 0.25 is about the upper limit of gold content that can be achieved. Lower ratio would result in reduction of CT and IVUS contrasting ability. In brief, 25, 50 and 100 mg (for Au/Fe = 0.15, 0.19 and 0.25, respectively) chloroauric acid tetrahydrate ($HAuCl_4 \cdot 4H_2O$) were dissolved in 1 ml of deionized water, and added to a suspension of Fe_3O_4 MNPs at 300 mg in 24 ml of deionized water. The reaction mixture was then homogenized in an ultrasonic bath. Urea (at 100:1 molar ratio compared with Au) was dissolved in 5 ml of deionized water and the solution was then added drop-wise to the Au/MNP reaction suspension under sonication. Urea acts as a weak base to neutralize chloroauric acid and precipitate gold on the Fe_3O_4 surface. The temperature of the ultrasonic bath was then increased to 80°C at a heating rate of 2°C/min and this suspension was sonicated for a further 6 h at 80°C. The solid samples were then separated using an NdFeB magnet and washed using deionized water for a minimum of ten-times. PEG-coated Au*MNP was carried out by coating PEG (Mw = 400) onto particle surface following a published procedure for all Au*MNPs [30]. For imaging experiments, samples with Au*MNP concentrations ranging from 0.01 to 0.2 mM were appropriately prepared to derive quantitative metrics from MR, CT and IVUS experiments.

PEG-coated and uncoated Au*MNPs were characterized using transmission electron microscopy (TEM), x-ray diffraction (XRD) and Fourier-transform infrared spectroscopy (FTIR). TEM and scanning TEM (STEM) were carried out in a JEOL JEL 2100 microscope operated at 200 kV. The microscope is equipped with a Schottky field-emission gun and ultrahigh resolution pole-piece (Cs = 0.5 mm). The TEM images were recorded by a Gatan Ultrascan 1000 camera. High-angle annular dark-field (HAADF-STEM), known as Z-contrast imaging, was acquired by a JEOL ADF detector. For sample preparation, 20 μl of a sample was drop-casted on a copper grid with carbon supporting films, and then air-dried. Powder XRD (PXRD) patterns were recorded using a Bruker D8 ADVANCE diffractometer with Cu Kα_1 radiation and a step size of 0.01°. FTIR spectra were recorded using a Nicolet is5 FTIR spectrometer (Thermo Fisher Scientific), fitted with an iD7 ATR-Diamond (KBr). The gold and iron content of Au*MNPs was quantified using an atomic absorption spectrometer (AAS, Thermo Fisher Scientifc). The hybrid samples were dissolved in aqua regia (ca. 10 mg Au*MNP in 10 ml aqua regia) and then the sample solutions were diluted × 600 for AAS measurements.

Cell culture, cytotoxicity & imaging

The human breast cancer cell line MCF7 was employed in this study. Cells were expanded in DMEM growth medium with 10% FBS and 1% penicillin–streptomycin, and maintained at 37°C in 5% CO_2 until approximately 90% confluent. Cells were seeded at a density of 1×10^4 cells per ml for experiments (unless stated otherwise), and were cultured for 24 h before the addition of the Au*MNP treatments. The same cell line not exposed to Au*MNP treatments was used as controls.

To assess the preliminary cell viability of MCF-7 breast cancer cells upon Au*MNP exposure, PrestoBlue™ proliferation assay was carried out using a resazurin-based solution (10% in DMEM) (Invitrogen™ cell viability reagent). Over a period of 3 days, the cell cultures were exposed to three different Au/Fe mass ratios = 0.15, 0.19, 0.25 at four different Au*MNP concentrations (50, 125, 250 and 500 μg/ml). At the end of 3 days (72 h), the

media was removed and the cells were washed using phosphate-buffered saline (PBS). Then a solution of fresh FBS-free DMEM containing 10% PrestoBlue™ cell viability reagent was added and the cell culture was incubated for 30 min at 37°C. After this, the reagent was replaced with fresh culture medium and transferred to a Corning™ 96-well solid white walled polystyrene microplate. The fluorescence was measured using a microplate reader (Turner BioSystems Inc., Modulus™ II). An unpaired two-sample t-test was used to compare the cell viability of the control culture with cell cultures that were exposed to Au*MNP samples with three different Au/Fe mass ratios (0.15, 0.19 and 0.25) at four different concentrations (50, 125, 250 and 500 μg/ml) for 72 h. The experiments were repeated in triplicates and a 95% CI for data analysis ($p < 0.05$) was used to establish statistically significant results.

To further assess cell viability for a longer time course, live/dead staining was conducted using ethidium homodimer (EthD-1; 0.1% in DMEM) and Calcein AM (0.1% in DMEM) (Invitrogen™ LIVE/DEAD™ viability/cytotoxicity kit, for mammalian cells). After both 24 h and 7-day culture with either 10 or 100 μg/ml Au*MNPs, the media from the MCF7 cells was removed and replaced with fresh media containing both EthD-1 and Calcein; the cells were incubated for 30 min at 37°C. After this, the cells were washed with fresh 37°C media and were visualized under a fluorescence microscope (Zeiss Axiovert 200 M).

To observe MCF7 interaction with the Au*MNPs, the cells were fixed and processed for scanning electron microscopic (SEM) analysis following 24 h of culture. The cells were fixed in 1.5% glutaraldehyde in 0.1 M sodium cacodylate buffer for 1 h, washed in cacodylate buffer for 10 min, then incubated in 1% osmium buffer for 1 h at room temperature. Cell samples were washed twice in cacodylate buffer (5 min) and incubated in 1% tannic acid (in buffer) for 1 h at room temperature. After washing, cells were dehydrated twice in methanol gradients (30, 50, 70%; 5 min), incubated in 2% uranyl acetate for 30 min, then further dehydrated in 90% methanol for 5 min and 100% ethanol for 10 min. Finally, cells underwent HMDS dehydration (5 min), stored in a desiccator, sputter coated in gold-palladium (using a Quorum Q150t ES) and mounted onto stands to be viewed under a JEOL JSM 6400 SEM (running at 10 kV). The SEM data were converted into .tiff files using the Olympus Scandium software.

Cellular uptake of Au*MNPs was also analyzed via TEM following a protocol that was published in prior work [31]. Cells were seeded at a density of 4×10^4 cells per ml onto Thermanox coverslips (13 mm diameter) and cultured to develop a confluent monolayer of cells. At this point, the Au*MNPs were added and cells were further cultured for 24 h. Cells were subsequently fixed with 1.5% glutaraldehyde in PBS for 2 h, and washed for 10 min with PBS. Cells were then post stained for 60 min with 1% osmium tetroxide in phosphate buffer, and post fixed in 1% buffer followed by 0.5% uranyl acetate for 1 h, prior to being taken through alcohol dehydration increments and left in resin (propylene oxide Epon 812 resin mix [1:1]) overnight. Cell layers were captured in pure resin and cured overnight in an oven. Blocks were then cut into ultrathin sections, stained with 2% methanolic uranyl acetate and Reynolds lead citrate, and viewed under a FEI Tecnai T20 (200 kV for cells).

MR imaging & analysis

To assess the MR contrast enhancement ability of the MNP component in our samples, Au*MNPs were imaged in a 7.0 Tesla preclinical MRI scanner (Agilent Technologies, CA, USA) at the Edinburgh Preclinical Imaging Laboratory, using a 72 mm internal diameter volume coil. T_2 imaging was performed using a multi-echo multislice gradient echo sequence to acquire a series of 25 images across five different slice positions with repetition time 2000 ms, first echo time (TE) 6.70 ms, echo spaning 6.70 ms, flip angle 90° and a slice thickness 2 mm. Images were reconstructed on a 256 × 256 pixel grid with 0.62 mm × 0.62 mm pixel size.

MR images were analyzed in MATLAB (MathWorks Inc., MA, USA), using a customized in-house MR analysis software [5]. MR signal intensities were extracted by using standardized circular regions of interest at the center of each sample tube (excluding the boundary areas) in MATLAB, across all successive TE images. T_2 signal changes were estimated by fitting the transverse relaxation time Equation 1 in the T_2 signal curves extracted across all successive TEs for each sample tube:

$$M_{xy} = M_0 e^{-\frac{t}{T_2}}$$

(Eq. 1)

where M_{xy} is the MR signal detected in the x-y plane by the scanner detector, M_0 is the initial net magnetization and t is the TE.

CT imaging & analysis

To assess the CT contrast enhancement of the Au component in our hybrids, Au*MNPs were imaged on a second generation Mediso microPET/CT scanner (nanoPET/CT, Mediso, Hungary) at the Edinburgh Preclinical Imaging

Laboratory. The quality assurance was performed daily on the Mediso nanoPET/CT, as previously described [32]. The CT imaging parameters were: tube voltage 50 kVp, exposure time 300 ms, slice thickness 0.38 mm, matrix 324 × 324 and pixel size 0.38 mm × 0.38 mm. Attenuation coefficients were numerically normalized to the attenuation coefficient of water in our calibrated scanner environment and all CT image pixels were automatically converted into Hounsfield Units (HU) as shown in Equation 2:

$$HU = 1000 \frac{\mu - \mu_{water}}{\mu_{water} - \mu_{air}} \qquad \text{(Eq. 2)}$$

where μ is the linear attenuation coefficient in a pixel measured by the CT scanner, and μ_{water} and μ_{air} are the linear attenuation coefficients of water and air, respectively. CT images were analyzed using PMOD (PMOD Technologies, Zurich, Switzerland). A cylindrical volume of interest was drawn at the center of each sample tube (excluding the boundary areas) and were used to quantify the mean HU values and standard deviation.

US imaging & analysis

To assess the US echogenicity, the Au*MNPs were scanned using a Boston Scientific Clearview IVUS scanner with an Atlantis SR Pro catheter and with nominal center frequency of 40 MHz. The catheter was inserted into each of the samples and an image was acquired on the scanner and downloaded onto a computer using an 8 bit, 20 MHz, image capture card (PicPort CameraTec AG, Weisslingen, Switzerland). The set-up of the scanner was identical for all acquisitions. Images were read and analyzed using MATLAB, where the average signal intensity and standard deviation were measured from each sample (excluding the boundary areas).

Results

Characterizations of Au*MNPs

Our synthesis process was designed to generate 'pristine strawberry-like' Au*MNPs, with PEG coating surrounding the hybrid surfaces to increase their biocompatibility, as shown in Supplementary Figure 1A. To support further functionalization, we used physical absorption of PEG onto the Au*MNPs, forming a temporary coating around these pristine materials. The HAADF-STEM images in Figure 1A–C reveal that these Au*MNPs possess a 'pristine strawberry-like' structure, with the Au nanoparticles (seeds) having a narrow size distribution dotted on the Fe_3O_4 MNP surface. At Au/Fe ratio of 0.25, it can be seen from the HAADF-STEM images that unattached Au nanoparticles were also formed (Figure 1C). Since the Fe_3O_4 surface was already saturated with Au 'seeds' at 0.25 Au/Fe mass ratio, further increase in the Au content beyond 0.25 may not be viable in terms of synthesis. Indeed, this protocol was adapted from Au on Fe_3O_4 catalyst preparation, in which Au/Fe = 0.20 tends to be the upper limit [29]. The AAS results have confirmed that the Au/Fe mass ratio on Au*MNPs are indeed 0.15, 0.19 and 0.25 based on the Fe results.

    Au seeds dotted on Fe_3O_4 MNPs with a similar structure have been reported [18], but those were prepared with a thiol-layer on the Fe_3O_4 surface (see Supplementary Figure 1B[i]). Our synthesis protocol has avoided the use of organosilane [33], keeping the Fe_3O_4 surface pristine for binding with other molecules. Due to the small size of these Au NP seeds, these cannot be observed from the powder XRD pattern (Supplementary Figure 2). FTIR spectra in Figure 1D depicted the PEG coating on the Au*MNPs with Au/Fe = 0.19, compared with the uncoated Au*MNPs. The spectrum showed five bands at 1155, 1420, 1470, 2870 and 2985 cm^{-1}, which are characteristic for PEG. The band at 1155 cm^{-1} can be attributed to the stretching mode of the ether linkage (-C–O–C-). The other four peaks are assigned to the CH_2 bending vibrations (1419 and 1470 cm^{-1}) and to the symmetric (2869 cm^{-1}) and asymmetric (2985 cm^{-1}) stretching modes of the $-CH_2$ repeating unit in PEG.

Effects on cells & cytotoxicity

Preliminary test on the effect of Au*MNPs on cell viability using breast cancer MCF-7 cell line was carried out using PrestoBlue™ cell viability assay (see Figure 2). Hybrids with a lower Au/Fe ratio (0.15 and 0.19) showed a cell viability over 90%, even at a very high MNP concentration (500 µg/ml) over 3 days exposure. When the Au content increases, the Au*MNP sample at Au/Fe = 0.25 showed an observable decrease in cell viability to around 80% at higher dose. To further evaluate the safe use of Au*MNPs, we carried out additional assessments on their effect on cell morphology and viability for a prolong period.

    A prolong study on viability was also carried out as Calcein AM and ethidium homodimer staining demonstrated no adverse effects on cell culture at both 10 and 100 µg/ml concentrations, for both uncoated and PEG-coated
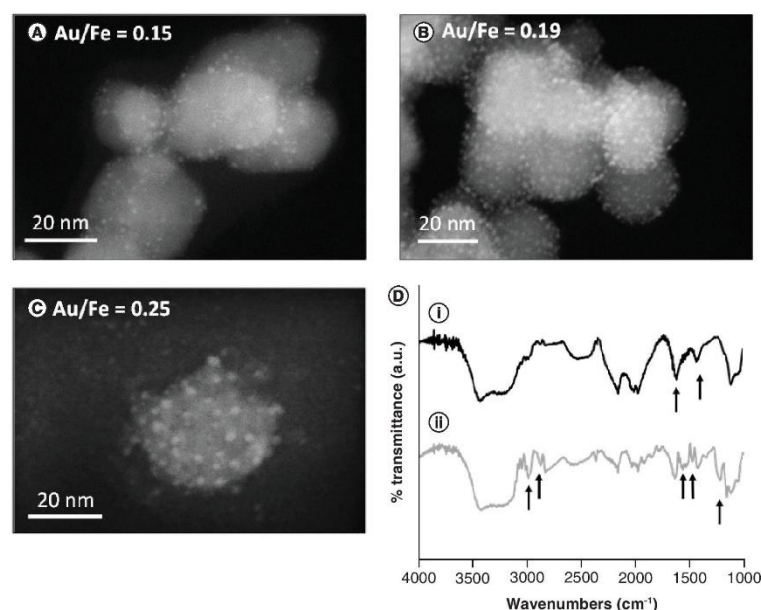
Figure 1.   Transmission electron microscopy images and Fourier-transform infrared spectroscopy spectra of gold-dotted magnetic nanoparticles. High-angle annular dark-field-scanning transmission electron microscopy images for gold-dotted magnetic nanoparticle hybrids at Au/Fe mass ratio = **(A)** 0.15, **(B)** 0.19 and **(C)** 0.25. **(D)** Fourier-transform infrared spectroscopy spectra for gold-dotted magnetic nanoparticles (Au/Fe = 0.19) **(i)** without PEG and **(ii)** with PEG coating.
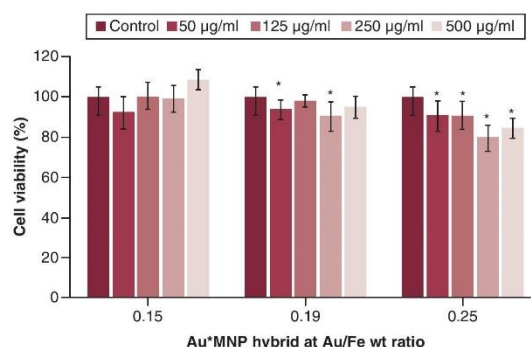
Figure 2.   Cell viability assay results for gold-dotted magnetic nanoparticles at Au/Fe mass ratio at 0.15, 0.19 and 0.25 using PrestoBlue™ assay with MCF-7 breast cancer cells after exposure of 3 days (72 h). Data are presented as mean ± SD. Statistics analysis was determined by two-sample t-test (*p < 0.05), compared with the control group in each concentration. All measurements were run in triplicates. Au*MNP: Gold-dotted magnetic nanoparticle.

Au*MNPs (Au/Fe = 0.19), which showed promising viability from PrestoBlue™ assay, and at both time points (1 and 7 days) (Supplementary Figure 3). Cells multiplied in number over the time course studied, suggesting no influence on cell proliferation. In order to study the cell membrane interaction and subsequent uptake of these Au*MNPs by cells, MCF-7 cells were exposed to 10 µg/ml of Au*MNPs (Au/Fe = 0.19, uncoated and PEG-coated) and studied by SEM and TEM. The SEM images of MCF-7 cells 24 h post Au*MNP exposure are shown in Figure 3. The cells were similar to the control cells in terms of their adherence (cell spreading), morphology and
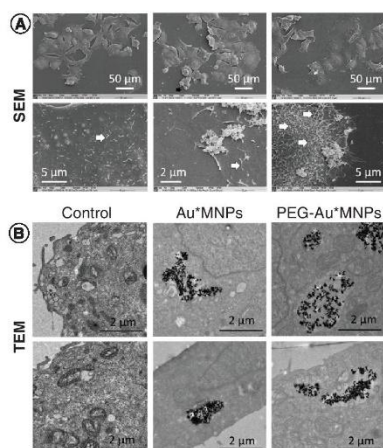
Figure 3. Scanning electron microscopy and transmission electron microscopy images of MCF-7 cells exposed to gold-dotted magnetic nanoparticles. (A) SEM and **(B)** TEM images of MCF-7 cells exposed to Au*MNPs (Au/Fe = 0.19) after 24 h. White arrowheads on SEM indicate the F-actin protrusions on cell surfaces.
Au*NP: Gold-dotted magnetic nanoparticle; SEM: Scanning electron microscopy; TEM: Transmission electron microscopy.

size (Figure 3A, upper panel). Au*MNPs were clearly visible on the cell surface, with increased levels of membrane activity, typically via F-actin protrusions (white arrows, Figure 3A), which were evident in cells treated with the PEG-coated Au*MNPs. This may suggest active cell internalization.

The TEM image of cells were taken after 24-h exposure to Au*MNPs (see Figure 3B). Both uncoated and PEG-coated Au*MNPs were clearly observed in vesicles/endosomes within the cell cytoplasm. From the images, PEG-coated Au*MNPs showed a higher internalization, compared with the uncoated NPs. Moreover, the PEG-coated Au*MNPs aggregates were less dense compared with the uncoated. This is consistent with similar observations from reports using PEG-coated NPs [30,34–36]. Overall, compared with the controls, Au*MNPs did not damage cells upon internalization.

Contrast enhancement ability in MRI

In this study, MR imaging was used to assess the contrast-enhancing ('negative contrast', i.e., dark contrast) ability of our Au*MNPs, using a T_2 sequence commonly recruited for anatomical imaging. Clear signal reductions were observed in all T_2 MR images, as MNPs concentrations increased from 0.01 to 0.2 mM Fe (Figure 4 & Supplementary Figure 4). Hence, all MR reductions were Au*MNP concentration-dependent. The multi-echo multislice gradient echo sequence used for T_2 MR images (see Materials & methods) can achieve high quality anatomical imaging *in vivo* [37], while its use is well-established in cardiovascular imaging [38,39].

In Figure 4E, we measured the T_2 (r_2) MR relaxivity. As shown, our MNP exhibited a relatively high r_2 value of 74.8 mM^{-1} s^{-1}, which is in agreement with a previous study [18] and is comparable with the commercial MNP (known as SHU-555C, with r_2 = 69 mM^{-1} s^{-1}) [40]. Our results demonstrate that these Au*MNPs can be used as an efficient MR contrast agent in the clinical setting.

Contrast enhancement ability in CT

CT imaging was performed to assess the CT contrast enhancement ability of Au*MNPs. To efficiently enhance the CT signal, Au*MNP samples with higher Au/Fe mass ratios (= 0.19 and 0.25) were examined. There were distinct increases shown in CT signal intensity as Au concentration was raised (Figure 5). This is consistent with a previous study assessing CT signal enhancement in the presence of Au on MNPs [18]. Moreover, the MNP component did not affect the CT signal enhancement, as MNP concentration increased across samples (from 0.01 to 0.2 mM MNP, for both Au/Fe mass ratios on MNP experiments; Figure 5). Note that CT signal quantification in Figure 5C consistently delineates even subtle differences observed in the visual assessment of Figure 5A & B.

Contrast enhancement ability in intravascular US

Figure 6A shows typical images acquired from the IVUS scanner for all three Au*MNP concentrations. There
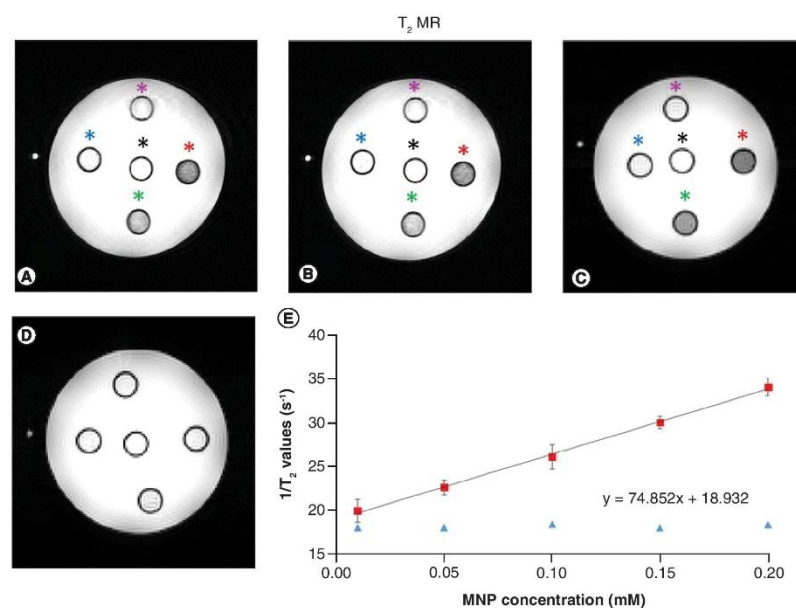
Figure 4.   Magnetic resonance imaging and analysis for gold-dotted magnetic nanoparticles. (A–C) Gold-dotted magnetic nanoparticle (Au*MNP) samples (Au/Fe = 0.15, 0.19 and 0.25 in **(A–C**, respectively) showing T_2 'negative contrast' as concentration increased. Black, blue, magenda, green and red stars denote 0.01, 0.05, 0.10, 0.15 and 0.20 mM Au*MNP concentrations, respectively. **(D)** The pure Au reference samples are shown. The slope in the **(E)** $1/T_2$ versus Au*MNP concentration graph indicates the r_2 relaxivity. The blue triangles show the pure Au reference signal extracted from the corresponding tubes in **(D)**.
MNP: Magnetic nanoparticle.

was consistently increasing signal enhancement as Au concentration increased (from 1 to 10 mg/ml Au*MNP concentration, and Au/Fe mass ratio from 0.15 to 0.25 on MNP). For low Au*MNP concentrations (1 mg/ml) little enhancement was observed in the image but increasing Au*MNP concentrations resulted in increasing enhancement. Figure 6B illustrates the quantitative results obtained from the MATLAB analysis showing a fourfold increase in mean signal intensity between 1 and 5 mg/ml Au*MNP concentration for the Au/Fe = 0.15 and 0.19 hybrids and a 2.5-fold increase for the Au/Fe = 0.25 sample. Au is known to have high density and therefore high acoustic impedance [21], which explains why the IVUS signal increased as Au concentration increased across samples. Furthermore, our IVUS results are consistent with previous studies demonstrating enhancement of ultrasonic emission in photoacoustic imaging due to the presence of Au, in a concentration-dependent mode [21,22]. Following careful adaptation of the Au*MNP concentrations, these materials can potentially be used as contrast agents in standard whole-body ultrasound imaging [21,22].

Discussion

The synthesis method for gold-iron oxide hybrid nanoparticles presented here is adapted from large scale preparation for 'metal-on-metal oxide' catalysts (e.g., Au on Fe_3O_4 in this work) [29]. There are several advantages offered from this method. First, it is scalable to 1 g per batch scale, which is a significant advantage over other methods for similar type of biomaterials. As in catalysis, there is a wide range of metal-metal oxide combinations that can be adapted using this method, not only limited to Au and Fe_3O_4 [41,42]. Moreover, the reagents used were considered to be biocompatible, for example urea as the reductant. This is aimed for high biocompatibility of the final contrast agent. We used physical absorption of PEG onto the Au*MNP, forming a temporary coating around these
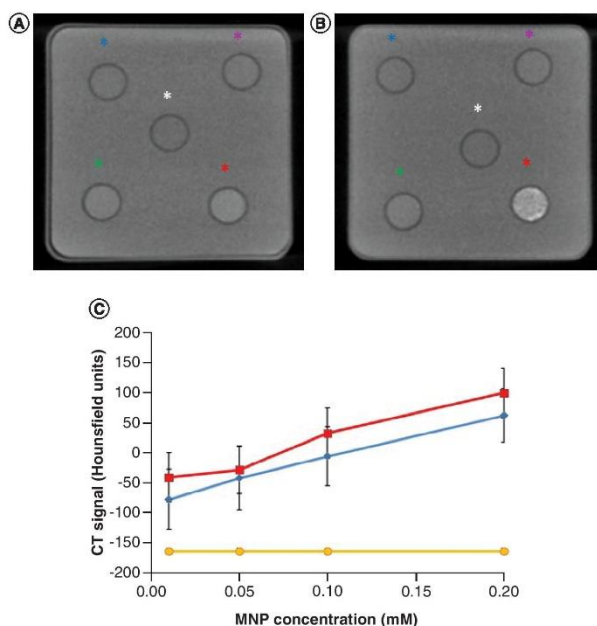
Figure 5. Computed tomography imaging and analysis for gold-dotted magnetic nanoparticles. (A & B) Gold-dotted magnetic nanoparticle (Au*MNP) (Au/Fe = 0.19 and 0.25 with no PEG, respectively) showing CT signal increases as concentration increased. Blue, magenta, green and red stars denote 0.05, 0.10, 0.15 and 0.20 mM concentrations of Au*MNP, respectively. **(C)** CT signal quantification. The Au*MNP (Au/Fe = 0.15 and 0.19) with no PEG are shown with the blue and red curve, respectively. The yellow line shows no changes in the CT signal derived from the reference sample (pure MNP content; white stars in **[A & B]**).
CT: Computed tomography; MNP: Magnetic nanoparticle.

pristine materials, which enhances biocompatibility while enables functionalization. Also, unlike other published methods [17–22], there is no organic functionalization, for example thiol groups, performed on the MNP surface (between the Au and Fe_3O_4 nanoparticles) [18]. As such, the surfaces of each component were kept pristine for further functionalization. This is essential when further functionalities are required, for example targeting molecules, for localization of the contrast agent on specific sites of interest [11].

In cytotoxicity assays, MCF-7 breast cancer cells were chosen for assessing the effect of the Au*MNP samples because MCF-7 cells (among other cancer cell lines e.g., HeLa and HEKT-293) are widely used as model cells for studies in a wide range of biomedical applications [43–47]. This also allows us to directly compare our Au*MNP samples against other nanoparticles published in the literature. A colorimetric assay PrestoBlue was used here as a preliminary test for Au*MNP's cytotoxicity. There are a number of commercial cytotoxicity assays available, but none was designed for solid materials, which usually absorbs lights, leading to lowering the accuracy of the test results [48]. To ensure safe use of these nanomaterials, more than one assay might be required such as *in vivo* assays. Moreover, a higher gold content on Au*MNPs seems to cause higher cytotoxicity and it could be a limitation of these Au*MNPs. Using the Au*MNPs with a lower Au content could be the solution as the Au/Fe = 0.15 sample showed no toxicity even at a high concentration of 250 µg/ml.

This is the first study demonstrating increased ultrasonic emission from an IVUS scanner, due to Au content increases within these Au*MNP samples. Moreover, our Au*MNP samples showed concentration-dependent contrast-enhancing ability in MR and CT imaging. IVUS imaging is among the reference standard techniques used to invasively assess the severity of atherosclerotic plaque development in cardiovascular disease [49]. Using MR
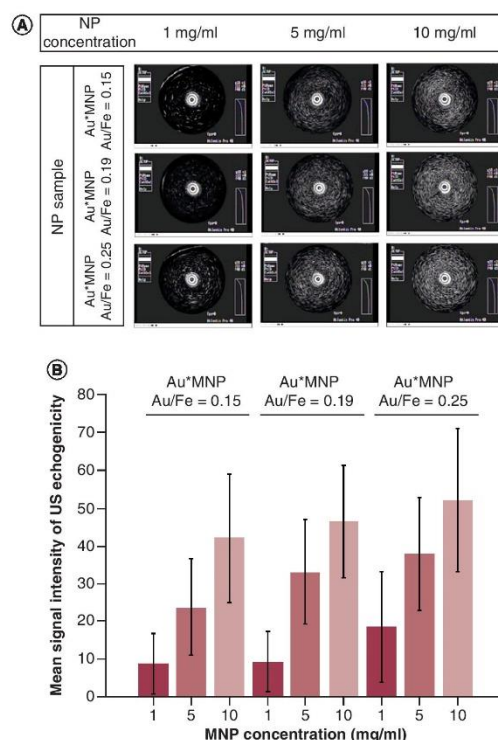
Figure 6. **Intravascular ultrasound imaging and analysis for gold-dotted magnetic nanoparticles. (A)** Qualitative signal differences in images acquired using the intravascular US scanner, showing signal enhancement, as Au*MNP concentration increased from 1 to 10 mg/ml and as Au/Fe mass ratio increased from 0.15 to 0.25. **(B)** Quantitative signal differences across the same Au*MNP samples derived in MATLAB. Au*MNP: Gold-dotted magnetic nanoparticle; US: Ultrasound.

imaging, our group has previously shown that MNP are taken up by macrophages in areas of cellular inflammation in the myocardium [14,50]. Being able to monitor cellular inflammation early in cardiovascular disease is critically important, as it could enable to predict atherosclerotic plaque rupture, which in turn is considered to be responsible for acute myocardial infarction [28,50,51]. Thus, our results indicate that our Au*MNPs can support a novel reference standard methodology which can enable to simultaneously assess atherosclerotic plaque development and inflammation, by using a single Au*MNP IVUS imaging setting. In our future work, we aim to investigate the three-modal contrast enhancement ability of our Au*MNP samples in animal models, where we can thoroughly examine their *in vivo* biocompatibility, tissue uptake and kinetic properties across all three imaging modalities.

Conclusion

In this work, we demonstrated the development of Au*MNPs synthesized using an impregnation method, leading to nanoparticles with pristine surfaces for either component. The pristine particle surfaces can be particularly important when functionalization needs to be engineered in molecularly targeted theragnostic applications. We evaluated the cytotoxicity of these Au*MNPs *in vitro* and showed that these were non toxic to cells, when a maximum concentration of 100 µg/ml was examined for a 7-day period. We further demonstrated a number of prominent imaging contributions. The contrast-enhancing ability of these Au*MNPs was also shown to be concentration-dependent across all three (MR, CT and IVUS) imaging techniques. Importantly, we demonstrated for the first time that the Au content of the Au*MNP can lead to evident increases of the IVUS signal. In conclusion, these materials are a promising tool toward enhancing theragnostic applications and improving tri-modal imaging accuracy in the clinical setting.

Summary points

- Gold-dotted magnetic nanoparticles (Au*MNPs) have been prepared by adapting a method designed for catalysts preparation.
- Gold nanoparticles of 1–2 nm were deposited on the surface of Fe_3O_4 MNPs (20–30 nm).
- From a scanning electron microscopy study, Au*MNPs did not cause changes in morphology on MFC-7 cells.
- PEG-coated Au*MNPs reduced agglomeration of nanoparticles after internalization in cells.
- Cytotoxicity of Au*MNPs seemed to correlate with increases in the Au content.
- The concentration-dependent contrast enhancing ability of Au*MNPs was shown in both MRI and computed tomography.
- For the first time concentration-dependent contrast enhancing ability of Au*MNPs in intravascular ultrasound imaging was demonstrated.
- Au*MNPs were shown to possess MR/computed tomography/intravascular ultrasound tri-modal contrasting capacity.

Supplementary data

To view the supplementary data that accompany this article please visit the journal website at: www.futuremedicine.com/doi/suppl/10.2217/nnm-2020-0236

References

Papers of special note have been highlighted as: ● of interest; ●● of considerable interest

1. Fihn SD, Gardin JM, Abrams J *et al.* 2012 ACCF/AHA/ACP/AATS/PCNA/SCAI/STS Guideline for the diagnosis and management of patients with stable ischemic heart disease: a report of the American College of Cardiology Foundation/American Heart Association Task Force on Practice Guidelines, and the American College of Physicians, American Association for Thoracic Surgery, Preventive Cardiovascular Nurses Association, Society for Cardiovascular Angiography and Interventions, and Society of Thoracic Surgeons. *J. Am. Coll. Cardiol.* 60(24), 44–164 (2012).

2. Graham LJ, Shupe MP, Schneble EJ *et al.* Current approaches and challenges in monitoring treatment responses in breast cancer. *J. Cancer* 5(5), 58–68 (2014).

3. Montalescot G, Sechtem U, Achenbach S *et al.* ESC guidelines on the management of stable coronary artery disease: the task force on the management of stable coronary artery disease of the European Society of Cardiology. *Eur. Heart J.* 34(38), 2949–3003 (2013).

4. Murakami T, Imai Y, Okada M *et al.* Ultrasonography, computed tomography and magnetic resonance imaging of hepatocellular carcinoma: toward improved treatment decisions. *Oncology* 81(Suppl. 1), 86–99 (2011).

5. Papanastasiou G, Williams MC, Kershaw LE *et al.* Measurement of myocardial blood flow by cardiovascular magnetic resonance perfusion: comparison of distributed parameter and Fermi models with single and dual bolus. *J. Cardiov. Magn. Reson.* 17, 17 (2015).

6. George RT, Arbab-Zadeh A, Cerci RJ *et al.* Diagnostic performance of combined noninvasive coronary angiography and myocardial perfusion imaging using 320-MDCT: the CT angiography and perfusion methods of the CORE320 multicenter multinational diagnostic study. *Am. J. Roentgenol.* 197(4), 829–837 (2011).

7. Blessberger H, Binder T. NON-invasive imaging: two dimensional speckle tracking echocardiography: basic principles. *Heart* 96(9), 716–722 (2010).

8. Papanastasiou G, González-Castro V, Gray CD *et al.* Multidimensional assessments of abdominal aortic aneurysms by magnetic resonance against ultrasound diameter measurements. In: *Medical Image Understanding and Analysis (Volume 723)* Hernández MV (Ed.). Springer International Publishing, Cham, Switzerland 133–143 (2017).

9.   Papanastasiou G, Williams MC, Dweck MR *et al.* Multimodality quantitative assessments of myocardial perfusion using dynamic contrast enhanced magnetic resonance and 15O-labelled water positron emission tomography imaging. *IEEE Trans. Radiat. Plasma Med. Sci.* 2(3), 259–271 (2018).

10. Casals E, Vázquez-Campos S, Bastús NG, Puntes V. Distribution and potential toxicity of engineered inorganic nanoparticles and carbon nanostructures in biological systems. *Trends Anal. Chem.* 27(8), 672–683 (2008).

11. Bertrand N, Wu J, Xu XY, Kamaly N, Farokhzad OC. Cancer nanotechnology: the impact of passive and active targeting in the era of modern cancer biology. *Adv. Drug Deliv. Rev.* 66, 2–25 (2014).

12. Sun C, Lee JSH, Zhang M. Magnetic nanoparticles in MR imaging and drug delivery. *Adv. Drug Deliv. Rev.* 60(11), 1252–1265 (2008).

13. Ruehm SG, Corot CA, Vogt PR, Kolb SE, Debatin JF. Magnetic resonance imaging of atherosclerotic plaque with ultrasmall superparamagnetic particles of iron oxide in hyperlipidemic rabbits. *Circulation* 103(3), 415–422 (2001).

14. Stirrat CG, Alam SR, MacGillivray TJ *et al.* Ferumoxytol-enhanced magnetic resonance imaging assessing inflammation after myocardial infarction. *Heart* 103(19), 1528–1535 (2017).

15. Girardi G, Fraser J, Lennen R, Vontell R, Jansen MG, Hutchison G. Imaging of activated complement using ultrasmall superparamagnetic iron oxide particles (USPIO) – conjugated vectors: an *in vivo in utero* non-invasive method to predict placental insufficiency and abnormal fetal brain development. *Mol. Psychiatr.* 20, 1017–1026 (2015).

16. Lee N, Choi SH, Hyeon T. Nano-sized CT contrast agents. *Adv. Mater.* 25(19), 2641–2660 (2013).

17. Wang GN, Qian K, Mei XF. A theranostic nanoplatform: magneto-gold@fluorescence polymer nanoparticles for tumor targeting T1&T2-MRI/CT/NIR fluorescence imaging and induction of genuine autophagy mediated chemotherapy. *Nanoscale* 10(22), 10467–10478 (2018).

••   **An example on tri-modal imaging capacity of a nanoparticle.**

18. Zhao HY, Liu S, He J *et al.* Synthesis and application of strawberry-like Fe$_3$O$_4$-Au nanoparticles as CT-MR dual-modality contrast agents in accurate detection of the progressive liver disease. *Biomaterials* 51, 194–207 (2015).

••   **Shows Au/magnetic nanoparticle modifying the computed tomography signal in a concentration-dependent mode, due to the Au component. The results of our computed tomography assessments on gold-dotted magnetic nanoparticles are consistent with this work.**

19. Kukreja A, Kang B, Kim HO *et al.* Preparation of gold core-mesoporous iron-oxide shell nanoparticles and their application as dual MR/CT contrast agent in human gastric cancer cells. *J. Ind. Eng. Chem.* 48, 56–65 (2017).

20. Han L, Zhang Y, Zhang Y, Shu Y, Chen XW, Wang JH. A magnetic polypyrrole/iron oxide core/gold shell nanocomposite for multimodal imaging and photothermal cancer therapy. *Talanta* 171, 32–38 (2017).

21. Hu Y, Wang RZ, Wang SG *et al.* Multifunctional Fe$_3$O$_4$@Au core/shell nanostars: a unique platform for multimode imaging and photothermal therapy of tumors. *Sci. Rep.* 6, 28325 (2016).

••   **Presents folic acid-targeted iron oxides-gold nanostars in photoacoustic imaging, in which ultrasonic emission was also produced and examined.**

22. Reguera J, Jiménez de Aberasturi D, Henriksen-Lacey M *et al.* Janus plasmonic–magnetic gold–iron oxide nanoparticles as contrast agents for multimodal imaging. *Nanoscale* 9(27), 9467–9480 (2017).

••   **A good example on the preparation of Janus nanoparticles for imaging applications.**

23. Beik J, Asadi M, Khoei S *et al.* Simulation-guided photothermal therapy using MRI-traceable iron oxide-gold nanoparticle. *J. Photochem. Photobiol. B.* 199, 111599 (2019).

24. Abed Z, Beik J, Laurent S *et al.* Iron oxide–gold core–shell nano-theranostic for magnetically targeted photothermal therapy under magnetic resonance imaging guidance. *J. Cancer Res. Clin. Oncol.* 145(5), 1213–1219 (2019).

25. Neshastehriz A, Khosravi Z, Ghaznavi H *et al.* Gold-coated iron oxide nanoparticles trigger apoptosis in the process of thermo-radiotherapy of U87-MG human glioma cells. *Radiat. Environ. Biophys.* 57(4), 405–418 (2018).

26. Hosseini V, Mirrahimi M, Shakeri-Zadeh A *et al.* Multimodal cancer cell therapy using Au@Fe$_2$O$_3$ core–shell nanoparticles in combination with photo-thermo-radiotherapy. *Photodiagnosis Photodyn. Ther.* 24, 129–135 (2018).

27. Yiu HHP. Engineering the multifunctional surface on magnetic nanoparticles for targeted biomedical applications: a chemical approach. *Nanomedicine* 6(8), 1429–1446 (2011).

28. Lutgens E, van Suylen RJ, Faber BC *et al.* Atherosclerotic plaque rupture local or systemic process? *Arterioscler. Thromb. Vasc. Biol.* 23(12), 2123–2130 (2003).

29. Huang J, Dai WL, Fan KN. Remarkable support crystal phase effect in Au/FeO$_x$ catalyzed oxidation of 1,4-butanediol to γ-butyrolactone. *J. Catal.* 266, 228–235 (2009).

•   **A representative example on catalyst preparation that can inspire materials scientists in developing new materials for biomedicine.**

30. Prabhu S, Mutalik S, Rai S, Udupa N, Rao BSS. PEGylation of superparamagnetic iron oxide nanoparticle for drug delivery applications with decreased toxicity: an *in vivo* study. *J. Nanopart. Res.* 17, 412 (2015).

193 | P a g e

31. McCully M, Conde J, V Baptista P, Mullin M, Dalby MJ, Berry CC. Nanoparticle-antagomiR based targeting of miR-31 to induce osterix and osteocalcin expression in mesenchymal stem cells. *PLoS One* 13(2), e0192562 (2018).

32. McDougald WA, Collins R, Green M, Tavares AAS. High dose MicroCT does not contribute toward improved MicroPET/CT image quantitative accuracy and can limit longitudinal scanning of small animals. *Front. Physics* 5, 50 (2017).

33. Bouffier L, Yiu HHP, Rosseinsky MJ. Chemical grafting of a DNA intercalator probe onto functional iron oxide nanoparticles: a physicochemical study. *Langmuir* 27(10), 6185–6192 (2011).

34. Gal N, Lassenberger A, Herrero-Nogareda L *et al.* Interaction of size-tailored PEGylated iron oxide nanoparticles with lipid membranes and cells. *ACS Biomater. Sci. Eng.* 3(3), 249–259 (2017).

35. Nissinen T, Näkki S, Laakso H *et al.* Tailored dual PEGylation of inorganic porous nanocarriers for extremely long blood circulation *in vivo. ACS Appl. Mater. Interfaces* 8(48), 32723–32731 (2016).

36. Illés E, Szekeres M, Kupcsik E *et al.* PEGylation of surfaced magnetite core–shell nanoparticles for biomedical application. *Colloid Surf. A-Physicochem. Eng. Asp.* 460, 429–440 (2014).

37. Reeder SB, Yu H, Johnson JW *et al.* T1- and T2-weighted fast spin-echo imaging of the brachial plexus and cervical spine with IDEAL water–fat separation. *J. Magn. Reson. Imaging* 24(4), 825–832 (2006).

38. Ridgway JP. Cardiovascular magnetic resonance physics for clinicians: part I. *J. Cardiov. Magn. Reson.* 12, 71 (2010).

•   **Provides a comprehensive review of MR sequences in clinical cardiovascular applications and highlights the broad applicability of the multi-echo multislice gradient echo sequence that we used for T2 MR imaging, to examine the contrast-enhancing ability of our gold-dotted magnetic nanoparticles in MRI.**

39. Biglands JD, Radjenovic A, Ridgway JP. Cardiovascular magnetic resonance physics for clinicians: part II. *J. Cardiov. Magn. Reson.* 14, 66 (2012).

40. Li Z, Yi PW, Sun Q *et al.* Ultrasmall water-soluble and biocompatible magnetic iron oxide nanoparticles as positive and negative dual contrast agents. *Adv. Funct. Mater.* 22(11), 2387–2393 (2012).

41. Sharma RK, Dutta S, Sharma S, Zboril R, Varma RS, Gawande MB. Fe$_3$O$_4$ (iron oxide)-supported nanocatalysts: synthesis, characterization and applications in coupling reactions. *Green Chem.* 18(11), 3184–3209 (2016).

42. Von Held Soares A, Atia H, Armbruster H, Barboza Passos F, Martin A. Platinum, palladium and nickel supported on Fe$_3$O$_4$ as catalysts for glycerol aqueous-phase hydrogenolysis and reforming. *Appl. Catal. A: Gen.* 548, 179–190 (2017).

43. Chattoraj S, Amin MA, Mohapatra S, Ghosh S, Bhattacharyya K. Cancer cell imaging using *in situ* generated gold nanoclusters. *Chemphyschem* 17(1), 61–68 (2016).

44. Lara-Cruz C, Jiménez-Salazar JE, Arteaga M *et al.* Gold nanoparticle uptake is enhanced by estradiol in MCF-7 breast cancer cells. *Int. J. Nanomedicine* 14, 2705–2718 (2019).

45. Baneshi M, Dadfarnia S, Shabani AMH, Sabbagh SK, Haghgoo S, Bardania H. A novel theranostic system of AS1411 aptamer-functionalized albumin nanoparticles loaded on iron oxide and gold nanoparticles for doxorubicin delivery. *Int. J. Pharm.* 564, 145–152 (2019).

46. Poursalehi Z, Salehi R, Samadi N, Rasta SH, Mansoori B, Majdi H. A simple strategy for chemo-photothermal ablation of breast cancer cells by novel smart gold nanoparticles. *Photodiagnosis Photodyn. Ther.* 28, 25–37 (2019).

47. Kodiha M, Hutter E, Boridy S, Juhas M, Maysinger D, Stochaj U. Gold nanoparticles induce nuclear damage in breast cancer cells, which is further amplified by hyperthermia. *Cell. Mol. Life Sci.* 71(21), 4259–4273 (2014).

48. Hoskins C, Wang L, Cheng WP, Cushieri A. Dilemmas in the reliable estimation of the *in vitro* cell viability in magnetic nanoparticle engineering: which tests and what protocols? *Nanoscale Res. Lett.* 7(1), 77 (2012).

49. Mintz GS, Nissen SE, Anderson WD *et al.* ACC Clinical Expert Consensus Document, American College of Cardiology Clinical Expert Consensus Document on Standards for Acquisition, Measurement and Reporting of Intravascular Ultrasound Studies (IVUS). A report of the American College of Cardiology Task Force on Clinical Expert Consensus Documents developed in collaboration with the European Society of Cardiology endorsed by the Society of Cardiac Angiography and Interventions. *Eur. J. Echocardiogr.* 2(4), 299–313 (2001).

50. Alam SR, Shah ASV, Richards J *et al.* Ultrasmall superparamagnetic particles of iron oxide in patients with acute myocardial infarction. *Circ. Cardiovasc. Imaging* 5(5), 559–565 (2012).

51. Fioranelli M, Bottaccioli AG, Bottaccioli F, Bianchi M, Rovesti M, Roccia MG. Stress and inflammation in coronary artery disease: a review psychoneuroendocrineimmunology-based. *Front. Immunol.* 9, 2031 (2018).

194 | P a g e

8.3. Recent developments on magnetic molecular imprinted polymers (MMIPs) for sensing, capturing, and monitoring pharmaceutical and agricultural pollutants

G. Aylaz, J. Kuhn, ECHT Lau, C-C Yeung, VAL Roy, M. Duman, HHP Yiu

Recent developments on magnetic molecular imprinted polymers (MMIPs) for sensing, capturing, and monitoring pharmaceutical and agricultural pollutants

Gulgun Aylaz,[a] Joel Kuhn,[b] Elizabeth CHT Lau,[b] Chi-Chung Yeung,[c] Vellaisamy AL Roy,[d] Memed Duman[a] and Humphrey HP Yiu[b]*

Abstract

Among the many classes of pollutants, bioactive contaminants including pesticides, herbicides, and other pharmaceutical active compounds (PhACs) are causing significant concern. These chemicals have been linked directly to contamination of freshwater and food sources, threatening water and food security. Contamination from antibiotics, one class of PhACs, is also considered to link strongly to the global problem of antimicrobial resistance (AMR). Pollution from these contaminants has hit developing countries harder as a consequence of less stringent legislation on waste discharge from agricultural industries. Current sampling and monitoring methods [e.g. liquid chromatography mass spectrometry (LC–MS)] are expensive, time-consuming, immobile and require skilled users. Recent development of devices fitted with molecular imprinted polymers (MIPs) have been found to be particularly attractive owing to their low cost, stability, high selectivity and mobility. MIPs also can be used to extract these organic pollutants at low concentrations. The latest development of magnetic MIPs (MMIPs) further facilitates the separation and recovery of these absorbents by using an external magnetic field after the target molecules have been bound, thus avoiding laborious centrifugation and filtration for separation and recovery. The purpose of this perspective is to summarize the recent development of MMIPs in the past ten years. We will focus on their applications in food industries and the agricultural sector. Several potential developments in combined analytical techniques using MMIPs also will be discussed. As pollution to our environment is now a focal point in human life, new analytical techniques based on MMIPs will be of great interest to the science communities.
© 2021 Society of Chemical Industry

Supporting information may be found in the online version of this article.

Keywords: wastewater; sorption; removal; pharmaceuticals; environmental; remediation; extraction

INTRODUCTION

The ever-expanding global population has put extreme pressure on both food and water supplies. To meet the ever increasing food demand, science and technology (particularly in agriculture) have provide many solutions to maintain a strong supply of food, by using drugs, growth hormones, pesticides and fungicides. However, excessive use of these pharmaceutical active compounds, or PhACs, has caused pollution problems to the environment, particularly in developing countries. PhACs can uncontrollably enter the natural water systems via agricultural activities, contaminating food stocks and threatening freshwater supplies.[1] Furthermore, some PhACs, such as antibiotics, have led to the development of antimicrobial resistance (AMR) in some bacteria.[2] These multidrug-resistant (MDR) bacteria are a major concern to the WHO.[3] Moreover, these pollutants also directly contribute to the contamination of food and freshwater for human consumption, directly threatening food and water security.

In order to tackle this problem efficiently and effectively, sophisticated monitoring of PhACs is urgently required but the challenge is the detection of ultra-low concentrations of PhACs (usually in ppb range) in food and water sources. Common methods to detect antibiotics and other PhACs include mass spectrophotometry,[4] liquid chromatography,[5] solid phase extraction (SPE),[6] capillary electrophoresis[7] and electrochemical techniques.[8] These methods have notable disadvantages as they are

* Correspondence to: HHP Yiu, Chemical Engineering, School of Engineering and Physical Sciences, Heriot-Watt University, Edinburgh, EH14 4AS, UK. E-mail: h.h.yiu@hw.ac.uk

a Nanotechnology and Nanomedicine Division, Institute of Science, Hacettepe University, Ankara, Turkey

b Chemical Engineering, School of Engineering and Physical Sciences, Heriot-Watt University, Edinburgh, UK

c Department of Chemistry, City University of Hong Kong, Hong Kong

d James Watt School of Engineering, University of Glasgow, Glasgow, UK

time-consuming, expensive, highly complex and require experienced users. Sophisticated automation systems also are necessary for continuous monitoring and the mobility of instrumentation for these purposes needs to be enhanced. Mobile systems also would aid in monitoring and sampling of water sources in remote areas. As a result, there is an urgent need for new detection methods and systems that are highly sensitive, specific, with fast response time, reproducible, cost-effective, reliable, portable and easy to implement by users.

DEVELOPMENT OF MOLECULARLY IMPRINTED POLYMERS (MIPS)

In the past few decades, the molecular imprinting technique with precise molecular recognition has been used in various scientific fields in the analysis of organics within the environment and biomedical diagnoses. Molecularly imprinted polymers (MIPs) have shown advantages including their rapid and highly selective adsorption on target analytes.[9] MIPs are synthesized from polymerization of specific functional monomers, an initiator and a stabilizer in the presence of molecules of a targeted template. The functional monomers have to be chosen with consideration of the covalent or noncovalent interactions with the targeted template (see Fig. 1). After polymerization, the template molecule is removed from the polymer matrix with a suitable desorption agent to generate printed cavities that have a complementary size, shape, 3D structure and binding sites with high affinity for a specific analyte, usually the template molecule itself.[10] For monitoring organic compounds from complex matrices including natural water resources, wastewater, food samples and human fluids, the high selectivity of MIPs is a clear advantage over conventional chromatography techniques. MIPs also have advantages over antibodies and natural receptors as they exhibit higher chemical and mechanical stability, as well as longer shelf life. The preparation of MIPs also is relatively simple and low-cost.

Recently, MIP nanoparticles have gained increasing interest as they have superior properties compared to conventional bulk MIPs such as cryogel, monolith, microparticles[11] and membranes.[12] These superior properties of MIP nanoparticles include large surface area, fast binding kinetics, high binding amounts, improved stability, good accessibility and easy handling during experiments.[13,14] One obstacle for using MIP nanoparticles lies on the recovery of these valuable materials. Separation using filtration causes a significant loss of materials because nanoparticles can easily be trapped in filters (e.g. filter papers). Some nanoparticles required filters with fine pores (<100 nm), which is not widely

available and can be easily blocked causing slow filtration. Centrifugation can be adapted but it is a laborious method.

MAGNETIC MOLECULAR IMPRINTED POLYMER (MMIP)

Separation and recovery of materials using a magnetic field have been used in biomolecular separation for decades[15-17] and this method is particularly advantageous when the amount of material is too small to recover through filtration or centrifugation. The combination of magnetic separation with molecular recognition ability of MIPs can be a powerful tool in analytical sciences, especially for the analysis of pollutants at low concentrations in complex analytes.

Magnetic MIPs can be prepared by embedding magnetic nanoparticles during the MIP synthesis. There are several different polymerization routes for the preparation of MMIPs but in general the principles are similar. The essential ingredients for preparing an MIP were discussed in the previous section. For MMIPs, an extra magnetic component is required. This magnetic component can either be embedded inside the MIP structure or act as a platform for coating the imprinted polymer on surface. The main aim is to ensure that the final MMIP materials can respond to an external magnetic field through the magnetic component firmly attached to the MIP. Iron oxide-based magnetic materials (e.g. Fe_3O_4 or γ-Fe_2O_3) are the most widely used for this application.[18,19] Surface functionalization usually is required for creating strong binding to the polymer but unfunctionalized iron oxide also has been used.[20] Commonly used functional surfaces include amine and vinyl groups.[21-23] For instance, vinyl groups on an iron oxide surface can be co-polymerized with vinyl monomers such as methacrylic acid, which is amongst the most popular monomers for MIP synthesis.[24,25] Other materials such as magnetic carbon nanotubes (MCNT) offer electrical conductivity properties and also have been used as a platform for coating MIP polymers.[26,27]

Applications of MMIPs so far have been limited to use in laboratory. In practice, the advantages of using MMIP over conventional nonmagnetic MIP stand out in the capture of target molecules from complex analyte samples. Because complex analyte samples can have large amounts of unwanted solid debris and particulates (e.g. soil samples, river water and sewage), if a nonmagnetic MIP is used, it becomes difficult to recover the MIP materials once it has captured the target molecules or pollutants, leading to difficulties in the follow-on analysis. Using MMIPs, the captured pollutants or targeted molecules can be isolated magnetically from these complex analytes, as shown in Fig. 2. Another scenario for needing MMIP is if nonmagnetic MIP cannot be made in large enough
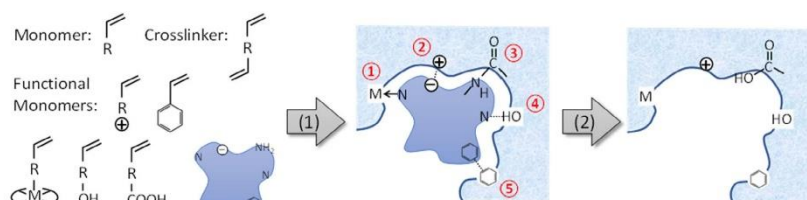
Figure 1. Schematic illustration of the formation of an MIP with binding sites. The five types of interactions that are used in MIP binding are highlighted as (1) co-ordination bonding, (2) opposite charge, (3) covalent bonding, (4) hydrogen bonding and (5) hydrophobic interaction.
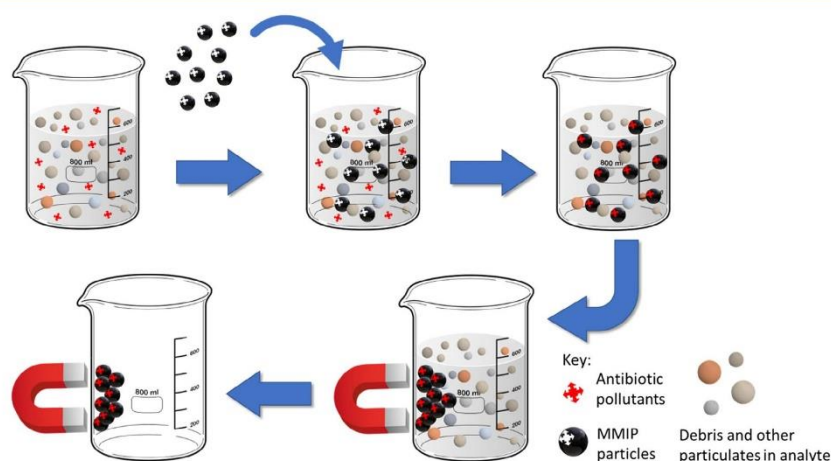
Figure 2. Illustration of the principle in separating/recovering MMIPs from a complex matrix with solid debris/particulates using a magnetic field.

quantities for other means of separation/recovery, including filtration or centrifugation. For instance, the template molecules are simply too expensive for use in a meaningful quantity, MMIP may be a possible solution to minimize the loss of MIP materials. Here we introduce some examples in three areas of applications that present particular challenges to nonmagnetic methods as a consequence of the complexity of the analytes.

MMIPs for extraction and monitoring for PhACs in sewage
There are many MMIP examples used in targeted applications for the extraction of PhACs from water sources. Many studies in the early stages were carried out in relatively clean samples (e.g. river water, tap water or seawater) spiked with pollutants.[28-30] Studies using MMIPs in sewage samples are few and far between. This highlights the challenge in working with real complex analytes. Qin et al.[31] prepared chitosan-based MMIP materials for the detection and removal of sulfonamides (a class of antibiotics) in water and sewage samples. It was found that 112 ng L^{-1} of sulfamethoxazole was in the sewage sample using MMIPs, whereas only 64 ng L^{-1} of sulfamethoxazole was found in the sample using a C-18 extraction column. This suggests that the MMIP was a more efficient extractor for sulfamethoxazole. Zuo et al. also demonstrated the synthesis of a MMIP for extracting dimethyl phthalate from soil samples.[32]

MMIPs for monitoring pesticides and herbicides in soil samples
As the food demand increases in response to the growing population in the world, increased use of pesticides and herbicides to ensure food productivity is inevitable. Despite advancements in modern technologies in agriculture, the application of active chemicals frequently is used in an uncontrolled fashion and in high quantities. Spraying crops is a widely practised method of agrochemical delivery worldwide, but this practice causes huge environmental problems; although aiming to destroy their targets (insects or weeds), it promotes pesticide resistance,[33] food contamination[34] and further environmental impacts. Furthermore, the residual pesticides and herbicides remain in soil as

contaminants and then leach and run-off to contaminate groundwater and surface water.[35] As a consequence, the concentration of these active chemicals can be different in each environmental compartment (soil, ground or surface water).

It is important to closely monitor these chemicals in low concentrations to avoid environmental problems and to detect the levels of contamination in agricultural areas, yet extracting the target contaminants from soil is not easy owing to the soil's complex composition. Several examples in the literature have demonstrated the possibility of using MMIP for extracting these agricultural contaminants from soil. One early example of research in this area was reported by Zhang et al. who demonstrated the use of 100–200 μm MMIP particles (prepared using microwave heating) for extracting triazine herbicides from soil, grains and vegetable samples.[36] Analysis using high performance liquid chromatography-mass spectrometery (HPLC–MS) showed >70% extraction of all triazines from spiked samples using MMIP after 30 min. Using a similar principle, Miao et al. demonstrated the preparation of 1–2-μm MMIP microspheres for extracting a herbicide bensulfuron-methyl (BSM), from soil, rice and rice water samples.[37] The binding capacity (Q) was found to be ≈38 mg g^{-1} but the nonimprinted sample also recorded a high Q (19 mg g^{-1}) at maximum, giving an imprinted factor (IF) of c. 2. A selectivity test also was carried out against other sulfurons, showing a selectivity factor (SF) from 1.8 to 10. Nonetheless, the MMIP microsphere was able to extract ≥90% of bensulfuron-methyl from spiked soil samples which was a ≈30% improvement from C-18 extraction cartridges. Xu et al. reported the synthesis of MMIP particles (0.5–1 μm) was prepared using silica-coated Fe_3O_4 as the magnetic component for the extraction of methyl parathion from a soil sample.[38] The MMIP sample showed a high IF of 12 but the binding capacity of the target methyl parathion was relatively low (at Q = 9.1 mg g^{-1}). A recovery of >80% of methyl parathion was shown from the spiked soil samples. These examples show that MMIPs can be used for extracting agricultural contaminants from soil with an improved efficiency than C-18 extraction columns.

1153

Table 1. Examples of MMIP used for extraction of contaminants from food and drink samples (ND = not determined)

| Test samples	Contaminants/MMIP templates	Magnetic component	Monomers/crosslinkers	Binding capacity (Q in mg g^{-1})	Ref.
Meat products					
Pork	Sulfamethazine	γ-Fe$_2$O$_3$@ZnO	MAA; EGDMA	653	39
Fish, pork, shrimp	Erythromycin	Fe$_3$O$_4$@SiO$_2$-MPS	MAA; EGDMA	94.1	40
Fish	Erythromycin	MMWCNTs	MAA; EGDMA	22.8	41
Fish, pork	E1, E2, E3, EE2	Fe$_3$O$_4$@ZIF-8	ABPA; ABPA; APS	ND	42
Fruits, crops and vegetables					
Rice	Chlorpyrifos	Fe$_3$O$_4$@SiO$_2$	MMA	171	43
Orange	Carbendazim, thiabendazole	Fe$_3$O$_4$@SiO$_2$	MAA; EGDMA	1.75	44
Fruits	β-Cyfluthrin, cyhalothrin, cyphenothrin, permethrin	MCNT@SiO$_2$-MPS	MAA; EGDMA;	225	45
Tomato	Triazines	Fe$_3$O$_4$/PEG	MAA; TRIM, DVB	ND	46
Drinks					
Honey	λ-Cyhalothrin	Fe$_3$O$_4$@SiO$_2$-MPS	AM, DVB	ND	47
Strawberry juice, milk	Triazines	Fe$_3$O$_4$/PEG	MAA; TRIM, DVB	ND	46
Tea	Dicofol, pyridaben	Fe$_3$O$_4$@OA	MAA; EGDMA; DDT	ND	48
Milk	Enrofloxacin	Fe$_3$O$_4$@POSS	MAA; POSS	67.3	49
Milk	β-Lactam	Fe$_3$O$_4$@OA	MAA; EGDMA; PENV	20.2–49	50
Milk	Bisphenol A	Fe3O4@MAPS	VP; EGDMA	390	51

MMIP for binding contaminants in food samples

Another area of interest is the extraction and monitoring of contaminants in food samples. Although food samples also are of high complexity, more research in this area has been seen in the literature than that on sewage or soil. This is possibly because food safety is of a higher priority in the public. Nonetheless, challenges in selective binding using MMIPs remain. Use of MMIPs has been seen for the extraction of a broad spectrum of contaminants (from antibiotics to pesticides) from a wide range of food samples (meat, dairy products, grains and vegetables). Table 1 summarizes several examples available in the literature.

Latest developments in this area include some responsive MMIP constructs. For example, a light responsive MMIP was prepared for extracting dimethoate from olive oil.[52] Unlike a conventional MIP, the release of the dimethoate template from this MMIP can be triggered by light. Li et al developed a flat 2D MMIP on boron nitride (BN) for extracting flavonoids from *Ginkgo biloba* leaf extracts.[53] Enhanced recoveries for all three tested flavonoids (>93%) were recorded compared with conventional MIPs. Wang et al. reported the preparation of a hollow MMIP construct for detecting triazines from crops including corn, wheat and soybean samples.[54] Unlike most MMIPs, where the magnetic component tends to be embedded inside or coated with the MIP polymer, this construct immobilized magnetic Fe$_3$O$_4$ nanoparticles by growing on the dialcohol groups on the nanoparticle surface. In addition to new design on the MMIPs, Zhang et al. demonstrated an internal extractive electrospray ionization (iEESI)-MS system for quantifying fluoroquinolones in milk samples.[55] This system bypassed the target molecule release stages, which can be time-consuming and reduce the accuracy of analysis if releasing is <100%.

COMBINED MMIP TECHNIQUES FOR ANALYSIS

As discussed previously, the advantages of using MIPs include high loading capacities and enhanced selectivity allowing for improved sample recovery. The added magnetic property of

MMIPs allows for an easier handling of samples. This has been demonstrated in the quantification of target organic molecules at low concentrations while the eluent is analyzed by various common instruments.[56-58] In recent years, the effect of PhAC pollutants has been an increasing cause for concern from evidence linking them to many global issues such as AMR, destruction of ecosystems, and threats to water and food security. Tetracycline (TC), for example, is a broad-spectrum antibiotic and widely used in agriculture due to its low cost. However, use of TC is mostly mismanaged; it is commonly added to animal feed as a supplement to reduce bacterial infections, regardless of the health conditions of the animals. This widespread use of TC has resulted in trace mount of residues in animal-derived food. These residues eventually transfer to humans via the food chain and are harmful to human health.[59] The European Union (EU) and US Food and Drug Administration (FDA) have established maximum TC residue limits in various food items.[60] Monitoring of TC residue levels in food has become essential, and although there are numerous methods to measure them currently, many (e.g. solid-phase dispersion[61] or magnetic MIP extraction,[62,63] followed by LC–MS/MS) require complex extraction and separation steps before measurement can take place. Gao et al.[64] highlighted the advantages of using MMIPs for the detection of pharmaceutical pollutants using a MMIP for TC detection in milk. They combined the MMIP with surface plasmon resonance (SPR) to achieve a very low detection limit of 1.0 pg mL^{-1}. In their study, methacrylic acid (MAA) was chosen as the functional monomer, ethylene glycol dimethylacrylate (EGDMA) as the cross-linker and citric acid-modified Fe$_3$O$_4$ nanoparticles as the magnetic component. The MMIPs were able to extract TCs from milk samples and allowed separation and recovery using a strong magnet. The TC-bound MMIPs were flowed over the mercaptoethylamine (MEA)-modified SPR chip. The SPR response is due to the interaction between amino groups of the chip surface and hydroxyl groups or carbonyl groups of the MMIPs. Figure 3 illustrates the whole working process using this MMIP-SPR combined detection method. Indeed, such a simple but delicate combined method
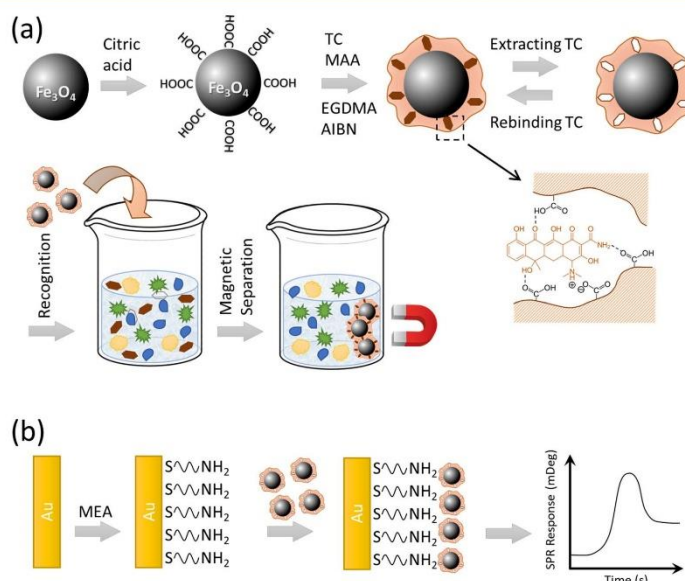
Figure 3. Schematic diagram illustrating TC detection by (a) MMIP extraction from water sample, and (b) MMIP-SPR measurement.

allows the detection of many organic molecule contaminants in a complex matrix with a low detection limit, rivalling high-end analytical techniques including HPLC-MS. A similar study using a combined MMIP-SPR technique also has demonstrated in the detection of pesticide residues.[65]

Magnetic MIPs also have been incorporated with electrochemical sensing methods, mostly as a coating material on a sensing electrode. Because this MMIP coating needs to be conductive, many research studies chose magnetic carbon nanotubes [or multi-walled carbon nanotubes (MWCN)] or magnetic graphene oxide (GO) as the magnetic component. For example, MMIPs have been used for the capture and preconcentration of sulfonamides before deposition onto the electrode surface for electrochemical detection.[66] The detection limit was found to be extremely low at 2.8×10^{-4} ppb (S/N = 3). However, in this work, the MMIP was not directly incorporated onto the electrode when the measurement was carried out. Another example had demonstrated a similar method for the detection of 17β-estradiol (E2) hormones and showed a low detection limit (0.82 nmol L^{-1}) with a good selectivity against other steroid hormones.[67]

In addition to SPR and electrochemical detecting methods, MIP techniques also can be incorporated with other analytical techniques for the detection of organic pollutants, such as resonant mass sensors, which consists mainly of Quartz Crystal Microbalance (QCM) and microcantilever sensor systems. They provide an advantage of label-free analysis and allow picogram mass resolutions. Combining resonant mass sensors with MIPs has becomes one of the key developments in sensing and monitoring pharmaceutical pollutants in water sources. In one study, a QCM sensor incorporated with a poly(2-hydroxyethyl methacrylate-N-methacryloly-l-tyrosine methylester) MIP was used for the real-time detection of

17β-estradiol.[68] This QCM-MIP sensor exhibited a high specificity and sensitivity in a wide range of concentration (3.67 pmol L^{-1}– 3.67 nmol L^{-1}) with the detection and quantification limits as low as 613 fmol L^{-1} and 2.04 pmol L^{-1}, respectively. This sensor also showed an almost 2.5-fold improvement in selectivity when the detection was carried out against similar molecules (stigmasterol and cholesterol). This sensor represents a promising, cost-friendly alternative for quantification and monitoring of estradiol pollutants in groundwater. In another study, an MIP microsphere-modified QCM sensor (prepared via a spin-coating method) was demonstrated to detect endosulfan from drinking water and milk samples.[69] The sensor showed a good selectivity against similar molecules and specificity for the recognition of endosulfan, with a good linear correlation over 10–40 ng mL^{-1} and a detection limit of 5.59 ng mL^{-1}. Moreover, the chips could be reused six times and have a shelf life of six months.

The micromechanical sensor is another technique that senses an accumulating mass through a MIP layer on cantilevers. Once the target molecule is in contact with the MIP cavity sites, it produces a frequency change of the cantilever. This technique has been demonstrated recently in the detection of antibiotic ciprofloxacin (CPX) in water sources.[70] In this study, highly specific CPX imprinted nanoparticles (160 nm) were chemically bound onto the cantilever surface via the carbodiimide (e.g. EDC) and N-hydroxysuccinimide (NHS) crosslinking route. This sensing system showed a linearity for the concentration range 1.5–150.9 μmol L^{-1} and a sensitivity of 2.6 Hz pg^{-1}. It also showed a high selectivity against another antibiotic with a similar structure, enrofloxacin (ENF). In a separate study, the particle size of MIP nanoparticles was found to have a positive effect on the sensitivity.[71] A similar system incorporated with erythromycin (ERY)

1155

imprinted polymeric nanoparticles of 22 nm were found to have a higher sensitivity of 1.58 Hz pg^{-1} in concentration range 0.68–67.94 µmol L^{-1}. Furthermore, the adsorption of target molecule ERY was found to follow the Freundlich model. The combination of imprinting technology with resonant mass sensor is simple and comparable to conventional techniques in terms of selectivity, sensitivity and reusability. However, use of magnetic MIPs has not been reported although their magnetic property may offer an additional advantage in adhesion onto the cantilever.

This will likely be the next stage of development in this research area.

MMIP PARTICLES FOR SELECTIVE BINDING OF ANTIBIOTICS: A CASE STUDY

Here, we demonstrate the preparation of a MMIP particle sample using erythromycin as the antibiotic template. Erythromycin is a widely prescribed antibiotic, which also is on the WHO's Essential
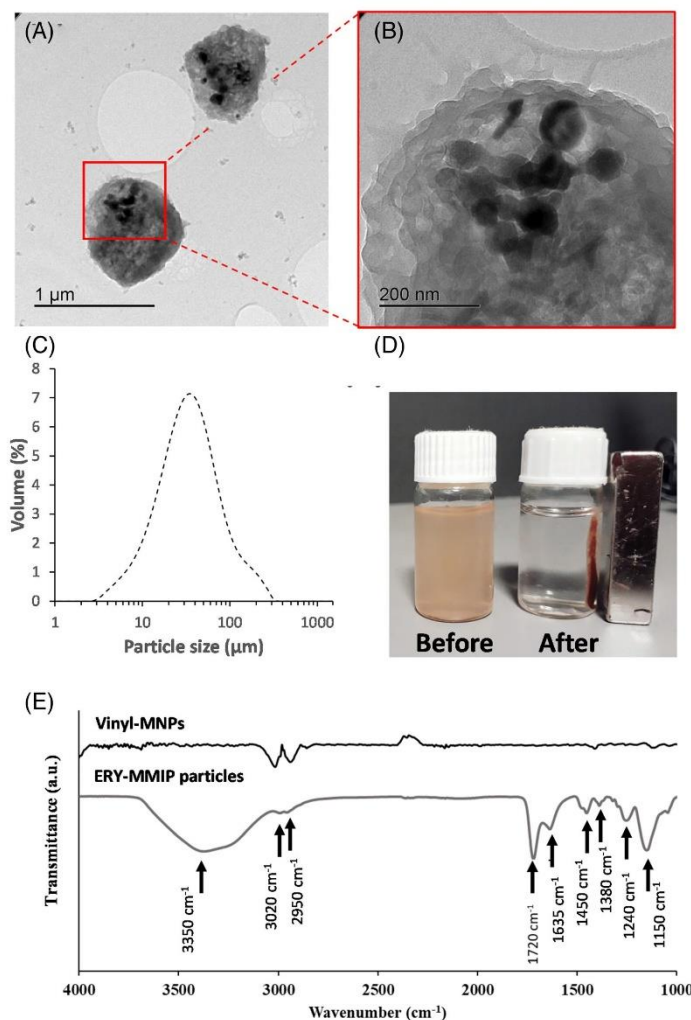
Figure 4. Characterization of ERY-MMIP particles. (a) TEM images of ERY-MMIP particles and (b) zoom-in TEM image of an ERY-MMIP particle to depict the embedded iron oxide MNP component, shown as darker particles. (c) Hydrodynamic size distribution analyzed of ERY-MMIP using DLS. (d) The separation of ERY-MMIP particles before and after magnetic separation. (e) FTIR spectra of ERY-MMIP compared to vinyl-MNPs.
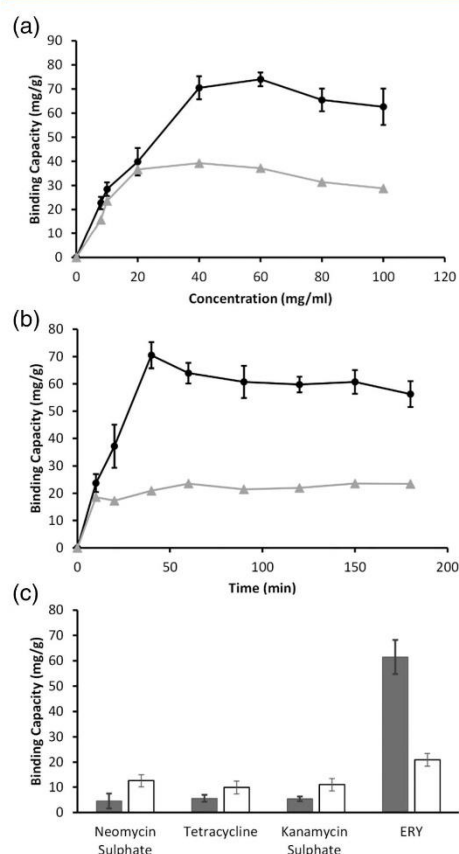
Figure 5. Binding capacities of ERY-MMIP particles. (a) Binding capacity of ERY-MMIP against various concentration of ERY after 40 min; (b) binding capacity of ERY-MMIP over time at 40 mg mL⁻¹ ERY; the grey line represents the binding from nonimprinted MNIP particle; (c) selectivity binding of ERY-MMIP on other antibiotics (grey bars) compared with nonimprinted particles (white bars).

Medicines List (EML).[72] Therefore, it can be found in municipal wastewater streams.[73] A system capable of selectively binding erythromycin in a complex medium would be essential for its monitoring in wastewater. In brief, erythromycin-specific MMIP particles (ERY-MMIP) were prepared using MAA as the monomer and EGDMA as the crosslinker via a two-phase microemulsion polymerization route (see Supplementary information Appendix S1). Vinyl-functionalized Fe_3O_4 nanoparticles (25 nm) were used as the magnetic component. A hand-held homogenizer was used to form particles of c. 1 μm diameter. It is worth noting that the power and speed of the homogenization is critical to the formation of the particles, which were isolated using a neodymium-iron-boron NdFeB magnet.

Transmission electron microscopy (TEM) analysis revealed that the MMIP particles formed had a diameter around 1–2 μm with magnetic nanoparticles embedded inside the polymer particles [Fig. 4(a)–(c)]. However, dynamic light scattering (DLS) results revelead a hydrodynamic size much larger than the particle size measured from our TEM study [Fig. 4(d)]. Although there are many reports in the literature showing DLS data (hydrodynamic size) for magnetic particles, the results can be questionable.[74] This is partly due to the inaccuracy for using DLS technique in measuring the hydrodynamic size of dark materials/particles. Moreover, we cannot rule out the effect of aggregation of particles. Figure 4(e) showed the Fourier transform infrared (FTIR) spectra of the particles, highlighting the PMAA coating. To test the selective binding properties of ERY-MMIP particles, three experiments were carried out. Figure 5(a) shows the binding capacity Q of ERY-MMIP particles against the concentration of erythromycin, with a plateau at ≈70 mg erythromycin per g ERY-MMIP apparent at ≈40–60 mg mL⁻¹. In a kinetic study shown in Fig. 5(b), the binding of erythromycin achieved the maximum after 40 min. The selectivity study shown in Fig. 5(c) highlights the ERY-MMIP particles with a high selectivity towards erythromycin over three other antibiotics. A high selectivity factor (SF) of >11.1 was recorded for all three competitors whereas the nonimprinted MNIP showed an SF around 2. These figures are comparable with the nonmagnetic MIP for other pharmaceutical pollutants reported in the literature.[75,76] The same technology should be applicable for the preparation of MMIP particles for many other organic pollutants, suitable for their capture and monitoring.

FURTHER CONSIDERATIONS

Although MMIP enhances recycling and reuse of MIPs and prolongs their shelf life, eventually the spent MMIPs need to be disposed of once the binding capacity has diminished. Problems with most MIPs reported in the literature are that they are synthesized with nonbiodegradable polymers (PMMA, PS etc). They also are crosslinked to maintain a certain degree of rigidity to allow for shape recognition. However, crosslinked polymers are even harder to degrade than noncrosslinked polymers. The small size of MIP micro- or nanoparticles could cause further issues upon disposal, leading to possible leakage to wastewater and eventually to the environment. Owing to the small size of MIP particles, conventional water treatment plants may not be able to completely remove them from sewage, although the amount is small compared to most other pollutants.

One possible solution is to use biodegradable polymers instead. A recent example prepared an MIP nanoparticle system based on poly(lactide-co-glycolide) (PLGA) using biotin as the template.[77] This MIP nanoparticle sample was tested for binding biotin and biotinated BSA. A very high binding imprinting factor of 21.1 was recorded but no selectivity test was carried out. More importantly, a degradation test in PBS at 37 °C showed a 54% mass loss after 30 days. Although the degradation is slow, the test conditions were mild and could be sped up using an enzyme. In another example in this area, a poly(ε-caprolactone) or PCL-based MIP was prepared using theophylline as a template, showing a 6.1 μmol g⁻¹ (1.1 mg g⁻¹).[78] This MIP was tested against caffeine for selectivity, with a selectivity factor of 2.55. More importantly, the MIP was submitted for degradation in 1 mol L⁻¹ NaOH and 90% degradation was recorded in 24 h. However, a much slower (10% over 30 days) was recorded in neutral PBS. Because the polymer component of MMIP in most studies is still PMAA-based nondegradable polymer, combining magnetic and (bio)degradable

1157

properties has still not been seen in MMIPs. This could be a new direction for MMIP development.

Another possible direction of development could be the multitarget capability of MMIPs, such as selective binding and detection for more than one chemical/contaminant. The need for multi-target monitoring is a consequence of the ever increasing complexity in formulation of additives used in food industries. Currently, this can be achieved by a mixture of a number of (M) MIPs for binding of multiple targets but those so-called 'chimera (M)MIPs' could help to simplify the system. However, applications of MMIP are still limited to laboratory-scale research because the preparation includes homogenizing the reaction mixtures. Scaling up this step is still an obstacle. Therefore, use of MMIPs for removing contaminants in real world settings is likely to be associated with a high operational cost. This issue is less prominent if the use of MMIP is in small-scale applications, such as in assembling sensors, or where the targeted molecules to be recovered or isolated are of high value (e.g. essential drugs or noble metals). We anticipate a rapid expansion in the application of MMIPs in a broad range of environmental applications.

ACKNOWLEDGEMENTS

SUPPORTING INFORMATION

Supporting information may be found in the online version of this article.

REFERENCES

1 Verraes C, van Boxstael S, van Meervenne E, van Coillie E, Butaye P, Catry B *et al.*, Antimicrobial resistance in the food chain: a review. *Int J Environ Res Public Health* **10**:2643–2669 (2013).
2 Miranda C and Zemelman R, Antimicrobial multiresistance in bacteria isolated from freshwater Chielan salmon farms. *Sci Total Environ* **293**:207–218 (2002).
3 Carlet J, Pulcini C and Piddock LJV, Antibiotic resistance: a geopolitical issue. *Clin Microbiol Infect* **20**:949–953 (2014).
4 Caro E, Marce R, Cormack P, Sherrington D and Borrull F, Direct determination of ciprofloxacin by mass spectrometry after a two-step solid-phase extraction using a molecularly imprinted polymer. *J Sep Sci* **29**:1230–1236 (2006).
5 Urraca J, Castellari M, Barrios C and Moreno-Bondi M, Multiresidue analysis of fluoroquinolone antimicrobials in chicken meat by molecularly imprinted solid-phase extraction and high performance liquid chromatography. *J Chromatogr A* **1343**:1–9 (2014).
6 Sun XL, Wang JC, Li Y, Yang JJ, Jin J, Shah SM *et al.*, Novel dummy molecularly imprinted polymers for matrix solid-phase dispersion extraction of eight fluoroquinolones from fish samples. *J Chromatogr A* **1359**:1–7 (2014).
7 Zhou XM, Xing D, Zhu DB, Tang YB and Jia L, Development and application of a capillary electrophoresis–electrochemiluminescent method for the analysis of enrofloxacin and its metabolite ciprofloxacin in milk. *Talanta* **75**:1300–1306 (2008).
8 Ionescu R, Jaffrezic-Renault N, Bouffier L, Gondran C, Cosnier S, Pinacho DG *et al.*, Impedimetric immunosensor for the specific label free detection of ciprofloxacin antibiotic. *Biosens Bioelectron* **23**: 549–555 (2007).
9 Yan HY, Cheng XL and Sun N, Synthesis of multi-core–shell magnetic molecularly imprinted microspheres for rapid recognition of dicofol in tea. *J Agric Food Chem* **61**:2896–2901 (2013).
10 Banerjee S and König B, Molecular imprinting of luminescent vesicles. *J Am Chem Soc* **135**:2967–2970 (2013).
11 Armutcu C, Bereli N, Bayram E, Uzun L, Say R and Denizli A, Aspartica-cidin-corporated monolithic columns for affinity glycoprotein purification. *Colloids Surf B Biointerfaces* **114**:67–74 (2014).
12 Yoshikawa M, Tharpa K and Dima S, Molecularly imprinted membranes: past, present, and future. *Chem Rev* **116**:11500–11528 (2016).
13 Hoshino Y, Kodama T, Okahata Y and Shea KJ, Peptide imprinted polymer nanoparticles: a plastic antibody. *J Am Chem Soc* **130**: 15242–15243 (2008).
14 Guan GJ, Liu RY, Mei QS and Zhang ZP, Molecularly imprinted shells from polymer and xerogel matrices on polystyrene colloidal spheres. *Chem A Eur J* **18**:4692–4698 (2012).
15 Schwaminger SP, Fraga-García P, Eigenfeld M, Becker TM and Berensmeier S, Magnetic separation in bioprocessing beyond the analytical scale: from biotechnology to the food industry. *Front Bioeng Biotechnol* **7**:233 (2019).
16 Berensmeier S, Magnetic particles for the separation and purification of nucleic acids. *Appl Microbiol Biotechnol* **73**:495–504 (2006).
17 Uhlen M, Magnetic separation of DNA. *Nature* **340**:733–734 (1989).
18 Azizi A, Shahhoseini F and Bottaro CS, Magnetic molecularly imprinted polymers prepared by reversible addition fragmentation chain transfer polymerization for dispersive solid phase extraction of polycyclic aromatic hydrocarbons in water. *J Chromatogr A* **1610**:460534 (2020).
19 Kuhn J, Aylaz G, Sari E, Marco M, Yiu HHP and Duman M, Selective binding of antibiotics using magnetic molecular imprint polymer (MMIP) networks prepared from vinyl-functionalized magnetic nanoparticles. *J Hazard Mater* **387**:121709 (2020).
20 Hossein Beyki M, Shemirani F and Shirkhodaie M, Aqueous Co(II) adsorption using 8-hydroxyquinoline anchored γ-Fe$_2$O$_3$@chitosan with Co(II) as imprinted ions. *Int J Biol Macromol* **87**:375–384 (2016).
21 Mehdinia A, Dadkhah S, Baradaran Kayyal T and Jabbari A, Design of a surface-immobilized 4-nitrophenol molecularly imprinted polymer via pre-grafting amino functional materials on magnetic nanoparticles. *J Chromatogr A* **1364**:12–19 (2014).
22 Kong X, Gao R, He X, Chen L and Zhang Y, Synthesis and characterization of the core-shell magnetic molecularly imprinted polymers (Fe$_3$O$_4$@MIPs) adsorbents for effective extraction and determination of sulfonamides in the poultry feed. *J Chromatogr A* **1245**:8–16 (2012).
23 Gao D, Wang DD, Fu QF, Wang LJ, Zhang KL, Yang FQ *et al.*, Preparation and evaluation of magnetic molecularly imprinted polymers for the specific enrichment of phloridzin. *Talanta* **178**:299–307 (2018).
24 Ji K, Luo X, He L, Liao S, Hu L, Han J *et al.*, Preparation of hollow magnetic molecularly imprinted polymer and its application in silybin recognition and controlled release. *J Pharm Biomed Anal* **180**: 113036 (2020).
25 Peng R, Zhou Z, Wang Q, Yu Q, Yan X, Qin H *et al.*, An investigation of template anchoring strategy for molecularly imprinting materials based on nanomagnetic polyhedral oligomeric silsesquioxanes composites. *J Chromatogr A* **1597**:28–38 (2019).
26 Deng D, He Y, Li M, Huang L and Zhang J, Preparation of multi-walled carbon nanotubes based magnetic multi-template molecularly imprinted polymer for the adsorption of phthalate esters in water samples. *Environ Sci Pollut Res Int* **28**:5966–5977 (2021).
27 Toudeshki RM, Dadfarnia S and Haji Shabani AM, Surface molecularly imprinted polymer on magnetic multi-walled carbon nanotubes for selective recognition and preconcentration of metformin in biological fluids prior to its sensitive chemiluminescence determination: central composite design optimization. *Anal Chim Acta* **1089**: 78–89 (2019).
28 Wang M, Fu Q, Zhang K, Wan Y, Wang L, Gao M *et al.*, A magnetic and carbon dot based molecularly imprinted composite for fluorometric detection of 2,4,6-trinitrophenol. *Microchim Acta* **186**:86 (2019).
29 Peng J, Liu D, Shi T, Tian H, Hui X and He H, Molecularly imprinted polymers based stir bar sorptive extraction for determination of cefaclor and cefalexin in environmental water. *Anal Bioanal Chem* **409**: 4157–4166 (2017).
30 Xie X, Liu X, Pan X, Chen L and Wang S, Surface-imprinted magnetic particles for highly selective sulfonamides recognition prepared by

reversible addition fragmentation chain transfer polymerization. *Anal Bioanal Chem* **408**:963–970 (2016).

31 Qin SL, Su LQ, Wang P and Gao Y, Rapid and selective extraction of multiple sulfonamides from aqueous samples based on Fe_3O_4–chitosan molecularly imprinted polymers. *Anal Methods* **7**: 8704–8713 (2015).

32 Zuo HG, Lin YS, Ma XX, Feng YH and Luo QH, Preparation of a novel restricted access material combined to core-shell magnetic molecularly imprinted polymers for determination of dimethyl phthalate in soils. *Soil Sediment Contam* **28**:529–546 (2019).

33 Hawkins NJ, Bass C, Dixon A and Neve P, The evolutionary origins of pesticide resistance. *Biol Rev Camb Philos Soc* **94**:135–155 (2018).

34 Aktar MW, Sengupta D and Chowdhury A, Impact of pesticides use in agriculture: their benefits and hazards. *Interdiscip Toxicol* **2**:1–12 (2009).

35 Hallberg GR, The impacts of agricultural chemicals on ground water quality. *GeoJournal* **15**:283–295 (1987).

36 Zhang Y, Liu RJ, Hu YL and Li G, Microwave heating in preparation of magnetic molecularly imprinted polymer beads for trace triazines analysis in complicated samples. *Anal Chem* **81**:967–976 (2009).

37 Miao SS, Wu MS, Zuo HG, Jiang C, Jin SF, Lu YC *et al.*, Coreshell magnetic molecularly imprinted polymers as sorbent for sulfonylurea herbicide residues. *J Agric Food Chem* **63**:3634–3645 (2015).

38 Xu SY, Guo CJ, Li YX, Yu ZR, Wei CH and Tang YW, Methyl parathion imprinted polymer nanoshell coated on the magnetic nanocore for selective recognition and fast adsorption and separation in soils. *J Hazard Mater* **264**:34–41 (2014).

39 Xu LC, Pan JM, Dai JD, Cao ZJ, Hang H, Li XX *et al.*, Magnetic ZnO surface-imprinted polymers prepared by ARGET ATRP and the application for antibiotics selective recognition. *RSC Adv* **2**:5571–5579 (2012).

40 Zhou YS, Zhou TT, Jin H, Jing T, Song B, Zhou YK *et al.*, Rapid and selective extraction of multiple macrolide antibiotics in foodstuff samples based on magnetic molecularly imprinted polymers. *Talanta* **137**:1–10 (2015).

41 Rao W, Cai R, Zhang ZH, Yin YL, Long F and Fu XX, Fast separation and determination of erythromycin with magnetic imprinted solid extraction coupled with high performance liquid chromatography. *RSC Adv* **4**:18503–18511 (2014).

42 Lan HZ, Gan N, Pan DD, Hu FT, Li TH, Long NB *et al.*, Development of a novel magnetic molecularly imprinted polymer coating using porous zeolite imidazolate framework-8 coated magnetic iron oxide as carrier for automated solid phase microextraction of estrogens in fish and pork samples. *J Chromatogr A* **1365**:35–44 (2014).

43 Ma GF and Chen LG, Determination of chlorpyrifos in rice based on magnetic molecularly imprinted polymers coupled with high performance liquid chromatography. *Food Anal Methods* **7**:377–388 (2014).

44 Díaz-Álvarez M, Turiel E and Martín-Esteban A, Molecularly imprinted polymer monolith containing magnetic nanoparticles for the stir-bar sorptive extraction of thiabendazole and carbendazim from orange samples. *Anal Chim Acta* **1045**:117–122 (2019).

45 Ma GF and Chen LG, Development of magnetic molecularly imprinted polymers based on carbon nanotubes - application for trace analysis of pyrethroids in fruit matrices. *J Chromatogr A* **1329**:1–9 (2014).

46 Liang R, Peng Y, Hu Y and Li G, A hybrid triazine-imine core-shell magnetic covalent organic polymer for analysis of pesticides in fruit samples by ultra high performance liquid chromatography with tandem mass spectrometry. *J Sep Sci* **42**:1432–1439 (2019).

47 Gao L, Wang JX, Li XY, Yan YS, Li CX and Pan JM, A core-shell surface magnetic molecularly imprinted polymers with fluorescence for lambda-cyhalothrin selective recognition. *Anal Bioanal Chem* **406**: 7213–7220 (2014).

48 Cheng XL, Yan HY, Wang XL, Sun N and Qiao XQ, Vortex-assisted magnetic dispersive solid-phase microextraction for rapid screening and recognition of dicofol residues in tea products. *Food Chem* **162**: 104–109 (2014).

49 He HB, Dong C, Li B, Dong JP, Bo TY, Wang TL *et al.*, Fabrication of enrofloxacin imprinted organic-inorganic hybrid mesoporous sorbent from nanomagnetic polyhedral oligomeric silsesquioxanes for the selective extraction of fluoroquinolones in milk samples. *J Chromatogr A* **1361**:23–33 (2014).

50 Zhang X, Chen L, Xu Y, Wang H, Zeng Q, Zhao Q *et al.*, Determination of beta-lactam antibiotics in milk based on magnetic molecularly imprinted polymer extraction coupled with liquid chromatography-tandem mass spectrometry. *J Chromatogr B* **878**:3421–3426 (2010).

51 Ji YS, Yin JJ, Xu ZG, Zhao CD, Huang HY, Zhang HX *et al.*, Preparation of magnetic molecularly imprinted polymer for rapid determination of

bisphenol A in environmental water and milk samples. *Anal Bioanal Chem* **395**:1125–1133 (2009).

52 Garcia R, Carreiro EP, Lima JC, Silva MGD, Freitas AMC and Cabrita MJ, Assessment of dimethoate in olive oil samples using a dual responsive molecularly imprinting-based approach. *Foods* **9**:618 (2020).

53 Li XX, Dai YL and Row KH, Preparation of two-dimensional magnetic molecularly imprinted polymers based on boron nitride and a deep eutectic solvent for the selective recognition of flavonoids. *Analyst* **144**:1777–1788 (2019).

54 Wang AX, Lu HZ and Xu SF, Preparation of magnetic hollow molecularly imprinted polymers for detection of triazines in food samples. *J Agric Food Chem* **64**:5110–5116 (2016).

55 Zhang H, Kou W, Bibi A, Jia Q, Su R, Chen HW *et al.*, Internal extractive electrospray ionization mass spectrometry for quantitative determination of fluoroquinolones captured by magnetic molecularly imprinted polymers from raw milk. *Sci Rep* **7**:14714 (2017).

56 Blanchaert B, Jorge EP, Jankovics P, Adams E and van Schepdael A, Assay of kanamycin A by HPLC with direct UV detection. *Chromatographia* **76**:1505–1512 (2013).

57 Pizan-Aquino C, Wong A, Avilés-Félix L, Khan S, Picasso G and Sotomayor MD, Evaluation of the performance of selective M-MIP to tetracycline using electrochemical and HPLC-UV method. *Mater Chem Phys* **245**:122777 (2020).

58 Fagerquist CK, Lightfield AR and Lehotay SJ, Confirmatory and quantitative analysis of β-lactam antibiotics in bovine kidney tissue by dispersive solid-phase extraction and liquid chromatography-tandem mass spectrometry. *Anal Chem* **77**:1473–1482 (2005).

59 Jing T, Wang Y, Dai Q, Xia H, Niu J, Hao Q *et al.*, Preparation of mixed-templates molecularly imprinted polymers and investigation of the recognition ability for tetracycline antibiotics. *Biosens Bioelectron* **25**:2218–2224 (2010).

60 Granados-Chinchilla F and Rodríguez C, Tetracyclines in food and feeding stuffs: from regulation to analytical methods, bacterial resistance, and environmental and health implications. *J Anal Method Chem* **2017**:1315497 (2017).

61 Mutavdžić Pavlović D, Pinušić T, Periša M and Babić S, Optimization of matrix solid-phase dispersion for liquid chromatography tandem mass spectrometry analysis of 12 pharmaceuticals in sediments. *J Chromatogr A* **1258**:1–15 (2012).

62 Chen L, Liu J, Zeng Q, Wang H, Yu A, Zhang H *et al.*, Preparation of magnetic molecularly imprinted polymer for the separation of tetracycline antibiotics from egg and tissue samples. *J Chromatogr A* **1216**:3710–3719 (2009).

63 Li Y, Ding MJ, Wang S, Wang RY, Wu XL, Wen TT *et al.*, Preparation of imprinted polymers at surface of magnetic nanoparticles for the selective extraction of tadalafil from medicines. *ACS Appl Mater Interfaces* **3**:3308–3315 (2011).

64 Gao WR, Li JY, Li P, Huang Z, Cao Y and Liu X, Preparation of magnetic molecularly imprinted polymer (MMIP) nanoparticles (NPs) for the selective extraction of tetracycline from milk. *Anal Lett* **53**: 1097–1112 (2020).

65 Yao GH, Liang RP, Huang CF, Wang Y and Qiu JD, Surface plasmon resonance sensor based on magnetic molecularly imprinted polymers amplification for pesticide recognition. *Anal Chem* **85**:11944–11951 (2013).

66 Baran W, Adamek E, Ziemiańska J and Sobczak A, Effects of the presence of sulfonamides in the environment and their influence on human health. *J Hazard Mater* **196**:1–15 (2011).

67 Li Y, Zhao X, Li P, Huang Y, Wang J and Zhang J, Highly sensitive Fe_3O_4 nanobeads/graphene-based molecularly imprinted electrochemical sensor for 17β-estradiol in water. *Anal Chim Acta* **884**:106–113 (2015).

68 Ozgur E, Yilmaz E, Sener G, Uzun L, Say R and Denizli A, A new molecular imprinting-based mass-sensitive sensor for real-time detection of 17B from aqueous solution-estradiol. *Environ Prog Sustain Energy* **32**:1164–1169 (2013).

69 Liu N, Han J, Liu Z, Qu L and Gao Z, Rapid detection of endosulfan by a molecularly imprinted polymer microsphere modified quartz crystal micro-balance. *Anal Methods* **5**:4442–4447 (2013).

70 Okan M, Sari E and Duman M, Molecularly imprinted polymer based micromechanical cantilever sensor system for the selective determination of ciprofloxacin. *Biosens Bioelectron* **88**:258–264 (2017).

71 Okan M and Duman M, Functional polymeric nanoparticle decorated microcantilever sensor for specific detection of erythromycin. *Sens Actuators B Chem* **256**:325–333 (2018).

1159

72 WHO Model List of Essential Medicines. Available: https://www.who.int/selection_medicines/list/en/ [2 November 2020].

73 Schafhauser BH, Kristofco LA, de Oliveira CMR and Brooks BW, Global review and analysis of erythromycin in the environment: occurrence, bioaccumulation and antibiotic resistance hazards. *Environ Pollut* **238**:440–451 (2018).

74 Lim JK, Yeap SP, Che HX and Low SC, Characterization of magnetic nanoparticle by dynamic light scattering. *Nanoscale Res Lett* **8**:381 (2013).

75 Li JM, Zhao LJ, Wei CL, Sun ZA, Zhao SW, Cai TP *et al.*, Preparation of restricted access media molecularly imprinted polymers for efficient separation and enrichment ofloxacin in bovine serum samples. *J Sep Sci* **42**:2491–2499 (2019).

76 Ou HX, Chen QH, Pan JM, Zhang YL, Huang Y and Qi XY, Selective removal of erythromycin by magnetic imprinted polymers synthesized from chitosan-stabilized Pickering emulsion. *J Hazard Mater* **289**:28–37 (2015).

77 Gagliardi M, Bertero A and Bifone A, Molecularly imprinted biodegradable nanoparticles. *Sci Rep* **7**:40046 (2017).

78 Lee KS, Kim DS and Kim BS, Biodegradable molecularly imprinted polymers based on poly(ε-caprolactone). *Biotechnol Bioprocess Eng* **12**:152–156 (2007).